Numerical Investigation of Laminar Natural Convention Flows in Obstructed Vertical Channels

by

Abdullah Moosa Muhanna

A Thesis Presented to the

FACULTY OF THE COLLEGE OF GRADUATE STUDIES

KING FAHD UNIVERSITY OF PETROLEUM & MINERALS

DHAHRAN, SAUDI ARABIA

In Partial Fulfillment of the
Requirements for the Degree of

MASTER OF SCIENCE

In

MECHANICAL ENGINEERING

January, 1991

INFORMATION TO USERS

This manuscript has been reproduced from the microfilm master. UMI films the text directly from the original or copy submitted. Thus, some thesis and dissertation copies are in typewriter face, while others may be from any type of computer printer.

The quality of this reproduction is dependent upon the quality of the copy submitted. Broken or indistinct print, colored or poor quality illustrations and photographs, print bleedthrough, substandard margins, and improper alignment can adversely affect reproduction.

In the unlikely event that the author did not send UMI a complete manuscript and there are missing pages, these will be noted. Also, if unauthorized copyright material had to be removed, a note will indicate the deletion.

Oversize materials (e.g., maps, drawings, charts) are reproduced by sectioning the original, beginning at the upper left-hand corner and continuing from left to right in equal sections with small overlaps. Each original is also photographed in one exposure and is included in reduced form at the back of the book.

Photographs included in the original manuscript have been reproduced xerographically in this copy. Higher quality 6" x 9" black and white photographic prints are available for any photographs or illustrations appearing in this copy for an additional charge. Contact UMI directly to order.

UMI

A Bell & Howell Information Company
300 North Zeeb Road, Ann Arbor MI 48106-1346 USA
313/761-4700 800/521-0600

NOTE TO USERS

The original document received by UMI
contained pages with
indistinct print. Pages were filmed as received.

This reproduction is the best copy available.

UMI

NUMERICAL INVESTIGATION OF LAMINAR NATURAL CONVECTION FLOWS IN OBSTRUCTED VERTICAL CHANNELS

BY

ABDULLAH MOOSA MUHANNA

A Thesis Presented to the

FACULTY OF THE COLLEGE OF GRADUATE STUDIES

KING FAHD UNIVERSITY OF PETROLEUM & MINERALS

DHAHRAN, SAUDI ARABIA

LIBRARY
KING FAHD UNIVERSITY OF PETROLEUM & MINERALS
DHAHRAN - 31261, SAUDI ARABIA

In Partial Fulfillment of the
Requirements for the Degree of

MASTER OF SCIENCE

In

MECHANICAL ENGINEERING

JANUARY 1991

UMI Number: 1381137

UMI Microform 1381137
Copyright 1996, by UMI Company. All rights reserved.

This microform edition is protected against unauthorized
copying under Title 17, United States Code.

UMI
300 North Zeeb Road
Ann Arbor, MI 48103

KING FAHD UNIVERSITY OF PETROLEUM & MINERALS

DHAHRAN, SAUDI ARABIA

This thesis, written by

ABDULLAH MOOSA MUHANNA

under the direction of his thesis committee, and approved by all the members, has been presented to and accepted by the Dean, College of Graduate Studies, in partial fulfillment of the requirements for the degree of

MASTER OF SCIENCE IN MECHANICAL ENGINEERING

Spec -
A
1
.M844
C.2
1069636 / 1069669

Thesis Committee

Chairman (Dr. S.A.M. Said)

Member (Dr. H.M. Badr)

Member (Dr. A.A. Shaikh)

Member (Dr. A.Z. Sahin)

Dr. H.I. Abualhamayel
Department Chairman

Dr. Ala H. Rabeh
Dean College of Graduate Studies

Date : 25 - 6 - 91

This thesis is dedicated

To

My beloved father, mother, brothers and sisters

for their love, support, encouregement

and sacrifice

and

all moslims in the world fighting against occupation

to librate their countries

especially the Children of Al-Aqssa Mosque

إهداء

إلى منبع العطاء ... أبى الحبيـــــب ،
إلى نبع الحنـان ... أمى الحبيبـــــة ،
إلى الأحبـــــة ... إخوتي وأخواتـي ،

و

إلى جميع المسلمين في شتى بقاع الأرض الذين
يجاهدون في سبيل الله لتحرير بلادهم من يد
الاحتلال وخصوصاً أطفال الحجارة
وشهداء المسجد الأقصى

أهدي هذه الرسالة

ACKNOWLEDGEMENT

Thanks be to ALLAH ALMIGHTY for all the knowledge he has given me. Also, praise and gratitude be to ALLAH ALMIGHTY, with whose gracious help it was possible to accomplish this work.

Acknowledgement is due to King Fahd University of Petroleum and Minerals for their support during this study.

My thanks and sincere appreciation are to my thesis advisor Dr. Syed-Ahmed Said who gave me the chance to extend my knowledge tremendously and who has been a constant source of help and encouragement during this study. I also greatly appreciate the help and support extended by Dr. Hasan Badr, Dr. Abdullah Shaikh and Dr. Ahmet Sahin who served as my thesis committee members.

Also I would like to thank the Data Processing Center (DPC) staff for their continuous assistance and help especially Mr. Hamed Qadri who gave me a lot of his own time.

Thanks are to my dear friends for their co-operation and moral support especially Mr. Eahab Al-Zaharnah who has been a friend indeed by being a friend in need.

Lastly, but not least, I am very thankful to my beloved Father, Mother, brothers and sisters for their pray, patience, ecouregement, support and understanding. I owe my friend and brother Aiman a tremendous gratitude for his support and encouregement all the way through my study. Thanks also are to all of my relatives who always have been a constant source of encouregement.

TABLE OF CONTENTS

LIST OF FIGURES

LIST OF TABLES

LIST OF SYMBOLS

AR	:	aspect ratio
b	:	distance between the walls of a parallel-walled Channel
Cp_o	:	specific heat at constant pressure
g	:	the magnitude of the acceleration
Gr	:	Grashof number
K_o	:	thermal conductivity
L	:	stream-wise length of the channel wall
$\overline{L}_1$	:	dimensional distace from the entrance of the channel to the obstruction center-line
L_1	:	dimensionless distace from the entrance of the channel to the obstruction center-line
$\overline{L}_2$	:	dimensional obstruction width
L_2	:	dimensionless obstruction width
n	:	normal direction
$\overline{Nu}$	:	average Nusselt number
Nu_l	:	local Nusselt number
$\overline{P}$	:	pressure of the fluid
$\overline{P'}$	:	motion pressure
$\overline{P}_\infty$	:	pressure of the fluid when it is at rest at uniform temperature

Pr	:	Prandtl number
Ra	:	Rayliegh number
Ra'	:	modified Rayliegh number
Re	:	Reynold number
S	:	distance between the walls of any channel
S_{min}	:	minimum distance between the walls of any channel
S_{max}	:	maximum distance between the walls of any channel
S_{avg}	:	the average of S_{min} and S_{max}
S_{ent}	:	the distance between the walls at the channel entrance
S_{exit}	:	the distance between the walls at the channel exit
$\overline{T}$	:	dimensional temperature
$\overline{T}_{\infty}$	:	dimensional surrounding temperature
$\overline{T}_{o}$	:	reference temperature
u	:	dimensionless velocity component in the x direction
$\overline{u}$	:	dimensional velocity component in the $\overline{x}$ direction
v	:	dimensionless velocity component in the y direction
$\overline{v}$	:	dimensional velocity component in the $\overline{y}$ direction
x	:	non-dimensional axis in the vertical direction
$\overline{x}$	:	dimensional axis in the vertical direction
y	:	non-dimensional axis in the horizontal direction
$\overline{y}$	:	dimensional axis in the horizontal direction

GREEK SYMBOLS

β_o	:	thermal expansion
γ	:	angle of inclination (convergence or divergence)
ρ	:	fluid density
μ	:	dynamic viscosity
ν	:	kinematic viscosity
θ	:	dimensionless temperature

THESIS ABSTRACT

NAME OF STUDENT : *ABDULLAH MOOSA NADHIR MUHANNA*

TITLE OF STUDY : *Numerical Investigation of Laminar Natural Convection Flows in Obstructed Vertical Channels*

MAJOR FIELD : *Mechanical Engineering*

DATE OF DEGREE : *January, 1991*

Natural convection heat transfer is numerically studied in a vertical parallel-walled, convergent and divergent channels with a single square obstruction. The channel walls are maintained at a uniform temperature which exceeds the ambient temperature. The working fluid is air. It can be seen that the average Nusselt number curve for the obstructed channel represents the three flow regimes (fully developed limit, transition and isolated plate limit). The presence of an obstruction reduces the average Nusselt number compared to the unobstructed channel. This reduction increases as the Rayliegh number decreases. The average Nusselt number depends on the Rayliegh number, the aspect ratio, the obstruction size, the obstruction location and the angle of convergence or divergence. The effects of all these parameters are studied and reported. It is found that moving the obstruction location away from the entrance towards the exit of the channel will decrease the average Nusselt number. Increasing the angle of convergence, increases the average Nusselt $(\overline{Nu}_{exit})$ *for Rayliegh number* $(Ra_{exit}) < 700$ *and decreases it for* $(Ra_{exit}) > 700$. *Basing the average Nusselt number and the Rayliegh number on the entrance width of the convergent channel* (S_{ent}), *average Nusselt number curves for the parallel-walled channel can be used for convergent channel with a maximum error of 20%. Increasing the angle of divergence increases the average Nusselt number at low Rayliegh numbers. Finally, a comparison between convergent and divergent channels having the same angle of convergence and divergence, shows that the average Nusselt number for the convergent channel is higher than that for the divergent one.*

MASTER OF SCIENCE DEGREE

KING FAHD UNIVERSITY OF PETROLEUM AND MINERALS

Dhahran , Saudi Arabia

January 1991

خلاصة الرسالة

إسم الطالـــــــب : عبدالله موسى نظير مهنا

عنوان الدراســـــة : استقصاء عددي للجريان غير المضطرب عن طريق الحمل في القنوات الرأسية ذات النتوء

مجال التخصـــــص : هندسة ميكانيكية

تاريخ الدرجةالعلمية : ٥ يناير ١٩٩١م

تمت دراسة انتقال الحرارة عن طريق الحمل في القنوات الرأسية (متوازية ، متقاربة ومنفرجة الجدارين) ذات نتوء مربع واحد على أحد الجدارين . تم ثبيت درجة حرارة جداري القناة والنتوء على درجة حرارة ثابتة تفوق درجة حرارة المحيط الخارجي للقناة وكان الهواء هو المائع المستخدم في الدراسة . يعتمد رقم نسلتْ المتوسط (Nu) على العناصر التالية : رقم الرالي (Ra) ، النسبة الباعية (AR) ، قياس بعد النتوء ، مكان وجود النتوء وكذلك زاوية التقارب أوالإنفراج . وقد تم بحث ودراسة كل العناصر السابقة . شُوهِدَ من الرسم البياني لـ Nu للقناة الرأسية ذات النتوء أنه يمثل ثلاث أنظمة (المتطور تماماً ، المقطع الانتقالي ، والجدران المنفصلة) . وجود النتوء قلّل من قيمة Nu إذا ما قورن بالقنوات التي ليس بها نتوء ويزداد هذا النقص كلما صَغُرتْ قيمة Ra . وُجِدَ أن تحريك مكان النتوء بعيداً عن مدخل القناة إلى ناحية مخرج القناة يقلّل من قيمة Nu . كما وُجِد أن زيادة زاوية التقارب يزيد من قيمة Nu في النطاق $Ra_{exit}<700$ ، بينما يقل في النطاق $Ra_{exit}>700$.

ثبت من الدراسة أن Nu للقنوات الرأسية المتوازية الجدران ممكن إستخدامها للقنوات الرأسية المتقاربة الجدران بحد أقصى للخطأ مقداره ٢٠٪ وذلك في حالة حساب قيمة Nu و Ra بدلالة عرض المدخل في القنوات المتقاربة الجدران (S_{ent}) . كما وُجد أن زيادة زاوية الإنفراج يزيد من قيمة Nu في القيم الصغيرة من Ra . أخيراً ، بمقارنة نتائج القنوات المتقاربة والمنفرجة الزوايا والتي لها نفس قيمة الزاوية (التقارب أو الإنفراج) وُجد أن Nu للقنوات الرأسية المتقاربة الزوايا أكبر من تلك التي للقنوات الرأسية المنفرجة الزوايا .

درجة الماجستير في العلوم

جامعة الملك فهد للبترول والمعادن

الظهران - المملكة العربية السعودية

يناير ١٩٩١م

CHAPTER 1

INTRODUCTION

Steady-state natural convection is often a convenient and inexpensive mode of heat transfer. Steady-state natural convection flows in vertical channels are of interest in a wide number of engineering applications. One of these applications is the cooling of electronic equipments, such as, transformers, power supplies, main-frame computers, radiators, transistors and many other equipments. A second application of natural convection flows in channels is the cooling of nuclear reactors by natural convection flows produced by the temperature difference between the nuclear reactor core and the gas surrounding it. Heating of buildings via trombe walls is another application.

A comprehensive literature review of natural convection heat transfer along vertical plates and channels is presented in the next chapter, however, special aspects will be presented here. Reviews of the importance of heat transfer considerations in the design of electronic equipment have been given in [1 − 4]. Many diverse flow configurations are of interest in electronic cooling applications. The most important of these configurations is the vertical channel.Vertical channels can be classified into two main categories. The first category is the smooth vertical channels (no protrusion from the channel walls) where the second category is the obstructed (with protrusion from the channel walls) vertical channels. Furthermore, each category can be classified into parallel, convergent and divergent vertical channels.

Laminar natural convection heat transfer in smooth parallel-walled vertical channels (unobstructed) has been investigated theoretically (on the basis of boundary-layer equations) , as well as experimentally. Many aspects of these flows are presently well understood. Governing equations describing the flows in an unobstructed channel are parabolic in nature and their analysis may be based on the boundary-layer equations. The case of natural convection heat transfer in convergent and divergent smooth vertical channels, using water as the working fluid, has been reported in the literature.

When obstructions (protrusions from a channel wall) are located inside a channel, the problem becomes elliptic and so difficult to be solved analytically. Very little is known about the natural convection phenomena in such complex flows. Very recently, numerical and experimental studies have been reported for natural convection heat transfer in parallel-walled obstructed vertical channels. However, to the best of the author's knowledge, the problem of natural convection flows in divergent and convergent obstructed vertical channels has not been studied yet. Thus there is a definite need for investigation of natural convection flows in obstructed parallel-walled, convergent and divergent vertical channels. ***Hence the objective of this research is to perform a numerical investigation on steady-state, laminar natural convection flows of air in parallel-walled, convergent and divergent vertical channels with a single square obstruction.***

CHAPTER 2

LITERATURE REVIEW

During the past 60 years cooling technology of electornic equipment has received a great attention. The evolution of cooling technology includes the progressive research of using natural convection, which is an inexpensive mode of heat transfer, in electronic equipments cooling. Vertical plates and channels are one of the most encountered configurations used in natural convection cooling of electronic equipments. In this chapter, a general review will be presented regarding the development of electronic equipment cooling technology, however, the major portion of the review will be devoted to natural convection in vertical channels.

In 1986 Bergles [5] presented a very general review for the historical papers presented in the development of cooling technology for electronic equipments. This review presented the major events in the evolution of cooling technology. Examples of these events are the development of the 30 ton modern digital computer in the 1940's, the rapid increase in the number of components (transistors, resistors, etc) per silicon chip from the order of 10 in 1960 to the order of 1000 in 1970 and from the order of 10,000 at the end of 1970's to the development of the latest supercomputer which has 500,000 components in a chip, and nearly 100 million instructions per second. Later, Incorpora [6] presented a comprehensive review of electronic equipment cooling by different modes of heat transfer. Natural convection heat transfer in parallel channels,

inclined channels and enclosures as well as other configurations with different operating conditions have been presented. Heat transfer by forced and mixed convection from different configurations have been reviewed also.

Actually, the importance of heat transfer considerations in the design of electronic equipment has been studied extensively by Aung and Chimah [1], Jaluria [2], Kraus and Bar-Cohen [3], and Stienberg [4]. The important aim in the design of electronic equipment is to increase circuit speeds which can be facilitated by the integration of circuit functions, by circuit miniaturaization and by higher density packaging [1]. Eventhough power dissipation per circuit is decreased as a result of the miniaturization of circuits, the power generation per unit volume,which is the important parameter in determining the circuit temperature, is actually increased due to the much higher packaging densities [1]. Different cooling techniques have been studied extensively by Kraus and Bar-Cohen [3] and Stienberg [4].

During the evolution of cooling technology, different configurations are encountered in cooling of electronic equipments. The following are examples of such configurations. Ortiga and Moffat [7] presented an experimental data for heat transfer from a uniformly heated array of cubical roughness elements mounted on an insulating wall in a channel. Meara and Poulikakos [8] studied experimentally cooling by natural convectin of an array of vertical plates with uniform and equal heat fluxes. Karki and Patankar [9] investigated the laminar natural convection in a vertical shrouded fin array, in which the flow is induced from the surroundings by the chimney effect.

Natural convection heat transfer from a flat plate in vertical, inclined and horizontal positions has been studied extensively both theoretically and experimentally. Analytical studies have been reported in refrences [10 – 16] for the case of plates kept at uniform surface temperature or uniform surface heat flux. Experimental investigations on the same subject have been reported in refrences [17 – 22] covering both laminar and turblent flows under either isothermal or constant heat flux conditions.

Fujii and Imura [20] studied experimentally the case of natural convection heat transfer from two different sized plates with arbitrary inclination. The working fluid was water. Different correlations for the average Nusselt number ($\overline{Nu}$) as a function of Rayleigh number (Ra) have been presented for the different cases of vertical, inclined and horizontal plates facing both downwards and upwards. Chen et al. [23] studied analytically the flow and heat transfer characteristics of natural convection heat transfer in which the wall temperature or surface heat flux varies as the power of the axial coordinate. Both air and water were used as working fluid. Later, Al-Arabi and Sakar [24] obtained experimentally local and average heat transfer data for natural convection heat transfer from isothermal vertical and inclined plates using air as the working fluid. They ensured the condition of infinite plate width and suggested equations representing their results.

Understanding heat transfer cooling in electronic equipments resulted in making the subject of natural convection in smooth vertical channels receive a great deal of attention. Elenbass [25] was the first to document a detailed

study of thermal characteristics of cooling by natural convection in smooth parallel- walled vertical channels using air as the fluid. A good agreement was found between the experimental data and the theoretical results. One of his main findings was that the single flat plate solution would have to be approached for large plate spacings. Measurements were done also for different angles of inclination for an inclined parallel-walled channels.

Bodoia and Osterle [26] studied numerically, using finite difference method, the development of free convection in air between heated vertical parallel plates. This study confirmed numerically the experimental results of Elenbass [25]. It was assumed that the fluid enters the channel with ambient temperature and a flat velocity profile. The calculated average Nusselt numbers ($\overline{Nu}$) showed that $\overline{Nu}$ increases monotonically with the Rayielgh number (Ra) in the range of Ra from 1 to 10^4. At the same time, its asymptotes for low and high Ra agreed with the fully developed flow and the single heated surface solutions, respectively. Engle and Muller [27] analysed the development of natural convection in channels of large lengths for a wide range of Prandtl numbers (Pr) and Rayleigh numbers for both constant heat flux and constant wall temperature boundary conditions.

Aung [28] presented a closed form solution for the fully developed flow for laminar free convection in a vertical parallel-walled channel but with asymmetric heating conditions. The walls were maintained either at uniform heat flux (UHF) or uniform wall temperature (UWT). Simultaneosly, Aung et al. [29] investigated the developing laminar free convection heat transfer in vertical par-

allel-walled channels experimentally and numerically using finite difference method. The boundary condition of the fluid at the entrance of the channel were assumed to be as those of Bodoia and Osterle [26]. For fully developed flow, the numerical solution asymptotically approached the closed form solution when the channel hight is considerably larger than the channel width. For the case of UHF , the result for a single vertical plate was found to be applicable for small channel hight. The theoritical results for the case of UWT were verified experimentally.

In 1972 Currie and Newman [30] measured experimentally the temperature and velocity profiles between an isothermal parallel-walled vertical channel for three diffrent spacings between the plates at different hights of the channel. The velocity profiles were found to be fitted by a parabola where the temperature profiles were found to be fitted by a hyperabola.The induced flow rate calculated from the experiments was found to be in good agreement with previous theoretical results [26 , 27].

Optimum plate spacings for laminar natural convection heat transfer from parallel vertical isothermal flat plates has been studied experimentally and theoretically. Experimentally, Elenbass [25] suggested that for the maximum amount of heat dissipation from the plate surfaces, the plate spacing can be determined by taking the modified Rayleigh number (Ra') (defined as (b/L)*Ra) to be Ra' = 46. Theoretically, Bodoia and Osterle [26] obtained a value of Ra' = 70 for the same condition. It should be noted that these values proposed by both Bodoia and Osterle [26] and Elenbass [25] correspond to the physical problem of determining the optimum number of isothermal vertiacl fins that

should be attached to a surface of a given size for maximizing the heat dissipation from that surface. Another optimum has been found analytically by Levy [31]. The minimum plate spacing for a minimum difference in temperature between the plates and the fluid is obtained from the relation $Ra' = 600$. It is seen that Elenbasss optimum [25] yields a temperature difference that is 38 percent higher than the minimum temperature difference of Levy [31]. Bar-Cohen and Rohsenow [32] established an approximate analytical structure for determining the channel width appropriate to various thermal constraints for symmetric and asymmetric, isothermal and isoflux boundary conditions.

In 1979 Akbari and Borgers [33] studied free convective laminar heat transfer between the channel surfaces of the trombe wall. The study was done using a line-by-line forward marching implicit finite-difference technique. The study was restricted to laminar flow between two parallel plates, each at some effective uniform temperature. As a starting condition, a uniform inlet velocity profile and a dynamic contribution to the inlet pressure reduction were selected. The investigation was done for dimensionless laminar flow rates from $Q = 0.003$ to 0.03 using air as the working fluid. Correlations have been developed for the computed results which can be used in building design.

In 1980 Sparrow and Bahrami [34] studied experimentally natural convection heat transfer along parallel, square vertical plates. The experimental study encompassed three different types of hydrodynamic conditions along the lateral edges : (1) fully open to ambient, (2) blockage of one of the edge gaps and (3) blockage along both of the edge gaps. For $Ra' > 10$, the results for both the singly and doubly blocked configurations are coincident with those for the fully

open configuration. For the singly blocked configuration, a modest effect was found at small modified Rayliegh number ($Ra' < 4$) . Therefore, lateral edges effect can be neglected and the system can be treated as if it were a parallel plate channel.

In 1981 Joshi and Gebhart [35] studied numerically the effect of both viscous dissipation and pressure stress on natural convection flows in parallel-walled vertical channels for various types of surface temperature variations. The Boussinesq approximation and boundary layer assumption were incorporated and the fluid properties were assumed to be constant. It was observed that the pressure stress term has a much greater effect than viscous dissipation, on heat transfer, for all surface conditions analysed.

In 1983 Yao [36] investigated the problem of mixed convection in vertical channel. An analytical solution is developed to study the hydrodynamically and thermally developing laminar flow (entry flow) in a heated channel. The solution indicates that the dominant heat transfer mode becomes the natural convection if $Gr^2 > Re$ for constant wall heat flux, and $Gr > Re$ for constant wall temperature.

In 1984 Sparrow et al. [37] performed experimental and numerical studies for natural convection in an open-ended vertical channel. One of the principal walls of the channel (the heated wall) was maintained at a uniform temperature, while the other wall was unheated. The experiments were carried out with water as the working fluid. The obtained numerical solutions via a parabolic finite difference scheme yielded Nusselt numbers in good agreement with those

of the experimental results.

In 1984 Azevedo and Sparrow [38] investigated experimentally the effect of inclination on natural convection in a parallel-walled channel. Three heating modes were included, namely, (1) both walls heated and maintained at the same uniform temperature, (2) heating only from the upper wall and (3) heating only from the lower wall. The last two modes were considered for inclined parallel-walled channels, however, it is considered as one mode, which is a channel with one heated wall and one unheated wall, for the case of the angle of inclination $\gamma = 0$. Different correlations have been reported for such different heating modes.

In 1985 Burch et al. [39] studied natural convection between finitely conducting vertical walls using finite difference method. It has been shown that conduction has a significant influence on the natural convection heat transfer, particularly at high Gr, low wall-to-fluid conductivity ratios and high wall thickness-to-channel width ratios. The solid-fluid interface temperature distribution was found to be non-uniform. Also, conduction affected both temperature and velocity profiles.

In 1986 Azevedo and Sparrow [40] were the first to study experimentally and numerically the response of natural convection heat transfer and fluid flow characterestics of one-sided heated vertical channel to fluid entering the channel through a vent in the unheated wall. They based their analysis on the standard boundary layer approximations and the Boussinesq model for the variation of density. The working fluid was water. Experimentally, the average nusselt num-

ber for the channel was found to be insensitive to either the vent opening size or the axial location of the vent and this result was in a good agreement with the numerical solution. It was found also that when the vent opening is at the lower position, near the entrance of the channel, no change is observed in the total mass flow rate ($\dot{m}_{tot}/\dot{m}_{no/vent} \cong 1$). On the other hand, a 10 percent increase in the total mass flow rate was found for the other two locations of the vent, the mid and higher positions, due to the existence of the vent. Numerically, it was found that the local Nusselt number along the heated wall exhibited sharp peaks due to the relatively cool fluid entering the channel through the vent. Upstream of the vent position, it was found that the local nusselt number is lower than that for the unvented channel. Downstream of the vent, the opposite criterion applied.

In 1985 Sparrow and Azevedo [41] investigated experimentally and numerically natural convection in vertical channels bounded by an isothermally heated wall and by unheated wall. The numerical results displayed virtually perfect agreement with the experiments leading to the conclusion that the experimentally determined Nusselt numbers were not affected by heat conduction in the unheated wall. A formula for the average Nusselt number representing the experimental data spanning the fully-developed and flat plate limits was developed.

From the above literature review it can be concluded that the configuration of vertical parallel-walled channel has received the attention and interest of several researchers during the last two decades. Many aspects of the problem are

presently well understood.

In 1988 Sparrow et al. [42] studied numerically bouyancy driven flow in a convergent (a decrease in cross-sectional area in the flow direction) smooth vertical channel. The two walls of the channel, were maintained at the same uniform temperature. Finite difference solutions were used for solving the governing differential equations on the basis of boundary layer approximations. A graphical representation of the results show the average Nusselt number ($\overline{Nu}_S$) as the ordinate while the modified Rayleigh number (Ra'_S) as the abssissa. Both ($\overline{Nu}_S$) and (Ra'_S) were based on (S) which is the spacing between the channel walls. Three channel spacings were considered, namely, S_{min} , S_{avg} ,and S_{max} which are the minimum, the mean and the maximum space between the channel walls respectivly. It was found that the average Nusselt number correlation deduced by Azevedo and Sparrow [38] can be used for the convergent channels with half angels of convergence less than 15° . The deviation between the convergent channel and parallel channel average nusselt numbers were limited to about 5 percent. Also Sparrow and Ruiz [43] extended their studies to include divergent channels (an increase in cross-sectional area in the flow direction). The flow visualization performed for the divergent channel indicated the presence of an up flow boundary layers adjacent to the channel walls, with a recirculation loop occupying the remainder of the cross-section. The central portion of the circulation loop was found to be downflow where the outer portion was found to be an upflow. This yields that at various sections of the divergent channel, there is both upflow and downflow. However, at all cross

sections in the convergent channel, the flow was exclusively an upflow. Regarding the heat transfer results, it was found that the correlation given by Azevedo and Sparrow [38] can be used as a universal correlation for divergent, convergent and parallel channels with the average Nusselt number being defined in terms of S_{max} for both convergent and divergent channels.

Heat transfer correlations in smooth parallel-walled vertical channels do not incorporate the effects of the finite disturbance introduced by the presence of the electronic component(s) in the channel. When an obstruction (protrusion from a channel wall) is located inside the channel, the problem becomes elliptic. Such problems have received little attention in the recent literarture. Habachi and Achraya [44] studied numerically the problem of laminar mixed convection of air in a parallel-walled channel with a vertical blockage on one wall. Two different cases have been considered which are symmetric heating and asymmetric heating. The differential equations were solved using an implicit, elliptic finite difference procedure called SIMPLER which was developed by Patanker [45] It was found that for both symmetric and asymmetric heating cases, the Nusselt numbers are smaller than the corresponding smooth parallel-walled channel Nusselt numbers. Sparrow and Chrysler [46] studied experimentally the problem of natural convection along a vertical plate with a short horizontal cylinder. Also, recently Said and Krane [47] investigated numerically and experimentally the problem of natural convection heat transfer in parallel-walled vertical channels with a single semi- circular obstruction. Air was used as the working fluid. The study covers the range of Rayleigh number from 10^2 to 10^4. Two thermal conditions of the parallel walls were considred : uniform

wall temperature (UWT) and uniform heat flux (UHF).

From this review, it can be concluded that natural convection heat transfer in smooth vertical channels, where the problem is parabolic, such as parallel-walled, convergent and divergent channels, have been investigated and studied experimentally and numerically, while very little study was conducted on natural convection in parallel walled obstrucated vertical channels and non on convergent and divergent obstructed vertical channels. ***Hence the objective of this study is to perform a numerical investigation on steady-state, laminar natural convection flows of air in parallel walled, convergent and divergent vertical channels with a single square obstruction.***

CHAPTER 3

FORMULATION OF THE PROBLEM

This study considers the two dimensional, steady-state, laminar natural convection flows of of Newtonian fluid in the obstructed vertical channel shown in Figures (3.1 and 3.2). It is assumed that the flows can be adequately modeled by the Boussinesq approximation and that compression work, viscous dissipation and radiative transport are negligibly small. Thus the conservation equations can be written as :

Conservation of Mass

$$\frac{\partial \bar{u}}{\partial \bar{x}} + \frac{\partial \bar{v}}{\partial \bar{y}} = 0 \tag{3-1}$$

Conservation of Momentum

$$\bar{u}\frac{\partial \bar{u}}{\partial \bar{x}} + \bar{v}\frac{\partial \bar{u}}{\partial \bar{y}} = -\frac{1}{\rho_o}\frac{\partial \bar{P'}}{\partial \bar{x}} + \nu_o\left\{\frac{\partial^2 \bar{u}}{\partial \bar{x}^2} + \frac{\partial^2 \bar{u}}{\partial \bar{y}^2}\right\} + g\beta_o(\bar{T} - T_\infty) \tag{3-2}$$

$$\bar{u}\frac{\partial \bar{v}}{\partial \bar{x}} + \bar{v}\frac{\partial \bar{v}}{\partial \bar{y}} = -\frac{1}{\rho_o}\frac{\partial \bar{P'}}{\partial \bar{y}} + \nu_o\left\{\frac{\partial^2 \bar{v}}{\partial \bar{x}^2} + \frac{\partial^2 \bar{v}}{\partial \bar{y}^2}\right\} \tag{3-3}$$

Conservation of Energy

$$\rho_o Cp_o\left\{\bar{u}\frac{\partial \bar{T}}{\partial \bar{x}} + \bar{v}\frac{\partial \bar{T}}{\partial \bar{y}}\right\} = K_o\left\{\frac{\partial^2 \bar{T}}{\partial \bar{x}^2} + \frac{\partial^2 \bar{T}}{\partial \bar{y}^2}\right\} \tag{3-4}$$

where $\bar{u}$, $\bar{v}$ are the velocity components in the $\bar{x}$ and $\bar{y}$ directions , $\bar{T}$ is the temperature at a point in the channel and g is the magnitude of the accelera-

tion due to gravity . $\overline{P'}$ is the "motion pressure" which is defined as the actual pressure in fluid less than the pressure when the fluid is at rest at uniform temperature, T_o. It is defined as $\overline{P'}(\bar{x}) = \overline{P}(\bar{x}) - \overline{P}_\infty(\bar{x})$. The other parameters, namely, ρ_o , ν_o , β_o , Cp_o , and K_o are the fluid density, kinematic viscosity, coefficeicnt of thermal expansion, specific heat at constant pressure and thermal conductivity for air all evaluated at a reference temperature, T_o.

The relevant hydrodynamic and thermal boundary conditions will be written for the convergent and divergent channels. Considering the limiting case of $\gamma = 0$, where γ is the angle of convergence or divergence, we can get directly those for the parallel-walled channel. The boundary conditions for the convergent channel are given as follows :

The Channel Entrance

$$\left.\begin{aligned} \bar{v} &= 0 \\ -\overline{P} + \mu\frac{\partial \bar{u}}{\partial \bar{x}} &= 0 \\ \overline{T} &= T_\infty \end{aligned}\right\} \qquad \begin{aligned} 0 \le \bar{y} \le 2L\sin\gamma + b \\ \bar{x} = 0 \end{aligned} \tag{3-5}$$

The Channel Exit

$$\left.\begin{aligned} \bar{v} &= 0 \\ -\overline{P} + \mu\frac{\partial \bar{u}}{\partial \bar{x}} &= 0 \\ \frac{\partial \overline{T}}{\partial \bar{x}} &= 0 \end{aligned}\right\} \qquad \begin{aligned} L\sin\gamma \le \bar{y} \le L\sin\gamma + b \\ \bar{x} = L\cos\gamma \end{aligned} \tag{3-6}$$

The Obstructed Wall

For convenience and clarity the obstructed plate has been divided into five parts as shown in Figure(3.1).

part a

$$\left.\begin{array}{l}\bar{u}\cos\gamma + \bar{v}\sin\gamma = 0\\ \bar{u}\sin\gamma + \bar{v}\cos\gamma = 0\\ \bar{T} = T_w\,(\text{const.})\end{array}\right\} \quad \begin{array}{c} L\sin\gamma + b \le \bar{y} \le \left(L + \bar{L}_1 - \dfrac{\bar{L}_2}{2}\right)\sin\gamma + b \\ \left(\bar{L}_1 + \dfrac{\bar{L}_2}{2}\right)\cos\gamma \le \bar{x} \le L\cos\gamma \end{array} \tag{3-7}$$

part b

$$\left.\begin{array}{l}\bar{u}\cos\gamma + \bar{v}\sin\gamma = 0\\ \bar{u}\sin\gamma + \bar{v}\cos\gamma = 0\\ \bar{T} = T_w\,(\text{const.})\end{array}\right\} \quad \begin{array}{c} \left(L + \bar{L}_1 - \dfrac{\bar{L}_2}{2}\right)\sin\gamma + b - \bar{L}_2\cos\gamma \le \bar{y} \le \left(L + \bar{L}_1 - \dfrac{\bar{L}_2}{2}\right)\sin\gamma + b \\ \left(\bar{L}_1 + \dfrac{\bar{L}_2}{2}\right)\cos\gamma - \bar{L}_2\sin\gamma \le \bar{x} \le \left(\bar{L}_1 + \dfrac{\bar{L}_2}{2}\right)\cos\gamma \end{array} \tag{3-8}$$

part c

$$\left.\begin{array}{l}\bar{u}\cos\gamma + \bar{v}\sin\gamma = 0\\ \bar{u}\sin\gamma + \bar{v}\cos\gamma = 0\\ \bar{T} = T_w\,(\text{const.})\end{array}\right\} \quad \begin{array}{c} \left(L + \bar{L}_1 - \dfrac{\bar{L}_2}{2}\right)\sin\gamma + b - \bar{L}_2\cos\gamma \le \bar{y} \le \left(L + \bar{L}_1 + \dfrac{\bar{L}_2}{2}\right)\sin\gamma + b - \bar{L}_2\cos\gamma \\ \left(\bar{L}_1 - \dfrac{\bar{L}_2}{2}\right)\cos\gamma - \bar{L}_2\sin\gamma \le \bar{x} \le \left(\bar{L}_1 + \dfrac{\bar{L}_2}{2}\right)\cos\gamma - \bar{L}_2\sin\gamma \end{array} \tag{3-9}$$

part d

$$\left.\begin{array}{l}\bar{u}\cos\gamma + \bar{v}\sin\gamma = 0\\ \bar{u}\sin\gamma + \bar{v}\cos\gamma = 0\\ \bar{T} = T_w\,(\text{const.})\end{array}\right\} \quad \begin{array}{c} \left(L + \bar{L}_1 + \dfrac{\bar{L}_2}{2}\right)\sin\gamma + b - \bar{L}_2\cos\gamma \le \bar{y} \le \left(2L - \bar{L}_1 + \dfrac{\bar{L}_2}{2}\right)\sin\gamma + b \\ \left(\bar{L}_1 - \dfrac{\bar{L}_2}{2}\right)\cos\gamma - \bar{L}_2\sin\gamma \le \bar{x} \le \left(\bar{L}_1 - \dfrac{\bar{L}_2}{2}\right)\cos\gamma \end{array} \tag{3-10}$$

part e

$$\left.\begin{array}{l}\bar{u}\cos\gamma + \bar{v}\sin\gamma = 0\\ \bar{u}\sin\gamma + \bar{v}\cos\gamma = 0\\ \bar{T} = T_w\,(\text{const.})\end{array}\right\} \quad \begin{array}{c} \left(2L - \bar{L}_1 + \dfrac{\bar{L}_2}{2}\right)\sin\gamma + b \le \bar{y} \le 2L\sin\gamma + b \\ 0 \le \bar{x} \le \left(\bar{L}_1 - \dfrac{\bar{L}_2}{2}\right)\cos\gamma \end{array} \tag{3-11}$$

The Non-Obstructed Wall

$$\left.\begin{array}{l} \bar{u}\cos\gamma + \bar{v}\sin\gamma = 0 \\ \bar{u}\sin\gamma + \bar{v}\cos\gamma = 0 \\ \bar{T} = T_w\ (= \text{const.}) \end{array}\right\} \qquad \begin{array}{l} 0 \le \bar{y} \le L\sin\gamma \\ 0 \le \bar{x} \le L\cos\gamma \end{array} \tag{3-12}$$

The boundary condition for the diveregent channel are given as follows :

The Channel Entrance

$$\left.\begin{array}{r} \bar{v} = 0 \\ -\bar{P} + \mu\dfrac{\partial\bar{u}}{\partial\bar{x}} = 0 \\ \bar{T} = T_\infty \end{array}\right\} \qquad \begin{array}{c} L\sin\gamma \le \bar{y} \le L\sin\gamma + b \\ \bar{x} = 0 \end{array} \tag{3-13}$$

The Channel Exit

$$\left.\begin{array}{r} \bar{v} = 0 \\ -\bar{P} + \mu\dfrac{\partial\bar{u}}{\partial\bar{x}} = 0 \\ \dfrac{\partial\bar{T}}{\partial\bar{x}} = 0 \end{array}\right\} \qquad \begin{array}{c} 0 \le \bar{y} \le 2L\sin\gamma + b \\ \bar{x} = L\cos\gamma \end{array} \tag{3-14}$$

The Non-Obstructed Wall

$$\left.\begin{array}{l} \bar{u}\cos\gamma + \bar{v}\sin\gamma = 0 \\ \bar{u}\sin\gamma + \bar{v}\cos\gamma = 0 \\ \bar{T} = T_w\ (\text{const.}) \end{array}\right\} \qquad \begin{array}{l} 0 \le \bar{y} \le L\sin\gamma \\ 0 \le \bar{x} \le L\cos\gamma \end{array} \tag{3-15}$$

The Obstructed Wall

For convenience and clarity the obstructed plate has been divided into five parts as shown in Figure(3.2).

part a

$$\left.\begin{array}{l}\bar{u}\cos\gamma + \bar{v}\sin\gamma = 0\\ \bar{u}\sin\gamma + \bar{v}\cos\gamma = 0\\ \bar{T} = T_w\,(\text{const.})\end{array}\right\} \quad \begin{array}{c} L\sin\gamma + b \le \bar{y} \le \left(L + \bar{L}_1 - \dfrac{\bar{L}_2}{2}\right)\sin\gamma + b \\ 0 \le \bar{x} \le \left(\bar{L}_1 - \dfrac{\bar{L}_2}{2}\right)\cos\gamma \end{array} \tag{3-16}$$

part b

$$\left.\begin{array}{l}\bar{u}\cos\gamma + \bar{v}\sin\gamma = 0\\ \bar{u}\sin\gamma + \bar{v}\cos\gamma = 0\\ \bar{T} = T_w\,(\text{const.})\end{array}\right\} \quad \begin{array}{c} \left(L + \bar{L}_1 - \dfrac{\bar{L}_2}{2}\right)\sin\gamma + b - \bar{L}_2\cos\gamma \le \bar{y} \le \left(L + \bar{L}_1 - \dfrac{\bar{L}_2}{2}\right)\sin\gamma + b \\ \left(\bar{L}_1 - \dfrac{\bar{L}_2}{2}\right)\cos\gamma \le \bar{x} \le \left(\bar{L}_1 - \dfrac{\bar{L}_2}{2}\right)\cos\gamma + \bar{L}_2\sin\gamma \end{array} \tag{3-17}$$

part c

$$\left.\begin{array}{l}\bar{u}\cos\gamma + \bar{v}\sin\gamma = 0\\ \bar{u}\sin\gamma + \bar{v}\cos\gamma = 0\\ \bar{T} = T_w\,(\text{const.})\end{array}\right\} \quad \begin{array}{c} \left(L + \bar{L}_1 - \dfrac{\bar{L}_2}{2}\right)\sin\gamma + b - \bar{L}_2\cos\gamma \le \bar{y} \le \left(L + \bar{L}_1 + \dfrac{\bar{L}_2}{2}\right)\sin\gamma + b - \bar{L}_2\cos\gamma \\ \left(\bar{L}_1 - \dfrac{\bar{L}_2}{2}\right)\cos\gamma + \bar{L}_2\sin\gamma \le \bar{x} \le \left(\bar{L}_1 + \dfrac{\bar{L}_2}{2}\right)\cos\gamma + \bar{L}_2\sin\gamma \end{array} \tag{3-18}$$

part d

$$\left.\begin{array}{l}\bar{u}\cos\gamma + \bar{v}\sin\gamma = 0\\ \bar{u}\sin\gamma + \bar{v}\cos\gamma = 0\\ \bar{T} = T_w\,(\text{const.})\end{array}\right\} \quad \begin{array}{c} \left(L + \bar{L}_1 + \dfrac{\bar{L}_2}{2}\right)\sin\gamma + b - \bar{L}_2\cos\gamma \le \bar{y} \le \left(2L - \bar{L}_1 + \dfrac{\bar{L}_2}{2}\right)\sin\gamma + b \\ \left(\bar{L}_1 + \dfrac{\bar{L}_2}{2}\right)\cos\gamma \le \bar{x} \le \left(\bar{L}_1 + \dfrac{\bar{L}_2}{2}\right)\cos\gamma + \bar{L}_2\sin\gamma \end{array} \tag{3-19}$$

part e

$$\left.\begin{array}{l}\bar{u}\cos\gamma + \bar{v}\sin\gamma = 0\\ \bar{u}\sin\gamma + \bar{v}\cos\gamma = 0\\ \bar{T} = T_w\,(\text{const.})\end{array}\right\} \quad \begin{array}{c} \left(2L - \bar{L}_1 + \dfrac{\bar{L}_2}{2}\right)\sin\gamma + b \le \bar{y} \le 2L\sin\gamma + b \\ \left(\bar{L}_1 + \dfrac{\bar{L}_2}{2}\right)\cos\gamma \le \bar{x} \le L\cos\gamma \end{array} \tag{3-20}$$

The two walls are kept at a constant temperature (T_w) greater than the temperature of the surroundings. The fluid enters the channel at the surrounding temperature. The horizontal velocity at both the entrance and the exit of the channel were taken to be zero. This is a reasonable assumption since the problem is heat transfer by natural convection and the fluid is in a vertical upflow motion. The effect of such boundary condition on the inclination angle of the channel wall and on the location of the obstruction will be presented later in the discussion of results. It should be mentioned that the same type of boundary condition has been used by Said and Krane [47]. It should be noted that the total stress or tractin (τ_n) normal to the boundary at the channel entrance and exit and the heat flux (q_n) normal to the boundary at the channel exit are prescribed equal to zero . The reason for such boundary conditions will be explained in the following chapter.

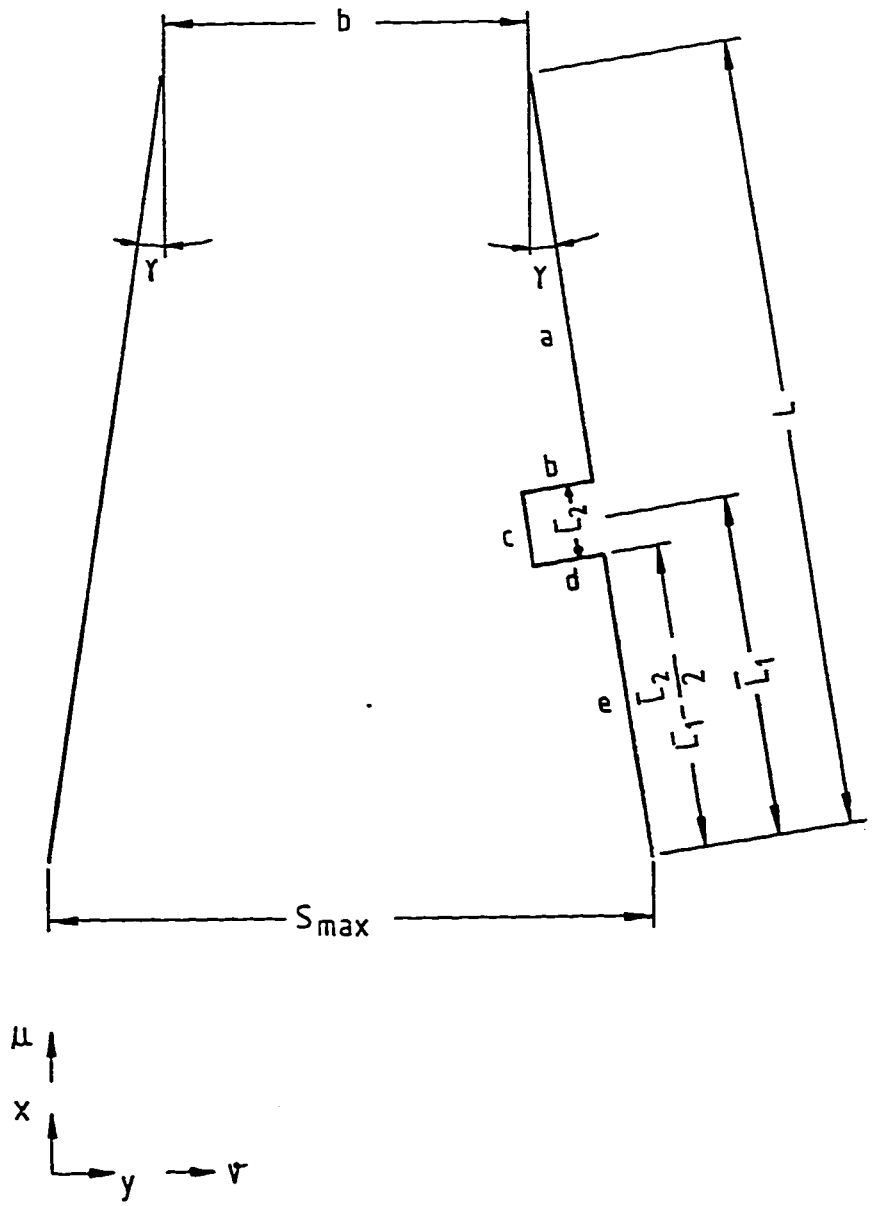

Figure (3.1) Configuration of Convergent Obstructed Vertical Channel

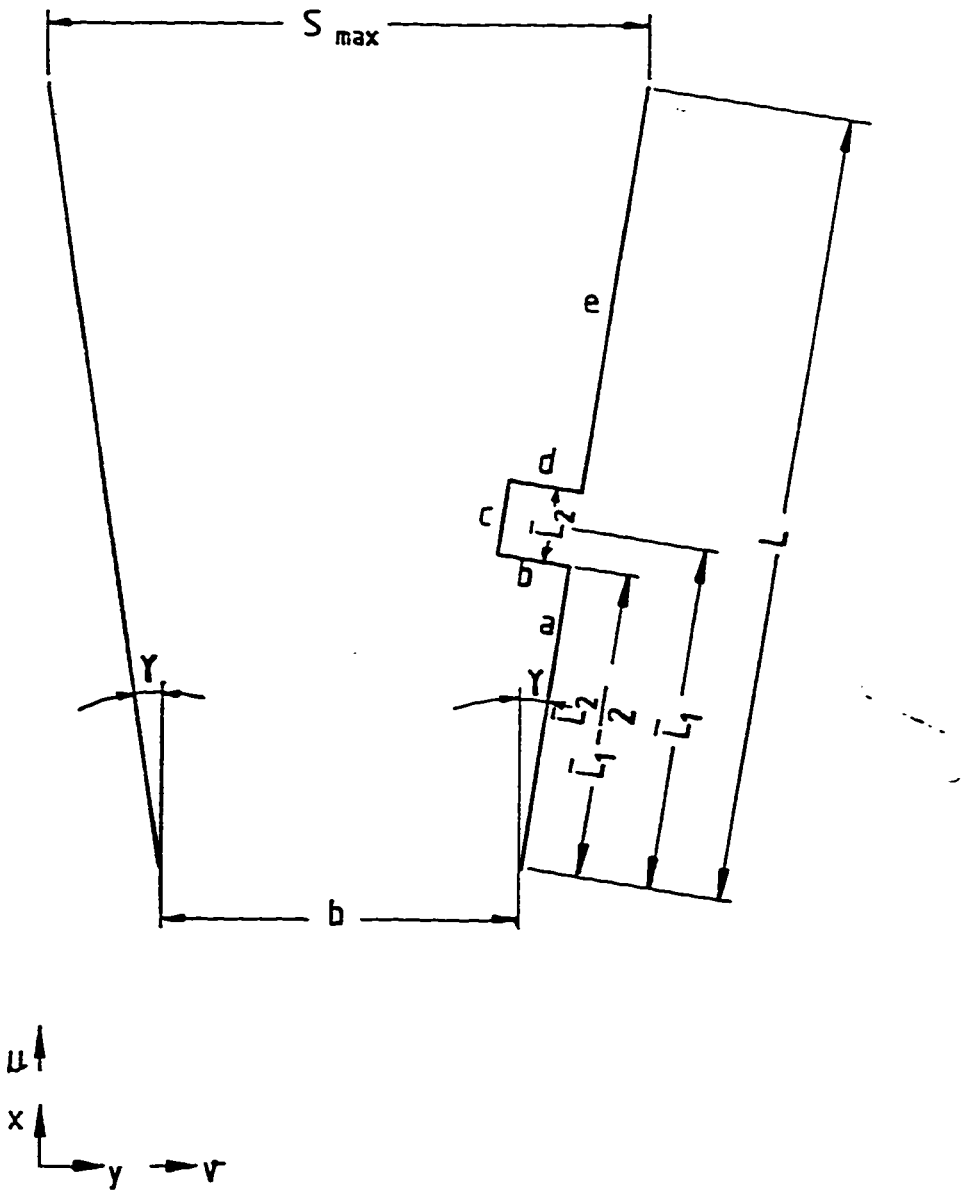

Figure (3.2) Configuration of Divergent Obstructed Vertical Channel

CHAPTER 4

METHOD OF SOLUTION

The governing equations described in the previous chapter are non-linear, coupled, elliptic partial differential equations. Exact solutions for such equations are too complicated (if they exist) and hence one must resort to the use of an approximate numerical method to obtain a solution. The most popular numerical methods are the finite difference methods (FDM) [48 , 49 , 50] and the finite element methods (FEM) [51 , 52 , 53]. The objective of both methods is to reduce the continuous problem (infinite number of degrees of freedom) described by a partial differential equation to a discrete problem (finite number of degrees of freedom) described by a system of algebraic equations [54]. Although the final results of both procedures are similar, the procedures are sufficiently different in their philosophies and implementation. Finite difference techniques are particularly convenient for use on domains with regularly-shaped boundaries. The capabilities for handling irregular boundaries is one of the main advantages of the finite element procedure over the finite difference procedure.

In this study, the numerical solution will be carried out using the general purpose finite element computer code called NACHOS. The NACHOS computer code was designed for the solution of two dimensional, incompressible fluid dynamics problems. A full description of the theoretical fluid mechnics background for the code as well as a discussion of the most important numerical procedures utilized by NACHOS are presented in [54]. At the same time,

a detailed discription of the input data necessary to access and excute the NACHOS code and a discription of program capabilities and organization are provided in [55].

4.1-Formulation of the Continuum Problem

The NACHOS program is designed for the analysis of a wide range of flow problems which includes both transition and steady-state analysis of isothermal flows, forced convection, free convection and mixed convection heat transfer problems. The following restrictions and assumptions define the problem areas of interest :

(1) NACHOS is limited to two-dimensional fluid/solid region, either planar or axially symmetric.

(2) The fluid is assumed to be Newtonian and incompressible within the Boussinesq approximation.

(3) All materials are assumed homogeneous and isotropic.

(4) The fluid motion is assumed to be laminar.

(5) Viscous dissipation effects are assumed to be negligible.

(6) Fluid flow with free surface boundaries is not considered.

Based on the above assumptions, the appropriate mathematical discription of the fluid motion is given by the Navier-Stokes equatioins,

the *continuity equation*

$$\frac{\partial u_i}{\partial x_j} = 0 \quad , \tag{4-1}$$

the *momentum equation*

$$\rho \frac{\partial u_i}{\partial t} + \rho u_j \frac{\partial u_i}{\partial x_j} - \rho g_i + \rho g_i \beta (T - T_{ref}) - \frac{\partial \tau_{ij}}{\partial x_j} = 0 \quad , \tag{4-2}$$

with,

$$\tau_{ij} = - P \delta_{ij} + \mu \left(\frac{\partial u_i}{\partial x_j} + \frac{\partial u_j}{\partial x_i} \right) \quad ,$$

and the *energy equation* is given by :

$$\rho C_p \frac{\partial T}{\partial t} + \rho C_p u_j \frac{\partial T}{\partial x_j} + \frac{\partial q_j}{\partial x_j} - S = 0 \quad , \tag{4-3}$$

with,

$$q_j = - k \frac{\partial T}{\partial x_j} \quad ,$$

where t is the time, u_i is the velocity component in the x_i coordinate direction, P is the pressure, T is the temperature, ρ is the density, τ_{ij} is the stress tensor, q_i is the heat flux vector, S is the volumetric heat source, μ is the viscosity, C_p is the heat capacity, k is the thermal conductivity, β is the volume expansion, T_{ref} is a refrence temperature for which buoyancy forces are zero, δ_{ij} is the identity ten-

sor and g_i is the gravitational constant (assumed to act in the negative y direction). All material properties are assumed to vary with temperature only while the volumetric heat source is assumed to vary with temperature and time.

Suitable boundary and initial conditions for the dependent variables are required in order to complete the formulation of the initial/ boundary value problem. The hydrodynamic part of the problem requires the velocity components or the total surface stress (or traction) to be specified on the boundary of the fluid region. For the thermal part of the problem, the temperature or the heat flux condition must be specified on all parts of the boundary. This can be expressed by,

$$\left.\begin{aligned} u_i &= f_i(s) \qquad on \quad \Gamma_u \,, \\ t_i &= \tau_{ij}(s)\, n_j(s) \qquad on \quad \Gamma_t \,, \end{aligned}\right\} \tag{4-4}$$

for the fluid and,

$$\left.\begin{aligned} T &= g(s) \qquad on \quad \Gamma_T \,, \\ [\, q_a(s) + q_c(s) + q_r(s)\,] &= \{\, k \frac{\partial T}{\partial x_i}\} \, n_i(s) \qquad on \quad \Gamma_q \,, \end{aligned}\right\} \tag{4-5}$$

for the heat transfer problem. In equations (4-4) and (4-5), S is the coordinate along the boundary, n_j is the outward unit normal to the boundary, $\Gamma_f = \Gamma_u + \Gamma_t$ is the total boundary enclosing the fluid region Ω_f, and $\Gamma_e = \Gamma_T + \Gamma_q$ is the total boundary enclosing the energy transfer region Ω_e. The flux boundary condition for the energy equation has been expressed as the sum of three parts where q_a is the applied heat flux, q_c is the heat flux due to

convection and q_r is the heat flux due to radiation. The initial conditions for the boundary value problem consist of specifying the value of each dependent variable at the initial time for all points in the appropriate region. This means,

$$\left.\begin{aligned} u_i &= a_i(x_i) \\ & \qquad at \quad t = 0 \quad \text{on } \Omega_f \,, \\ P &= b(x_i) \\ T &= C(x_i) \qquad at \quad t = 0 \quad \text{on } \Omega_e \,, \end{aligned}\right\} \tag{4-6}$$

where Ω_f and Ω_e are the fluid and energy transfer regions, respectively. As mentioned earlier, the total stress normal to the boundary at the channel entrance and exit and the heat flux normal to the boundary at the channel exit are prescribed equal to zero. These boundary conditions are not required to be explicitly enforced at each node at the entrance and at the exit of the channel when using the finite element algorithm. Instead they are naturally enforced through the elemental surface integrals generated by the method of weighted residuals (MWR) formulation of the finite element algorithm.

4.2-Formulation of the Finite Element Equations

The first step in solving the given boundary value problem using the finite element method is to divide the continuum region of interest into a number of simply shaped regions called finite elements as shown in figure (4-1). The elements are assumed to be fixed in space because the Eulerian description of the fluid motion was used in the fluid equations (4-1) through (4-3). Within each element, the dependent variables (u_i , P and T) are interpolated by continuous functions, in terms of values to be determined at a set of nodal points. In order

to develop the equations of the unknown variables at these nodal points, an individual element may be seperated from the assembled system. Within each element, the velocity, pressure and temperature fields are approximated by,

$$\left.\begin{aligned} u_i(x_i, t) &= \vec{\Phi}^T(x_i) \bullet \vec{u}_i(t) \quad , \\ p(x_i, t) &= \vec{\Psi}^T(x_i) \bullet \vec{p}(t) \quad , \\ T(x_i, t) &= \vec{\Theta}^T(x_i) \bullet \vec{T}(t) \quad , \end{aligned}\right\} \tag{4-7}$$

where the $\vec{u}_i$, $\vec{p}$ and $\vec{T}$ are vectors of element nodal point unknowns, $\vec{\Phi}$, $\vec{\Psi}$ and $\vec{\Theta}$ are vectors of interpolation functions and subscript T denotes a vector transpose.

Substitution of the previous approximations into equations (4-1) through (4-5), gives the following equations

$$\left.\begin{aligned} &\textit{Momentum}: && \vec{f}_1(\vec{\Phi}, \vec{\Psi}, \vec{\Theta}, \vec{u}_i, \vec{p}, \vec{T}) = \vec{R}_1 \quad , \\ &\textit{Continuity}: && f_2(\vec{\Phi}, \vec{u}_i) = R_2 \quad , \\ &\textit{Energy}: && f_3(\vec{\Phi}, \vec{\Theta}, \vec{u}_i, \vec{T}) = R_3 \end{aligned}\right\} \tag{4-8}$$

where R_i are the residuals (errors) resulting from the use of the approximations in equation (4-7).

In this study, the Galerkin form of the method of weigthed residuals [56] is used to reduce these errors to zero, in a weighted sense, by making the reisduals orthogonal to the interploation functions [equation (4-8)] over each element. The orthogonality conditions are expressed by

$$\left.\begin{aligned} <\vec{f}_1, \vec{\Phi}> &= <\vec{R}_1, \vec{\Phi}> = 0 \ , \\ <f_2, \vec{\Psi}> &= <R_2, \vec{\Psi}> = 0 \ , \\ <f_3, \vec{\Theta}> &= <R_3, \vec{\Theta}> = 0 \ , \end{aligned}\right\} \qquad (4\text{-}9)$$

where $<\ ,\ >$ denotes the inner product, defined by,

$$< a, b > = \int_v a \bullet b \ dv \quad ,$$

with v being the volume of the element. More detailed manipulations involving the integrals defined in equation (4-9) are presented clearly in refernce [54] The results of those computations can be expressed by the matrix equations,

Momentum : $$\overline{M}\vec{V} + \overline{C}(\vec{u})\,\vec{V} + \overline{K}(\vec{T})\,\vec{V} = \vec{F}(\vec{T}) \quad , \qquad (4\text{-}10)$$

Energy : $$\overline{N}\vec{T} + \overline{D}(\vec{u})\,\vec{T} + \overline{L}(\vec{T})\,\vec{T} = \vec{G}(\vec{T}) \ , \qquad (4\text{-}11)$$

with

$$\vec{u}^T = (\vec{u}^T_1, \ \vec{u}^T_2) \quad ,$$

and

$$\vec{V}^T = (\vec{u}^T_1, \ \vec{u}^T_2 \ , \vec{p}^T) \quad .$$

The $\overline{C}$ and $\overline{D}$ matrices represent the advection (convection) of both momentum and energy, respectively; the $\overline{K}$ and $\overline{L}$ matrices represent the diffusion of momentum and energy (the $\overline{K}$ matrix also contains the continuity equation). The $\overline{M}$ and $\overline{N}$ matrices represent the mass and capacitance terms in the field equations. The $\vec{F}$ and $\vec{G}$ vectors provide the forcing functions for the system in terms of volume forces (body force, volumetric heating) and sur-

face forces (stress, heat flux).

Equations (4-10) and (4-11) represent the discrete analogues of the conservation equations for an individual fluid finite element. However, for a solid (non-flowing) material, then only the convection terms are dropped from the momentum and energy equations (4-10) and (4-11), respectively.

As mentioned before, the above derivation has been concerned with a single finite element and the limited portion of the continuum it represents. For the entire continuum region of interest, the discrete representation can be obtained through an assemblage of elements such that interelement continuity of the approximate velocity, pressure and temperature is enforced. This is met through the appropriate summation of equations for nodes common to adjacent elements. This yields a system of matrix equations of the form given by equations (4-10) and (4-11).

4.3-Element Construction

The choice of particular element, which is to be included in the element library, is important in using finite element method. Four basic elements are included in NACHOS program. From the geometrical point of view, quadrilateral and triangular elements are included. Then each geometrical type could be isoparametric or subparamatric element (will be discussed later). No curvature boundaries exist in this study, hence, only quadrilateral elements have been used as shown in figure (4-2).

The coordinate system x and y can be converted to natural coordinate sys-

tem s and t . A natural coordinate system is a system that permits each point within the system to be specified by a dimensionless number(s) whose absolute magnitude never exceeds unity. The advantge of the natural coordinate system s and t is the -1 to +1 limits of numerical computed integration. The coordinate transformation is given by

$$x = \vec{N}^T \vec{x} \quad , \quad y = \vec{N}^T \vec{y} \quad , \quad \vec{N}^T = \vec{N}^T (s , t) \tag{4-12}$$

where $\vec{N}$ is a vector of interpolation functions over the element and $\vec{x}, \vec{y}$ are vectors of nodal point coordinates.

Within each of these elements the velocity components and temperature are approximated using quadratic interpolation functions where the pressure and the material properties are approximated by linear functions. The interpolation functions for this element and given by the vectors,

$$\vec{\Phi} = \vec{\Theta} = \begin{Bmatrix} (1/4)(1-s)(1-t)(-s-t-1) \\ (1/4)(1+s)(1-t)(s-t-1) \\ (1/4)(1+s)(1+t)(s+t-1) \\ (1/4)(1-s)(1+t)(-s+t-1) \\ (1/2)(1-s^2)(1-t) \\ (1/2)(1+s)(1-t^2) \\ (1/2)(1-s^2)(1+t) \\ (1/2)(1-s)(1-t^2) \end{Bmatrix} \tag{4-13}$$

$$\vec{\Psi} = \vec{\eta} = (1/4) \begin{Bmatrix} (1-s)(1-t) \\ (1+s)(1-t) \\ (1+s)(1+t) \\ (1-s)(1+t) \end{Bmatrix} \tag{4-14}$$

where $\vec{\eta}$ is is the vector of interploation functions for the material property quantities at the nodal points and where the ordering of the functions corre-

sponds to the ordering of unknowns shown in figure (4-2). These shape functions are expressed in terms of the normalised or natural coordinates s and t . s and t, which vary from -1 to +1 as shown in figure (4-2). If $\vec{N} = \vec{\Phi}$, the element is said to be isoparametric (i.e., the functions defining the dependent variables are of the same order as the functions defining the element geometry). If $\vec{N} = \vec{\Psi}$, a linear interpolation of the element boundary is possible and the element is said to be subparametric.

4.4-Solution Procedure

4.4.1-Solution Algorithm

The NACHOS code offers both steady-state and transient iterative algorithms for solving the matrix equations. For the analysis of steady state problems, NACHOS uses Picard or Newton-Raphson iteration scheme to compute the matrix coefficients. A comparison of the Picard and the Newton-Raphson procedures has indicated a superior rate of convergence for the second method [57]. All the solutions that will be presented here were performed using steady-state Newton-Raphson iteration scheme. In the present problem the momentum equation depends on the temperature field(i.e.free convection with temperature dependent gravity) . This problem is called strongly coupled convection problem. Therefore, a simultaneous solution for momentum and energy equations is needed. A particularly simple algorithm for this type of problem is an alternating solution scheme given by ,

$$\overline{D}\,(\vec{u}^{n})\;\vec{T}^{n+1} + \overline{L}\,(\vec{T}^{n})\;\vec{T}^{n+1} = \vec{G}(\,\vec{T}^{n}) \quad ,$$

$$\overline{C}\,(\vec{u}^{n})\;\vec{V}^{n+1} + \overline{K}\,(\vec{T}^{n+1})\;\vec{V}^{n+1} = \vec{F}(\,\vec{T}^{n+1}) \quad ,$$

$$\overline{D}\,(\vec{u}^{n+1})\;\vec{T}^{n+2} + \overline{L}\,(\vec{T}^{n+1})\;\vec{T}^{n+2} + \vec{G}(\,\vec{T}^{n+1}) \quad , \qquad (4\text{-}15)$$

.

.

.

etc.

The basic iteration scheme in equation (4-15) can often be accelerated by choosing a suitable interpolation procedure for the dependent variables used to evaluate the coefficient matrices. For example, the $\overline{K}$ or $\overline{L}$ matrices can be evaluated at $\vec{T}^{*n+1}$ with,

$$\vec{T}^{*n+1} \doteq \alpha\,\vec{T}^{n+1} + (1-\alpha)\,\vec{T}^{n} \qquad (0\le\alpha\le 1)\,. \qquad (4\text{-}16)$$

NACHOS uses the above interpolation for the temperature field with $\alpha = 1/2$.

When the Newton-Raphson method is applied at a given iteration or time step (i.e. computing the coefficients of the matrix) the general result is a matrix equation of the follwoing form :

$$\overline{A}\,\vec{x} = \vec{b} \qquad (4\text{-}17)$$

The $\overline{A}$ matrix is very large (i.e. several thousands equations), sparse, bounded and generally unsymmetric in most of the problems. The equation system (after each iteration) given by equation (4-17) can be solved by two basic methods -- iterative methods such as Gauss-Seidel Procedure or by direct methods such as

Gauss elimination. The solution procedure used in NACHOS is a form of Gauss elimination developed by Irons [58], called the frontal solution method. The frontal method, in general, assembles the system matrix, $\overline{A}$, from the individual element matrices. Then it reduces the $\overline{A}$ matrix by standard Gauss elimination.

4.4.2-Convergence criterion

The use of an iterative solution method necessitates the definition of a convergence and stopping criteria to terminate the iteration process. The measure of convergence is a norm on the change in the solution vector between successive iterations. The iterative algorithm is terminated after a fixed number of iterations given in the input of the program. This criteria is used to prevent very slowly convergent or divergent problems from wasting computation time. Convergence in this study is defined to have been obtained when the maximum change in temperature (in average) is less than 1.0% where the change in the average Nusselt number is less than 3 % .

4.5- Pre-and post- Processing Operations

NACHOS is a self contained analysis program with its own mesh generator, data analysis and plotting packages. The mesh generator is based on an isoparametric mapping procedure and allows any general mesh to be prepared easily and accurately. Local heat fluxes, fluid stresses, stream function values for the flow field can be calculated using the data analysis portions of the code. Graphic output of the element meshs, nodal point locations, contour plots of

temperature, stream function or pressure and time histories of any dependent variable can be provided by the plotting package. More detailed information about the computation of both stream functions and the heat flux is found in [54].

4.6-Program Organization

A schematic diagram of the NACHOS code structure is shown in figure (4-3). The program is written in OVERLAY form with each overlay performing a specific task in the analysis sequence. As indicated by figure(4-3), the main overlay acts as a control program for the remaining primary overlays. The following list provids a brief description of the function of each overlay :

(1) OVERLAY (1,0) SETUP - reads material property data, reads mesh data, creats mesh, reads element and boundary condition data.

(2) OVERLAY (2,0) FORMKF - forms coefficient matrices for each element, applies boundary conditions, creates unique "nick- names" for each degree of freedom.

(2) OVERLAY (10,0) FORMKF - is the axisymmetric version of the previous overlay.

(3) OVERLAY (3,0) UNZIPP - reads element coefficient matrices, assembles global coefficient matrecies using "nick-names" to establish connectivity, solves either transient or steady state matrix equa-

tion.

(4) OVERLAY (4,0) STREAM - creates stream function field from velocity solution for each element.

(5) OVERLAY (5,0) STRESS - calculates fluid stress field and/or heat flux fields for each element.

(6) OVERLAY (6,0) PLOTZ - plot package,plots grid points,elements, contours and time histories.

4.7-The Validity of The Program

Prior experience with NACHOS code yielded average heat transfer results for both obstructed and unobstructed parallel-walled channels that agreed very well with those of the literature [47]. Also NACHOS was one of the computer codes included in the contents of a benchmark numerical solution presented by D. Davis and G. James [59]. NACHOS results compared well with the bechmark solutions. Also to revalidate NACHOS after it has been installed in KFUPM main frame, average Nusselt numbers for smooth parallel-walled channel with uniform wall temperature boundary conditions were computed using NACHOS program. The mesh generated for the smooth parallel-walled channel is shown in figure (4-4).

The computed average Nusselt numbers ($\overline{Nu}$) were plotted versus Ra' with Elenbass's correlation [25] and Churchill's correlation [60] as shown in figure (4-5). Eelnbasse's correlation has been deduced based on an experimental data. The computed results agree very well (within an average difference of 4%) with those of the literarture. Higher deviations ($\approx$20 %) are noted at high

modified Rayliegh numbers ($Ra' > 10^4$). This deviation can be decreased by increasing the number of iterations used to solve the problem.

For the obstructed channel, a non-uniform mesh of 248 elements was employed. The elements were clustered near the obstruction and the wall boundaries. To determine the grid size at which grid-independent solutions could be obtained, calculations were also done on a non-uniform of 364 quadrilateral elements (an increase of 46.8%). The two grid results compared very well with each other with a maximum average difference of 4.6% in the two solutions. Based on this comparison and the fact that the central processor time needed to run NACHOS is directly dependent on the number of elements in the mesh, a grid size of 248 elements was used. The computations were performed in terms of the non-dimensional variables.

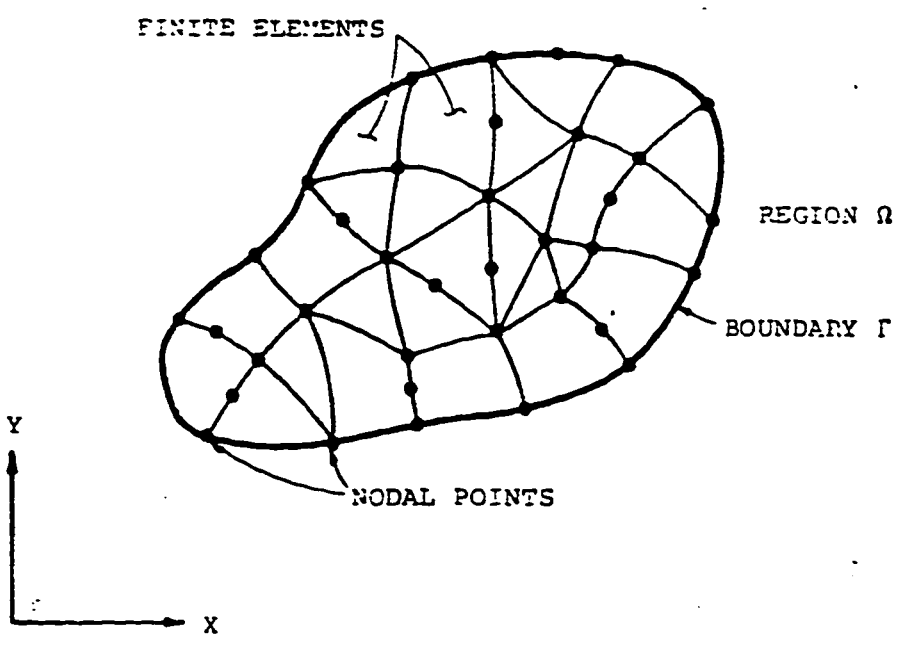

Figure 4.1 Configuration of A General Continuum Region divided into A Number of Simply Shaped Regions Called Finite Elements.

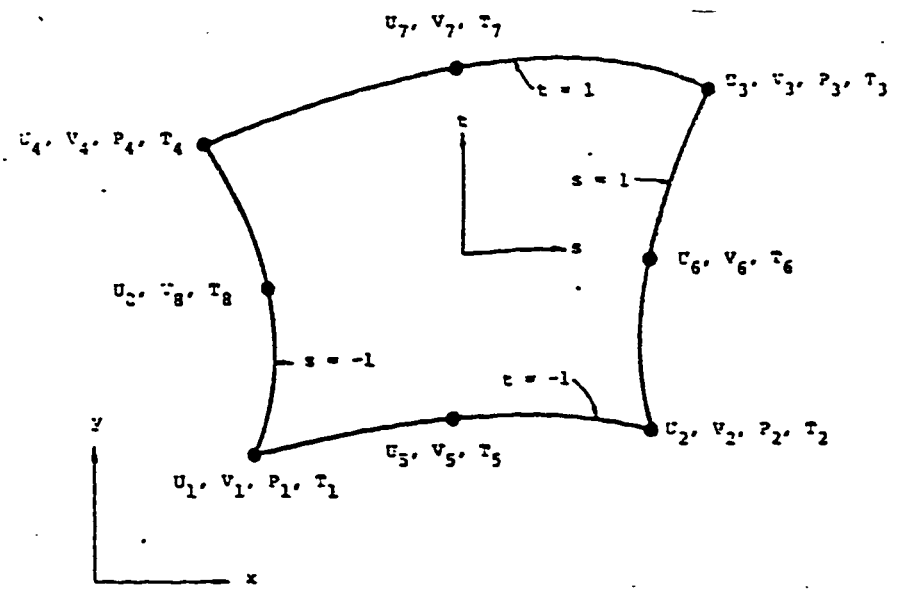

Figure 4.2 Construction of A Finite Element with nodal points at Which the Unknown Variables Have to be Computed.

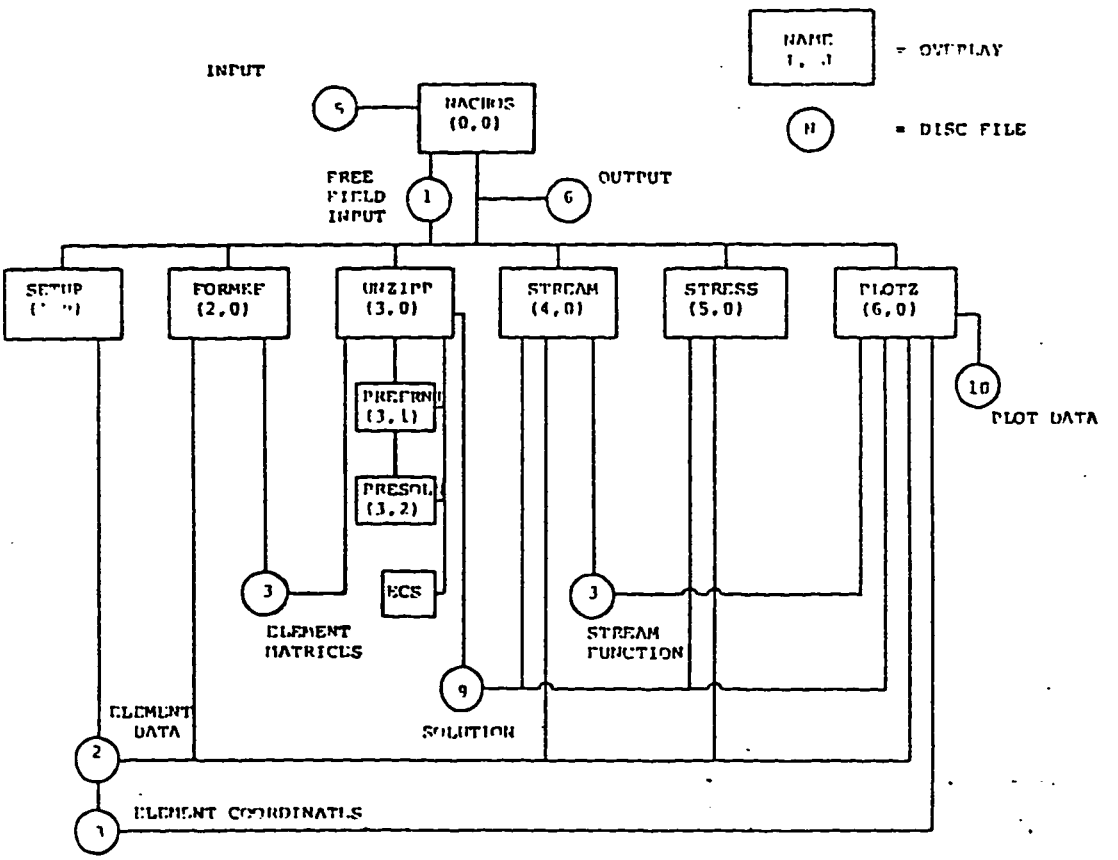

Figure 4.3 A Schematic Diagram of the NACHOS Code Program.

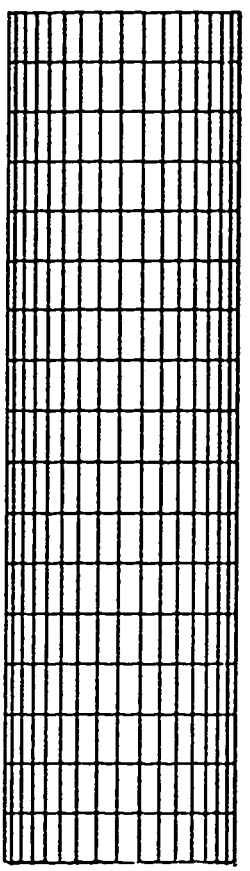

Figure 4.4 Mesh Generated For Smooth (Unobstructed) Vertical Channel For $AR = 0.2727$ and $\gamma = 0$.

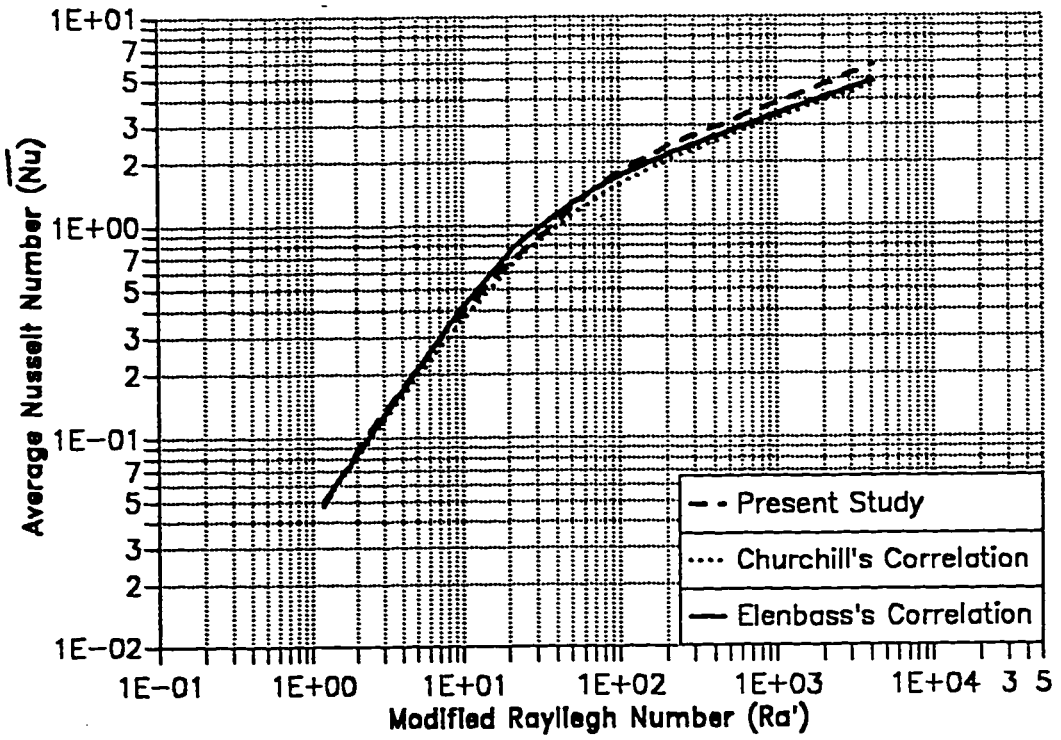

Figure 4.5 Comparison of Computed Average Nusselt Number for an Unobstructed Channel Between NACHOS Program and Literature.

CHAPTER 5

COMPUTATIONAL MATRIX

To set up a computational matrix,the governing equations and boundary conditions, equations (3-1) to (3-20), are expressed in terms of the following dimensionless variables and paramaters :

$$\left.\begin{aligned} u &= \frac{\bar{u}b^2}{\alpha L} \quad ; \quad v = \frac{\bar{v}b}{\alpha} \quad ; \quad Pr = \frac{\nu}{\alpha} \\ x &= \frac{\bar{x}}{L} \quad ; \quad y = \frac{\bar{y}}{b} \\ L_1 &= \frac{\bar{L}_1}{L} \quad ; \quad L_2 = \frac{\bar{L}_2}{L} \end{aligned}\right\} \tag{5-1}$$

$$\theta = \frac{(\bar{T} - T_\infty)}{(T_w - T_\infty)} \tag{5-2}$$

$$P = \frac{\bar{P}}{g\beta\rho_\infty(T_w - T_\infty)L} \tag{5-3}$$

with the definition of the Rayleigh number , Ra , given by :

$$Ra = Pr \cdot Gr = Pr\,\frac{\beta g (T_w - T_\infty) b^3}{\nu^2} \tag{5-4}$$

The resulting dimensionless governing equations are as follwos :

Conservation of Mass

$$\frac{\partial u}{\partial x} + \frac{\partial v}{\partial y} = 0 \tag{5-5}$$

Conservation of Momentum

$$\frac{1}{Pr}\left\{ u\frac{\partial u}{\partial x} + v\frac{\partial u}{\partial y} \right\} = Ra\left(\frac{b}{L}\right)\left(\theta - \frac{\partial P}{\partial x}\right) + \left\{ \left(\frac{b}{L}\right)^2 \frac{\partial^2 u}{\partial x^2} + \frac{\partial^2 u}{\partial y^2} \right\} \tag{5-6}$$

$$\frac{1}{Pr}\left\{ u\frac{\partial v}{\partial x} + v\frac{\partial v}{\partial y} \right\} = -Ra\left(\frac{L}{b}\right)\frac{\partial P}{\partial y} + \left\{ \left(\frac{b}{L}\right)^2 \frac{\partial^2 v}{\partial x^2} + \frac{\partial^2 v}{\partial y^2} \right\} \tag{5-7}$$

Conservation of Energy

$$u\frac{\partial \theta}{\partial x} + v\frac{\partial \theta}{\partial y} = \left(\frac{b}{L}\right)^2 \frac{\partial^2 \theta}{\partial x^2} + \frac{\partial^2 \theta}{\partial y^2} \tag{5-8}$$

The relevant hydrodynamic and thermal dimensionless boundary conditions will be written for the convergent and divergent channels. Considering the limiting case of $\gamma=0$ we can get directly those for the parallel-walled channel. The dimensionless boundary conditions for the convergent channel are given as follows :

The Channel Entrance

$$\left.\begin{array}{c} v = 0 \\ \theta = 0 \\ -P + \left(\frac{b}{L}\right)\frac{1}{Ra}\frac{\partial u}{\partial x} = 0 \end{array}\right\} \qquad \begin{array}{c} 0 \le y \le 2\left(\frac{L}{b}\right)\sin\gamma + 1 \\ x = 0 \end{array} \tag{5-9}$$

The Channel Exit

$$\left.\begin{array}{c} v = 0 \\ \frac{\partial\theta}{\partial x} = 0 \\ -P + \left(\frac{b}{L}\right)\frac{1}{Ra}\frac{\partial u}{\partial x} = 0 \end{array}\right\} \qquad \begin{array}{c} \frac{L}{b}\sin\gamma \le y \le \left(\frac{L}{b}\right)\sin\gamma + 1 \\ x = \cos\gamma \end{array} \tag{5-10}$$

The Non-Obstructed Wall

$$\left.\begin{array}{c} \left(\frac{L}{b}\right) u\cos\gamma + v\sin\gamma = 0 \\ \left(\frac{L}{b}\right) u\sin\gamma + v\cos\gamma = 0 \\ \theta = 1 \end{array}\right\} \qquad \begin{array}{c} 0 \le y \le \left(\frac{L}{b}\right)\sin\gamma \\ 0 \le x \le \cos\gamma \end{array} \tag{5-11}$$

The Obstructed Wall

part a

$$\left.\begin{array}{r}\left(\frac{L}{b}\right)u\cos\gamma + v\sin\gamma = 0\\ \left(\frac{L}{b}\right)u\sin\gamma + v\cos\gamma = 0\\ \theta = 1\end{array}\right\} \begin{array}{l}\left(\frac{L}{b}\right)\sin\gamma + 1 \le y \le \left(\frac{L}{b}\right)\left(1 + L_1 - \frac{L_2}{2}\right)\sin\gamma + 1\\ \left(L_1 + \frac{L_2}{2}\right)\cos\gamma \le x \le \cos\gamma\end{array} \qquad (5\text{-}12)$$

part b

$$\left.\begin{array}{r}\left(\frac{L}{b}\right)u\cos\gamma + v\sin\gamma = 0\\ \left(\frac{L}{b}\right)u\sin\gamma + v\cos\gamma = 0\\ \theta = 1\end{array}\right\} \begin{array}{l}\left(\frac{L}{b}\right)\left(1 + L_1 - \frac{L_2}{2}\right)\sin\gamma + 1 - \left(\frac{L}{b}\right)L_2\cos\gamma \le y \le \left(\frac{L}{b}\right)\left(1 + L_1 - \frac{L_2}{2}\right)\sin\gamma + 1\\ \left(L_1 + \frac{L_2}{2}\right)\cos\gamma - L_2\sin\gamma \le x \le \left(L_1 + \frac{L_2}{2}\right)\cos\gamma\end{array} \qquad (5\text{-}13)$$

part c

$$\left.\begin{array}{r}\left(\frac{L}{b}\right)u\cos\gamma + v\sin\gamma = 0\\ \left(\frac{L}{b}\right)u\sin\gamma + v\cos\gamma = 0\\ \theta = 1\end{array}\right\} \begin{array}{l}\left(\frac{L}{b}\right)\left\{\left(1 + L_1 - \frac{L_2}{2}\right)\sin\gamma - L_2\cos\gamma\right\} + 1 \le y \le \left(\frac{L}{b}\right)\left\{\left(1 + L_1 + \frac{L_2}{2}\right)\sin\gamma - L_2\cos\right\} - i\\ \left(L_1 - \frac{L_2}{2}\right)\cos\gamma - L_2\sin\gamma \le x \le \left(L_1 + \frac{L_2}{2}\right)\cos\gamma - L_2\sin\gamma\end{array} \qquad (5\text{-}14)$$

part d

$$\left.\begin{array}{r}\left(\frac{L}{b}\right)u\cos\gamma + v\sin\gamma = 0\\ \left(\frac{L}{b}\right)u\sin\gamma + v\cos\gamma = 0\\ \theta = 1\end{array}\right\} \begin{array}{l}\left(\frac{L}{b}\right)\left\{\left(1 + L_1 + \frac{L_2}{2}\right)\sin\gamma + L_2\cos\gamma\right\} + 1 \le y \le \left(\frac{L}{b}\right)\left\{\left(2 - L_1 + \frac{L_2}{2}\right)\sin\gamma + \right\} + 1\\ \left(L_1 - \frac{L_2}{2}\right)\cos\gamma - L_2\sin\gamma \le x \le \left(L_1 - \frac{L_2}{2}\right)\cos\gamma\end{array} \qquad (5\text{-}15)$$

part e

$$\left.\begin{array}{r}\left(\frac{L}{b}\right)u\cos\gamma - v\sin\gamma = 0\\ \left(\frac{L}{b}\right)u\sin\gamma - v\cos\gamma = 0\\ \theta = 1\end{array}\right\} \begin{array}{l}\left(\frac{L}{b}\right)\left\{\left(2 - L_1 + \frac{L_2}{2}\right)\sin\gamma\right\} - 1 \le y \le 2\left(\frac{L}{b}\right)\sin\gamma + 1\\ 0 \le x \le \left(L_1 - \frac{L_2}{2}\right)\cos\gamma\end{array} \qquad (5\text{-}16)$$

The dimensionless boundary conditions for the divergent channel are given as follows :

The Channel Entrance

$$\left.\begin{array}{c} v = 0 \\ \theta = 0 \\ -P + \left(\frac{b}{L}\right)\frac{1}{Ra}\frac{\partial u}{\partial x} = 0 \end{array}\right\} \quad \begin{array}{c} \left(\frac{L}{b}\right)\sin\gamma \le y \le \left(\frac{L}{b}\right)\sin\gamma + 1 \\ x = 0 \end{array} \tag{5-17}$$

The Channel Exit

$$\left.\begin{array}{c} v = 0 \\ \frac{\partial\theta}{\partial x} = 0 \\ -P + \left(\frac{b}{L}\right)\frac{1}{Ra}\frac{\partial u}{\partial x} = 0 \end{array}\right\} \quad \begin{array}{c} 0 \le y \le 2\left(\frac{L}{b}\right)\sin\gamma + 1 \\ x = \cos\gamma \end{array} \tag{5-18}$$

The Non-Obstructed Wall

$$\left.\begin{array}{c} \left(\frac{L}{b}\right)u\cos\gamma + v\sin\gamma = 0 \\ \left(\frac{L}{b}\right)u\sin\gamma + v\cos\gamma = 0 \\ \theta = 1 \end{array}\right\} \quad \begin{array}{c} 0 \le y \le \left(\frac{L}{b}\right)\sin\gamma \\ 0 \le x \le \cos\gamma \end{array} \tag{5-19}$$

The Obstructed Wall

part a

$$\left.\begin{array}{l}\left(\frac{L}{b}\right)u\cos\gamma - v\sin\gamma = 0\\ \left(\frac{L}{b}\right)u\sin\gamma + v\cos\gamma = 0\\ \theta = 1\end{array}\right\}\begin{array}{l}\left(\frac{L}{b}\right)\sin\gamma + 1 \le y \le \left(\frac{L}{b}\right)\left(1 + L_1 - \frac{L_2}{2}\right)\sin\gamma + 1\\ 0 \le x \le \left(L_1 - \frac{L_2}{2}\right)\cos\gamma\end{array} \qquad (5\text{-}20)$$

part b

$$\left.\begin{array}{l}\left(\frac{L}{b}\right)u\cos\gamma - v\sin\gamma = 0\\ \left(\frac{L}{b}\right)u\sin\gamma + v\cos\gamma = 0\\ \theta = 1\end{array}\right\}\begin{array}{l}\left(\frac{L}{b}\right)\left(1 + L_1 - \frac{L_2}{2}\right)\sin\gamma + 1 - \left(\frac{L}{b}\right)L_2\cos\gamma \le y \le \left(\frac{L}{b}\right)\left(1 - L_1 - \frac{L_2}{2}\right)\sin\gamma + 1\\ \left(L_1 - \frac{L_2}{2}\right)\cos\gamma \le x \le \left(L_1 - \frac{L_2}{2}\right)\cos\gamma + L_2\sin\gamma\end{array} \qquad (5\text{-}21)$$

part c

$$\left.\begin{array}{l}\left(\frac{L}{b}\right)u\cos\gamma + v\sin\gamma = 0\\ \left(\frac{L}{b}\right)u\sin\gamma + v\cos\gamma = 0\\ \theta = 1\end{array}\right\}\begin{array}{l}\left(\frac{L}{b}\right)\left\{\left(1 + L_1 - \frac{L_2}{2}\right)\sin\gamma - L_2\cos\gamma\right\} + 1 \le y \le \left(\frac{L}{b}\right)\left\{\left(1 + L_1 + \frac{L_2}{2}\right)\sin\gamma - L_2\cos\gamma\right\} + 1\\ \left(L_1 - \frac{L_2}{2}\right)\cos\gamma + L_2\sin\gamma \le x \le \left(L_1 + \frac{L_2}{2}\right)\cos\gamma + L_2\sin\gamma\end{array} \qquad (5\text{-}22)$$

part d

$$\left.\begin{array}{l}\left(\frac{L}{b}\right)u\cos\gamma + v\sin\gamma = 0\\ \left(\frac{L}{b}\right)u\sin\gamma + v\cos\gamma = 0\\ \theta = 1\end{array}\right\}\begin{array}{l}\left(\frac{L}{b}\right)\left\{\left(1 + L_1 + \frac{L_2}{2}\right)\sin\gamma + L_2\cos\gamma\right\} + 1 \le y \le \left(\frac{L}{b}\right)\left\{\left(2 - L_1 + \frac{L_2}{2}\right)\sin\gamma + \right\} + 1\\ \left(L_1 + \frac{L_2}{2}\right)\cos\gamma \le x \le \left(L_1 + \frac{L_2}{2}\right)\cos\gamma + L_2\sin\gamma y\end{array} \qquad (5\text{-}23)$$

part e

$$\left.\begin{array}{l}\left(\frac{L}{b}\right)u\cos\gamma + v\sin\gamma = 0\\ \left(\frac{L}{b}\right)u\sin\gamma + v\cos\gamma = 0\\ \theta = 1\end{array}\right\}\begin{array}{l}\left(\frac{L}{b}\right)\left\{\left(2 - L_1 - \frac{L_2}{2}\right)\sin\gamma\right\} + 1 \le y \le 2\left(\frac{L}{b}\right)\sin\gamma + 1\\ \left(L_1 - \frac{L_2}{2}\right)\cos\gamma \le x \le \cos\gamma\end{array} \qquad (5\text{-}24)$$

From equations (5-5) to (5-24) it is anticipated that the solution for the non-dimensional temperature will be of the functional form

$$\theta = f_1 (x , y , Ra , AR , L_1 , L_2 , \gamma , Pr) \qquad (5\text{-}25)$$

with $AR = (b/L)$. However, from energy balance at the plate surface

$$\frac{h_{local}}{K} = - \frac{\partial \theta}{\partial n} \qquad (5\text{-}26)$$

where n is the direction normal to the wall surface . Hence the functional dependence of the average Nusselt number is :

$$\overline{Nu} = f_2 (Ra , AR , L_1 , L_2 , \gamma , Pr) \qquad (5\text{-}27)$$

Hence, the dimensionless parameters of interest in the problem are six parameters, namely, Rayleigh number (Ra), Prandtl number (Pr), the aspect ratio (AR) the dimensionless distance of the obstruction centerline above the entrance of the channel (L_1), the dimensionless obstruction width (L_2), and the angle of convergence (or divergence) (γ). ***In this study the interest is to find out the effect of only five parameters using air as the working fluid*** ***(Pr = 0.72)*** **.**

The numerical calculations were performed for 120 different cases. Thirteen of these cases were run for the unobstructed channel ($\overline{L_2} = 0$) . The solutions for these cases were obtained for the sake of comparison with those of the other authers in order to verify the code and the accuracy of the numerical procedure. Five cases were run to find out the effect of L_1 . Another seven cases were run for studying the effect of L_2 . All the remaining cases were run with constant values of L_1 , L_2 , and Pr and have been devoted for finding out the effect of Ra,AR and γ . The computational matrix is shown in TABLE (5-1).

TABLE (5-1) COMPUTATIONAL MATRIX

Ra	AR	L_1	L_2	γ
4.38	0.2727	0.5	0.0945	0
8.46	0.2727	0.5	0.0945	0
14.60	0.2727	0.5	0.0945	0
29.00	0.2727	0.5	0.0945	0
39.40	0.2727	0.5	0.0945	0
98.50	0.2727	0.5	0.0945	0
491.00	0.2727	0.5	0.0945	0
725.00	0.2727	0.5	0.0945	0
978.00	0.2727	0.5	0.0945	0
4743.00	0.2727	0.5	0.0945	0
9132.00	0.2727	0.5	0.0945	0
15531.00	0.2727	0.5	0.0945	0
3.46	0.3636	0.5	0.0945	0
10.38	0.3636	0.5	0.0945	0
20.76	0.3636	0.5	0.0945	0
35.00	0.3636	0.5	0.0945	0
47.00	0.3636	0.5	0.0945	0
93.00	0.3636	0.5	0.0945	0
467.00	0.3636	0.5	0.0945	0
932.00	0.3636	0.5	0.0945	0
4713.00	0.3636	0.5	0.0945	0
9168.00	0.3636	0.5	0.0945	0
21647.00	0.3636	0.5	0.0945	0
1000.00	0.2727	0.1	0.0945	0
1000.00	0.2727	0.3	0.0945	0
1000.00	0.2727	0.5	0.0945	0
1000.00	0.2727	0.7	0.0945	0
1000.00	0.2727	0.9	0.0945	0
1000.00	0.2727	0.5	0.0000	0
1000.00	0.2727	0.5	0.0218	0
1000.00	0.2727	0.5	0.0582	0
1000.00	0.2727	0.5	0.1382	0
1000.00	0.2727	0.5	0.1818	0
1000.00	0.2727	0.5	0.2182	0
1000.00	0.2727	0.5	0.2400	0

Continued TABLE (5-1)

Ra	AR	L_1	L_2	γ
4.38	0.2727	0.5	0.0945	5(c)
8.76	0.2727	0.5	0.0945	5(c)
14.60	0.2727	0.5	0.0945	5(c)
29.00	0.2727	0.5	0.0945	5(c)
143.00	0.2727	0.5	0.0945	5(c)
275.00	0.2727	0.5	0.0945	5(c)
491.00	0.2727	0.5	0.0945	5(c)
1988.00	0.2727	0.5	0.0945	5(c)
2701.00	0.2727	0.5	0.0945	5(c)
3451.00	0.2727	0.5	0.0945	5(c)
4915.00	0.2727	0.5	0.0945	5(c)
9126.00	0.2727	0.5	0.0945	5(c)
4.38	0.2727	0.5	0.0945	5(d)
8.76	0.2727	0.5	0.0945	5(d)
14.60	0.2727	0.5	0.0945	5(d)
29.00	0.2727	0.5	0.0945	5(d)
143.00	0.2727	0.5	0.0945	5(d)
275.00	0.2727	0.5	0.0945	5(d)
491.00	0.2727	0.5	0.0945	5(d)
3.46	0.3636	0.5	0.0945	5(c)
10.38	0.3636	0.5	0.0945	5(c)
20.68	0.3636	0.5	0.0945	5(c)
35.00	0.3636	0.5	0.0945	5(c)
69.00	0.3636	0.5	0.0945	5(c)
175.00	0.3636	0.5	0.0945	5(c)
339.00	0.3636	0.5	0.0945	5(c)
651.00	0.3636	0.5	0.0945	5(c)
934.00	0.3636	0.5	0.0945	5(c)
1858.00	0.3636	0.5	0.0945	5(c)
4712.00	0.3636	0.5	0.0945	5(c)
9167.00	0.3636	0.5	0.0945	5(c)
11562.00	0.3636	0.5	0.0945	5(c)
3.46	0.3636	0.5	0.0945	5(d)
10.38	0.3636	0.5	0.0945	5(d)
20.68	0.3636	0.5	0.0945	5(d)
35.00	0.3636	0.5	0.0945	5(d)
69.00	0.3636	0.5	0.0945	5(d)
175.00	0.3636	0.5	0.0945	5(d)
339.00	0.3636	0.5	0.0945	5(d)
651.00	0.3636	0.5	0.0945	5(d)

** (c) for convergent ** (d) for divergent

Continued **TABLE (5-1)**

Ra	AR	L_1	L_2	γ
4.38	0.2727	0.5	0.0945	10(c)
8.76	0.2727	0.5	0.0945	10(c)
14.60	0.2727	0.5	0.0945	10(c)
29.00	0.2727	0.5	0.0945	10(c)
143.00	0.2727	0.5	0.0945	10(c)
275.00	0.2727	0.5	0.0945	10(c)
491.00	0.2727	0.5	0.0945	10(c)
978.00	0.2727	0.5	0.0945	10(c)
1365.00	0.2727	0.5	0.0945	10(c)
1988.00	0.2727	0.5	0.0945	10(c)
2701.00	0.2727	0.5	0.0945	10(c)
3451.00	0.2727	0.5	0.0945	10(c)
4.38	0.2727	0.5	0.0945	10(d)
8.76	0.2727	0.5	0.0945	10(d)
14.60	0.2727	0.5	0.0945	10(d)
29.00	0.2727	0.5	0.0945	10(d)
44.50	0.2727	0.5	0.0945	10(d)
58.00	0.2727	0.5	0.0945	10(d)
3.46	0.3636	0.5	0.0945	10(c)
10.38	0.3636	0.5	0.0945	10(c)
20.68	0.3636	0.5	0.0945	10(c)
35.00	0.3636	0.5	0.0945	10(c)
69.00	0.3636	0.5	0.0945	10(c)
175.00	0.3636	0.5	0.0945	10(c)
339.00	0.3636	0.5	0.0945	10(c)
651.00	0.3636	0.5	0.0945	10(c)
934.00	0.3636	0.5	0.0945	10(c)
1858.00	0.3636	0.5	0.0945	10(c)
4712.00	0.3636	0.5	0.0945	10(c)
3.46	0.3636	0.5	0.0945	10(d)
10.38	0.3636	0.5	0.0945	10(d)
20.68	0.3636	0.5	0.0945	10(d)
35.00	0.3636	0.5	0.0945	10(d)
69.00	0.3636	0.5	0.0945	10(d)

**** (c) for convergent**

**** (d) for divergent**

CHAPTER 6

RESULTS AND DISCUSSION

In this discussion, primary emphasis will be placed on the average Nusselt number for the channel as a whole. The numerical results presented here are for Ra up to 10^4, Pr = 0.72 and aspect ratios of 0.2727 and 0.3636 . The average Nusselt number will be presented for all the cases studied.

6.1 The Effect of the Obstruction

The first results to be presented pertain to comparison between the average Nusselt numbers of the unobstructed and the obstructed parallel-walled channels. These results are presented in figure (6.1). The obstructed channel Nusselt numbers are for the aspect ratio b/L = 0.2727 . The abscissa variable (Ra′ = Ra (b/L)) has been used to correlate the dependence of the average Nusselt number on both Ra and AR for unobstructed parallel-walled channels. The curve for the unobstructed channel shown in figure (6.1) is the one obtained using NACHOS. This curve represents the three flow regimes (fully developed, transition and isolated vertical plates) for the unobstructed channel. It can be seen that the average Nusselt number curve for the obstructed channel also represents three flow regimes. In the first regime (Ra′ < 20) the average Nusselt number approaches that of fully developed regime values. Also, in this regime, the presence of the obstruction causes a decrease in the average Nusselt number. This decrease is very significant at small Ra′ .

The second regime ($20 < Ra' < 200$) joins the first regime with the third one. This regime represents the transition region between the fully developed limit and the isolated vertical plate limit. The third regime ($Ra' > 200$) represents the isolated vertical plate limit. A comparison of these regimes (for obstructed and unobstructed channels) shows that the presence of the obstruction causes a reduction in the average Nusselt number. This reduction ranges from about 25% at high Ra' to about 60% at low Ra' . Although the presence of an obstruction increased heat transfer area, the local heat transfer rate around the tip of the obstruction and at the entrance region, this does not compensate for the reduced flow rate and the existence of regions of recirculating flow, which resulted in a lower average Nusselt number. Similar trend is observed for AR = 0.3636 .

6.2 The Effect of the Rayliegh Number (Ra)

The second set of results pertains to the effect of the Rayliegh number. The study covers a range of Ra from 1.0 to 10^4. The maximum dimensionless vertical velocity in the channel (Umax), the dimensionless mass flow rate (Q) and the average Nusselt number ($\overline{Nu}$) are given in TABLE (6-1). The dimensionless mass flow rate is defined as $Q = (\dot{m}*AR)/(\rho*\alpha)$ where $\dot{m}$ is the dimensional mass flow rate, AR is the aspect ratio, ρ is the density and α is the thermal diffusivity.

Figures (6.2) and (6.3) show the plot of computed Q and $\overline{Nu}$ versus the Rayliegh number. It can be noted that as the Rayliegh number increases both

the average Nusselt number ($\overline{Nu}$) and the dimensionless mass flow rate (Q) increases.

To study the effect of the Rayliegh number on the flow field and the heat transfer characteristics, plots of isotherms, streamlines, velocity vectors, temperature and velocity profiles are presented for three different Rayliegh numbers representing the three different regimes that were identified in figure (6.1).

The first form of the hydrodynamic results is the plot of the dimensionless vertical velocity versus the dimensionless distance across the channel ($\bar{y}$ /b) at different channel cross-sections for a specific value of Ra . The dimensionless vertical velocities have been plotted at the channel entrance ($\bar{x}$ /L = 0.0), channel mid-plane ($\bar{x}$ /L = 0.5) and at the channel exit ($\bar{x}$ /L = 1.0) as shown in figures (6.4) to (6.6). The velocity profiles in figures (6.4) and (6.5) are similar while for high Rayliegh number, two velocity peaks do occur as shown in figure (6.6). This means that at high Rayliegh numbers each channel wall approaches the isolated vertical plate limit.

The second form of the hydrodynamic results shows the variation of the dimensionless vertical velocity across the dimensionless channel's width ($\bar{y}$ /b) at a given cross-section in the channel ($\bar{x}$ /L) for different Rayliegh numbers. Figures (6.7) to (6.9) show the velocity distribution at the channel entrance ($\bar{x}$ /L = 0.0), at the channel mid-plane ($\bar{x}$ /L = 0.5) and at the channel exit ($\bar{x}$ /L = 1.0) for different Rayliegh numbers. It is noted that the dimensionless vertical velocity and the dimensionless mass flow rate (i.e. the area under the velocity curve) increase as the Rayliegh number increases.

The third form of the hydrodynamic results is the streamlines. plots as shown in figures (6.10-a) to (6.10-c). It is noted that due to the reduction in the channel's cross- sectional area caused by the presence of the obstruction, the streamlines are clustered in the obstruction region. Examining streamlines numerical results, negative values are observed in the region right above the obstruction. These values are very small, that it was not possible to show circulation zones through streamline plots. Hence, the fourth form of the hydrodynamic results were introduced to be the velocity vector plots.

Figures (6.11-a) through (6.11-c) show the velocity vector plots. As expected the magnitude of velocity is higher at the channel mid-plane due to the reduction in cross-sectional area caused by the presence of the obstruction. Also it can be seen that at Ra = 15531, each velocity profile has two peak points. To be able to show the circulation zones, velocity vectors right at the top of the obstruction have been magnified fifteen times its value and plotted in figures (6.12-a) through (6.12-c). No circulation zone are observed at low Rayliegh numbers while it can be noted that as Rayliegh number increases, the size of the circulation zone increases.

The hydrodynamic results can be summerized by stating that the dimensionless mass flow rate increases as the Rayliegh number increases. No circulation zones are observed in the channel at low Rayliegh numbers (fully developed flows), while circulation zones do exist at moderate and high Rayliegh numbers. The size of circulation zone increases with increase in Rayliegh number. The fully developed limit solution is approached at low Rayliegh numbers; while at high Rayliegh numbers the isolated single plate limit is approached.

The thermal results are presented in three forms. The first form is the plot of the variation of the average Nusselt number versus the Rayliegh number as shown in figure (6.3). The second form of the thermal results is the plot of the dimensionless temperature versus the dimensionless distance across the channel ($\bar{y}$ /b) at the channel mid-plane ($\bar{x}$ /L = 0.5) and at the channel exit ($\bar{x}$ /L = 1.0). These plots are shown in figures (6.13) to (6.15) for three representative Rayliegh numbers. As expected, the fluid temperature increases along the flow direction. The dimensionless temperature distribution at the channel mid-plane ($\bar{x}$ /L = 0.5) and at the channel exit ($\bar{x}$ /L = 1.0) have been plotted for different values of Rayliegh numbers as shown in figures (6.16) and (6.17) respectivly. It can be noted that at the same cross-sections in the channel the temperature decreases as the Rayliegh number increases.

The third form of the thermal results is the plot of isotherms. These plots are shown in figures (6.18-a) through (6.18-c). It can be noted that at low Rayliegh numbers the flow becomes thermally fully developed (figure 6.18-a) while a transition regime (figure 6.18-b) occurs at moderate Rayliegh numbers and the single isolated plate limit is approached at high Rayliegh numbers (figure 6.18-c). It can also be noted that the boundary layer thickness decreases as the Rayliegh number increases which leads to an increase in the average Nusselt number. The third form of the thermal results is the plot of the variation of the average Nusselt number versus the Rayliegh number as shown in figure (6.3). It can be seen from the previous discussion that the average Nusselt number increases as the Rayliegh number increases.

In conclusion, it was found that the average Nusselt number increases as the Rayliegh number increases due to two factors. The first one is the increase in the dimensionless mass flow rate and the second one is the decrease in the thermal boundary layer thickness as the Rayliegh number increases.

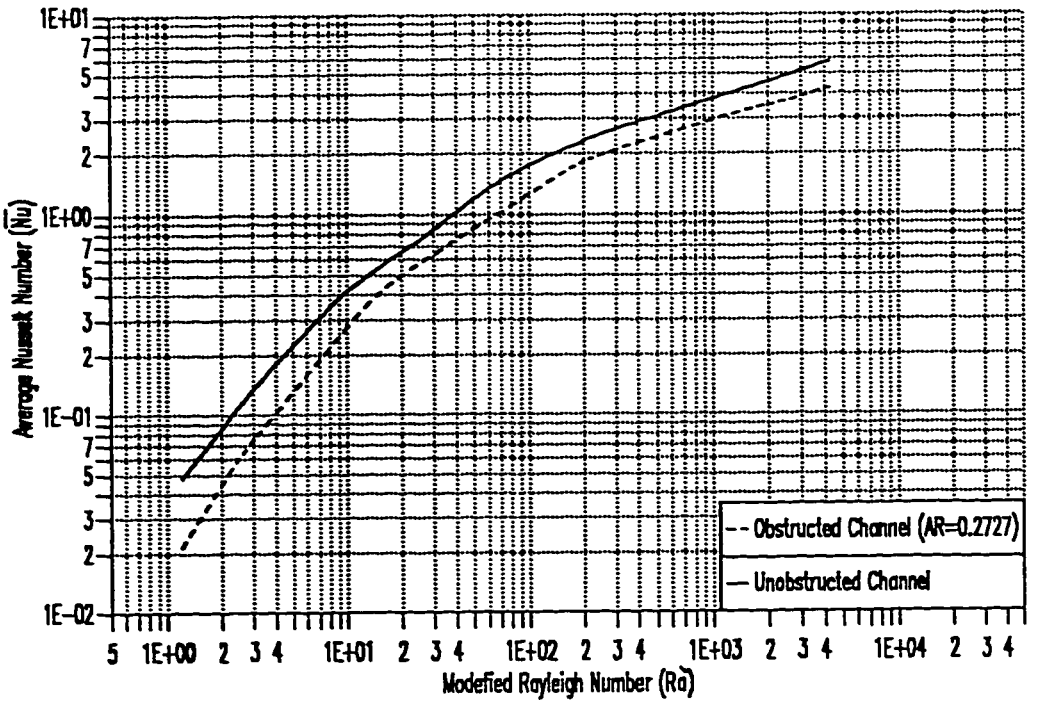

Figure 6.1 The Variation of the Average Nusselt Number Versus the Modified Rayliegh Number For Obstructed and Unobstructed Channels.

TABLE(6-1) COMPUTED Umax,Q and $\overline{Nu}$ FOR OBSTRUCTED VERTICAL CHANNEL WITH AR = 0.2727, $L_1 = 0.50$, $L_2 = 0.0945$ and $\gamma = 0$.

Ra′	Ra	Umax	Q	$\overline{Nu}$
1.19	4.38	0.098	0.0587	0.0214
2.39	8.76	0.217	0.1150	0.0545
3.98	14.60	0.453	0.1900	0.1015
7.91	29.00	0.633	0.3740	0.2166
10.74	39.40	0.893	0.5020	0.2987
26.86	98.50	2.390	1.1590	0.5968
134.90	491.00	8.804	3.9500	1.4781
197.71	725.00	10.426	5.5128	1.7750
266.70	978.00	13.421	6.1428	2.0073
1293.42	4743.00	32.014	15.5936	3.1500
2490.30	9132.00	45.741	22.6727	3.6536
4235.30	15531.00	59.803	26.9097	4.2572

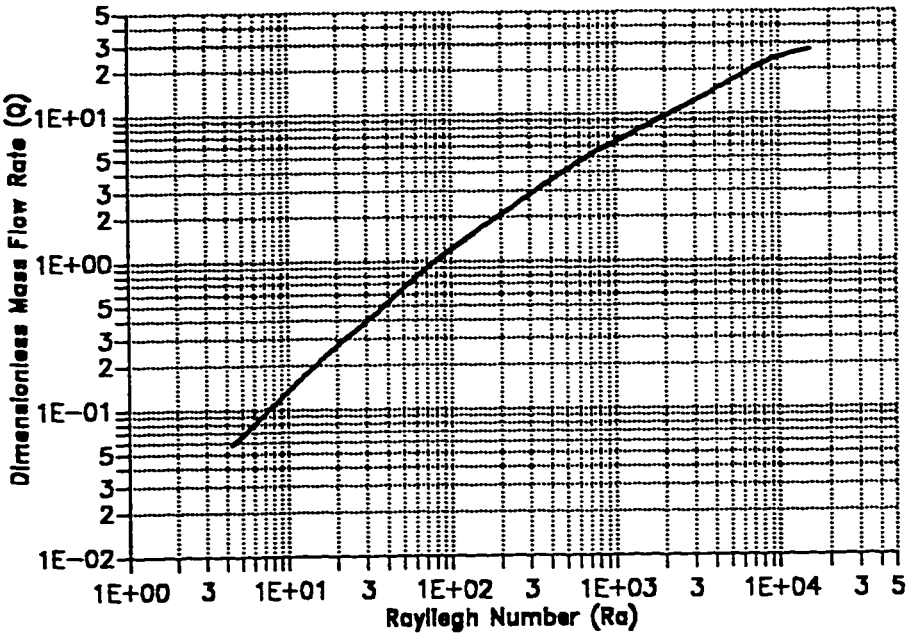

Figure 6.2 The Variation of Dimensionless Mass Flow Rate Versus the Rayliegh Number (Ra) For Obstructed Parallel-Walled Channel (AR = 0.2727).

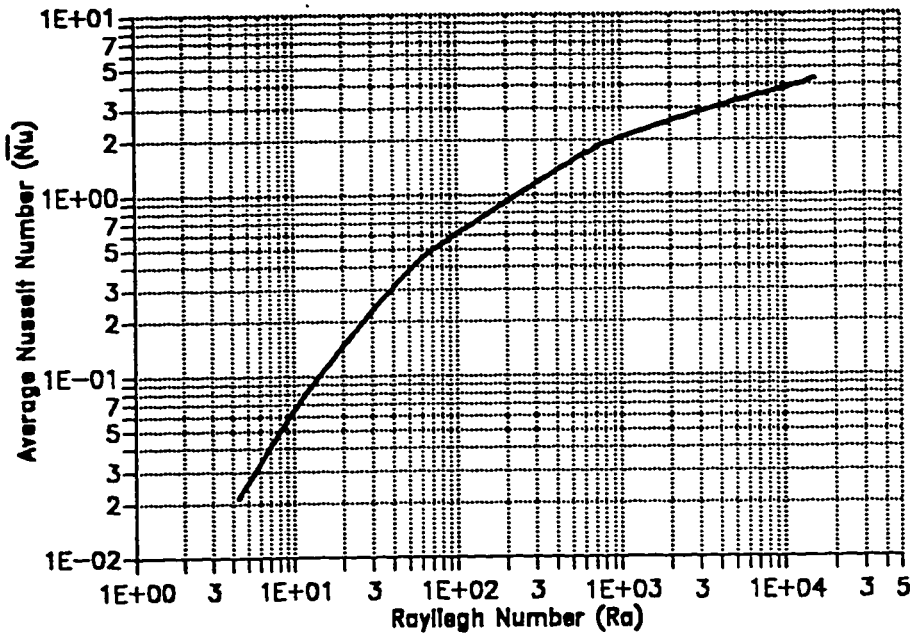

Figure 6.3 The Variation of Average Nusselt Number Versus the Rayliegh Number (Ra) For Obstructed Parallel-Walled Channel (AR = 0.2727).

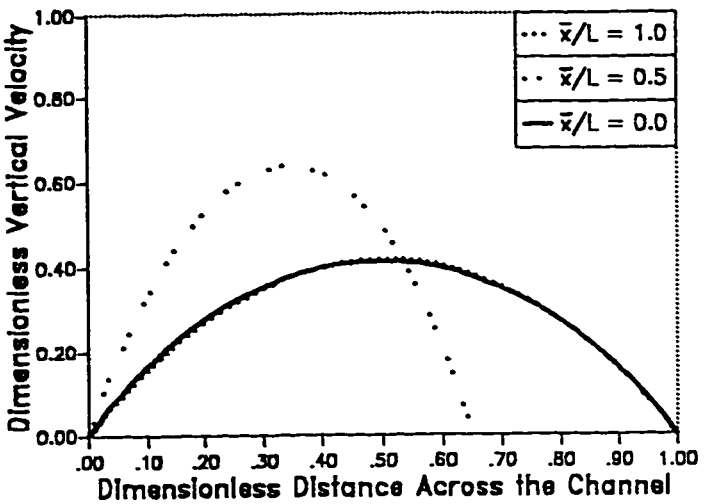

Figure 6.4 Transverse Velocity Distribution at Different Cross-Sections in the Channel for Ra = 29

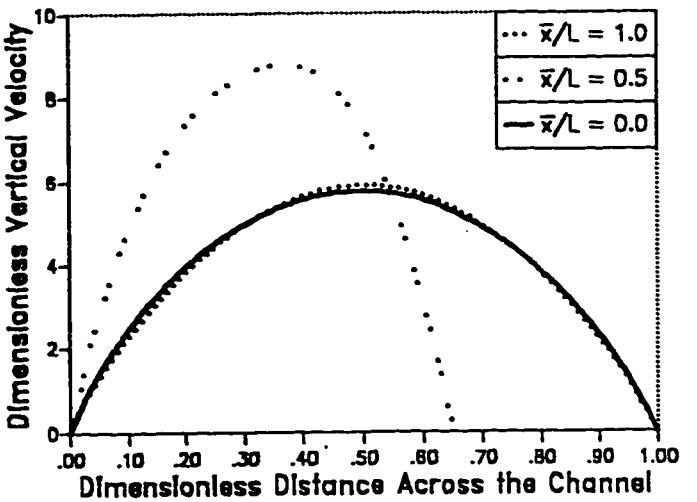

Figure 6.5 Transverse Velocity Distribution at Different Cross-Sections in the Channel for Ra = 491

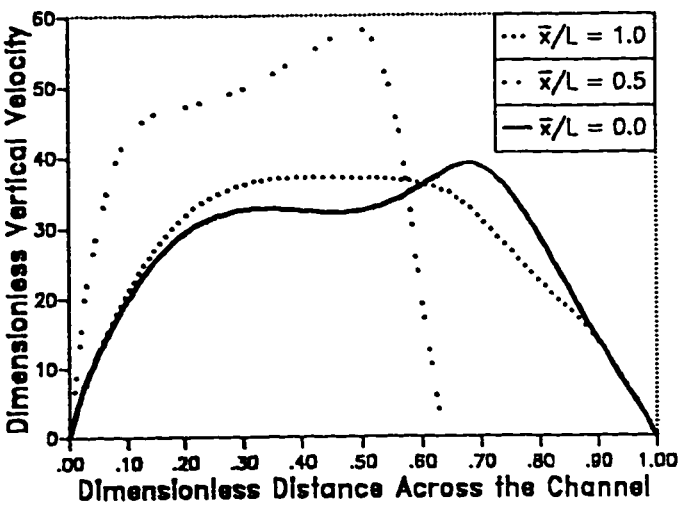

Figure 6.6 Transverse Velocity Distribution at Different Cross-Sections in the Channel for Ra = 15531

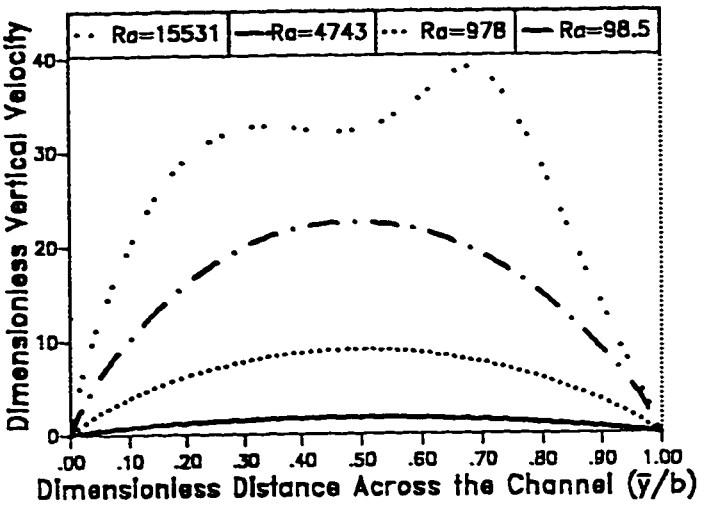

Figure 6.7 Transverse Velocity Distribution at the Entrance of the Channel for Different Values of Ra.

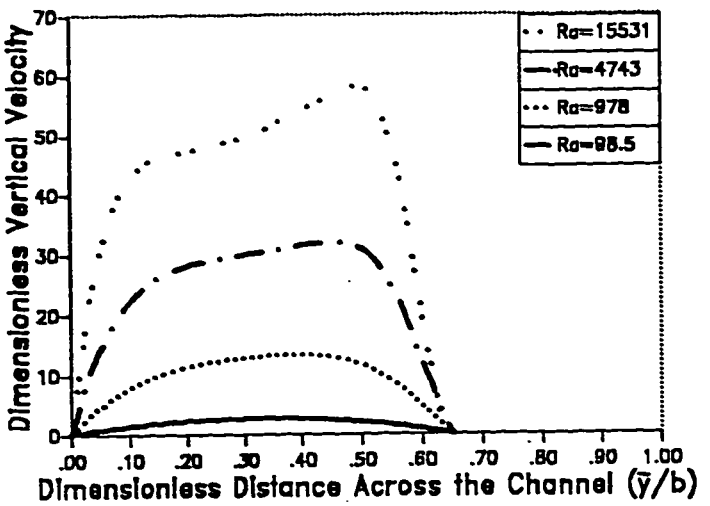

Figure 6.8 Transverse Velocity Distribution at the Obstruction Center-Line for Different Values of Ra.

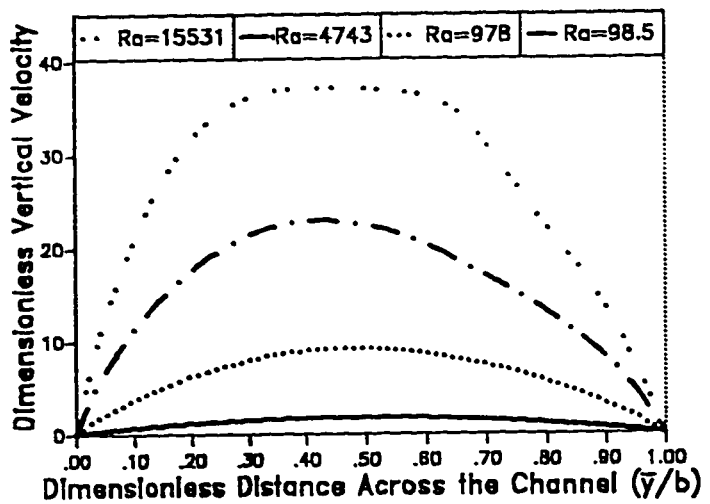

Figure 6.9 Transverse Velocity Distribution at the Exit of the Channel for Different Values of Ra.

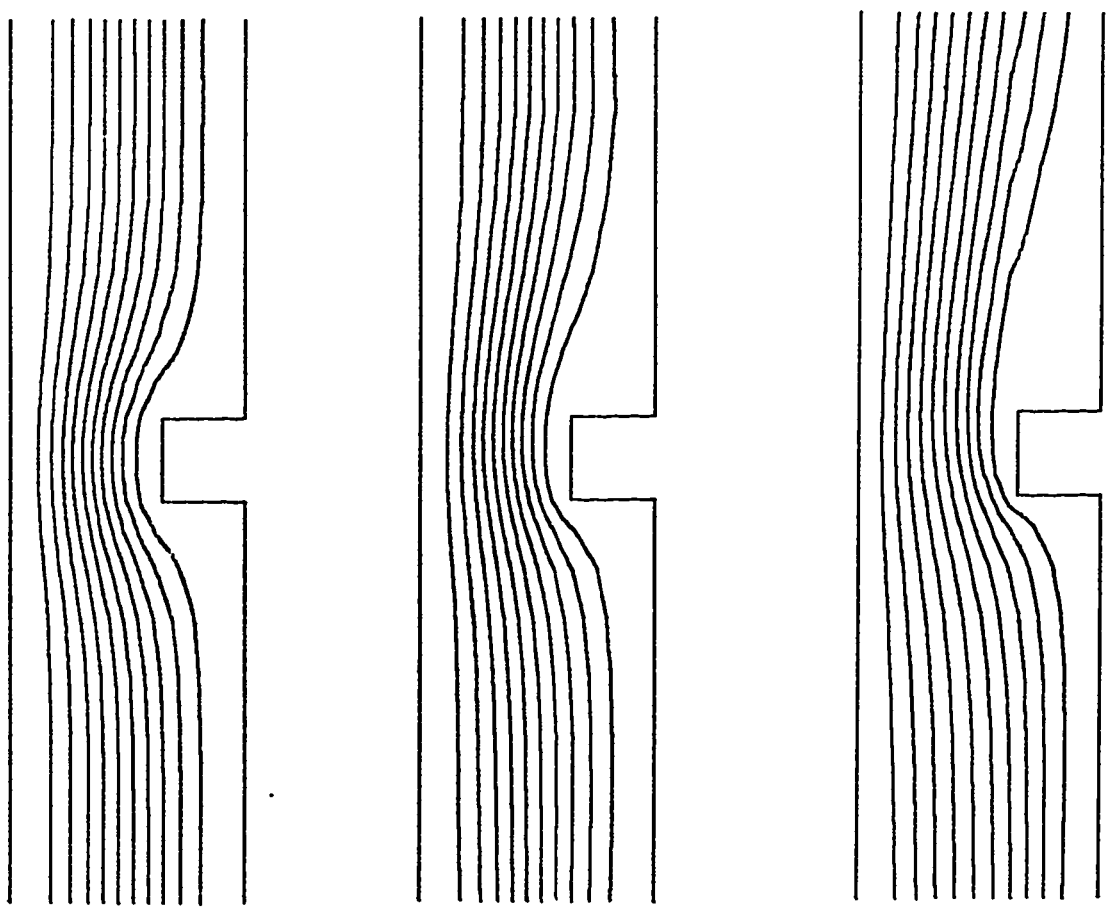

(a) Ra = 29 (b) Ra = 491 (c) Ra = 15531

Figure 6.10 Computed Streamlines for AR = 0.2727, γ = 0 , L_2 = 0.0945 , L_1 = 0.5 ,Pr = 0.72 .

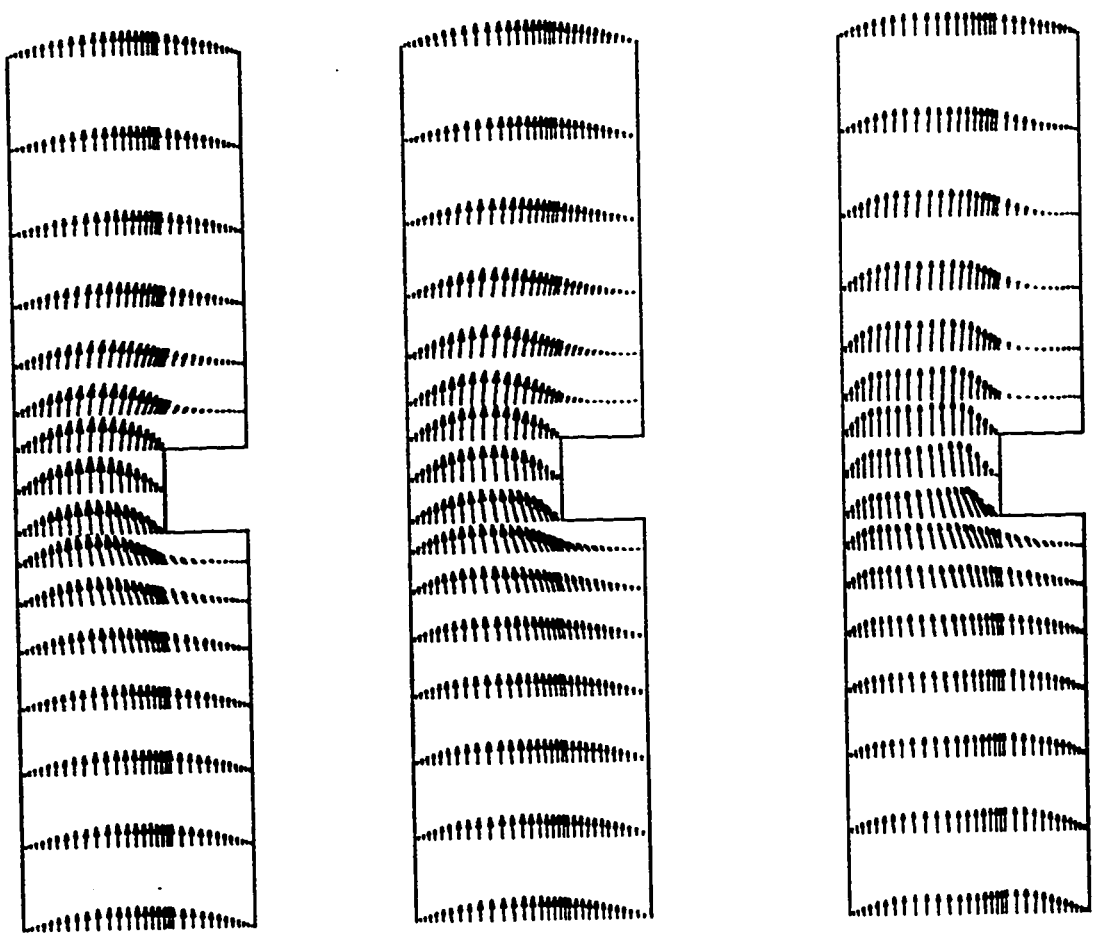

(a) Ra = 29 (b) Ra = 491 (c) Ra = 15531

Figure 6.11 Computed Velocity Vectors for AR = 0.2727, Pr = 0.72
$\gamma = 0$, $L_2 = 0.0945$, $L_1 = 0.5$.

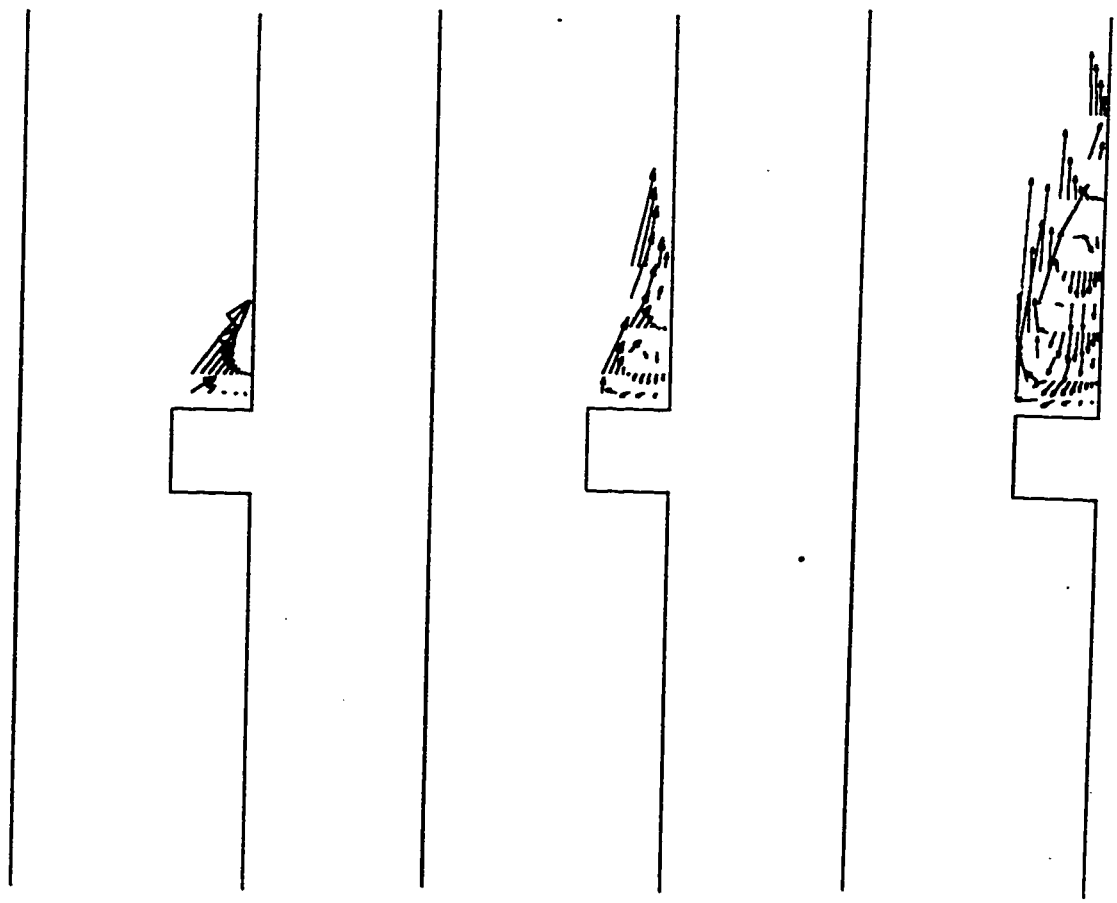

(a) Ra = 29 (b) Ra = 491 (c) Ra = 15531

Figure 6.12 Computed Velocity Vectors (Enlarged) for AR = 0.2727, Pr = 0.72
$\gamma = 0$, $L_2 = 0.0945$, $L_1 = 0.5$.

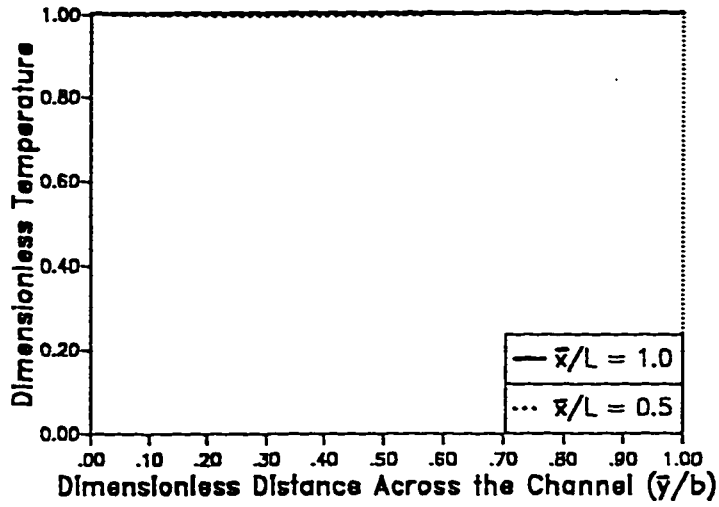

Figure 6.13 Transverse Temperature Distribution at Different Cross-Sections in the Channel for Ra = 29

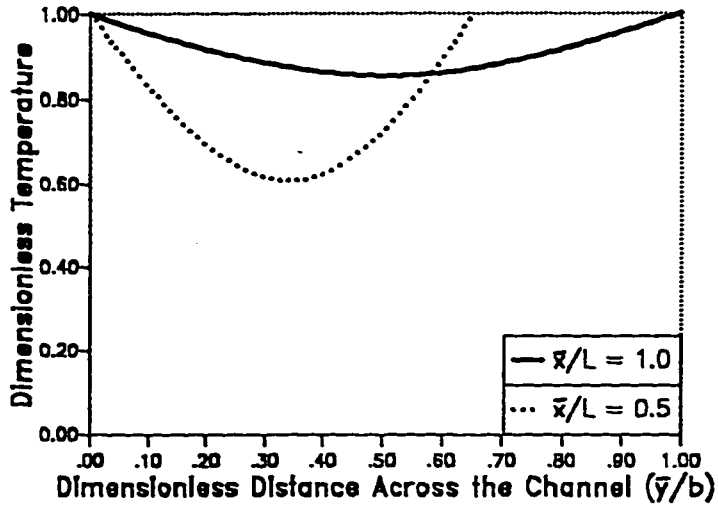

Figure 6.14 Transverse Temperature Distribution at Different Cross-Sections in the Channel for Ra = 491

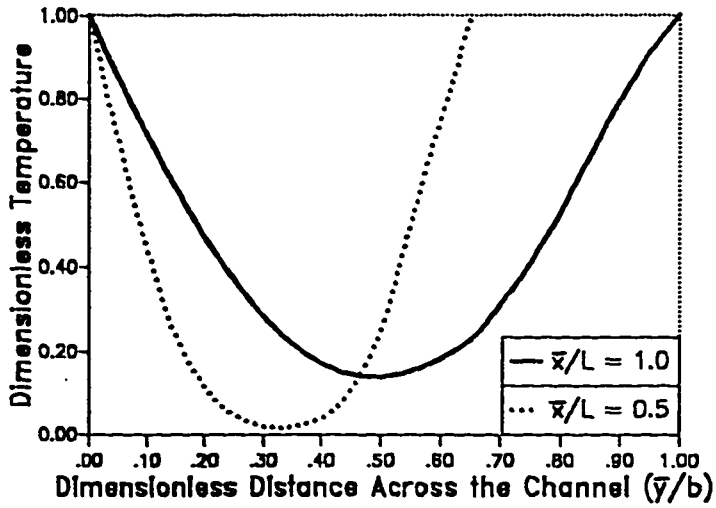

Figure 6.15 Transverse Temperature Distribution at Different Cross-Sections in the Channel for Ra = 15531

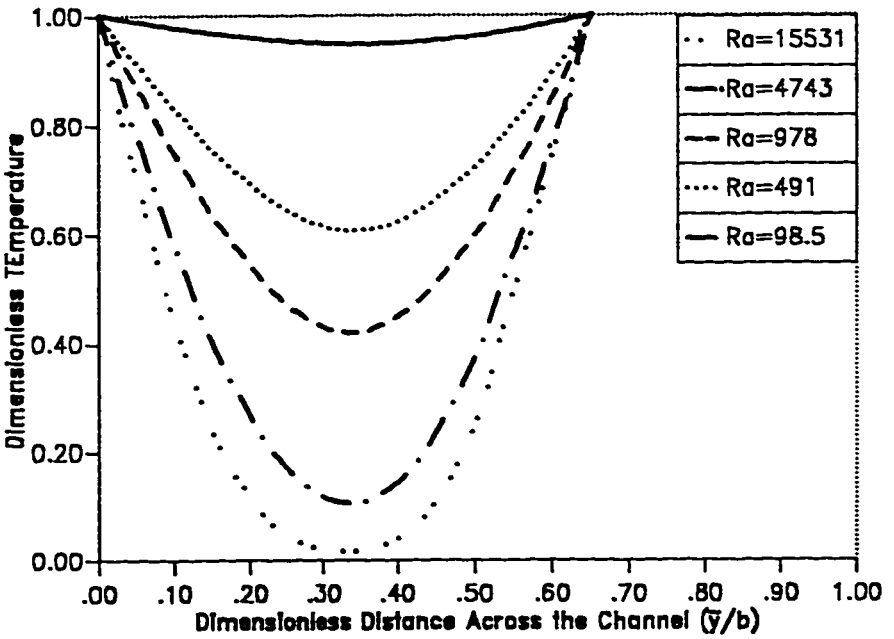

Figure 6.16 Transverse Temperature Distribution at the Obstruction Center-Line for Different Values of Ra.

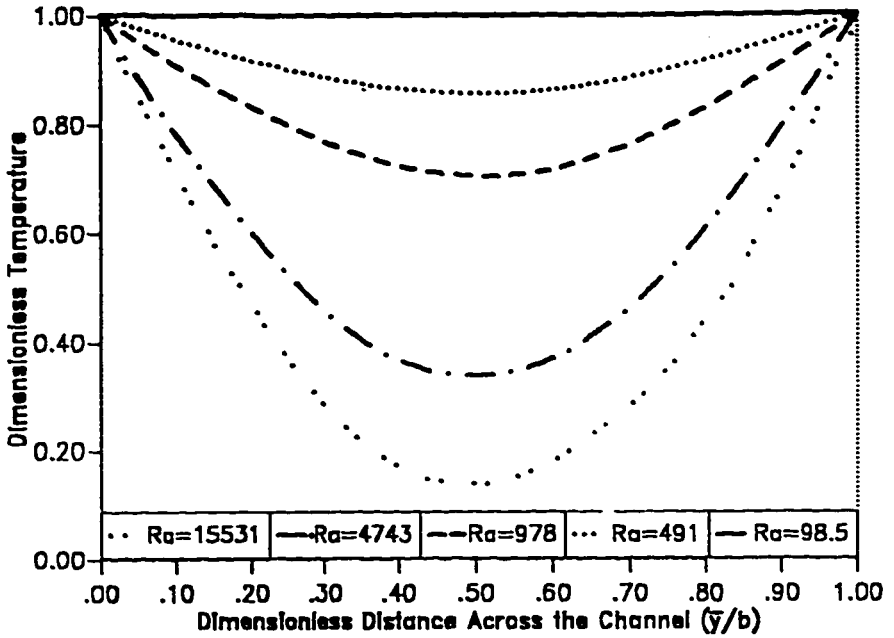

Figure 6.17 Transverse Temperature Distribution at the Exit of the Channel for Different Values of Ra.

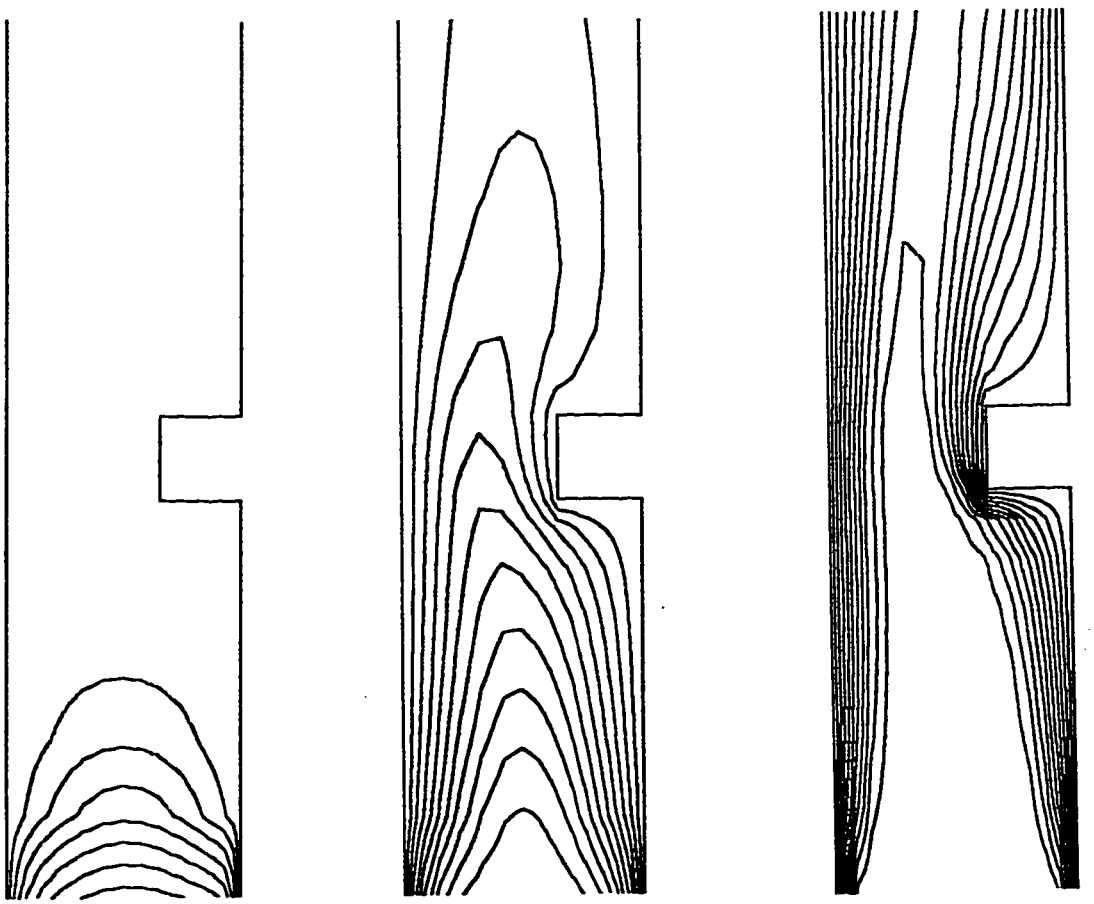

(a) Ra = 29 (b) Ra = 491 (c) Ra = 15531

Figure 6.18 Computed Isotherms for AR = 0.2727, γ = 0 , L_2 = 0.0945 , L_1 = 0.5 ,Pr = 0.72 .

6.3 The Effect of the Aspect Ratio (AR)

The third set of results pertains to the effect of the aspect ratio (AR). The previous results discussed so far were for AR = 0.2727 . To study the effect of the aspect ratio on the flow field and heat transfer characteistics, another aspect ratio is considered.

The mesh generated for this case is shown in figure (6.19). The computed maximum dimensionless velocities, the dimensionless mass flow rates and the average Nusselt numbers are given in TABLE (6-2). The dimensionless mass flow rates (Q) and the average Nusselt numbers ($\overline{Nu}$) are plotted versus the Rayliegh number (Ra) as shown in figures (6.20) and (6.21). It is noted that Q and $\overline{Nu}$ increase as the Ra increases. A comparison of dimensionless mass flow rate and average Nusselt number versus Rayliegh number for the two aspect ratios is shown in figures (6.22) and (6.23). It can be seen that the dimensionless mass flow rates and the average Nusselt numbers increase as the ascpect ratio increases. Figure (6.23) shows that as the Rayliegh number increases the effect of the aspect ratio decreases. This can also be observed from the non-dimensional form of the governing equations by noting that the aspect ratio term multiplies the terms which can reasonably be expected to be relatively small,e.g. the term in the energy equation representing conduction in streamwise direction. Figure (6.24) shows the plot of the average Nusselt number versus the modified Rayliegh number (Ra*AR) for the two aspect ratios. The two curves agree very well with each other (almost identical) especially at very low and very high Rayliegh numbers.

The hydrodynamic results are presented in four different forms. The first form of the hydrodynamic results is the plot of the dimensionless vertical velocities versus the dimensionless channel's width ($\bar{y}/b$) for some representative values of Rayliegh numbers at the channel entrance ($\bar{x}/L=0.0$) , channel mid-plane ($\bar{x}/L=0.5$) and at the channel exit ($\bar{x}/L=1.0$) . These plots are shown in figures (6.25) to (6.27). The second form is the plot of the dimensionless vertical velocity versus the dimensionless channel's width ($\bar{y}/b$) at a given cross-section ($\bar{x}/L$) for different Rayliegh numbers as shown in figures (6.28) through (6.30). It can be seen from these figures that the dimensionless mass flow rates increase as the Rayliegh number increases. The third form of the hydrodynamic results is the streamlines plots as shown in figures (6.31-a) through (6.31-c). Finally, the velocity vectors are shown in figures (6.32-a) through (6.32-c). The velocities right at the top of the obstruction have been magnified and plotted again for the same reasons discussed earlier and plotted in figures (6.33-a) through (6.33-c). No circulation zones exist at low Rayliegh numbers (fully developed channel flow) while at moderate and high Rayliegh numbers circulation zone do exit. The hydrodynamic results for aspect ratio 0.3636 exhibite a similar trend to the hydrodynamic results for aspect ratio 0.2727 .

Three different forms of thermal results will be presented. The first form of the thermal results is the plot of the variation of the average Nusselt number versus the the Ra as shown in Figure (6.21). The second form is the plot of the dimensionless temperature versus the dimensionless distance across the channel ($\bar{y}/b$) at channel mid-plane ($\bar{x}/L=0.5$) and channel exit ($\bar{x}/L=1.0$) for some representative values of Rayliegh numbers. These plots are shown in figures (6.34

to 6.36). The plot of the dimensionless temperature versus the dimensionless channel's width at a channel mid-plane ($\bar{x}/L=0.5$) and channel exit ($\bar{x}/L=1.0$) for different Rayliegh numbers are shown in figures (6.37) and (6.38) respectively. The third form of the thermal results is the isotherms plots for three representative Rayliegh numbers. These plots are shown in figures (6.39-a) through (6.39-c). From these plots, it can be seen that, in the case of low Rayliegh numbers ($Ra < 40$) thermally fully developed limit is reached, while in the case of large Rayliegh numbers ($Ra > 2.0x10^4$) the isolated vertical plate limit will be reached (i.e. a boundary layer is formed on each plate). Since similar trends to $AR=0.2727$ were observed for $AR=0.3636$, the previous discussion for $AR=0.2727$ applies here.

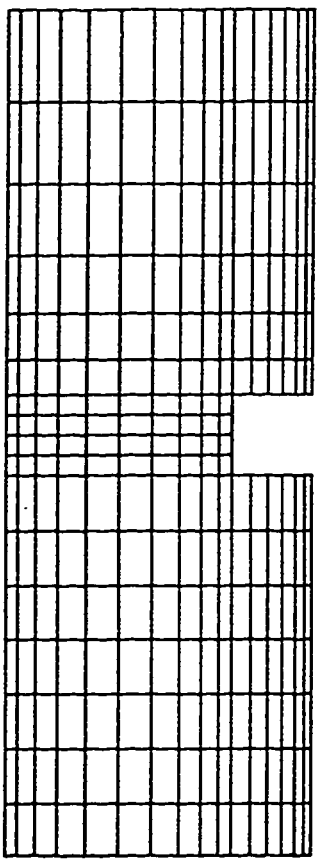

Figure 6.19 Mesh Generated for Parallel-walled Obstructed Channel with $L_1 = 0.5$, $L_2 = 0.0945$, $\gamma = 0$, $Pr = 0.72$ and $AR = 0.3636$.

TABLE(6-2) COMPUTED Umax,Q and $\overline{Nu}$ FOR OBSTRUCTED VERTICAL CHANNEL WITH AR = 0.3636, $L_1 = 0.50$, $L_2 = 0.0945$ and $\gamma = 0$.

Ra′	Ra	Umax	Q	$\overline{Nu}$
1.26	3.46	0.113	0.0578	0.0245
3.77	10.38	0.398	0.2011	0.1038
7.55	20.76	0.775	0.3953	0.2194
12.53	35.00	1.267	0.6431	0.3659
17.09	47.00	1.635	0.8593	0.4814
33.81	93.00	3.143	1.5792	0.7297
169.80	467.00	9.754	5.0933	1.7835
338.91	932.00	15.899	8.3146	2.2843
1713.65	4713.00	38.851	20.6821	3.4747
3333.48	9168.00	55.067	33.5821	4.0757
7870.85	21647.00	82.904	50.4982	4.9591

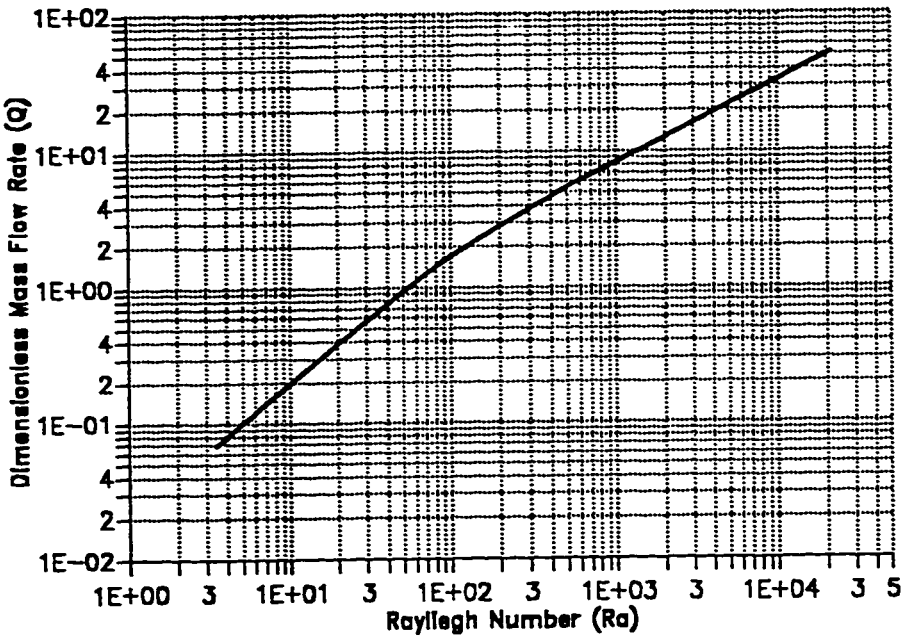

Figure 6.20 The Variation of Dimensionless Mass Flow Rate Versus the Rayliegh Number (Ra) For Obstructed Parallel-Walled Channel (AR = 0.3636).

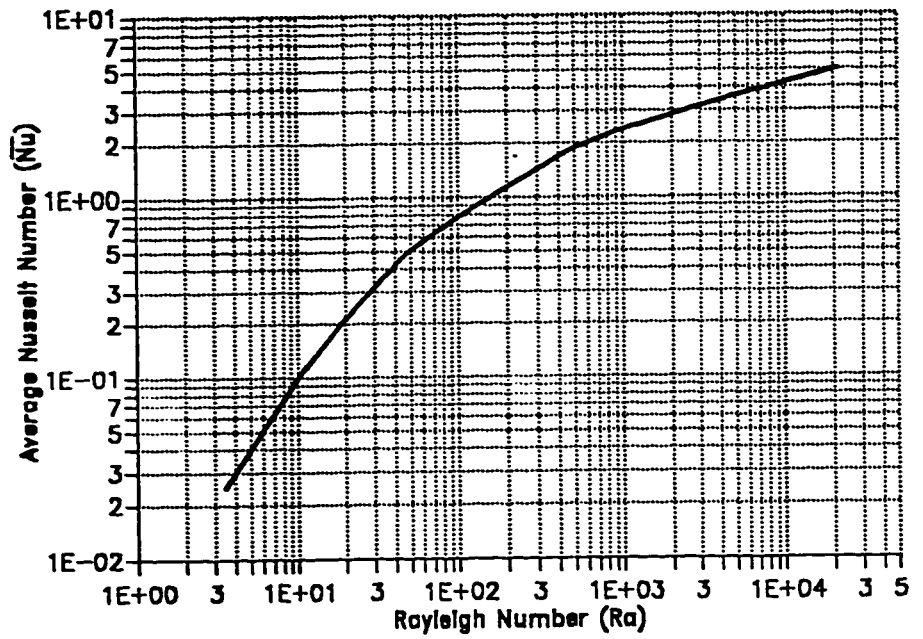

Figure 6.21 The Variation of Average Nusselt Number Versus the Rayliegh Number (Ra) For Obstructed Parallel-Walled Channel (AR = 0.3636).

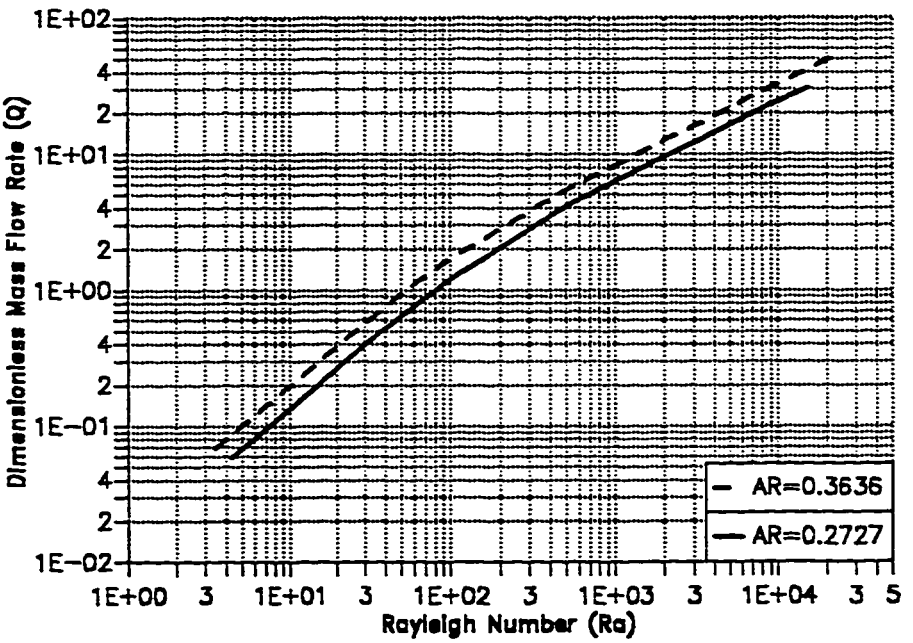

Figure 6.22 The Variation of Dimensionless Mass Flow Rate Versus the Rayliegh Number (Ra) For Obstructed Parallel-Walled Channel.

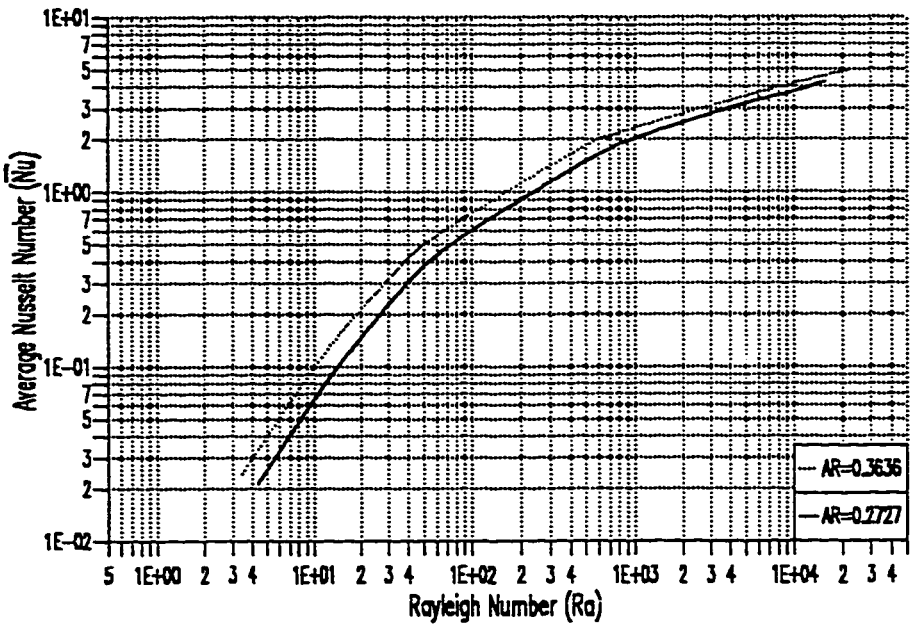

Figure 6.23 The Variation of Average Nusselt Number versus the Rayliegh Number (Ra) For Obstructed Parallel-Walled Channel.

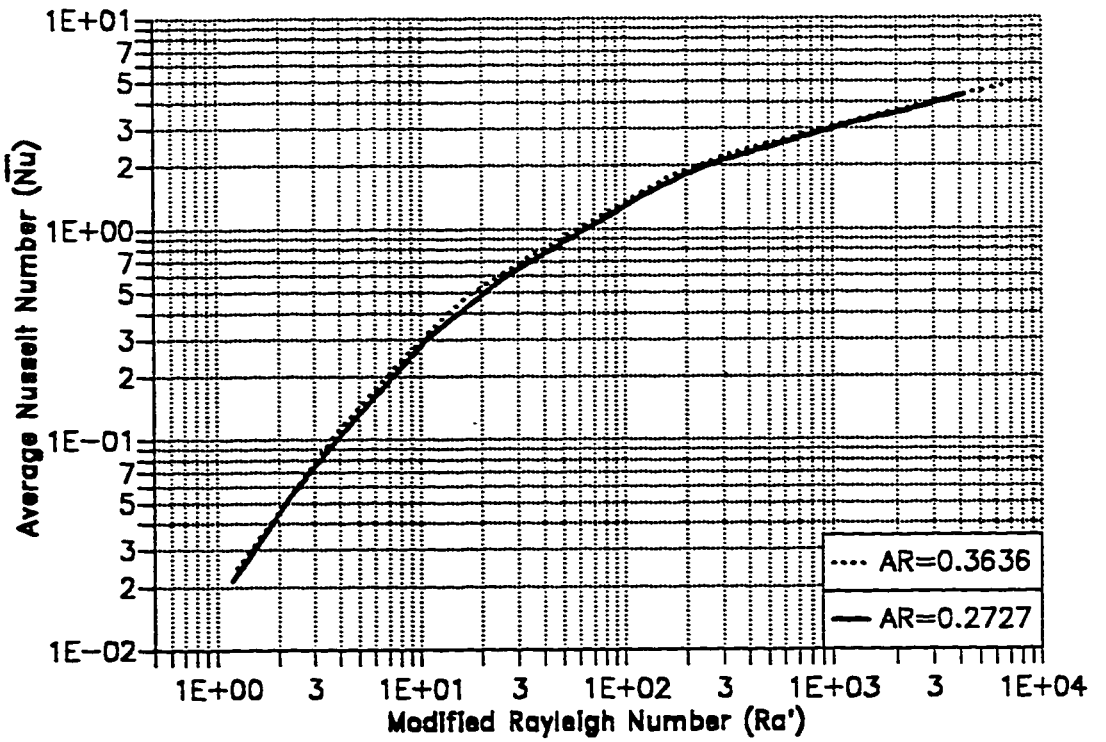

Figure 6.24 The Variation of the Average Nusselt Number of Parallel Walled Obstructed Vertical Channels Versus Ra' for Two Aspect Ratios.

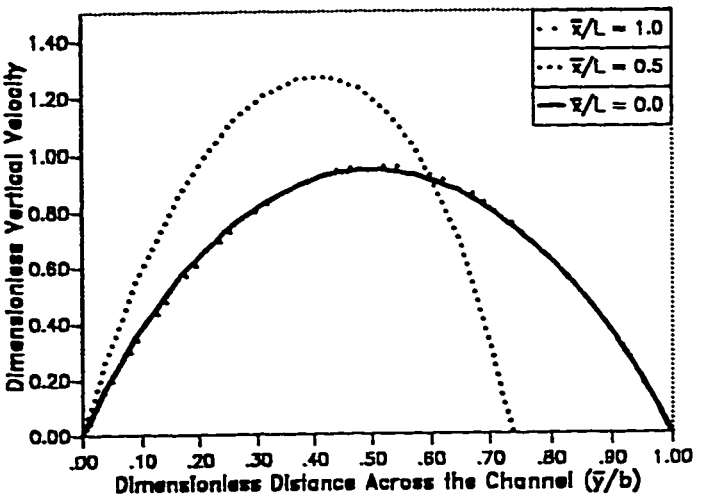

Figure 6.25 Transverse Velocity Distribution at Different Cross-Sections in the Channel for Ra = 35.

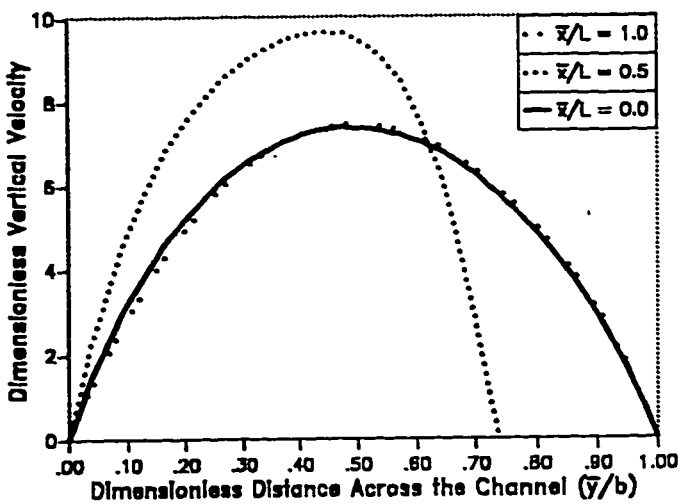

Figure 6.26 Transverse Velocity Distribution at Different Cross-Sections in the Channel for Ra = 467.

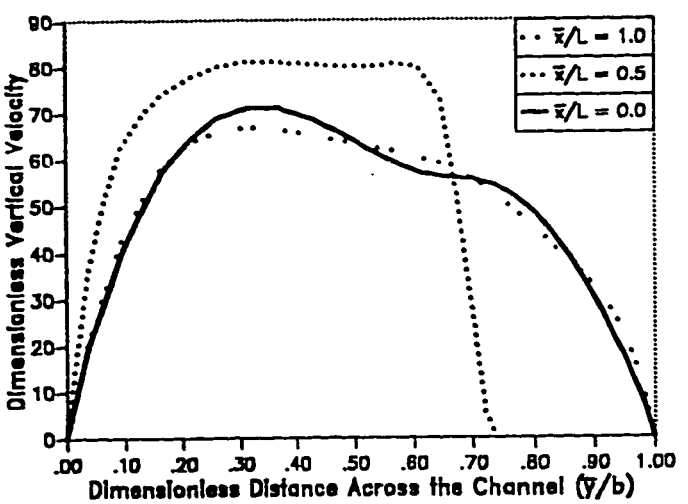

Figure 6.27 Transverse Velocity Distribution at Different Cross-Sections in the Channel for Ra = 21647.

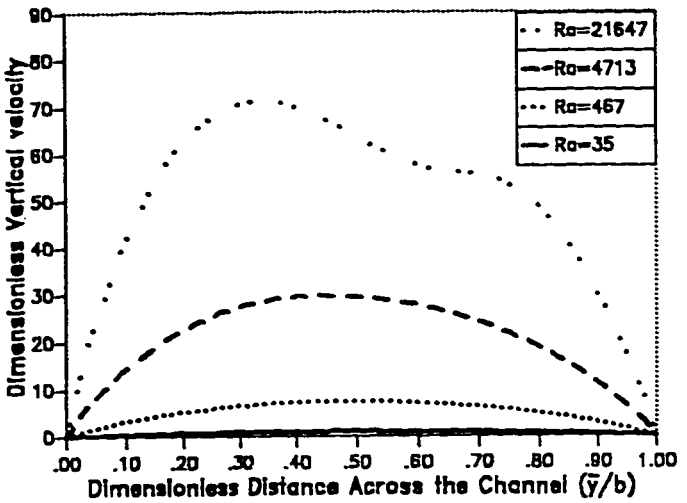

Figure 6.28 Transverse Velocity Distribution at the Entrance of the Channel for Different Values of Ra.

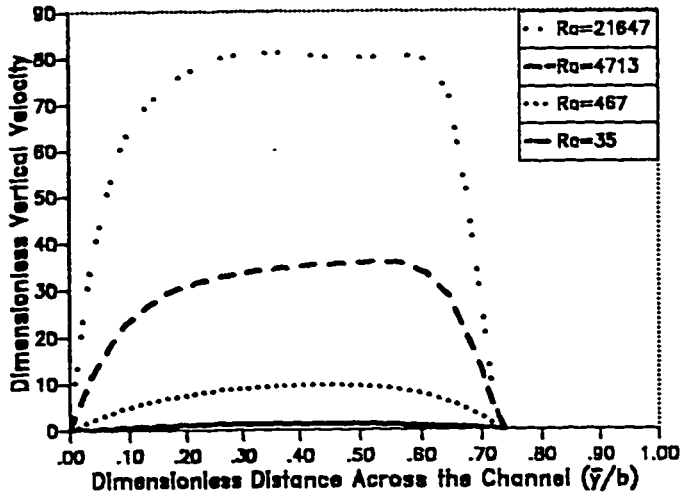

Figure 6.29 Transverse Velocity Distribution at the Obstruction Center-Line for Different Values of Ra.

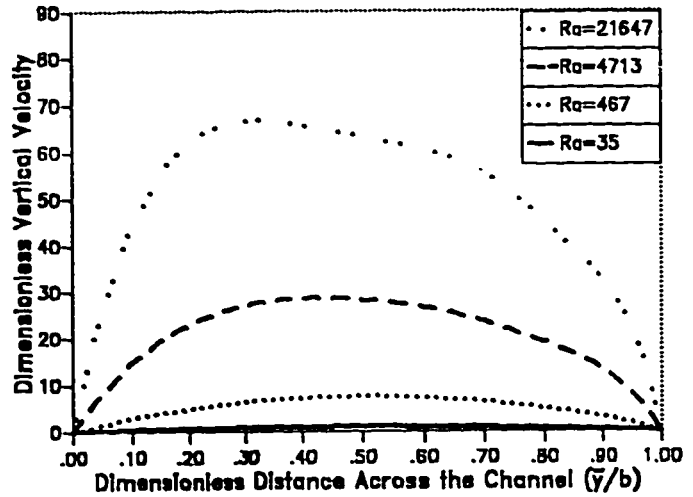

Figure 6.30 Transverse Velocity Distribution at the Exit of the Channel for Different Values of Ra.

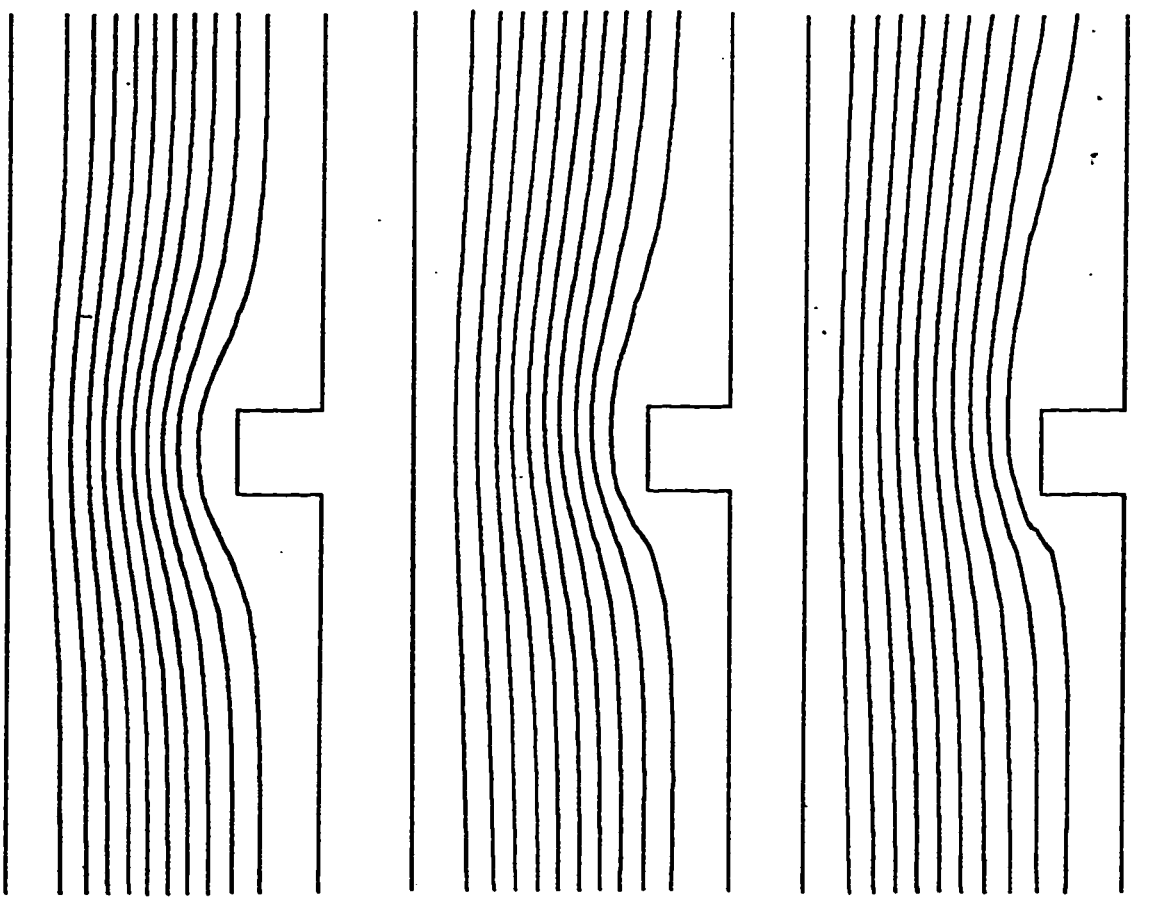

(a) Ra = 35 (b) Ra = 467 (c) Ra = 21647

Figure 6.31 Computed Streamlines for AR = 0.3636, γ = 0, L_2 = 0.0945, L_1 = 0.5, Pr = 0.72.

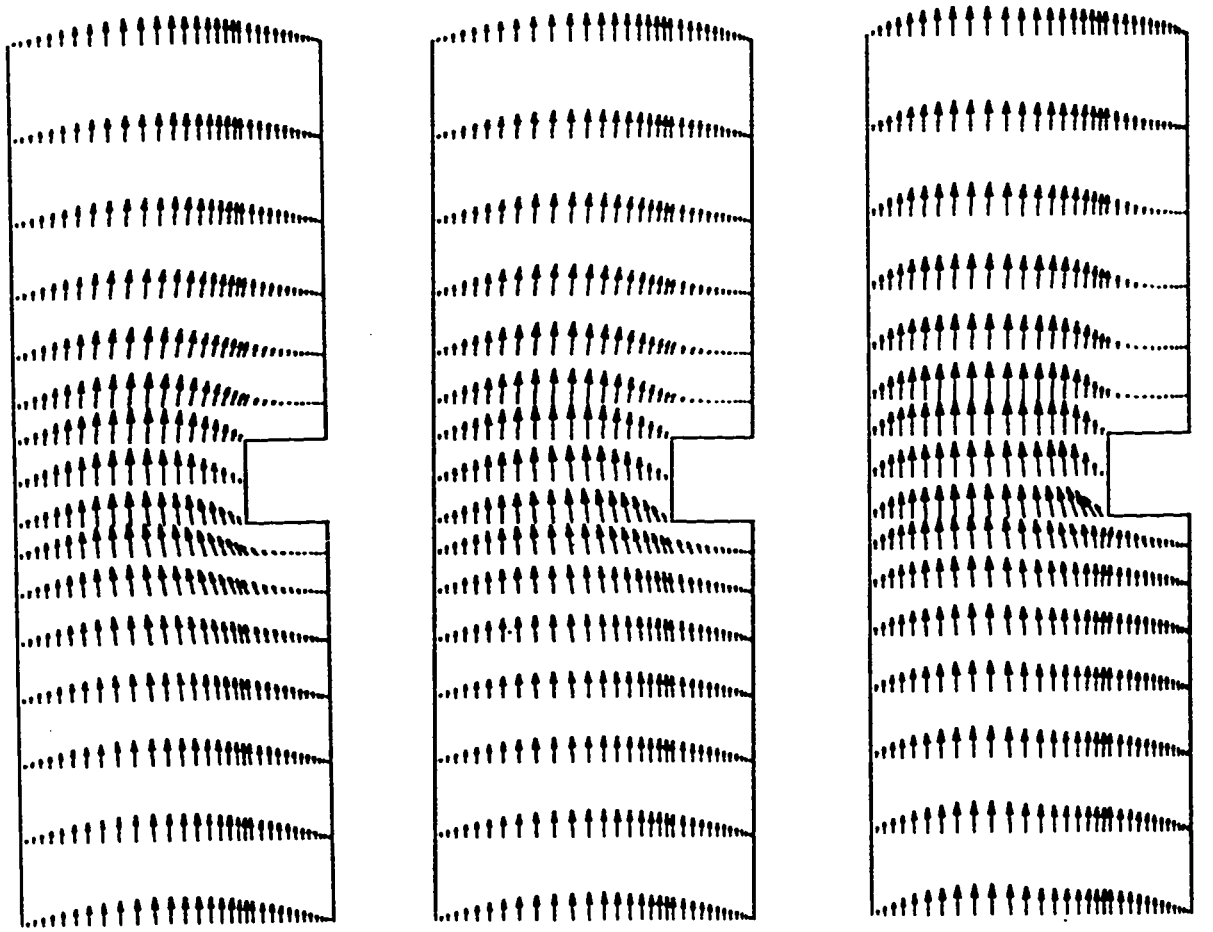

(a) Ra = 35 (b) Ra = 467 (c) Ra = 21647

Figure 6.32 Computed Velocity Vectors for AR = 0.3636, Pr = 0.72
$\gamma = 0$, $I_2 = 0.0945$, $I_1 = 0.5$.

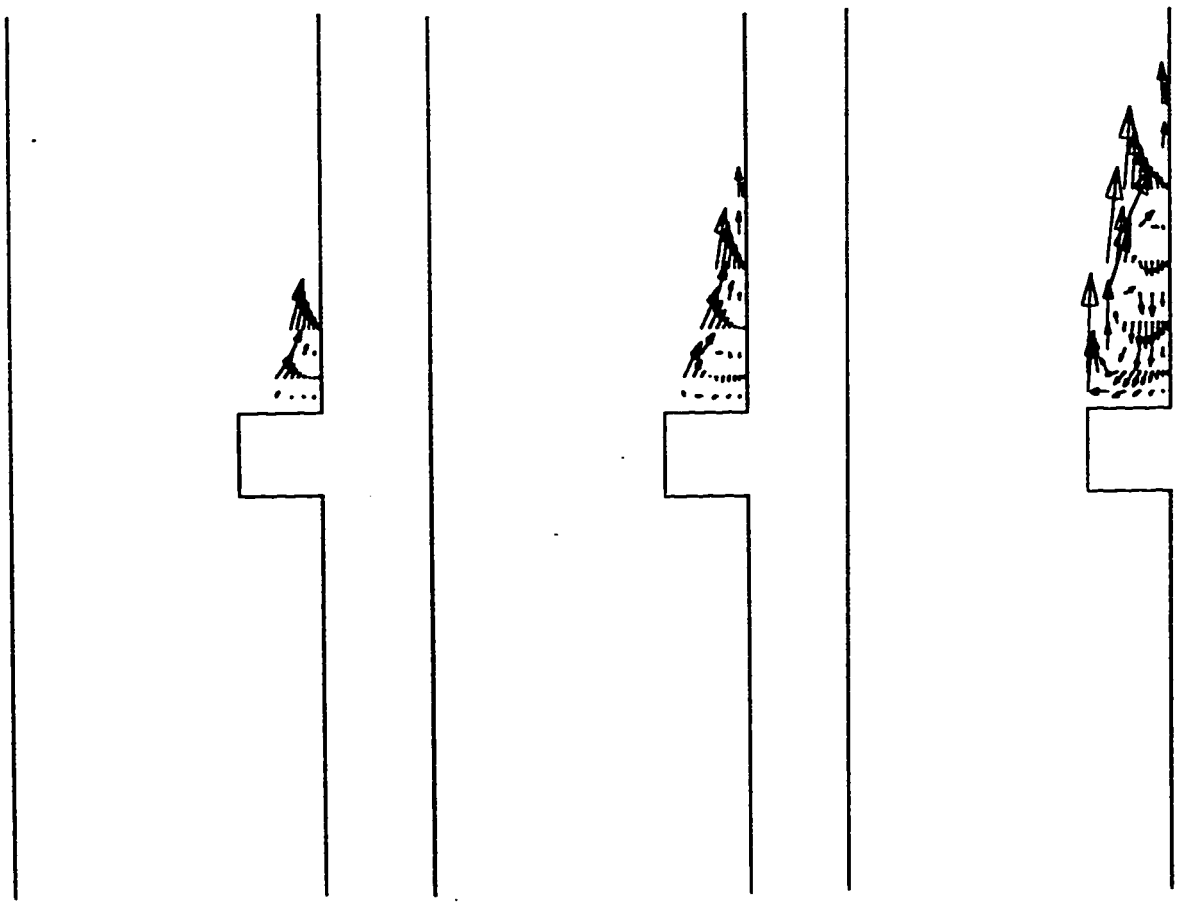

(a) Ra = 35 (b) Ra = 467 (c) Ra = 21647

Figure 6.33 Computed Velocity Vectors (Enlarged) for AR = 0.3636, Pr = 0.72
$\gamma = 0$, $L_2 = 0.0945$, $L_1 = 0.5$.

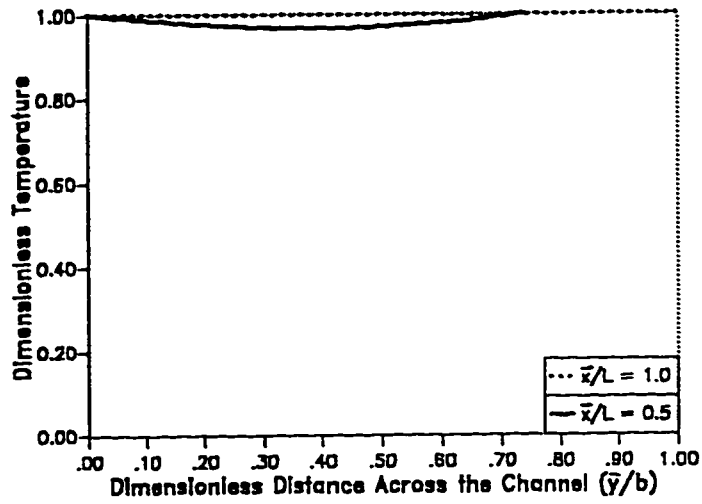

Figure 6.34 Transverse Temperature Distribution at Different Cross-Sections in the Channel for Ra = 35

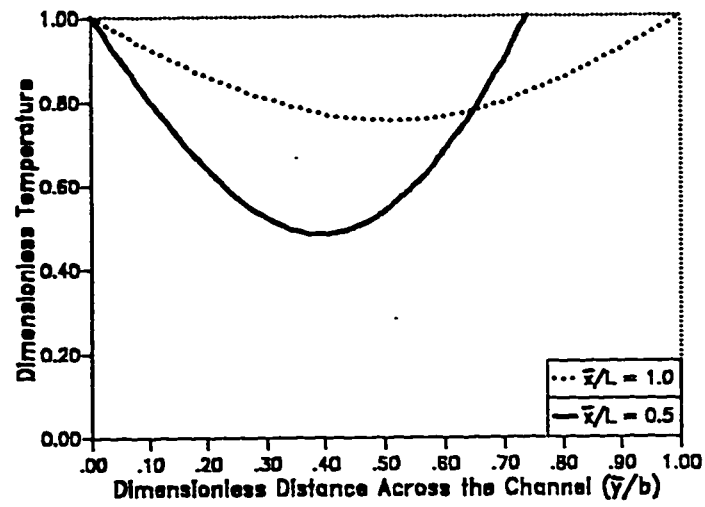

Figure 6.35 Transverse Temperature Distribution at Different Cross-Sections in the Channel for Ra = 467

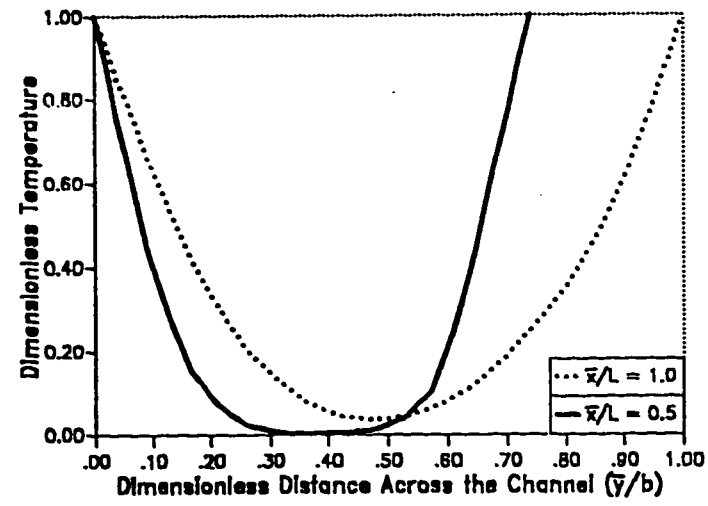

Figure 6.36 Transverse Temperature Distribution at Different Cross-Sections in the Channel for Ra = 21647

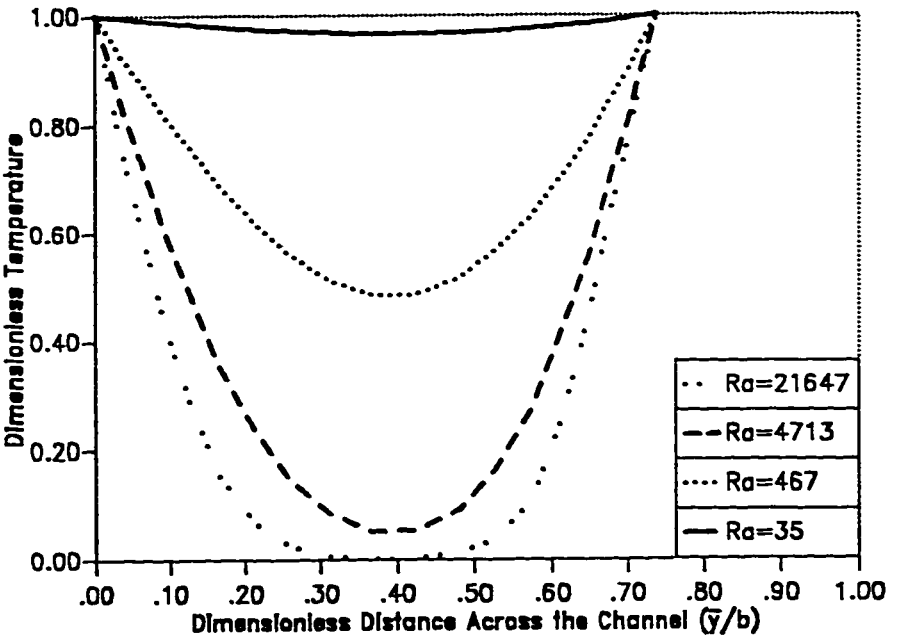

Figure 6.37 Transverse Temperature Distribution at the Obstruction Center-Line for Different Values of Ra.

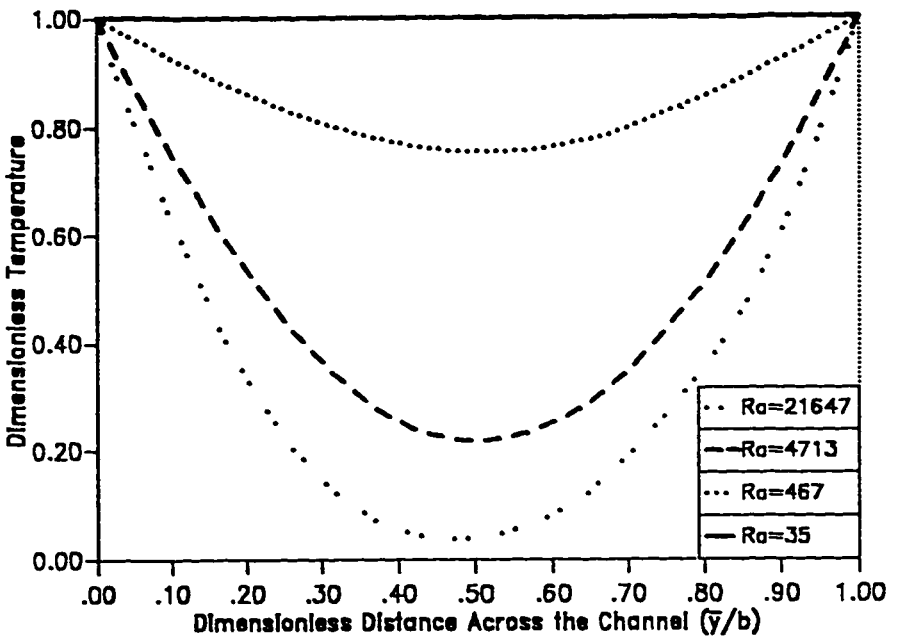

Figure 6.38 Transverse Temperature Distribution at the Exit of the Channel for Different Values of Ra.

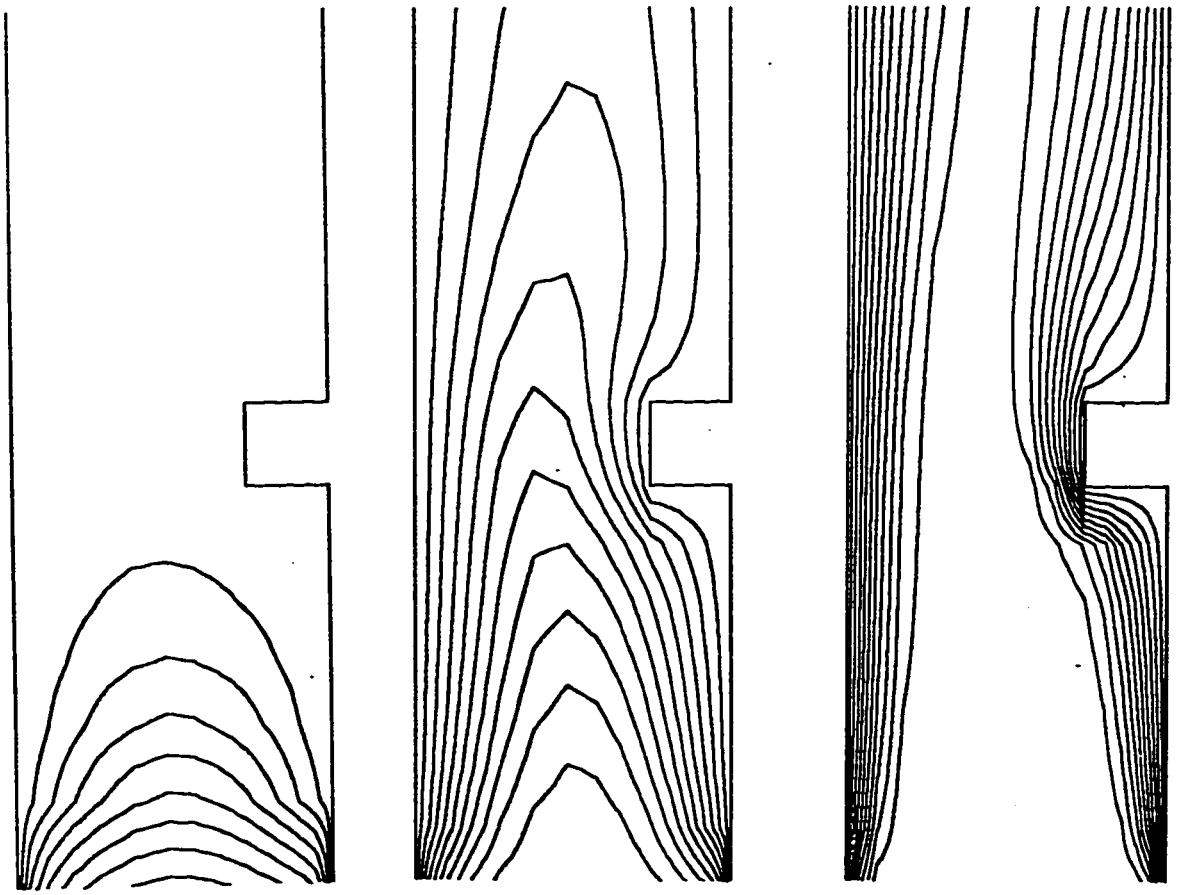

(a) Ra = 35 (b) Ra = 467 (c) Ra = 21647

Figure 6.39 Computed Isotherms for AR = 0.3636, γ = 0 , I_2 = 0.0945 , I_1 = 0.5 , Pr = 0.72 .

6.4 The Effect of L_1

The fourth set of results pertains to the effect of the dimensionless hight L_1. The study considers five different values of L_1, namely, L_1 = 0.1, 0.3, 0.5, 0.7 and 0.9.

The mesh generated for three different cases are shown in figures (6.40-a) through (6.40-c). The computed maximum dimensionless velocity (Umax), the Dimensionless mass flow rate (Q) and the average Nusselt number ($\overline{Nu}$) for each value of L_1 are given in Table (6-3). It can be noted that Umax,Q and $\overline{Nu}$ decrease as L_1 increases. Figures (6.41) and (6.42) show the variation of $\overline{Nu}$ and Q versus L_1 respectively. It can be noted that the reduction rate of Umax,Q and $\overline{Nu}$ increases as the obstruction moves away from the channel mid-plane towards the entrance or the exit. Recalling the hydrodynamic boundary condition at the entrance and at the exit of the obstructed channel, which is taking the horizontal velocity to be zero, one can say that such boundary condition has some effect in the solution of the present problem when the obstruction is located close to the entrance or to the exit of the channel. Therefore such variation in the average Nusselt number could be a result of the previous boundary condition. The hydrodynamic and the thermal results will be presented below.

The hydrodynamic results are presented in four different forms. The first form is the plot of the dimensionless vertical velocity versus the dimensionless channel's width ($\bar{y}$ /b) at the channel entrance ($\bar{x}$ /L = 0.0), the obstruction center-line ($\bar{x}$/L = L_1) and the channel exit ($\bar{x}$ /L = 1.0) for each value of L_1. These

plots are shown in figures (6.43) through (6.45). Figure (6.43) shows that the point of maximum dimensionless vertical velocity at the entrance of the channel ($\bar{x}/L = 0.0$) is towards the non-obstructed wall. This is due to the presence of the obstruction close to the entrance ($L_1 = \bar{x}/L = 0.1$). Figure (6.44) shows that the the dimensionless vertical velocity profiles at the entrance and at the exit of the channel are similar owing to the presence of the obstruction at the mid-plane of the channe ($L_1 = \bar{x}/L = 0.5$). Figure (6.45) shows that the point of maximum dimensionless vertical velocity at the channel exit ($\bar{x}/L = 1.0$) is also towards the non-obstructed wall. This is due to the presence of the obstruction close to the exit of the channel ($L_1 = \bar{x}/L = 0.9$). For $L_1 = 0.9$ negative velocities are observed at the exit of the channel in the region right at the top of the obstruction. From these figures it can be noted that the maximum dimensionless velocity at the mid-plane of the obstruction where the channel cross-sectional area is minimal.

The second form of the hydrodynamic results are shown in figures (6.46 to 6.48). The velocity profile at a given elevation in the channel is plotted versus the dimensioless distance across the channel ($\bar{y}/b$) for three different values of L_1. Two main conclusions can be derived from these figures. The first one is as L_1 increases (the obstruction moves away from the entrance), the mass flow rate decreases. And the second one is as L_1 increases the magnitude of the maximum velocity at the obstruction mid-plane ($\bar{x}/L = L_1$) decreases and the point at which this occurs tends to shift towards the obstruction.

The third form of the hydrodynamic results is the streamline plots as shown in figures (6.49-a) through (6.49-c). It can be seen that the density of the streamlines increases in the region arround the vertical side of the obstruction due to the reduction in the channel's cross-sectional area. Hence, the flow speeds up in this region. Due to the same reasons mentioned before, velocity vectors are computed and plotted in figures (6.50-a) through (6.50-c). These plots show clearly the variation of the velocity vectors through out the channel. However, it is clear that the magnitude of the velocity vectors right at the top of the obstruction are very small. Hence, velocity vectors at the top of the obstruction have been magnified fifteen times and shown in figures (6.51-a) through (6.51-c). Regions of recirculating flow are detected above the obstruction.

The thermal results are presented by four different forms. The first form is the plot of dimensionless temperature of air at ($\bar{x}/L = L_1$ and 1.0) versus the dimensionless channel's width ($\bar{y}/b$) for three different values of L_1 as shown in figures (6.52 to 6.54). From these figures it can be seen that the the fluid temperature increases in the streamwise direction (as $\bar{x}$ /L increases) for any value of L_1 . The dimensionless temperature has been plotted versus the demensionless channel's width ($\bar{y}$ /b) at the obstruction mid-plane and the channel exit for different values of L_1 (different location for the obstruction). These plots are shown in figures (6.56) and (6.57). The dimensionless temperature at a given cross-section ($\bar{x}$ /L) increases as L_1 increases (the obstruction moves away from the entrance).

The second form of thermal results is the isotherm plots. These plots are

shown in figures (6.57-a) through (6.57-c). Examining these plots, it can be noted that the boundary layer thickness at the channel entrance increases as the obstruction moves away from the entrance (as L_1 increases). Hence, the temperature gradients at the wall decreases as L_1 increases and this will lead to reduced values of Nusselt numbers.

The third form of thermal results is the variation of the local Nusselt number along the obstructed and non-obstructed walls as shown in figures (6.58 to 6.60). It can be noted that the Nu_L for the non-obstructed wall decreases as $\bar{x}$ /L increases. The local Nusselt number curves for the obstructed wall have two points of maximum (apart from the leading edge) and two points of minimum due to the presence of the obstruction. The two points of maximum are caused by the flow speeding up in these regions due to the reduction in the flow cross-sectional area caused by the presence of the obstruction. The two points of minimum local Nusselt number are caused due to the decrease of the velocity right at the top and bottom of the obstruction and the presence of the circulation zones. The variation of local Nusselt numbers along the non-obstructed wall at different values of L_1 is shown in figure (6.61) while the variation of the local Nusselt numbers along the obstructed wall is shown in figure (6.62) . It is clear that as L_1 increases the maximum point for the local Nusselt number decreases. The fourth form of the thermal results are the variation of the average Nusselt number versus L_1 as shown earlier in figure (6.41).

To conclude on the effect of L_1 on the heat transfer characteristics, it can be said that as the obstruction moves away from the entrance of the channel (as L_1

increases) towards the exit, the rate of heat transfer decreases. This results agrees with those found by Said and Krane [47]. However, the obstruction used in their case was a semi-circle obstruction. Hence, in spite of the obstruction geometry, using air as the working fluid, it is advisable to locate the obstruction as close as possible to the entrance of the channel in order to ensure that maximum rate of heat transfer occurs.

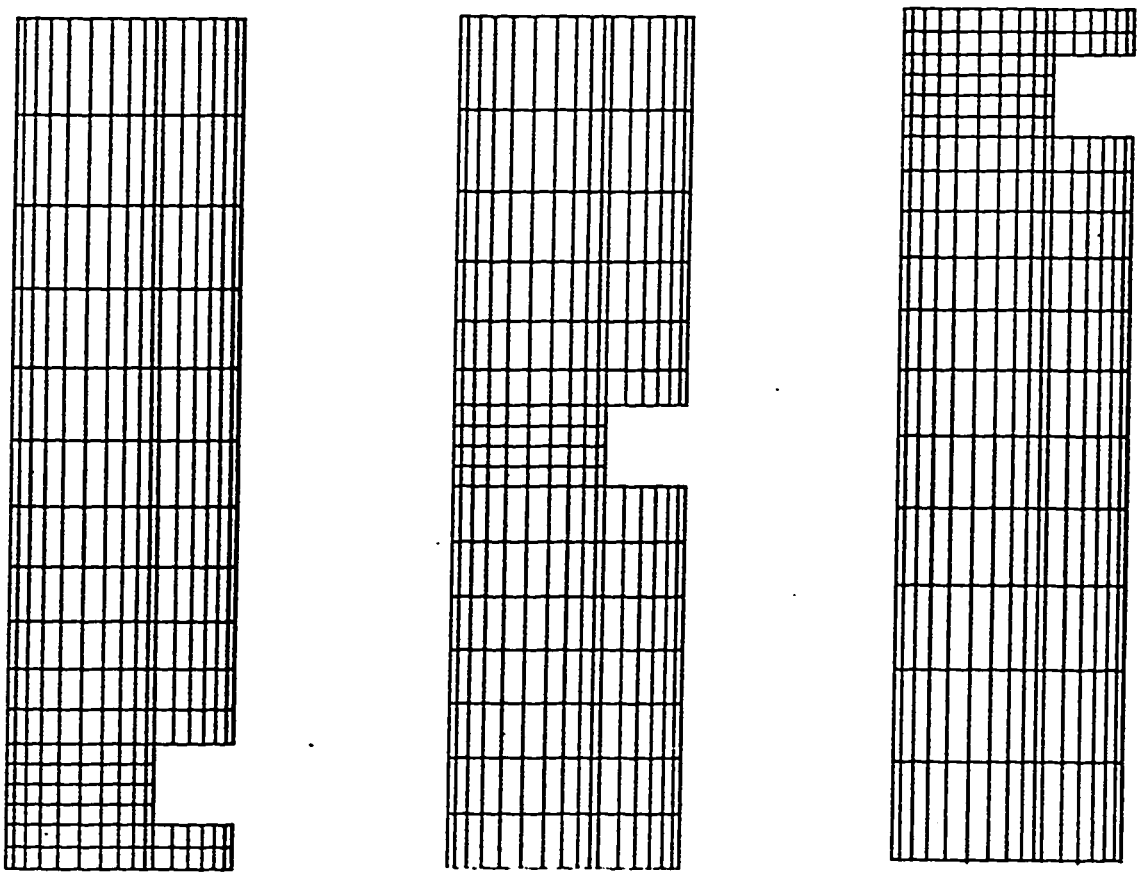

(a) $L_1 = 0.1$ (b) $L_1 = 0.5$ (c) $L_1 = 0.9$

Figure 6.40 Generated Mesh for AR = 0.2727, $\gamma = 0$, $L_2 = 0.0945$, Ra = 1000, Pr = 0.72 .

TABLE (6-3) COMPUTED Umax,Q and $\overline{Nu}$ FOR OBSTRUCTED VERTICAL CHANNEL WITH AR = 0.2727, Ra = 1000, L_2 = 0.0945 and γ = 0.

L_1	Umax	Q	$\overline{Nu}$
0.1	16.16	7.50	2.3670
0.3	13.82	6.40	2.1138
0.5	13.54	6.23	2.0698
0.7	13.11	6.01	2.0192
0.9	11.91	5.42	1.8486

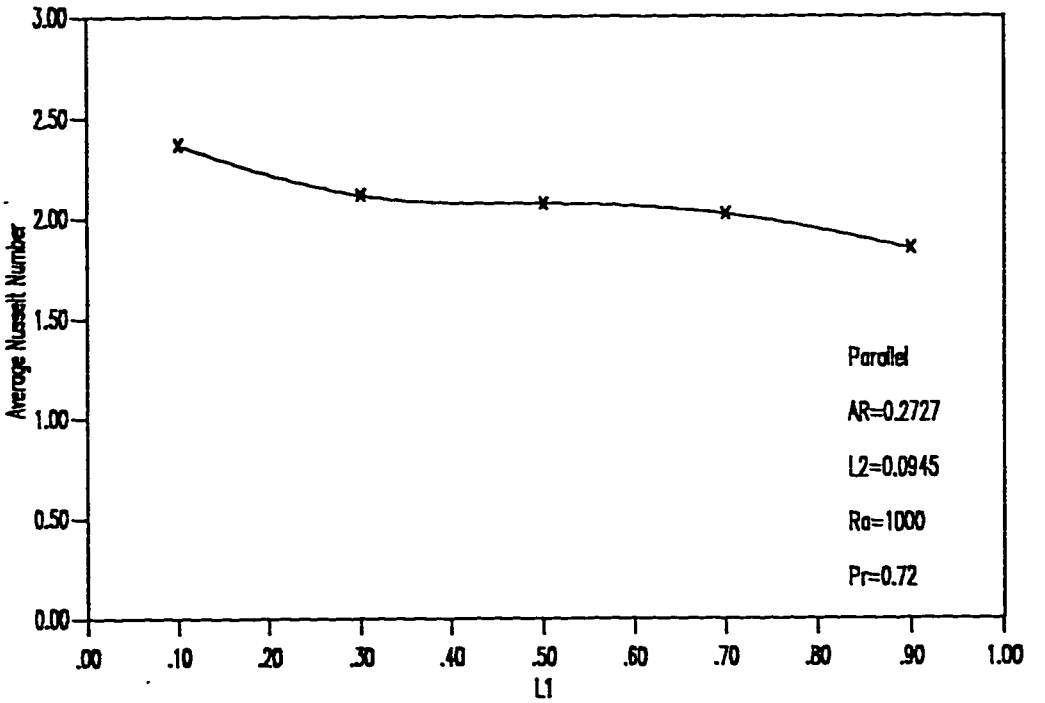

Figure 6.41 The Variation of Average Nusselt Number against the Location of the Obstruction (L1)

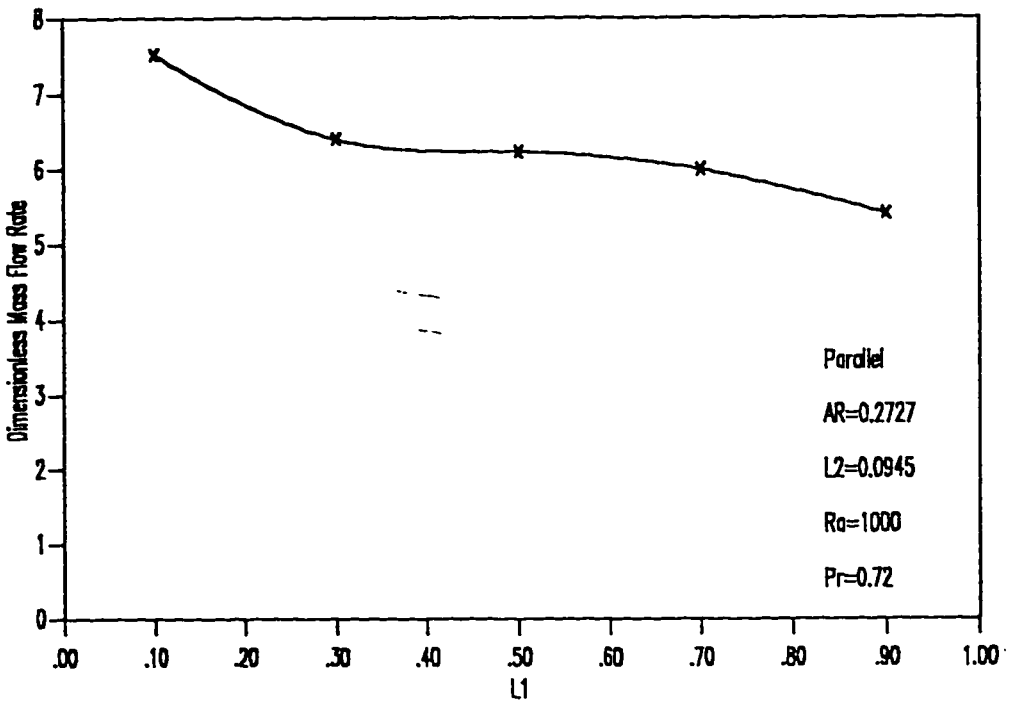

Figure 6.42 The Variation of Dimensionless Mass Flow rate against the Location of the Obstruction (L1)

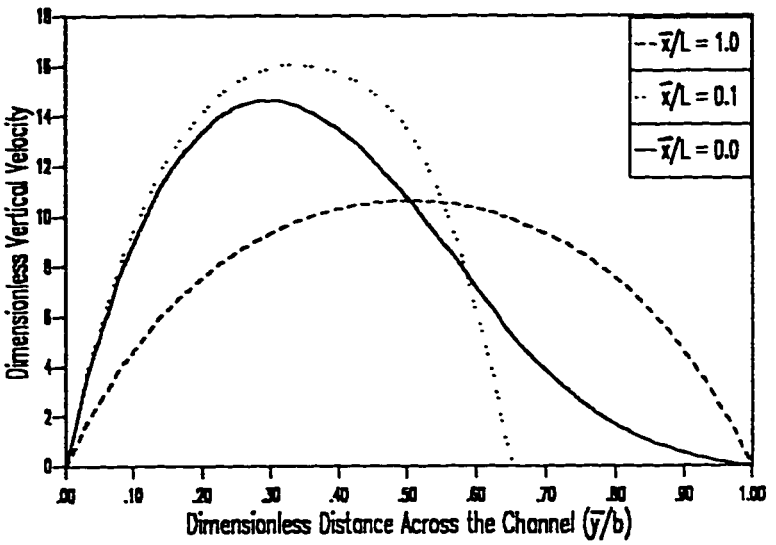

Figure 6.43 Transverse Velocity Distribution at Different Cross-Sections in the Channel for L1 = 0.1

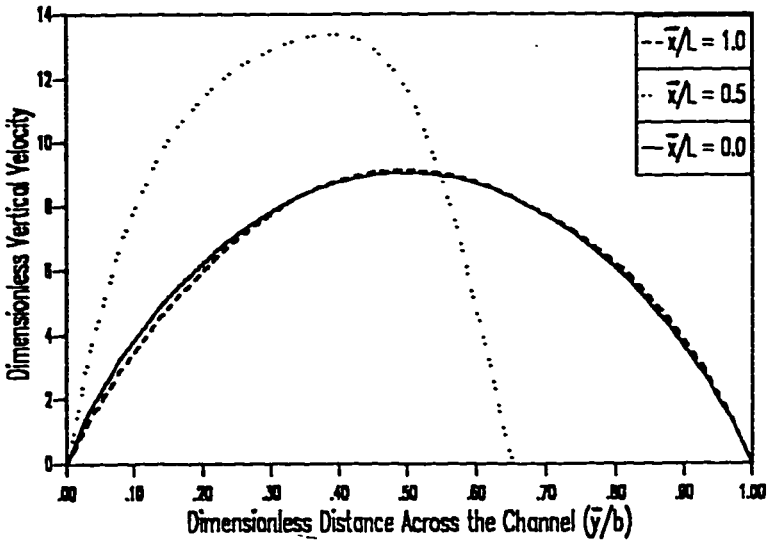

Figure 6.44 Transverse Velocity Distribution at Different Cross-Sections in the Channel for L1 = 0.5

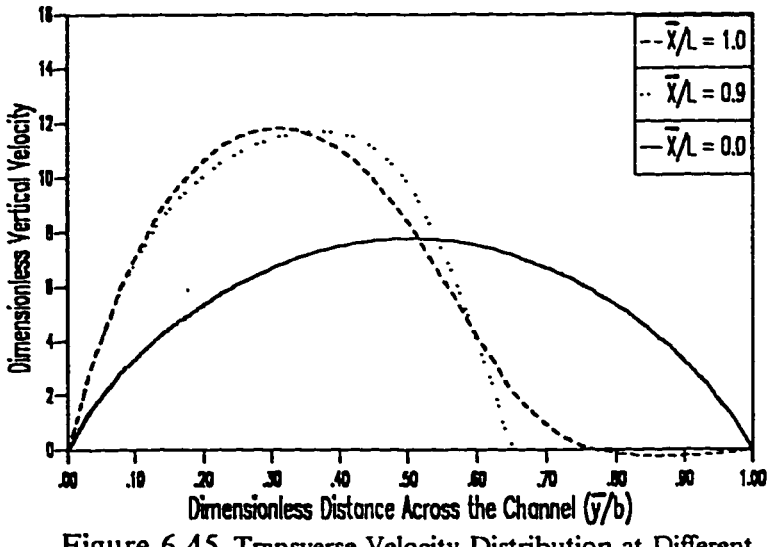

Figure 6.45 Transverse Velocity Distribution at Different Cross-Sections in the Channel for L1 = 0.9

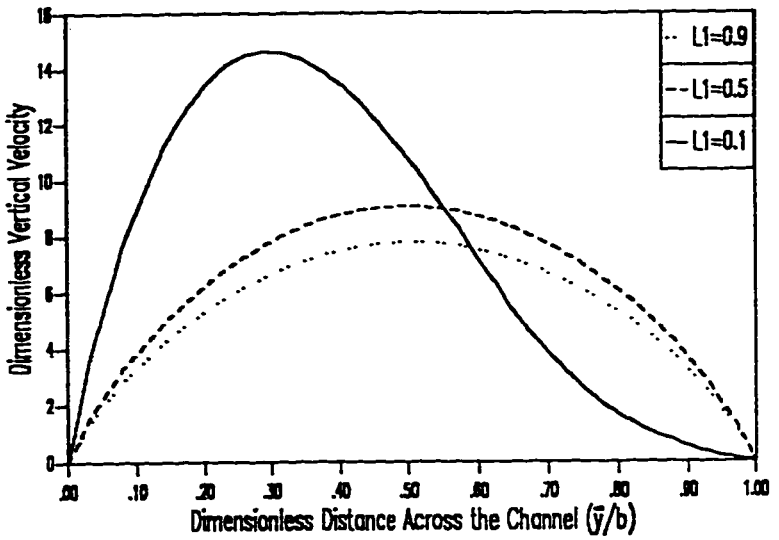

Figure 6.46 Transverse Velocity Distribution at the Entrance of the Channel for Different Obstruction Positions.

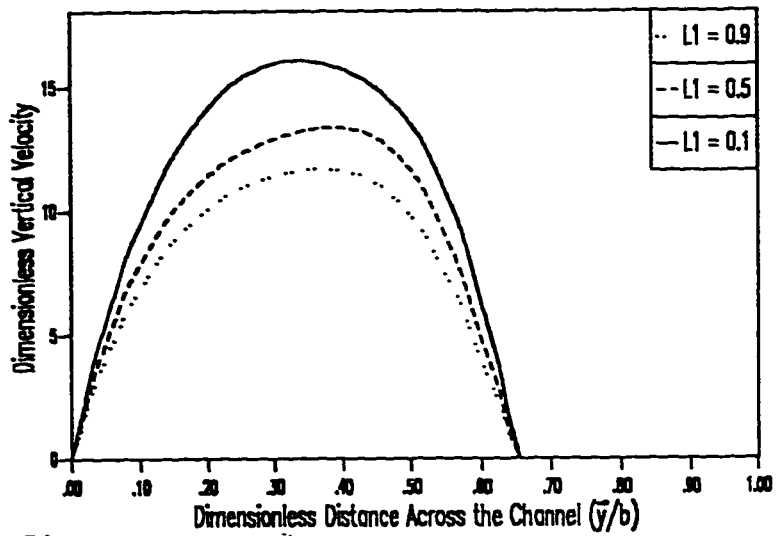

Figure 6.47 Transverse Velocity Distribution at the Obstruction Center-Line for Different Obstruction Positions.

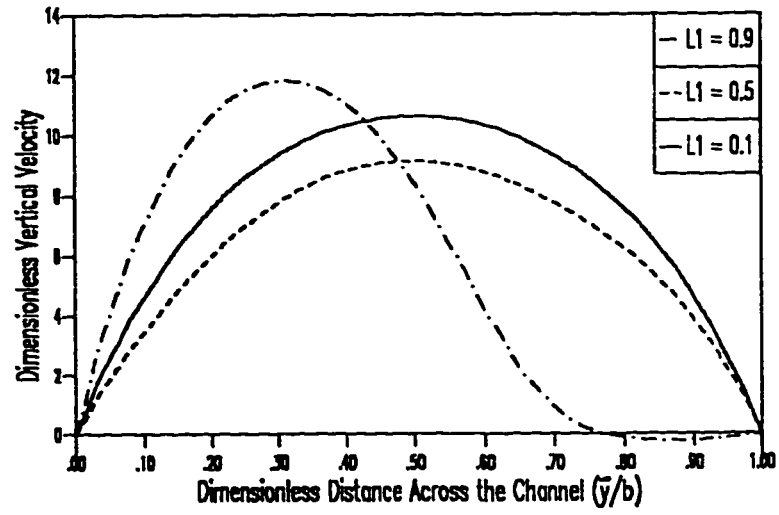

Figure 6.48 Transverse Velocity Distribution at the Exit of the Channel for Different Obstruction Positions.

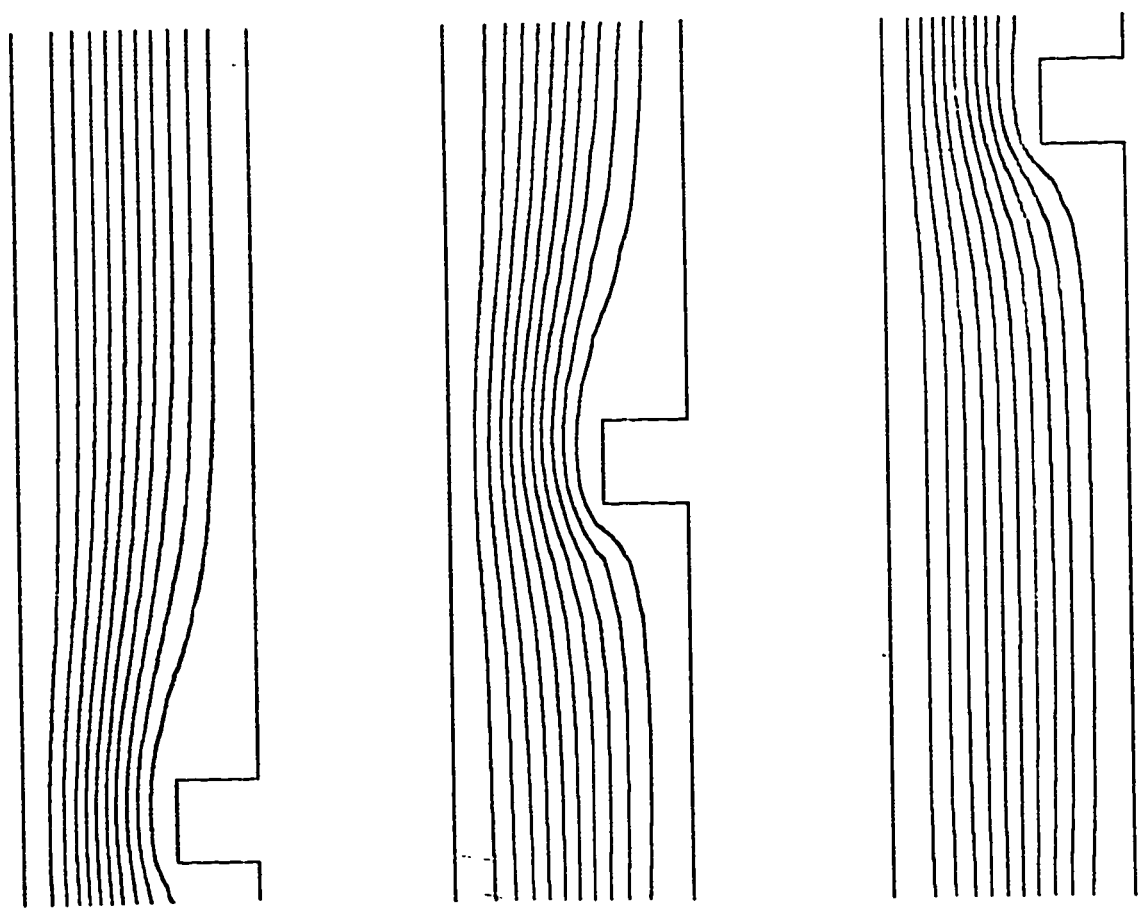

(a) $L_1 = 0.1$ (b) $L_1 = 0.5$ (c) $L_1 = 0.9$

Figure 6.49 Computed Streamlines for AR = 0.2727, $\gamma = 0$, $L_2 = 0.0945$, Ra = 1000, Pr = 0.72 .

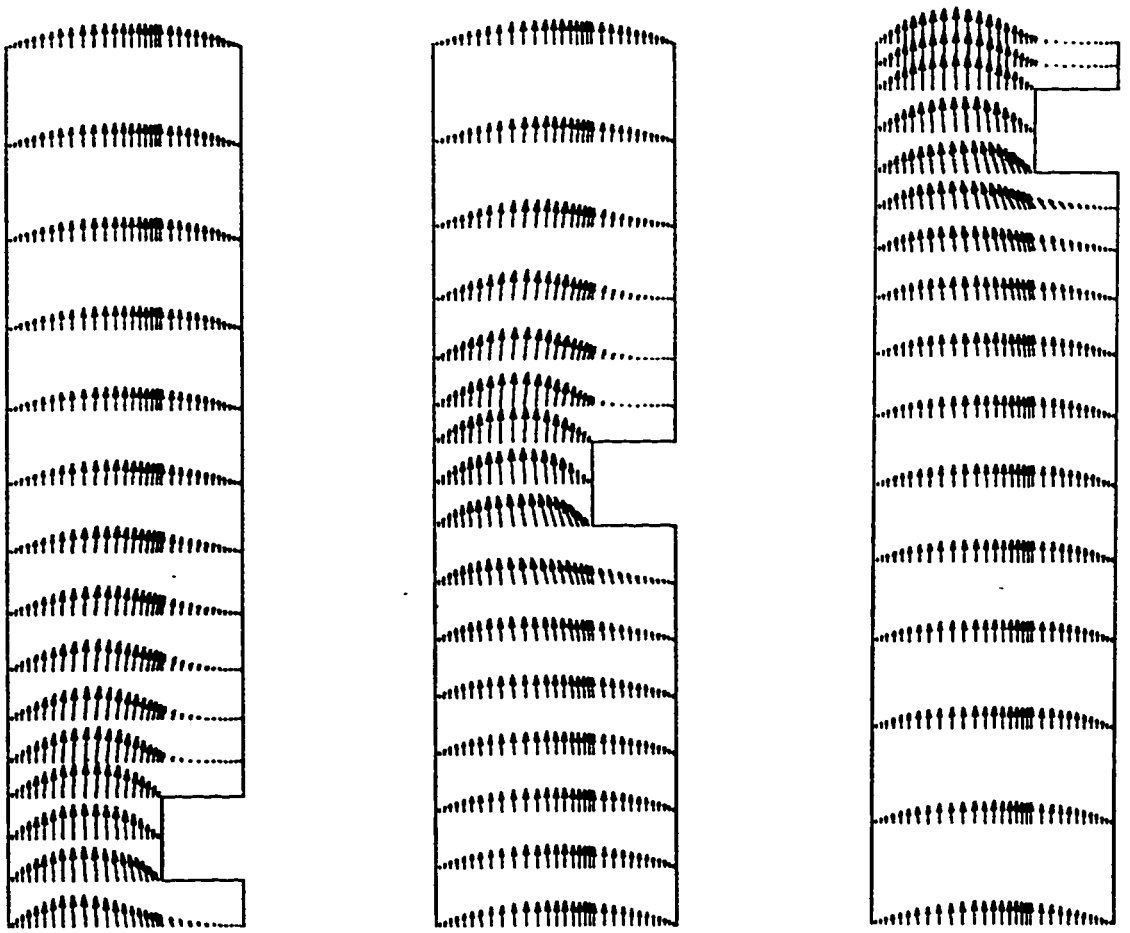

(a) $L_1 = 0.1$ (b) $L_1 = 0.5$ (c) $L_1 = 0.9$

Figure 6.50 Computed Velocity Vectors for AR = 0.2727, Ra = 1000
$\gamma = 0$, $L_2 = 0.0945$, Pr = 0.72 .

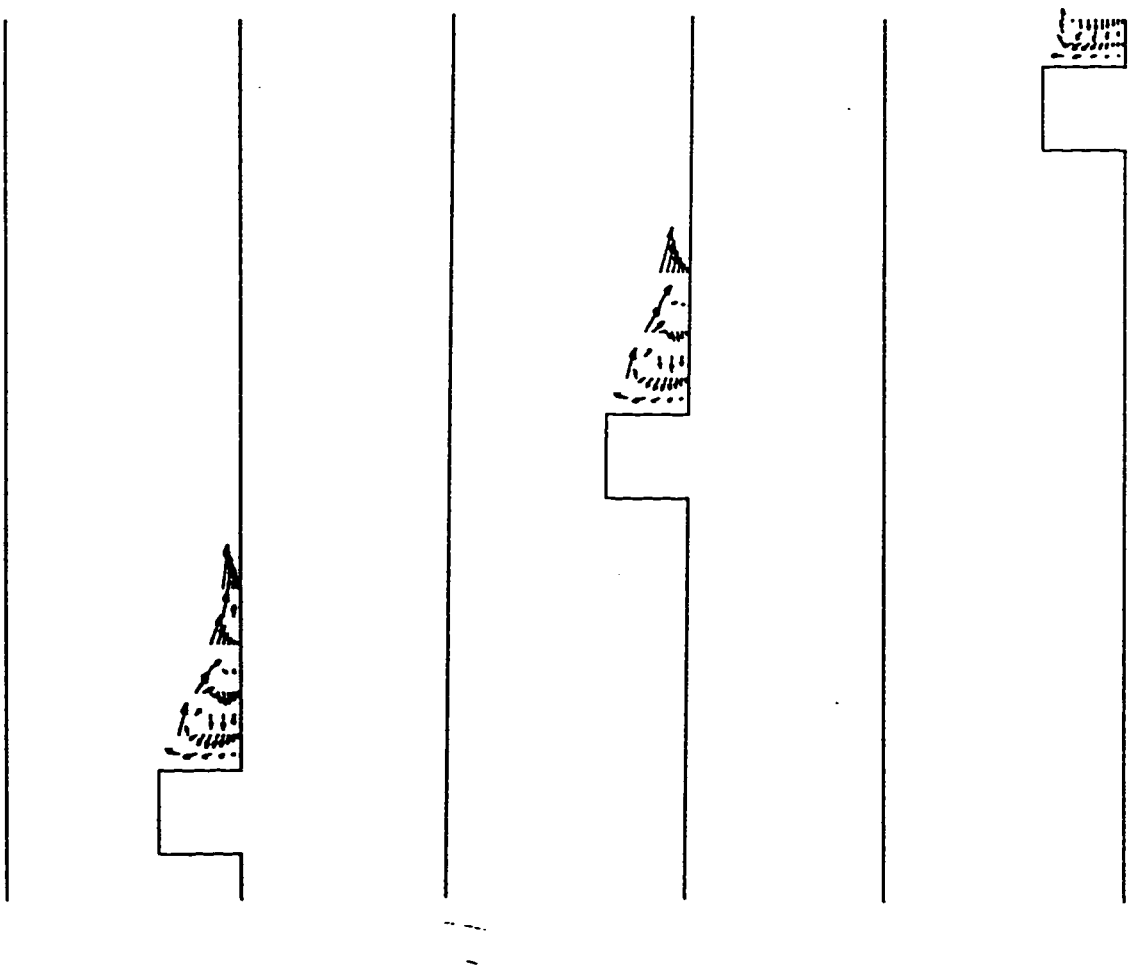

(a) $L_1 = 0.1$ (b) $L_1 = 0.5$ (c) $L_1 = 0.9$

Figure 6.51 Computed Velocity Vectors (Enlarged) for AR = 0.2727, RA = 1000
$\gamma = 0$, $L_2 = 0.0945$, Pr = 0.72 .

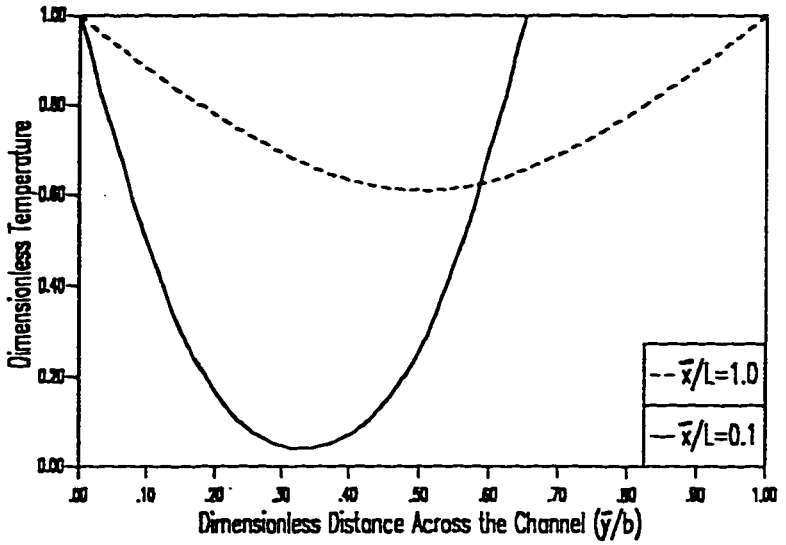

Figure 6.52 Transverse Temperature Distribution at Different Cross-Sections in the Channel for L1 = 0.1

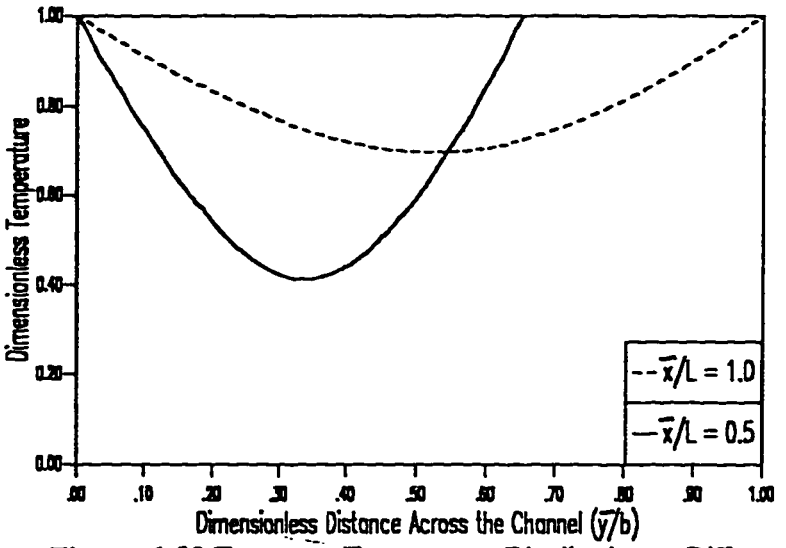

Figure 6.53 Transverse Temperature Distribution at Different Cross-Sections in the Channel for L1 = 0.5

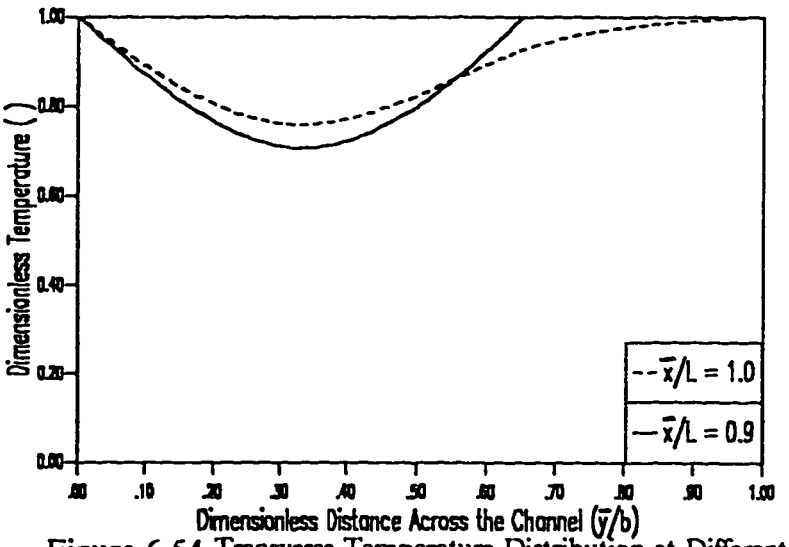

Figure 6.54 Transverse Temperature Distribution at Different Cross-Sections in the Channel for L1 = 0.9

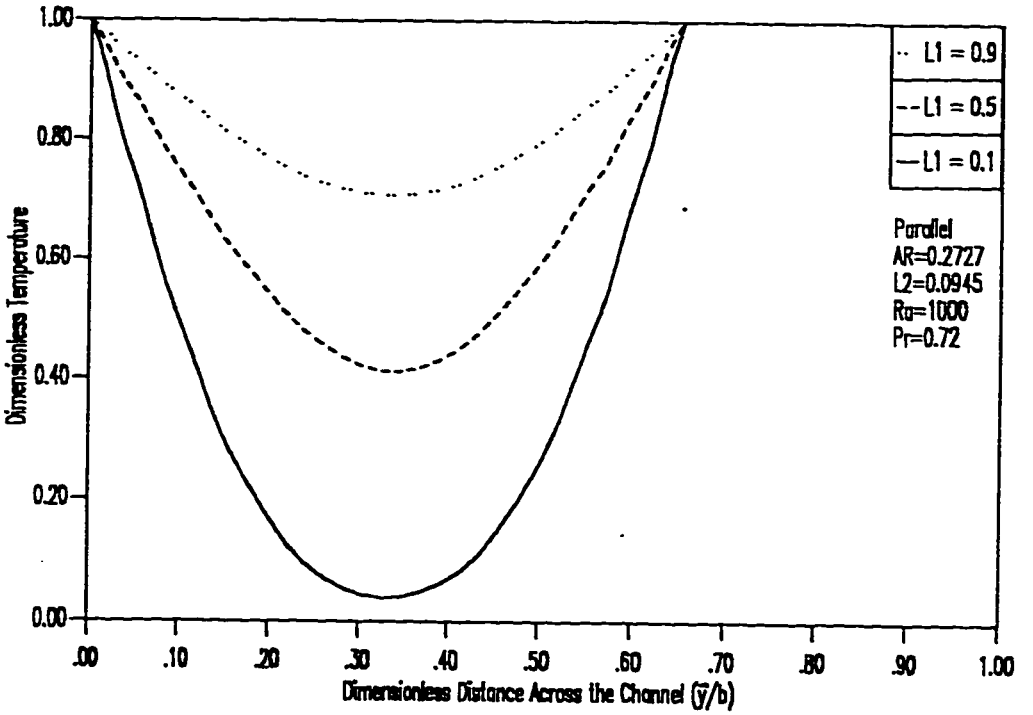

Figure 6.55 Transverse Temperature Distribution at the Obstruction Center-Line for Different Obstruction Positions.

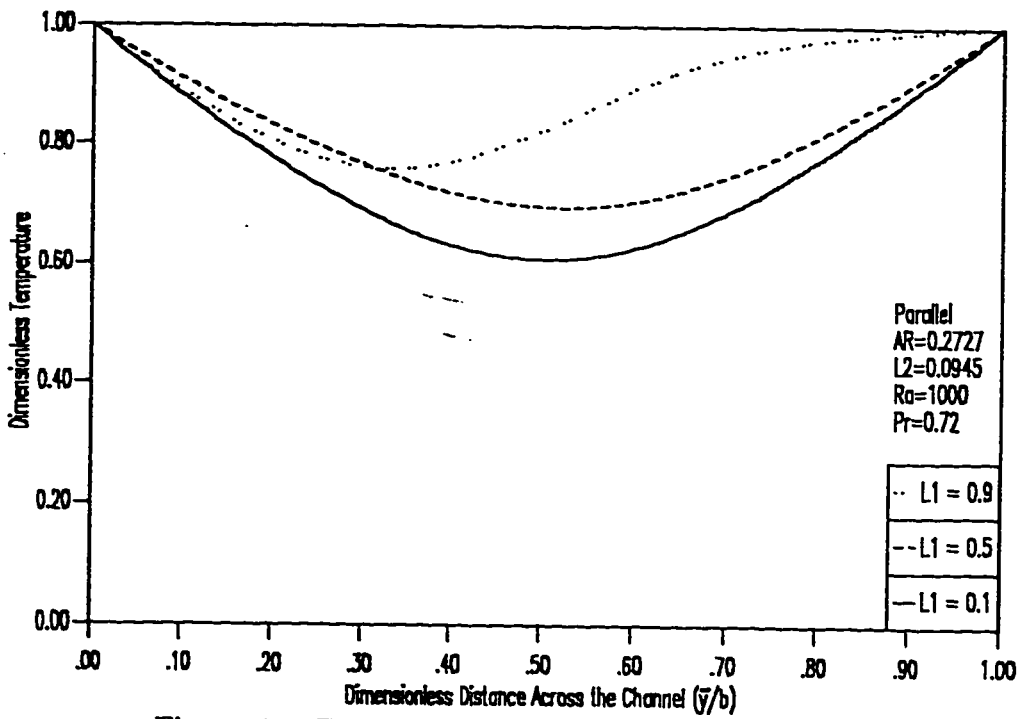

Figure 6.56 Transverse Temperature Distribution at the Exit of the Channel for Different Obstruction Positions.

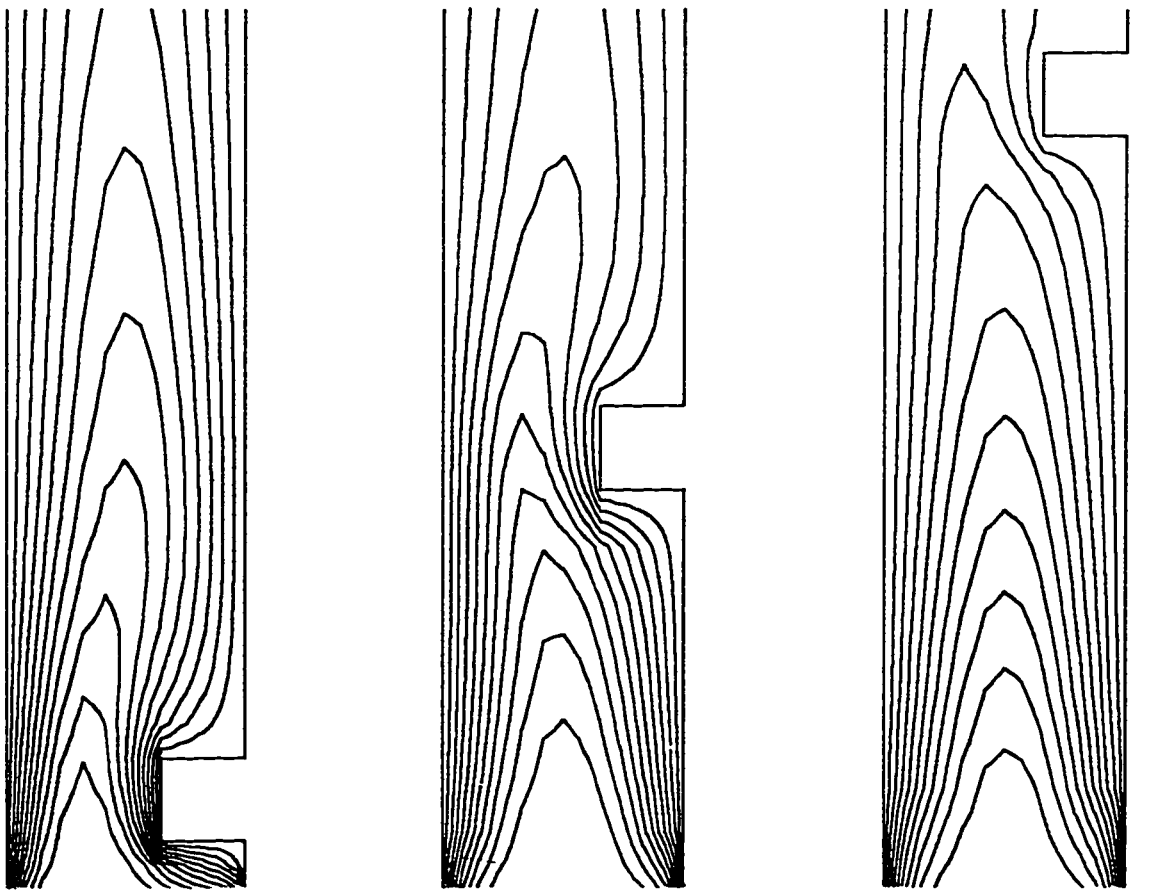

(a) $L_1 = 0.1$ (b) $L_1 = 0.5$ (c) $L_1 = 0.9$

Figure 6.57 Computed Isotherms for AR = 0.2727, $\gamma = 0$, $L_2 = 0.0945$, Ra = 1000, Pr = 0.72 .

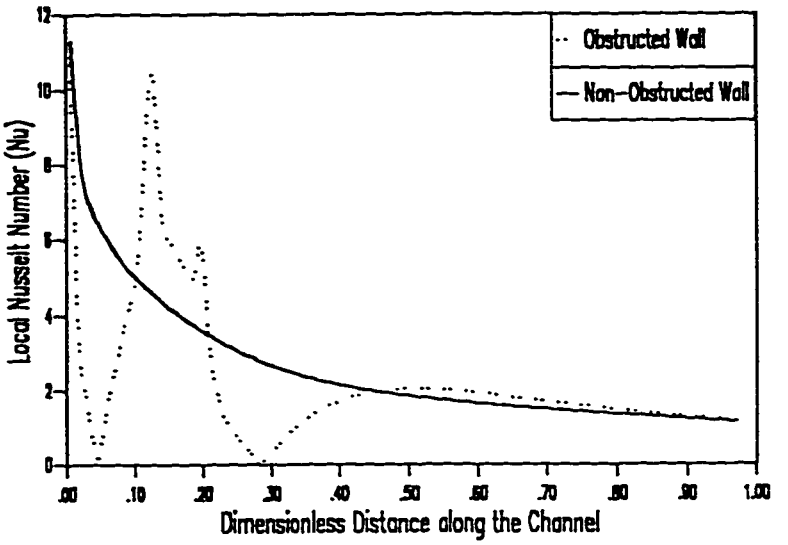

Figure 6.58 Variation of Local Nusselt Number Along the Channel for L1 = 0.1

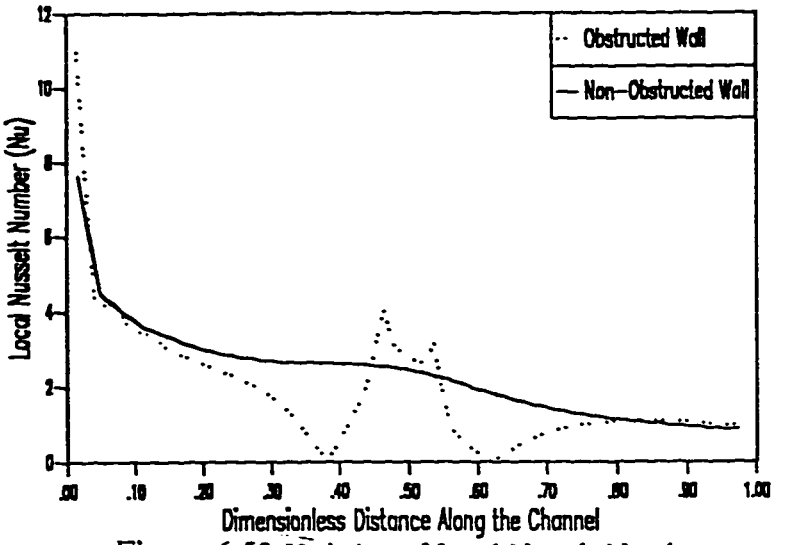

Figure 6.59 Variation of Local Nusselt Number Along the Channel for L1 = 0.5

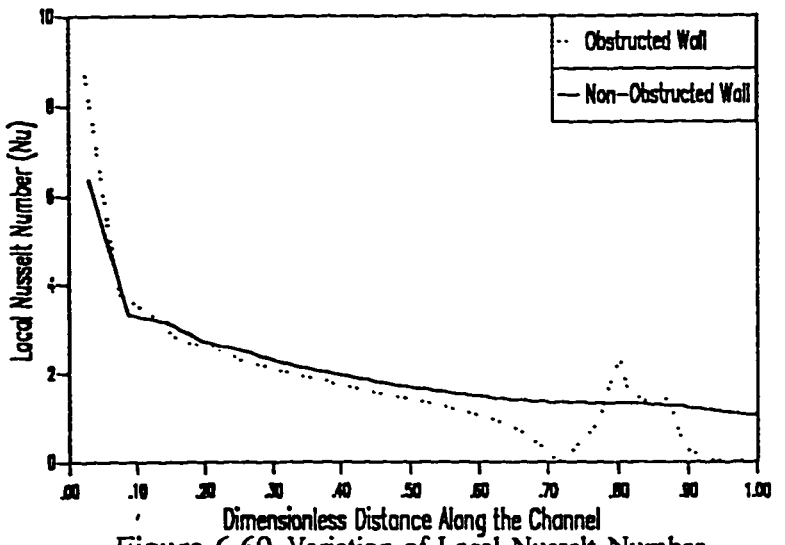

Figure 6.60 Variation of Local Nusselt Number Along the Channel for L1 = 0.9

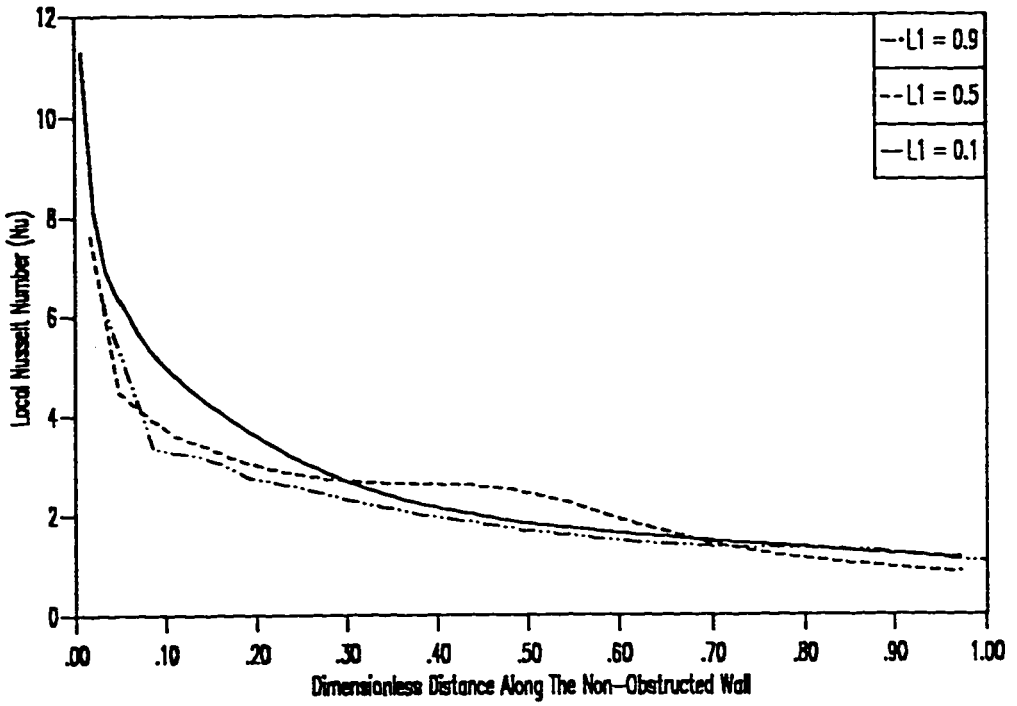

Figure 6.61 Variation of Local Nusselt number along the Non-Obsteructed wall for Different Values of L_1.

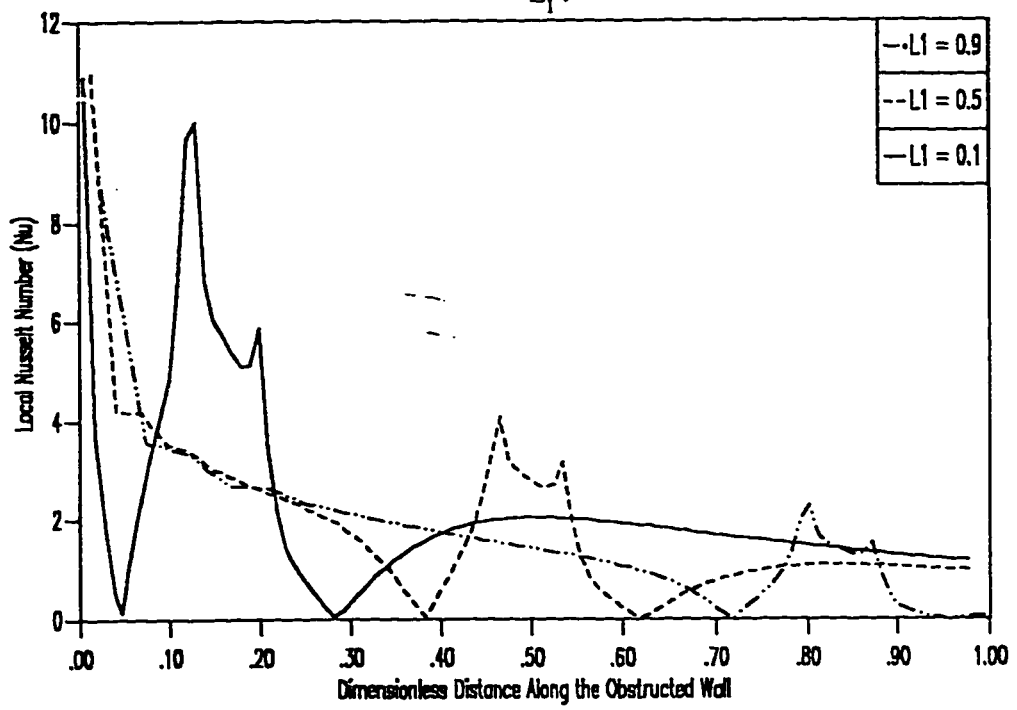

Figure 6.62 Variation of Local Nusselt number along the Obsteructed wall for Different Values of L_1.

6.5 The Effect of L_2

The fifth set of results pertains to the effect of the obstruction size ($\overline{L_2}$). The possible obstruction sizes that can be considered range between 0 and AR (i.e. $0 \leq L_2 \leq AR$). Eight different values of L_2 within the possible range have been considered. The upper range of L_2 will result in a blocked channel.

The mesh generated for three different values of L_2 is shown in figures (5.63-a) through (5.63-c). The computed values for the maximum dimensionless velocity (Umax), the dimensionless mass flow rate (Q) and the average Nusselt number ($\overline{Nu}$) are given in TABLE (6-4). It can be seen that both Q and $\overline{Nu}$ decreases as L_2 increases. Figures (6.64 and 6.65) show the plots of average Nusselt number and the dimensionless mass flow rate versus the dimensionless obstruction size (L_2) respectively. As expected the unobstructed channel ($L_2 = 0.0$) gives the maximum Q and $\overline{Nu}$.

Four different forms have been used to present the hydrodynamic results. The first form is the plot of the dimensionless vertical velocity versus the dimensionless distance across the channel ($\bar{y}$ /b) at the channel entrance ($\bar{x}$ /L = 0.0),the channel mid-plane (($\bar{x}$/L=0.5) and at the channel exit ($\bar{x}$ /L = 1.0). The plots are shown in figures (6.66 to 6.68) for three different values of the dimensionless obstruction size (L_2) . From these figures it can be seen that the maximum velocity, for each value of L_2 occurs at the obstruction mid-plane. This is due to the reduction in the channel's cross-sectional area caused by the presence of the obstruction. It can also be noted that the velocity profiles at

both the entrance and the exit are almost similar especially when the dimensionless obstruction size (L_2) is small. However, the velocity at the channel entrance starts to have a different profile for values of L_2 larger than 0.2 (i.e. the obstruction has blocked more than 80 % of the channel width). It is noted that for $L_2 > 0.2$ the velocity at the entrance has two peaks. The minimum peak is toward the obstructed wall where the maximum peak is towards the non-obstructed wall as shown in figure (6.68). Negative velocities have been observed at the entrance for $L_2 = 0.24$. This is shown clearly by the velocity vector profiles which will be discussed later.

The second form of the hydrodynamic results is the plot of the dimensionless vertical velocity versus the dimensionless channel's width ($\bar{y}$ /b) for different values of L_2 at the channel entrance, mid-plane and exit. These plots are shown in figures (6.69 to 6.71). From these figures it can be shown that as the obstruction size increases the dimensionless mass flow rate decreases as expected. It can also be noted that the maximum dimensionless vertical velocity decreases as L_2 increases for $\bar{x}/L = 0.0$ and 1.0 (i.e. the entrance and the exit of the channel respectively). However, this is not the case at the obstruction mid-plane ($\bar{x}/L = 0.5$) due to the fact that the rate at which the dimensionless mass flow rate decreases is different from the rate at which the cross-sectional area decreases. Since the mass flow rate is a function of the cross-sectional area and the velocity, the maximum dimensionless velocity is not always decreasing.

The third form of the hydrodynamic results is the streamline plots which are shown in figures (6.72-a) through (6.72-c). The streamlines are clustered due to

the presence of the obstruction, arround the obstruction vertical side.

The fourth form of the hydrodynamic results is the velocity vector plots that are shown in figures (6.73-a) through (6.73-c). Figure (6.74) show the velocity vector plots that have been magnified fifteen times. It can be noted that as (L_2) increases no circulation zones occur until $L_2 \geq 0.0582$. For $L_2 \geq 0.0582$, a circulation zone occurs right at the top of the obstruction and it increases in size as L_2 increases up to a value of $L_2 = 0.1818$. No circulation zone are observed above the obstruction for $L_2 \geq 0.1818$. However, as shown in figure (6.74-c) (i.e. $L_2 = 0.24$) there exists a reverse flow (a downward flow) in the middle region just above the entrance of the channel. This behavior will be explained when discussing the thermal results.

As a summary of the hydrodynamic results for this section, two main conclusions should be stated. The first one is the decrease of the mass flow rate as L_2 increases as expected. The second one is that no circulation zones are observed above the obstruction for very small and very high values of L_2 . A circulation zone exists above the obstruction, for moderate values of L_2 . At higher values of L_2 a reverse flow is observed in the middle region above the entrance channel.

The thermal results are presented in four different forms. The first form is the plot of temperature profiles versus the dimensionless channel width ($\bar{y}$ /b) at different hights in the channel (i.e. $\bar{x}$ /L) for the same value of L_2 . These plots are shown in figures (6.75) through (6.77). As expected, due to the heat transfer

from the channel walls to the fluid, the fluid temperature increases in the streamwise direction. It can be noted that for $L_2 > 0.20$, the fluid temperature in most portions of the channel (i.e. the region above the obstruction) is almost equal to the wall temperature. This means that the fluid temperature is invariant along the channel in this region ($d\theta/dx \approx 0$). This leads to the conclusion that thermally fully developed flows are observed for large values of L_2.

Figures (6.78 and 6.79) show the plot of temperature across the channel for different values of L_2 at the channel mid-plane and the channel exit respectively. From these figures it can be shown that the fluid temperature across the channel increases as the obstruction size increases (i.e. as L_2 increases).This means that the temperature difference between the wall and the fluid decreases as L_2 increases which will result in Nusselt number reduction.

The second form of the thermal results is the isotherm plots as shown in figures (6.80-a) through (6.80-c). These figures show that the thermal boundary layer thickness (δ) increases as L_2 increases which will lead to a decrease in the temperature gradient and hence a decrease in the average Nusselt number. The flow being thermally fully developed (at large L_2) and natural (the driving force due to temperature difference) explains the disappearance of circulation zones above the obstruction. The presence of a reverse flow at the channel entrance for large values of L_2 is due to the fact that the fluid is almost inclosed from three sides.

The third form of the thermal results is the variation of the local Nusselt

number along the channel walls. The local Nusselt number variation for both the obstructed and non- obstructed wall is shown in figures (6.81 to 6.83). As discussed earlier, two points of maximum local Nusselt number (apart from the leading edge) and two points of minimum local Nusselt number as shown in figures (6.81 and 6.82). However, for large values of L_2, both the obstructed and the unobstructed walls have almost the same profile and this is due to the thermally fully developed limit as shown in figure (6.83). Figures (6.84 and 6.85) show the variation of local Nusselt number along both the non-obstructed and the obstructed walls for different values of L_2. The fourth form of the thermal results are the variation of the average Nusselt number versus L_2 as shown earlier in figure (6.64).

To sum it up, it can be concluded that eventhough the surface area increases as the obstruction size increases, the decrease in the mass flow rate and the presence of circulation zones result in average Nusselt number reduction.

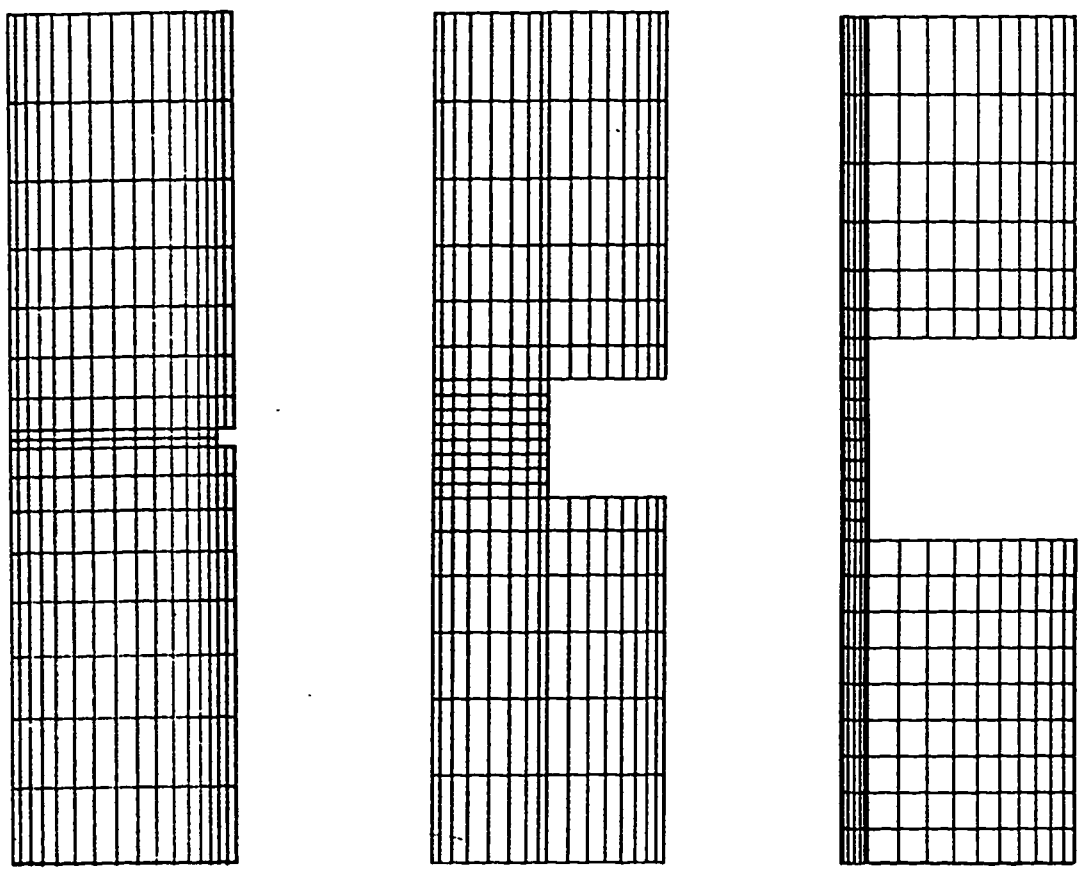

(a) $L_2 = 0.0218$ (b) $L_2 = 0.1382$ (c) $L_2 = 0.24$

Figure 6.63 Mesh Generated for AR = 0.2727, $\gamma = 0$, $L_1 = 0.5$, Ra = 1000, Pr = 0.72 .

TABLE(6-4) COMPUTED Umax,Q and $\overline{Nu}$ FOR OBSTRUCTED VERTICAL CHANNEL WITH AR = 0.2727,Ra = 1000, L_1 = 0.50 and γ = 0.

L_2	$\overline{Nu}$	Q	Umax
0.0000	2.5230	8.7070	12.8015
0.0218	2.5022	8.4980	12.5162
0.0582	2.3024	7.6235	13.1492
0.0945	2.0698	6.2329	12.8946
0.1382	1.5884	4.2840	12.8875
0.1818	0.8172	2.0997	9.4609
0.2182	0.2500	0.5880	4.4426
0.2400	0.0883	0.1383	1.7625

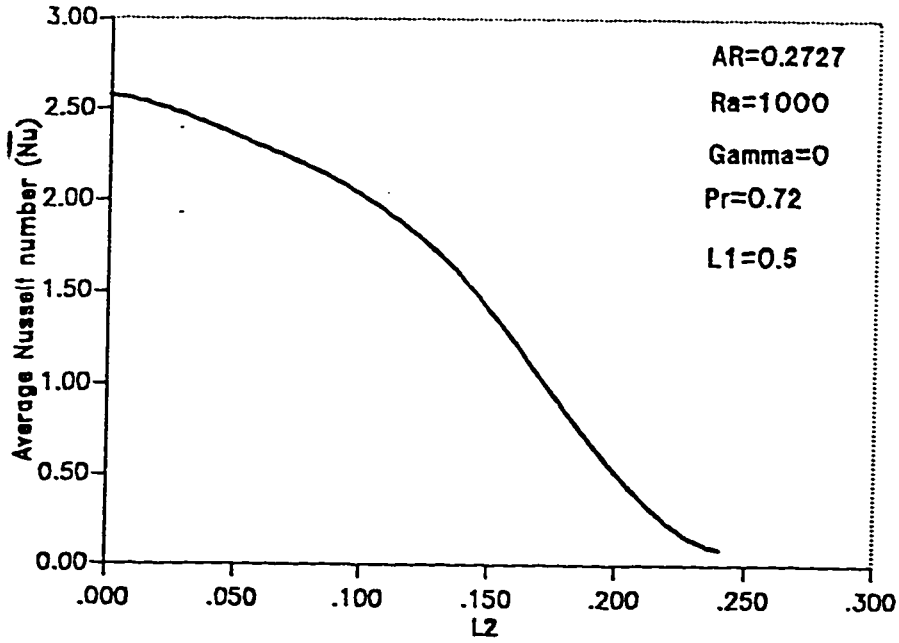

Figure 6.64 The Variation of Average Nusselt Number Versus the Dimensionless Obstruction Width.

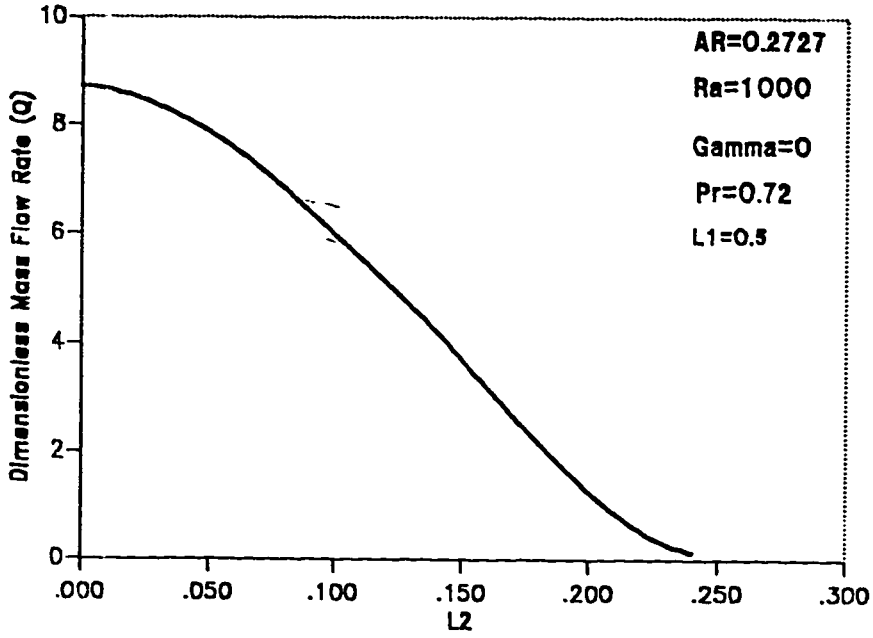

Figure 6.65 The Variation of Dimensionless Mass Flow Rate Versus the Dimensionless Obstruction Width.

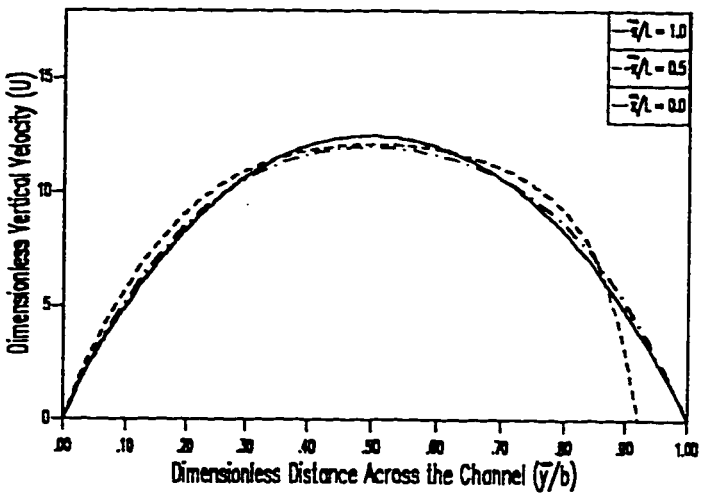

Figure 6.66 Transverse Velocity Distribution at Different Cross-Sections in the Channel for L_2 = 0.0218.

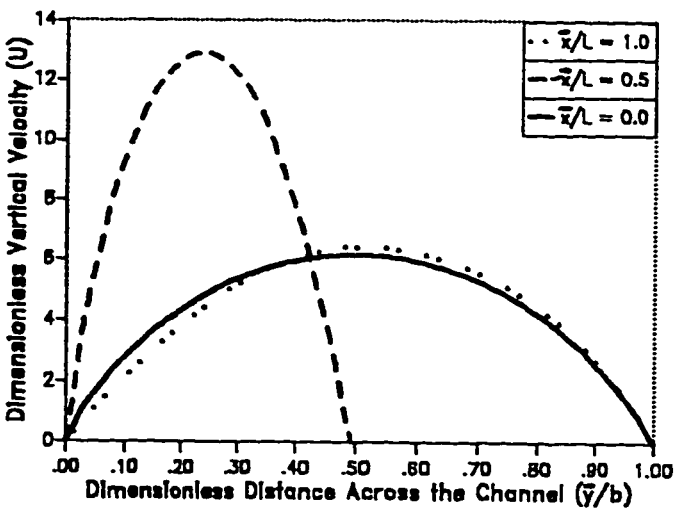

Figure 6.67 Transverse Velocity Distribution at Different Cross-Sections in the Channel for L_2 = 0.1382.

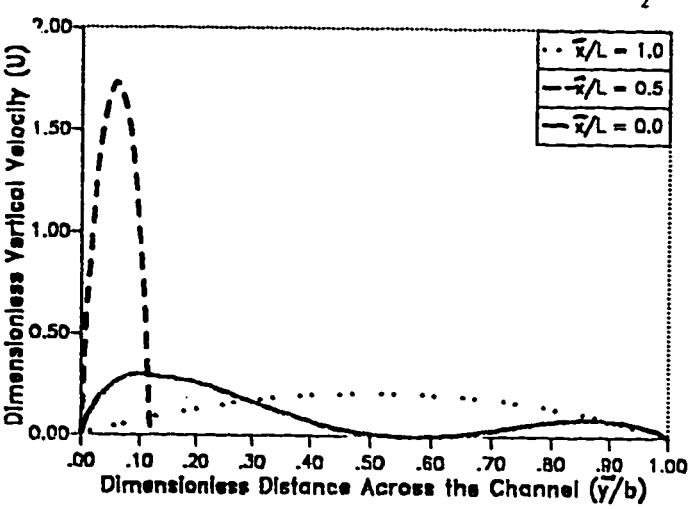

Figure 6.68 Transverse Velocity Distribution at Different Cross-Sections in the Channel for L_2 = 0.24.

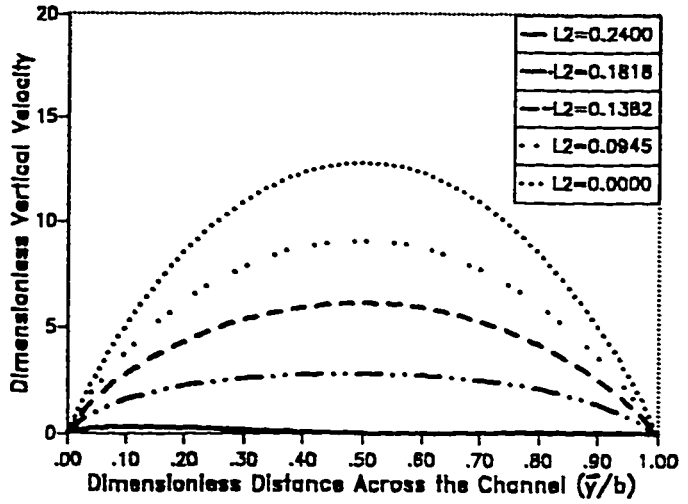

Figure 6.69 Transverse Velocity Distribution at the Entrance of the Channel for Different Values of L_2.

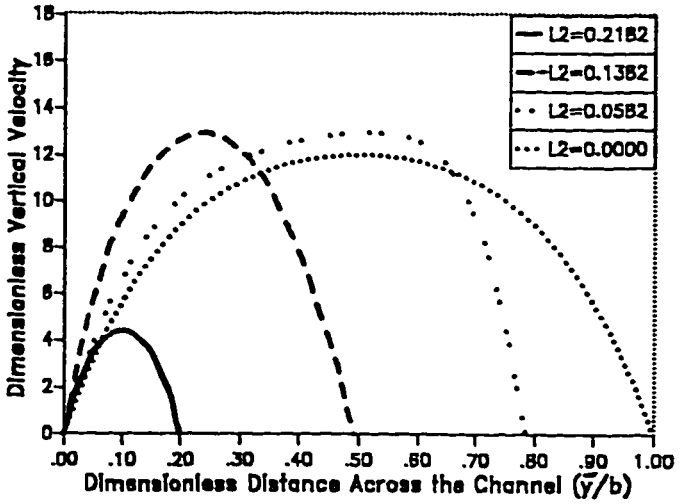

Figure 6.70 Transverse Velocity Distribution at the Obstruction Center-Line for Different Values of L_2.

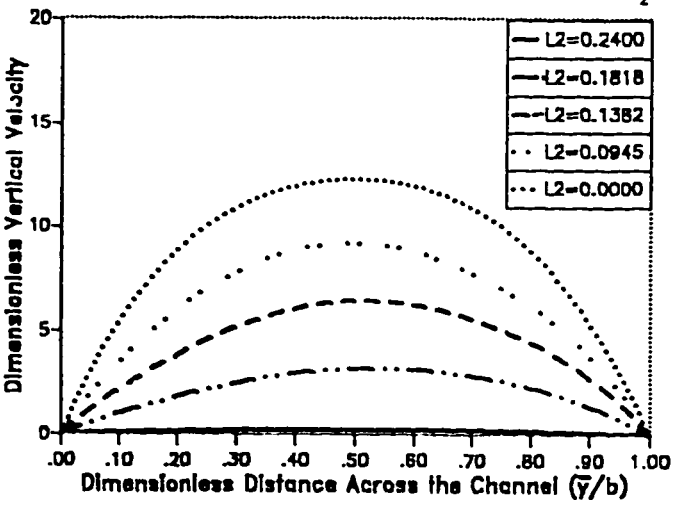

Figure 6.71 Transverse Velocity Distribution at the Exit of the Channel for Different Values of L_2

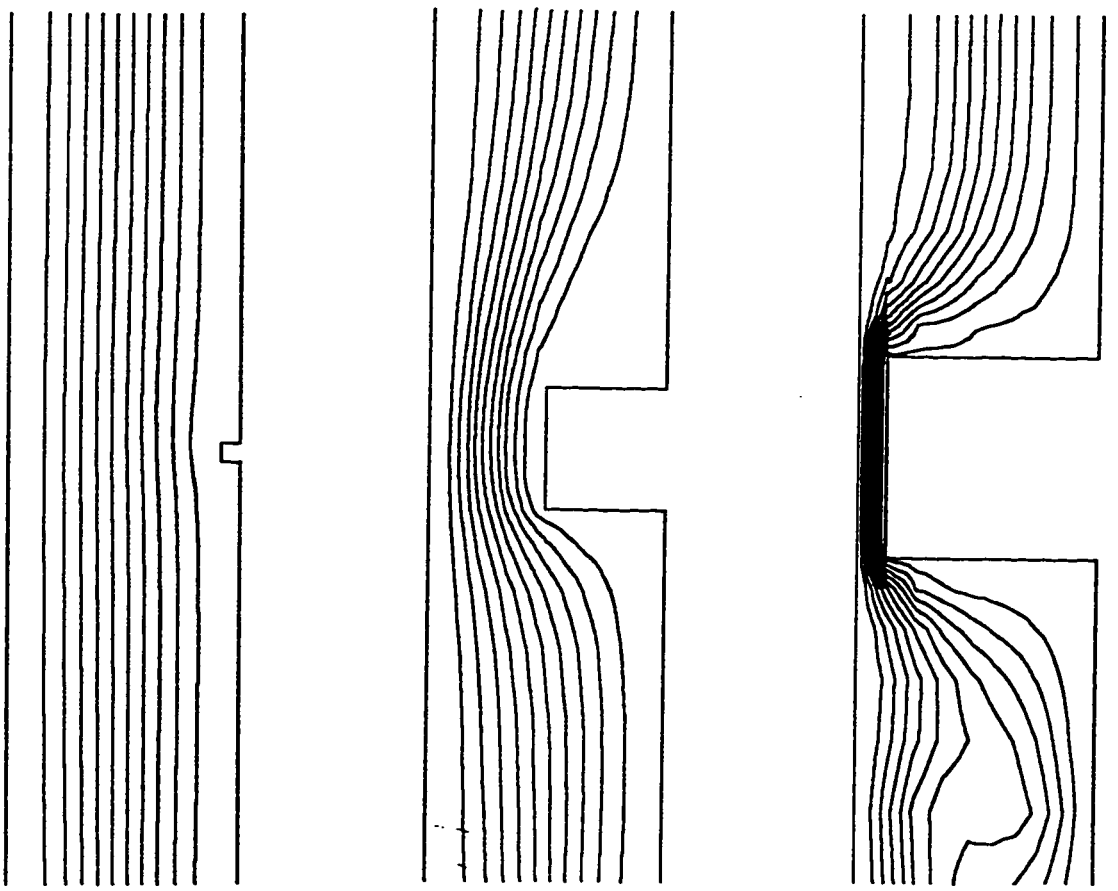

(a) L_2 = 0.0218 (b) L_2 = 0.1382 (c) L_2 = 0.24

Figure 6.72 Computed Streamlines for AR = 0.2727, γ = 0 , L_1 = 0.5 , Ra = 1000, Pr = 0.72 .

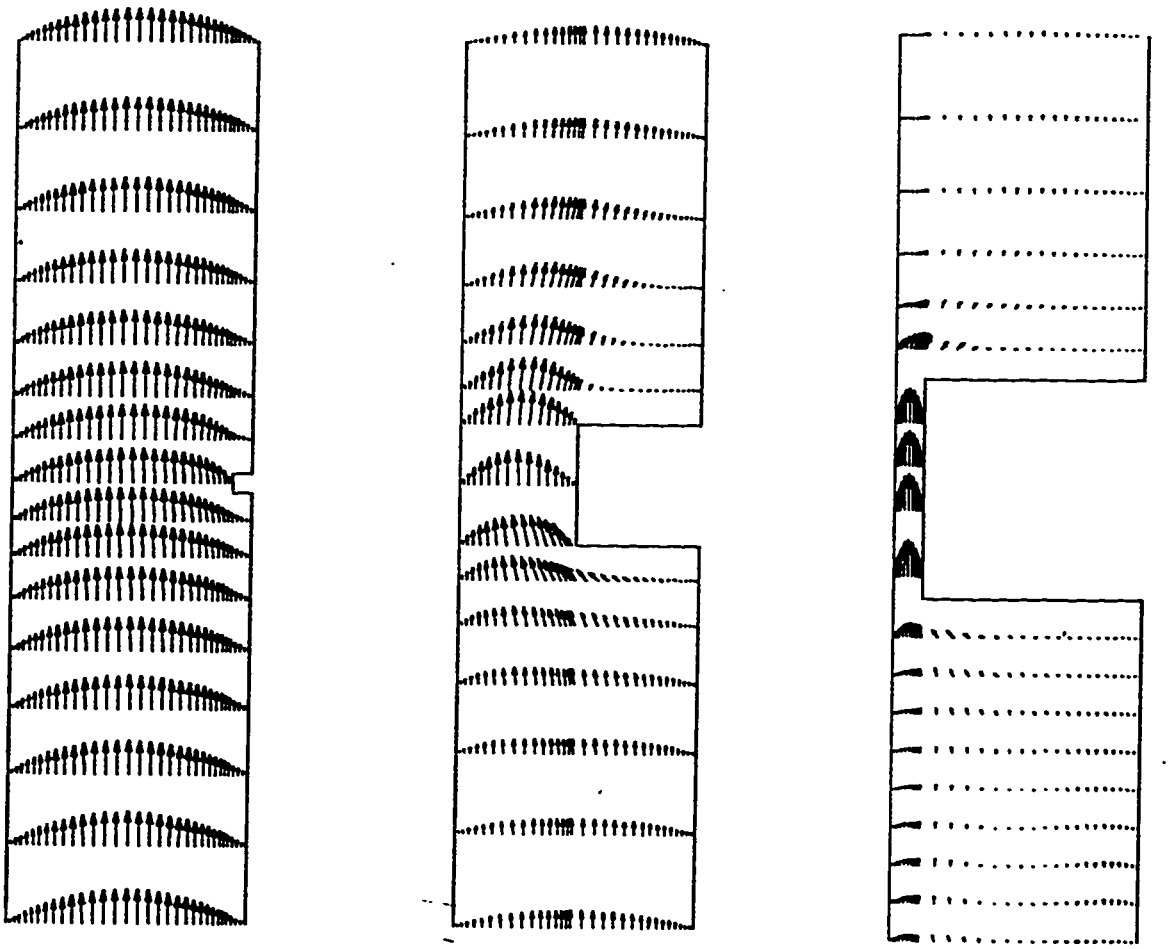

(a) L_2 = 0.0218 (b) L_2 = 0.1382 (c) L_2 = 0.24

Figure 6.73 Computed Velocity Vectors for AR = 0.2727, Ra = 1000 , γ = 0 , L_1 = 0.5 , Pr = 0.72 .

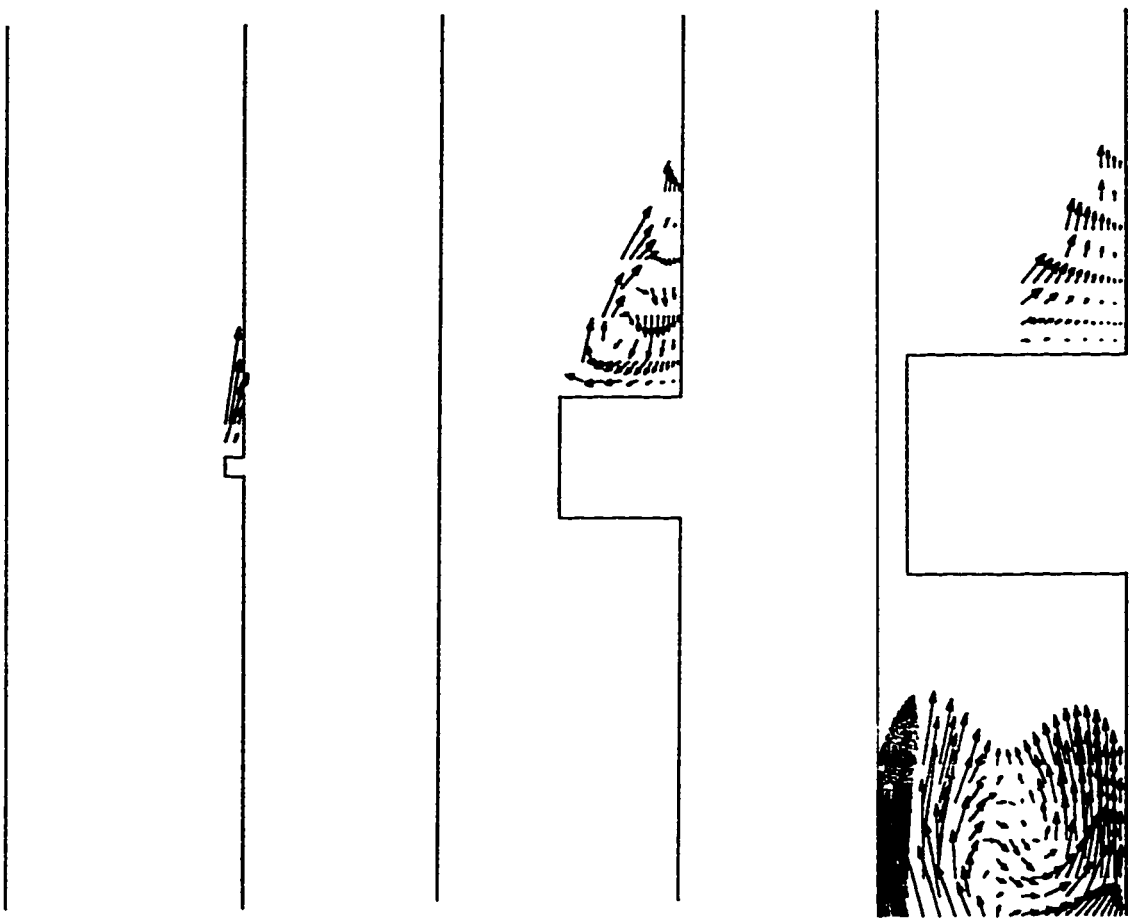

(a) $L_2 = 0.0218$ (b) $L_2 = 0.1382$ (c) $L_2 = 0.24$

Figure 6.74 Computed Velocity Vectors (Enlarged) for AR = 0.2727, Ra = 1000 , $\gamma = 0$, $L_1 = 0.5$, Pr = 0.72 .

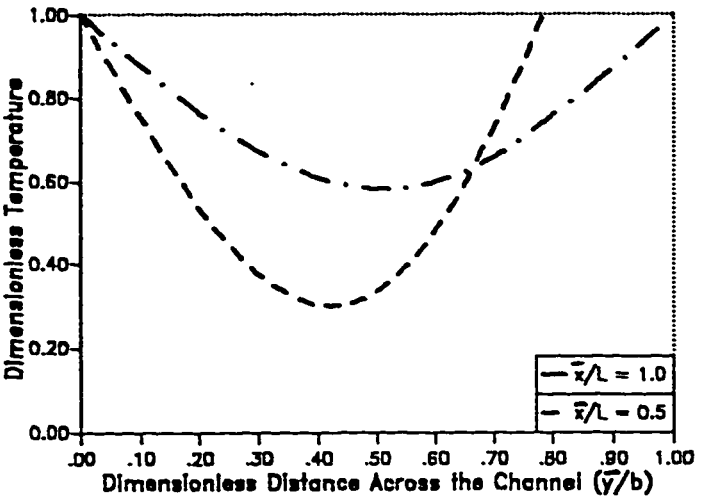

Figure 6.75 Transverse Temperature Distribution at Different Cross-Sections in the Channel for $L_2 = 0.0218$.

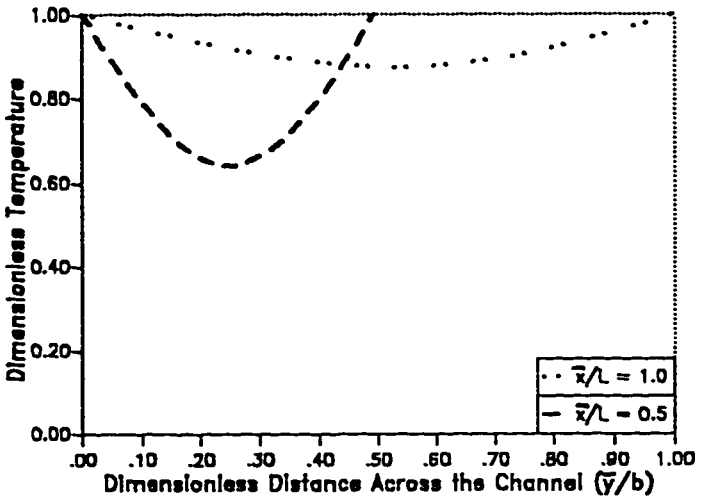

Figure 6.76 Transverse Temperature Distribution at Different Cross-Sections in the Channel for $L_2 = 0.1382$.

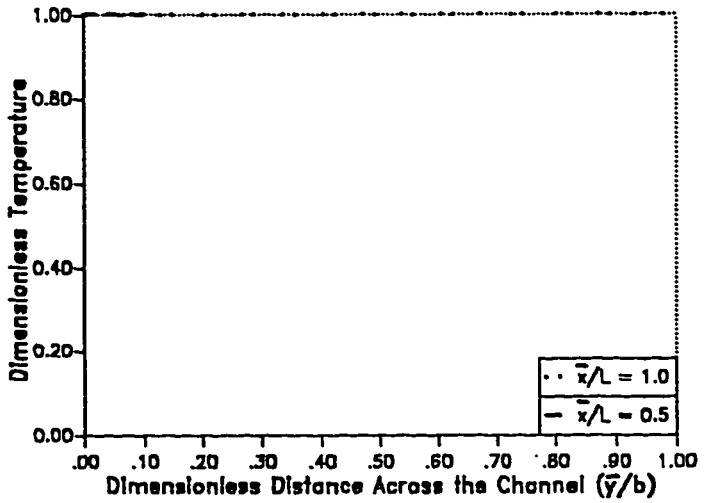

Figure 6.77 Transverse Temperature Distribution at Different Cross-Sections in the Channel for $L_2 = 0.24$.

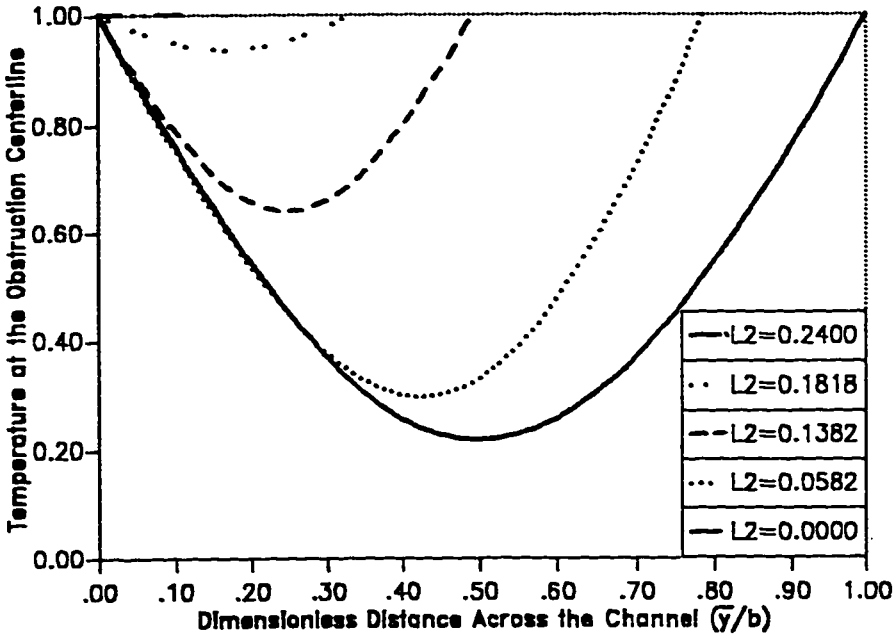

Figure 6.78 Transverse Temperature Distribution at the Obstruction Center-Line for Different Values of L_2.

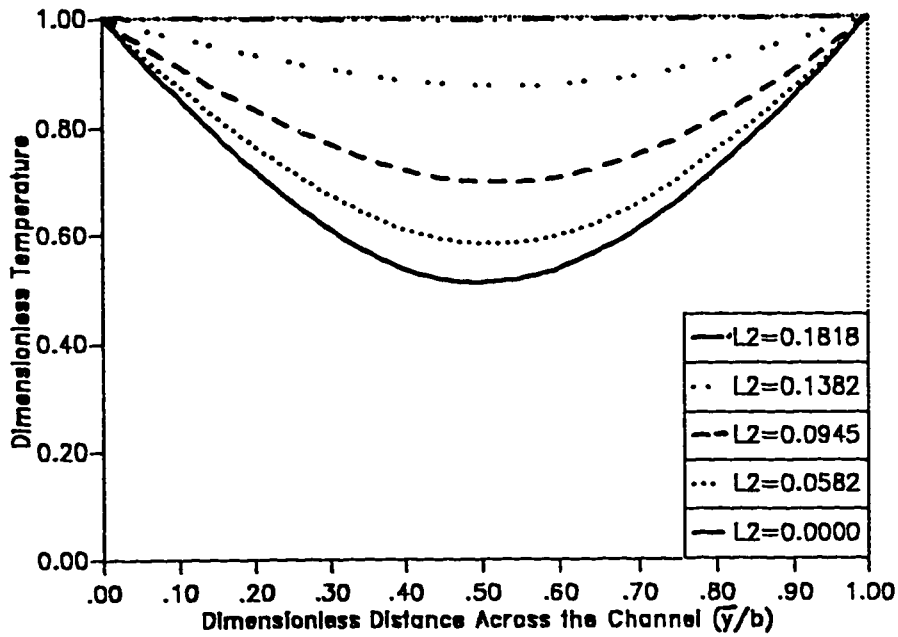

Figure 6.79 Transverse Temperature Distribution at the Exit of the Channel for Different Values of L_2

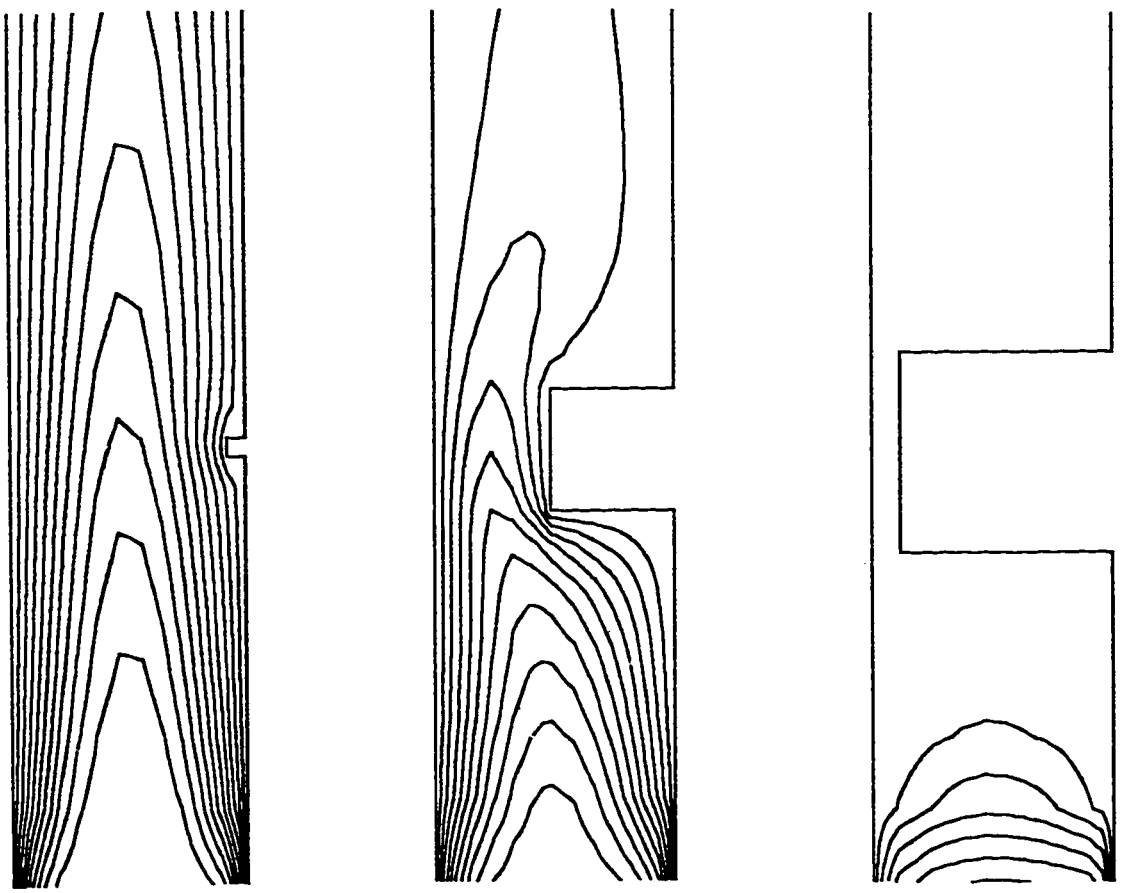

(a) L_2 = 0.0218 (b) L_2 = 0.1382 (c) L_2 = 0.24

Figure 6.80 Computed Isotherms for AR = 0.2727, γ = 0 , L_1 = 0.5 , Ra = 1000, Pr = 0.72 .

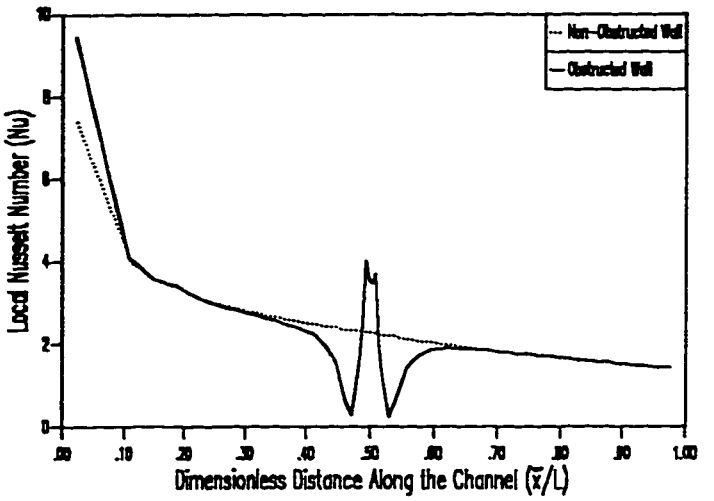

Figure 6.81 Variation of Local Nusselt Number Along the Channel for $L_2 = 0.0218$.

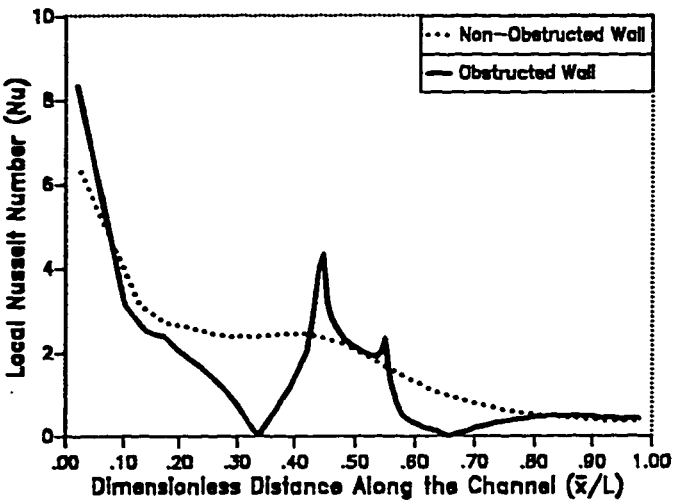

Figure 6.82 Variation of Local Nusselt Number of the Channel for $L_2 = 0.1382$.

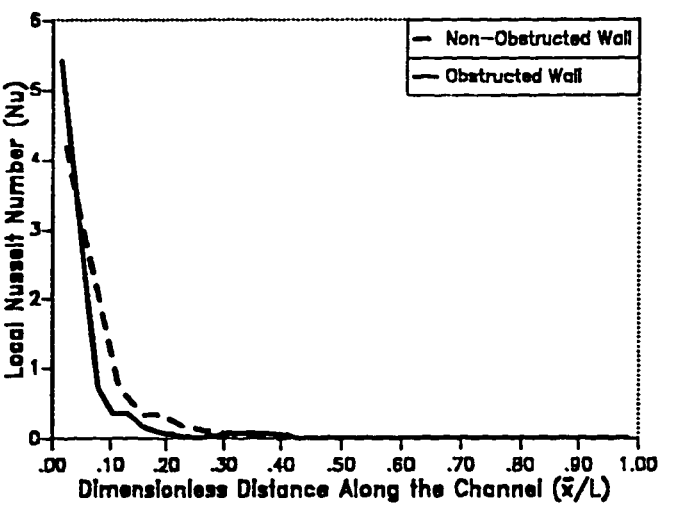

Figure 6.83 Variation of Local Nusselt Number of the Channel for $L_2 = 0.24$.

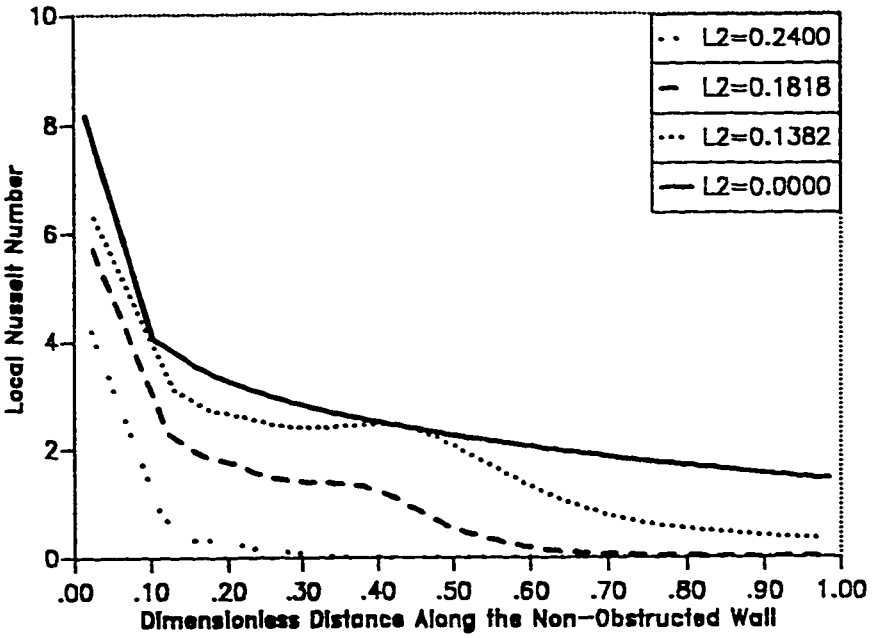

Figure 6.84 Variation of Local Nusselt number along the Non-Obsteructed wall for Different Values of L_2.

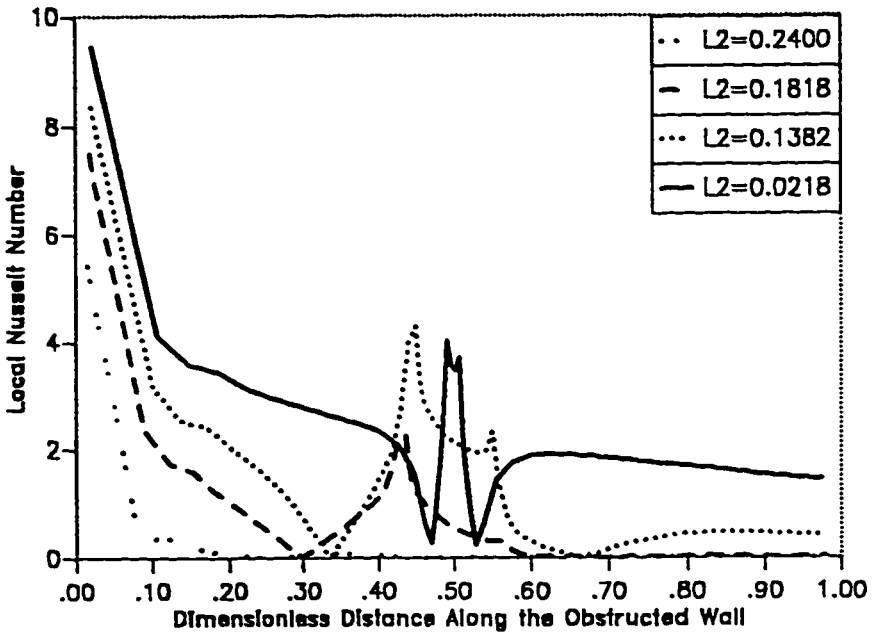

Figure 6.85 Variation of Local Nusselt number along the Obsteructed wall for Different Values of L_2.

6.6 The Effect of the Angle (γ)

The sixth set of results pertains to the effect of the angle of convergence or divergence (γ) on the flow field and heat transfer characteristics in obstructed vertical channels. This set of results conclude this study of natural convection heat transfer in obstructed vertical channel (using air as the working fluid). To the best knowledge of the author, niether convergent nor divergent obstructed vertical channels have been studied. In general, the convergent channel is considered to be the channel which has a decreasing cross-sectional area along the axial direction of the channel. On the other hand, the divergent channel is the channel which has an increasing cross-sectional area along the axial direction of the channel.

In this part of the study, the effect of convergence and divergence angles for an obstructed vertical channel on the average Nusselt number will be presented. The study considers two angles of convergence and two angles of divergence, namely, $\gamma = 5°$ and $10°$. The effect of each angle has been studied for two values of aspect ratios. Therefore, in total eight different cases have been studied for convergent and divergent obstructed vertical channels. Each of these cases has been studied for some range of Rayliegh numbers. This range depends on the convergence criteria and the number of iterations as discussed earlier. The dimensionless length of the obstruction (L_1) and the dimensionless hight (L_2) are kept constant.

6.6.1 Convergent Obstructed Vertical Channel

In this section the effect of the angle of convergence on the flow field and the heat transfer characteristics will be presented. The hydrodynamic and thermal results of the two convergence angles, namely, $\gamma = 5°$ and $10°$ will be presented seperately and then a comparison between the $\overline{Nu}$ for both angles along with the results of the parallel-walled obstructed channel $\gamma = 0°$ will be presented later. It should be pointed out that the dimensional parameter (b) is equal to the dimensional width at the channel exit (S_{exit}) for the convergent channel, the dimensional width at the channel entrance (S_{ent}) for the divergent channel and the dimensional width at the channel entrance or exit for the parallel-walled channel. This was necessary so that the required angle of convergence or divergence can be attained. Hence, the average Nusselt number, the Rayliegh number and the aspect ratio for the convergent obstructed channel will be based on S_{exit} .

6.6.1.1 Convergent Channel , $\gamma = 5°$

In this sub-section, the results of the convergence angle $\gamma = 5°$ will be presented. The study was carried out for two values of $AR_{S_{exit}}$, namely, $AR_{S_{exit}} = 0.2727$ and 0.3636 and a range of $Ra_{S_{exit}}$ from 1.0 to 1.0×10^4. The discussion of results will be presented only for the case of $AR_{S_{exit}} = 0.2727$ due to the similar behavior observed for the two aspect rat-

ios. For $AR_{S_{exit}} = 0.3636$, the curves of the average Nusselt number and the dimensionless mass flow rate will be shown.

The mesh generated for the convergent obstructed vertical channel is shown in figure (6.86). The computed values for the maximum dimensionless velocities (Umax), the dimensionless mass flow rates (Q) and the average Nusselt numbers ($\overline{Nu}_{S_{exit}}$) are shown in TABLE (6-5). The dimensionless mass flow rates (Q) and the average Nusselt numbers ($\overline{Nu}_{S_{exit}}$) versus the $Ra_{S_{exit}}$ were plotted in a log-log scale as shown in figures (6.87) and (6.88) respectively. As shown in the figures, as the $Ra_{S_{exit}}$ increases $\overline{Nu}_{S_{exit}}$ increase for each aspect ratio. It can also be seen that as the aspect ratio increases Q and $\overline{Nu}_{S_{exit}}$ increase.

Similar to the previous discussions, the hydrodynamic results will be prsented in four different forms. The first form is the plot of dimensionless vertical velocity versus the dimensionless channel's width ($\bar{y}/S_{max}$) at three different hights ($\bar{x}$ /L) at the channel entrance ($\bar{x}$ /L=0.0) at the channel mid-plane ($\bar{x}$ /L=0.5) and at the channel exit ($\bar{x}$ /L=1.0) for $Ra_{S_{exit}} = 29,491$ and 9126 respectively. As expected, the maximum dimensionless vertical velocity occurs at the mid-plane ($\bar{x}$ /L=0.5) for each value of $Ra_{S_{exit}}$. This is due to the reduction in the channel cross-sectional area at ($\bar{x}$ /L=0.5) because of the presence of the obstruction. As can be seen from these figures, the entrance velocity profile appears to be parabolic when the

entrance velocity disribution is determined by applying the natural boundary condition.

The second form of the hydrodynamic results is the plot of the dimensionless vertical velocity versus the dimensionless channel's width ($\bar{y}/S_{max}$) at a given cross-section in the channel for different values of Ryliegh numbers. Figure (6.92) shows the plots of the dimensionless vertical velocities at the entrance of the channel ($\bar{x}$ /L=0.0) for different Rayliegh numbers. Figure (6.93) shows the same plots at the center line ($\bar{x}$ /L=0.5) of the channel while the plots of the dimensionless vertical velocities at the exit (x/L=1.0) of the channel are shown in figure (6.94). It can be noticed that the dimensionless mass flow rates (the area under the dimensionless vertical velocity curve) increase as the Rayliegh number increases. At high Rayliegh numbers, two peaks have been observed. This means that each wall of the channel will behave as an isolated vertical plate at high Rayliegh numbers. The point of maximum dimensionless vertical velocity at the entrance and at the exit of the channel is located close to the unobstructed wall. However, the point of maximmum vertical velocity at the center line of the channel is located close to the obstructed wall. This is similar to the results observed for the parallel-walled obstructed channel.

The third form of the hydrodynamic results is the streamlines plots. The plots of the computed streamlines at three different Rayliegh numbers are shown in figures (6.95-a) through (6.95-c). The streamlines are clustered at the channel center-line due to the presence of the obstruction. Hence, the flow

speeds up due to the reduction of the channel cross-sectional area in this region. The fourth form of the hydrodynamic results is the velocity vector plots as shown in figures (6.96-a) through (6.96-c) The variation of the velocity vectors along the axial direction of the channel can be clearly noticed. Examining the velocity data, it is observed that negative velocities occur at the top corner between the wall and the obstruction side. The magnitude of these velocities in this region is very small that they can not be observed from the streamlines or/and velocity vector plots. These velocities have been magnified and plotted again in figures (6.97-a) through (6.97-c). From these figures it can be seen that regions of recirculating flow are formed at the top corner of the obstruction. Regions of recirculating flow are also detected in the numerical results by examining the streamlines values at those nodes, but they are quite small. Since heat is transfered across recirculating flow regions by conduction only, the existance of these regions will affect the heat transfer rate.

The thermal results are presented in four different forms. The first form is the plot of the computed dimensionless temperature versus the dimensionless distance across the channel ($\bar{y}/S_{max}$) for $Ra_{S_{exit}}$ = 29 , 491 and 9126 as shown in figures (6.98) through (6.100) respectively. The plots were done at the mid-plane ($\bar{x}$ /L=0.5) of the channel and at the exit ($\bar{x}$ /L = 1.0) of the channel . As expected, the air temperature increases as $\bar{x}$ /L increases (i.e.as it moves along the axial direction of the channel).

The second form of the thermal results is the plot of the dimensionless

temperature at a given hight of the channel ($\bar{x}$ /L) for different values of $Ra_{S_{exit}}$. Figure (6.101) shows the variation of the dimensionless temperature at the mid-plane (x/L=0.5) of the channel for five different values of Rayliegh numbers. Figure (6.102) shows the same variation at the exit ($\bar{x}$ /L=1.0) of the convergent obstructed channel. As can be seen from these figures, as Rayliegh number increases the maximum temperature at these two planes ($\bar{x}$ /L=0.5 and $\bar{x}$ /L =1.0) decreases.

The third form of the thermal results is the isothermal lines. The plots for the computed isotherms are shown in figures (6.103-a) through (6.103-c). At $Ra_{S_{exit}}$ = 29 , the flow is fully developed which means that a thermal boudary layer has been developed at each wall and they emerge just in the region above the entrance cross-sectional area of the channel. For most portion of the channel (approximately $\bar{x}$ /L > 0.25), the dimensionless temperature gradient in the axial direction (i.e. $\frac{d\theta}{dx} \approx 0.0$) since the temperature of the air is almost equal to the wall's temperature. As the Rayliegh number increases, the boundary layer thickness (δ) decreases. This decrease will cause an increase in the dimensionless temperature gradient in the y-direction (i.e. $\frac{d\theta}{dy} \propto \frac{1}{\delta}$). Since the heat transfer rate is directly proportional to the temperature gradient in the y-direction, therefore the average Nusselt number will increase. Hence, from the isotherm plots, it can be seen that, in the case of very large Rayliegh numbers, a boundary layer is formed on each wall and the single vertical plate limit will be approached. In the case of a very low Rayliegh

numbers the fully developed limit will be approached. The fourth form of the thermal results is the average Nusselt number. The computed average Nusselt numbers ($\overline{Nu}_{S_{exit}}$) based on S_{exit} were plotted versus the $Ra_{S_{exit}}$ as shown in figure (6.88).A comparison between the computed values of the average Nusselt numbers for the convergence angle $\gamma = 5^{\circ}$ and the parallel walled vertical channel $\gamma = 0^{\circ}$ will be presented in the next section to include the case of the convergence angle $\gamma = 10^{\circ}$.

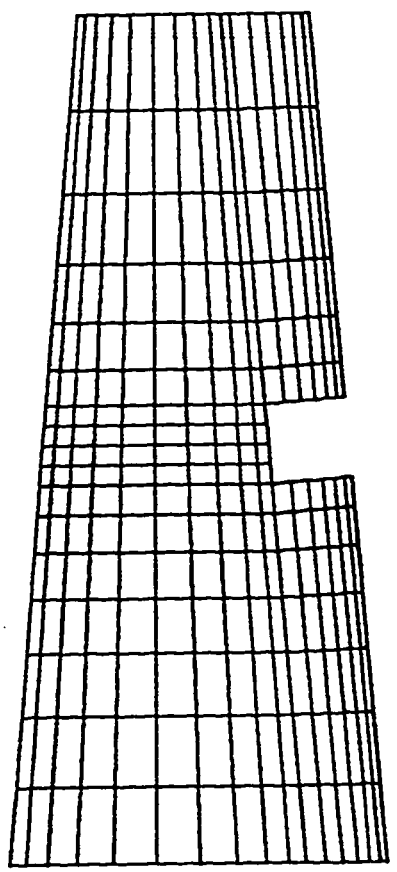

Figure 6.86 Mesh Generated for Convergent Obstructed Channel AR = 0.2727 , γ = 5 , L_1 = 0.5 , L_2 = 0.0945 , Ra = 1000,Pr = 0.72 .

TABLE(6-5) COMPUTED Umax,Q and $\overline{Nu}$ FOR OBSTRUCTED CONVERGENT CHANNEL WITH AR = 0.2727, $L_1 = 0.50$, $L_2 = 0.0945$ and $\gamma = 5$.

Ra	Umax	Q	$\overline{Nu}$
4.38	0.260	0.0846	0.0727
8.76	0.403	0.1587	0.1426
14.60	0.791	0.2659	0.2455
29.00	1.164	0.4729	0.4473
143.00	3.528	1.5485	1.0548
275.00	5.574	2.4241	1.3949
491.00	8.726	3.2161	1.7053
1988.00	14.253	6.5709	2.4595
2701.00	16.031	7.4934	2.6528
3451.00	19.427	8.8939	2.7970
4915.00	23.102	10.1717	3.0677
9126.00	30.278	13.7361	3.5319

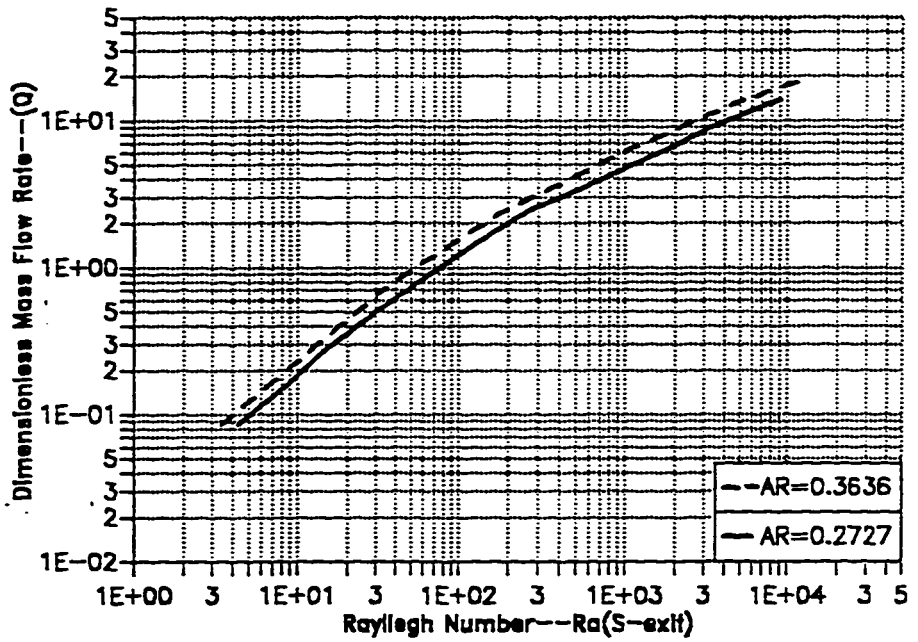

Figure 6.87 The Variation of Dimensionless Mass Flow Rate (Q) Versus the Rayliegh Number ($Ra_{S_{exit}}$) for the Convergent Obstructed Channel ($\gamma = 5$).

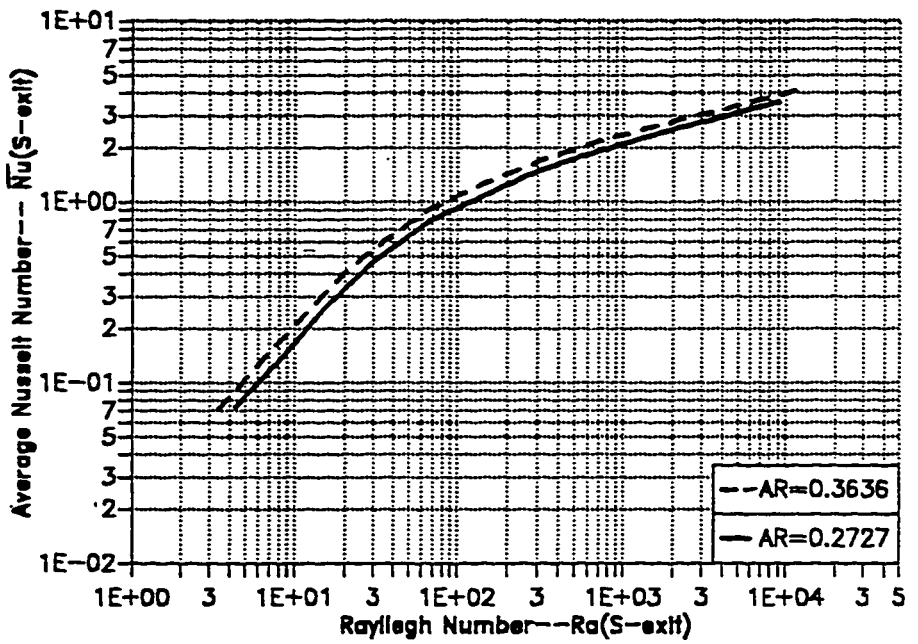

Figure 6.88 The Variation of Average Nusselt Number ($\overline{Nu}_{S_{exit}}$) Versus the Rayliegh Number ($Ra_{S_{exit}}$) for the Convergent Obtructed Channel ($\gamma = 5$).

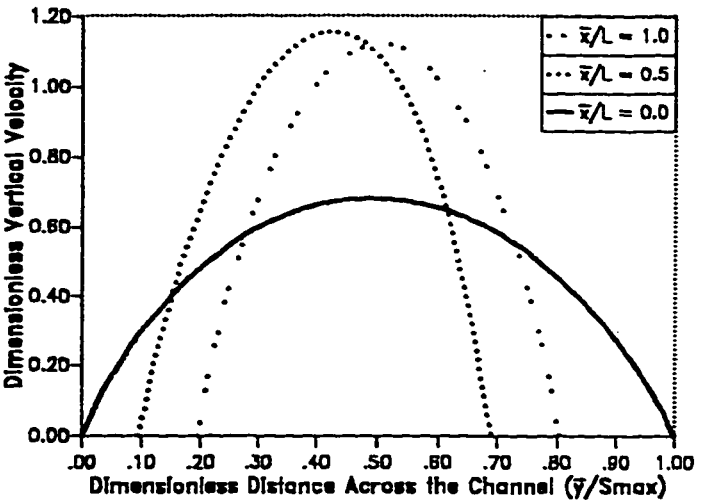

Figure 6.89 Transverse Velocity Distribution at Different Cross-Sections in the Channel for Ra = 29

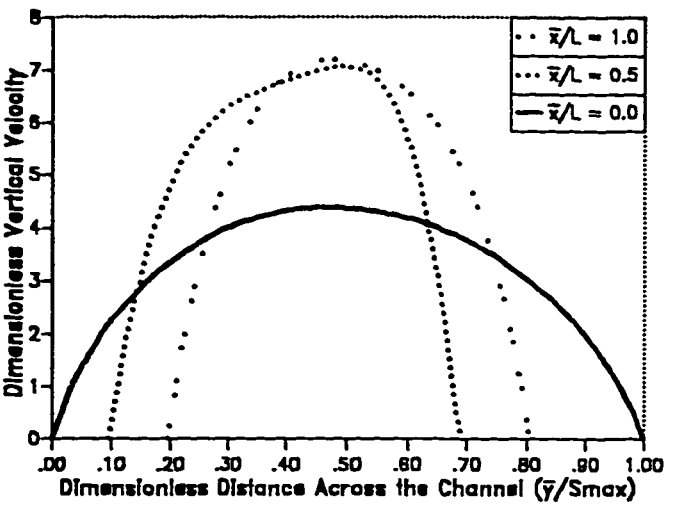

Figure 6.90 Transverse Velocity Distribution at Different Cross-Sections in the Channel for Ra = 491

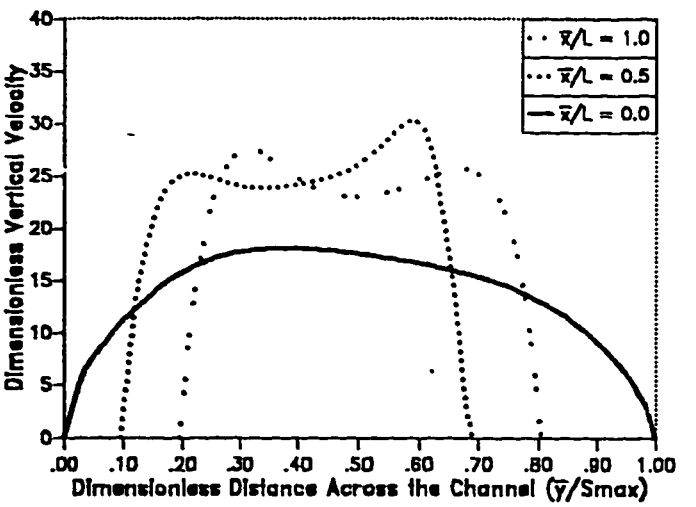

Figure 6.91 Transverse Velocity Distribution at Different Cross-Sections in the Channel for Ra = 9126

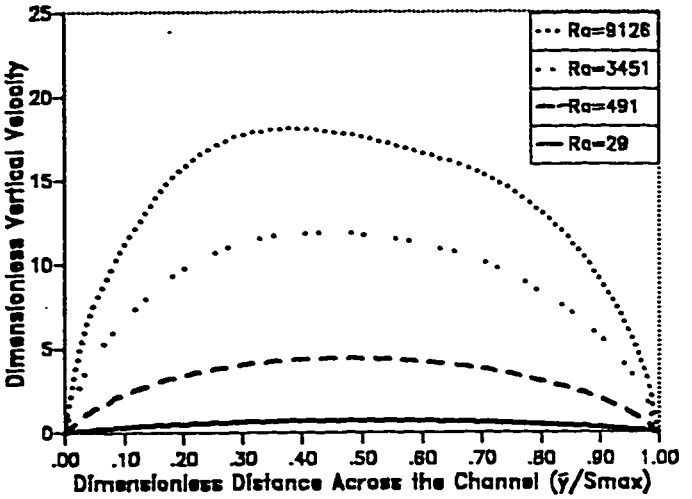

Figure 6.92 Transverse Velocity Distribution at the Entrance of the Channel for Different Values of Ra.

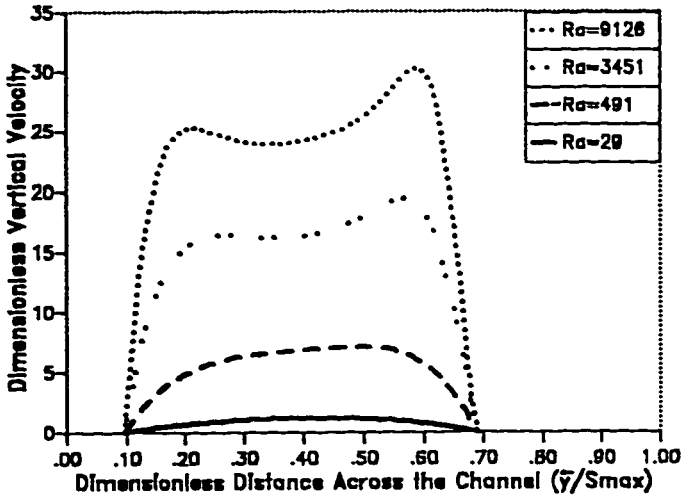

Figure 6.93 Transverse Velocity Distribution at the Middle high of the Channel Different Values of Ra.

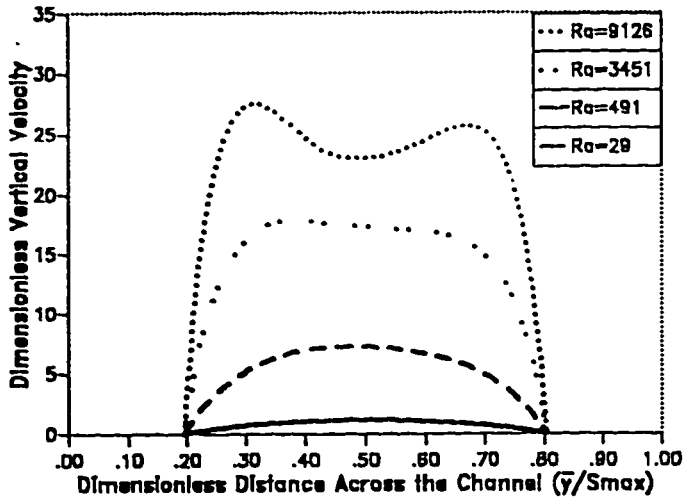

Figure 6.94 Transverse Velocity Distribution at the Exit of the Channel for Different Values of Ra.

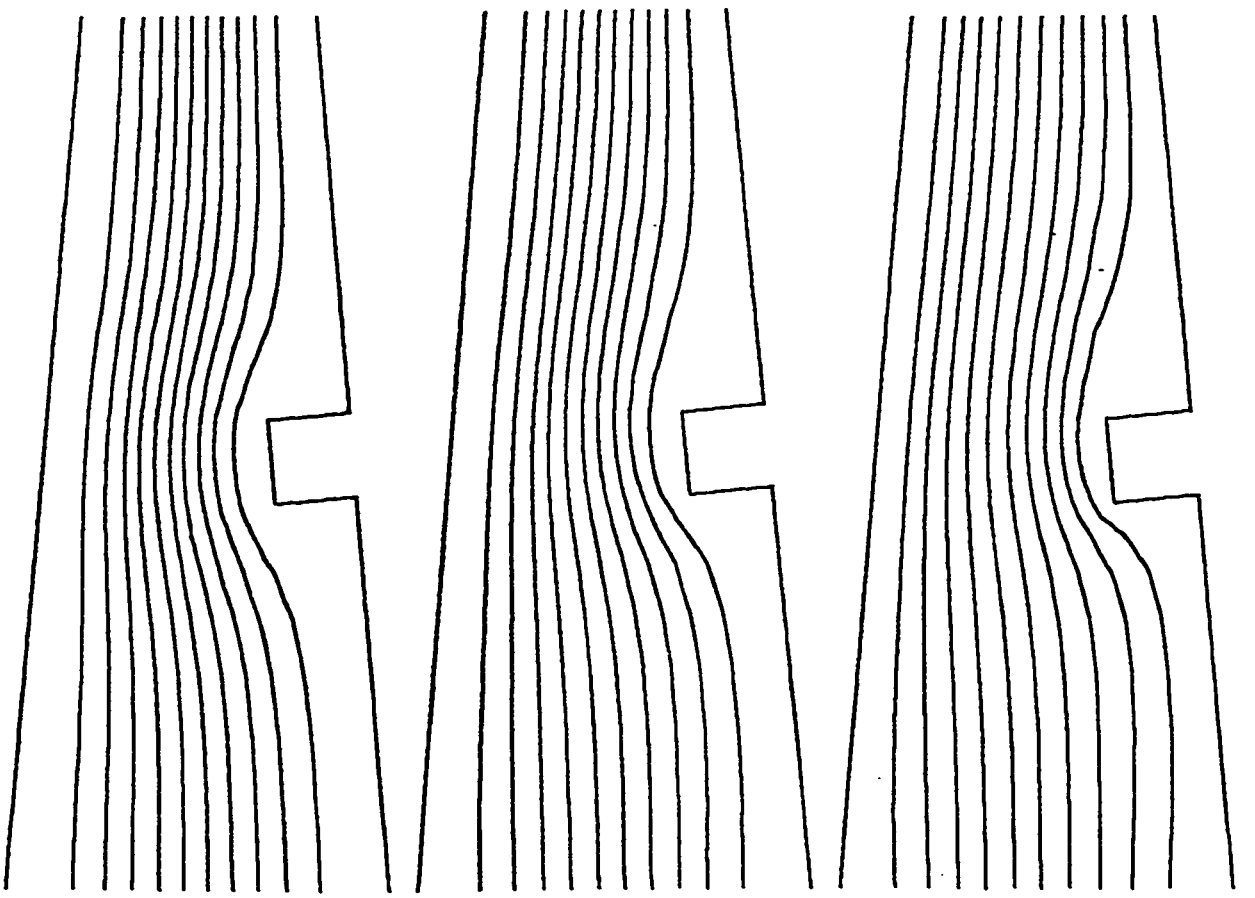

(a) Ra = 29 (b) Ra = 491 (c) Ra = 9126

Figure 6.95 Computed Streamlines for AR = 0.2727, Pr = 0.72, Convergent (γ = 5), L_1 = 0.5 , L_2 = 0.0945 .

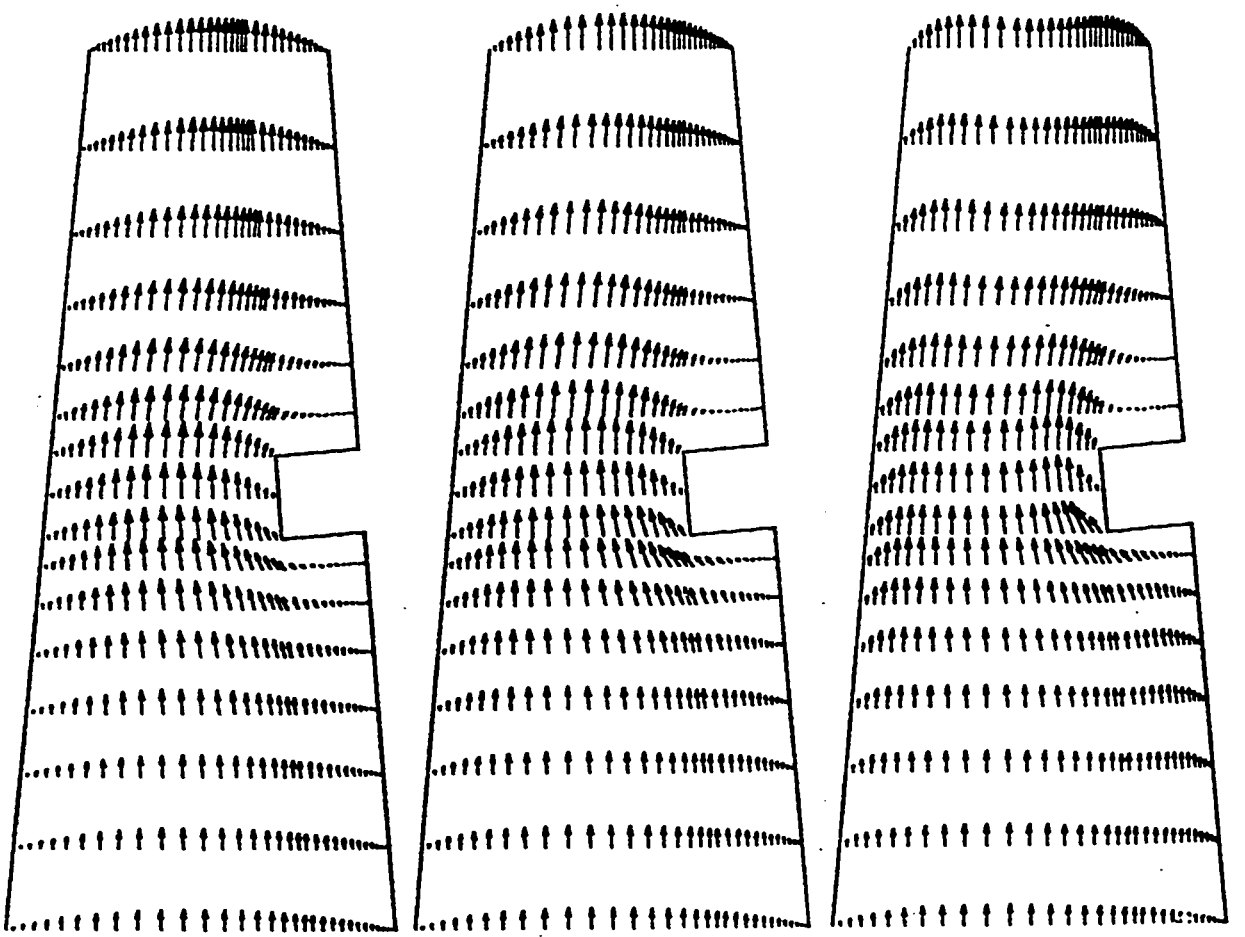

(a) Ra = 29 (b) Ra = 491 (c) Ra = 9126

Figure 6.96 Computed Velocity Vectors for AR = 0.2727, Pr = 0.72, Convergent (γ = 5), L_2 = 0.0945, L_1 = 0.5 .

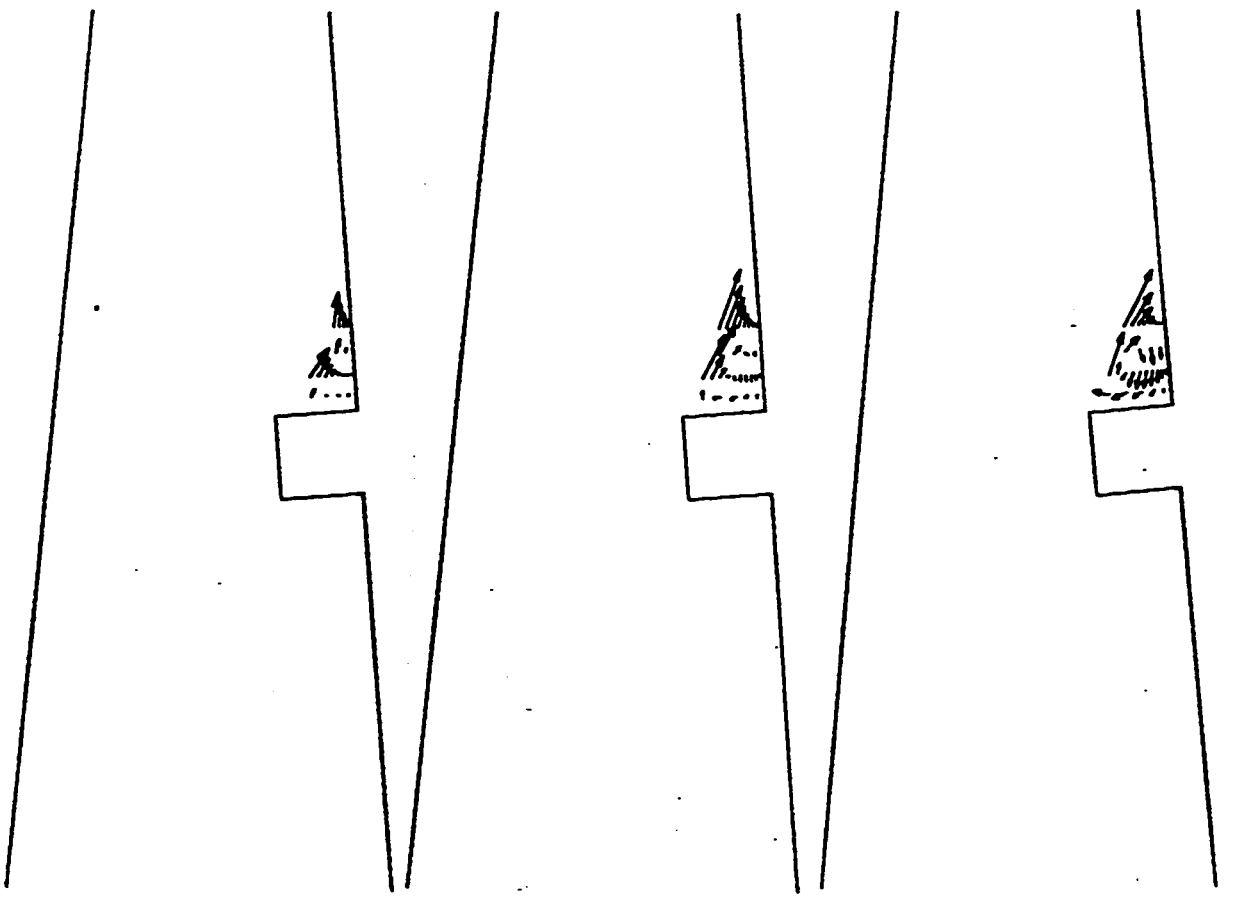

(a) Ra = 29 (b) Ra = 491 (c) Ra = 9126

Figure 6.97 Computed Velocity Vectors (Enlarged) for AR = 0.2727, Pr = 0.72, Convergent ($\gamma = 5$), $L_2 = 0.0945$, $L_1 = 0.5$.

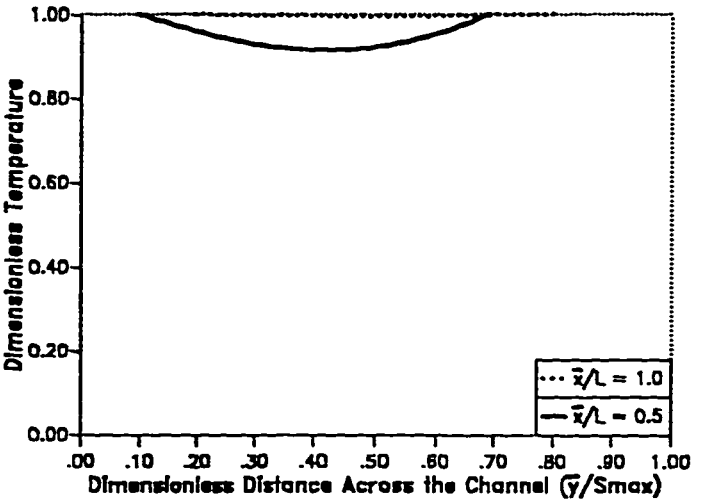

Figure 6.98 Transverse Temperature Distribution at Different Cross-Sections in the Channel for Ra = 29 .

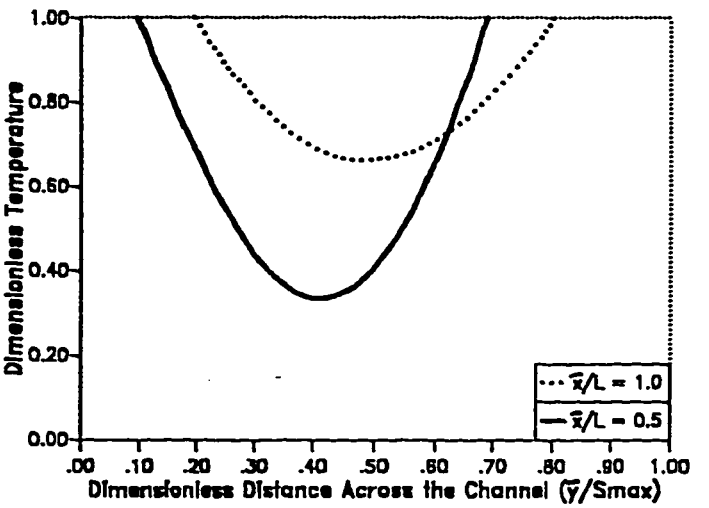

Figure 6.99 Transverse Temperature Distribution at Different Cross-Sections in the Channel for Ra = 491 .

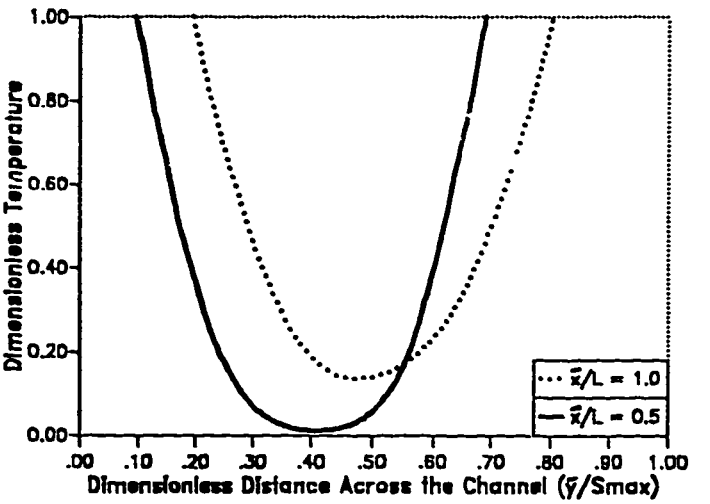

Figure 6.100 Transverse Temperature Distribution at Different Cross-Sections in the Channel for Ra = 9126 .

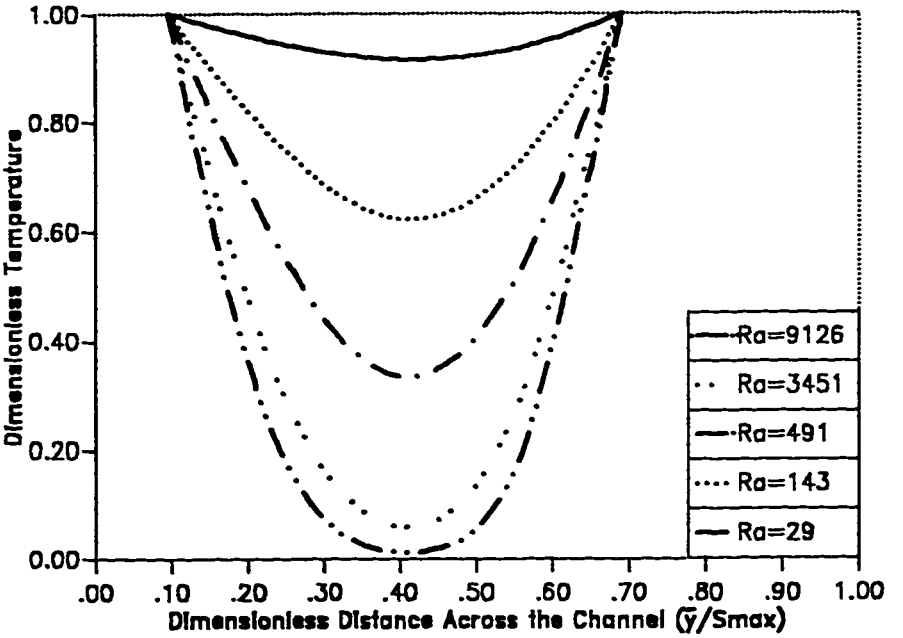

Figure 6.101 Transverse Temperature Distribution at the Middle Hight of the Channel for Different Values of Ra.

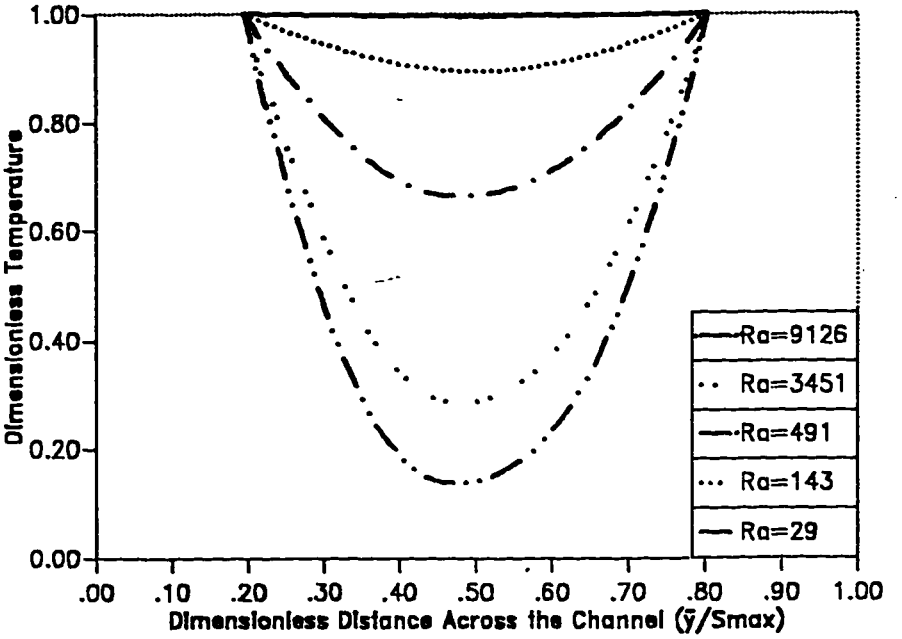

Figure 6.102 Transverse Temperature Distribution at the Exit of the Channel for Different Values of Ra.

(a) Ra = 29 (b) Ra = 491 (c) Ra = 9126

Figure 6.103 Computed Isotherms for AR = 0.2727, Pr = 0.72, Convergent (γ = 5), L_2 = 0.0945 , L_1 = 0.5 .

6.6.1.2 Convergent Channel , $\gamma = 10°$

In this sub-section, the case of convergence angle $\gamma = 10°$ will be investigated. The study was carried out for two values of $AR_{S_{exit}}$, namely, $AR_{S_{exit}} = 0.2727$ and 0.3636. Due to the convergence criteria, a $Ra_{S_{exit}}$ range from 1.0 to 5.0×10^3 has been considered in this investigation. Since similar trends have been observed in previous results for both aspect ratios, a complete analysis will be presented only for the $AR_{S_{exit}} = 0.2727$. The computed values of the dimensionless mass flow rates and the average Nusselt numbers for $AR_{S_{exit}} = 0.3636$ will also be presented.

The mesh generated for the case of $AR_{S_{exit}} = 0.2727$ and $\gamma = 10°$ is shown in figure (6.104). The maximum dimensionless vertical velocities (Umax), the dimensionless mass flow rates (Q) and the average Nusselt numbers ($\overline{Nu}_{S_{exit}}$) for each $Ra_{S_{exit}}$ are given in TABLE (6-6). For the sake of comparison, the dimensionless mass flow rates and the average Nusselt numbers for the two $AR_{S_{exit}} = 0.2727$ and 0.3636 were plotted versus the $Ra_{S_{exit}}$ in a log-log scale as shown in figures (6.105) and (6.106) respectively. It can be noted that as $Ra_{S_{exit}}$ increases Q and $\overline{Nu}_{S_{exit}}$ increase. Also it can be noted that as the aspect ratio increases Q and $\overline{Nu}_{S_{exit}}$ increase. The effect of the aspect ratio decreases as the Rayliegh number increases.

Similar to the previous discussions, the hydrodynamic results will be prsented in four different forms. The first form is the plot of dimensionless vertical velocity versus the dimensionless channel's width ($\bar{y}/S_{max}$) for some representative Rayliegh numbers as shown in figures (6.107) through (6.109). In each figure, the dimensionless vertical velocity profile at the entrance of the channel ($\bar{x}$ /L=0.0), at the mid-plane of the channel ($\bar{x}$ /L=0.5) and at the exit of the channel ($\bar{x}$ /L=1.0) were plotted. As expected, the maximum dimensionless vertical velocity occurs at $\bar{x}$ /L=1.0 for each value of $Ra_{S_{exit}}$. This is due to the fact that the cross-sectional area at the channel exit is the smallest one of the chosen locations. At high Rayliegh numbers two velocity peaks are observed. This means that at high Rayliegh number each wall will approach the isolated vertical plate limit.

The second form of the hydrodynamic results is the plot of the dimensionless vertical velocity versus the dimensionless channel's width ($\bar{y}/S_{max}$) at $\bar{x}$ /L=0.0,0.5 and 1.0 for different Rayliegh numbers as shown in figures (6.110) through (6.112) respectively. As explained for the case of $\gamma = 5$, it can be shown that the dimensionless mass flow rate increases as the $Ra_{S_{exit}}$ increases.

The third form of the hydrodynamic results is the streamlines plots. The plots of the computed streamlines at four different Rayliegh numbers are shown in figures (6.113-a) through (6.113-d). No circulation zones have been picked up by the streamlines plots, although examining the com-

puted values indicate circulation zones in the obstruction top corner at high Rayliegh numbers. The velocity vectors plots have been produced. The variation of the air velocity along the channel can be observed as shown in figures (6.114-a) through (6.114-d). At $Ra_{S_{exit}} = 3451$ the two velocity peaks are shown clearly in figure (6.114-d). To be able to show the circulation zone, the velocities right at the top of the obstruction have been magnified and replotted as shown in figures (6.115-a) through (6.115-d). At low Rayliegh numbers (i.e. $Ra_{S_{exit}} = 4.38$ and 29), no circulation zones have been observed in figures (6.115-a) and (6.115-b) respectively. However, a circulation region is shown at $Ra_{S_{exit}} = 491$. The size of the circulation zone icreases as the Rayliegh number increases as shown in figures (6.97-c) and (6.97-d). Since heat is transfered across the circulation flow regimes by conduction only, the existence of these zones will affect the heat transfer rate.

The thermal results are presented in four different forms. The first form is the plot of the computed dimensionless temperature versus the dimensionless distance across the channel ($\bar{y}/S_{max}$) for $Ra_{S_{exit}} = 29, 491$ and 3451 as shown in figures (6.116) through (6.118) respectively. The plots were done at the mid-plane ($\bar{x}/L = 0.5$) of the channel and at the exit ($\bar{x}/L = 1.0$) of the channel. As expected, the air temperature increases as $\bar{x}/L$ increases (i.e.as it rises up along the axial direction of the channel).

The second form of the thermal results is the plot of the dimensionless temperature at a given hight of the channel ($\bar{x}$ /L) for different values of $Ra_{S_{exit}}$. Figure (6.119) shows the variation of the dimensionless temperature at the mid-plane of the channel ($\bar{x}$ /L=0.5) for different values of Rayliegh numbers. Figure (6.120) shows the same variation at the exit ($\bar{x}$ /L=1.0) of the convergent obstructed channel. As can be seen from these figures, as Rayliegh number increases the minimum temperature at these two plnes ($\bar{x}$ /L=0.5 and $\bar{x}$ /L=1.0) decreases.

The third form of the thermal results is the isothermal lines. The plots for the computed isotherms are shown in figures (6.121-a) through (6.121-d). It is noted that as the $Ra_{S_{exit}}$ increases the boundary layer thickness (δ) decreases and hence the average Nusselt number increases.

The fourth form of the thermal results is the average Nusselt number. The average Nusselt numbers ($\overline{Nu}_{S_{exit}}$) for both the parallel-walled obstructed vertical channel ($\gamma = 0°$) and the convergent obstructed vertical channel ($\gamma = 5°$ and $10°$) are plotted in figures (6.122-6.123) versus the Rayliegh number $Ra_{S_{exit}}$. It is noted that increasing the angle of convergence leads to a dramatic increase in the average Nusselt number ($\overline{Nu}_{S_{exit}}$) especially at low Rayliegh numbers $Ra_{S_{exit}}$ (i.e. fully developed flow). This effect of convergence angle decreases as $Ra_{S_{exit}}$ increases. Then it starts to overlap. This means that at $Ra_{S_{exit}} > 850$ the increase of the con-

vergence angle will decrease the ($\overline{Nu}_{S_{exit}}$) . The same trend is observed for $AR_{S_{exit}} = 0.3636$ as shown in figure (6.123). All the previous computations of the average Nusselt numbers and the Rayliegh number were based on S_{exit} . An attempt is made to change the base and see if this will collapse those three curves (for $\gamma = 0, \gamma = 5$ and $\gamma = 10$) into one curve. Hence, the average Nusselt numbers as well as the Rayliegh numbers were computed based on S_{ent} and S_{avg} . S_{ent} is the distance between the channel walls at the entrance while S_{avg} is the average of S_{exit} and S_{ent} respectively.This has been done to find out which of the parameters (i.e. S_{exit} , S_{ent} and S_{avg}) will give close values of the average Nusselt number to those of the parallel-walled channel. Figures (6.124) and (6.125) show the plot of the $\overline{Nu}_{S_{avg}}$ versus $Ra_{S_{avg}}$ for $AR_{S_{exit}} = 0.2727$ and 0.3636 respectively. Figures (6.126) and (6.127) show the plot of the $\overline{Nu}_{S_{ent}}$ versus $Ra_{S_{ent}}$ for $AR_{S_{exit}} = 0.2727$ and 0.3636 respectively. It can be noted that basing the convergent channel average Nusselt number and the Rayliegh number on S_{ent} give average Nusselt number curves that are in a good agreement with those for parallel-walled obstructed channel. A maximum error of about 20% may be encountered when parallel-walled average Nusselt number curves are used for convergent channels.

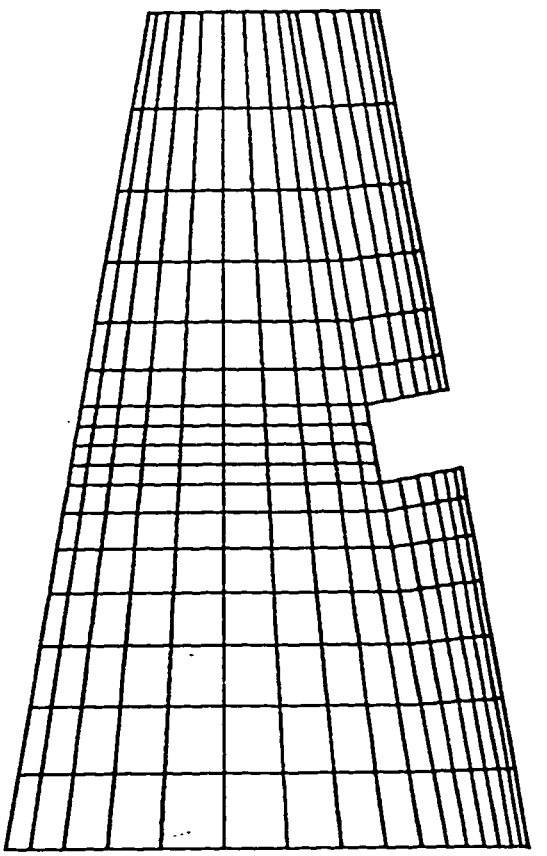

Figure 6.104 Generated Mesh for Convergent Obstructed Channel AR = 0.2727 , γ = 10 , L_1 = 0.5 , L_2 = 0.0945 , Ra = 1000, Pr = 0.72 .

TABLE(6-6) COMPUTED Umax,Q and $\overline{Nu}$ FOR OBSTRUCTED CONVERGENT VERTICAL CHANNEL WITH AR = 0.2727, $L_1 = 0.50$, $L_2 = 0.0945$ and $\gamma = 10$.

Ra	Umax	Q	$\overline{Nu}$
4.38	0.2964	0.0988	0.1395
8.76	0.4592	0.1701	0.2386
14.60	0.8809	0.2650	0.3578
29.00	1.4891	0.4637	0.5778
143.00	3.8902	1.3621	1.1556
275.00	5.7848	1.9747	1.4231
491.00	7.5923	2.6998	1.6574
978.00	9.8783	3.6551	1.9161
1365.00	11.0921	4.2226	2.1377
1988.00	13.9209	5.0541	2.2964
2701.00	14.1298	5.6892	2.5513
3451.00	14.8110	6.4888	2.7066

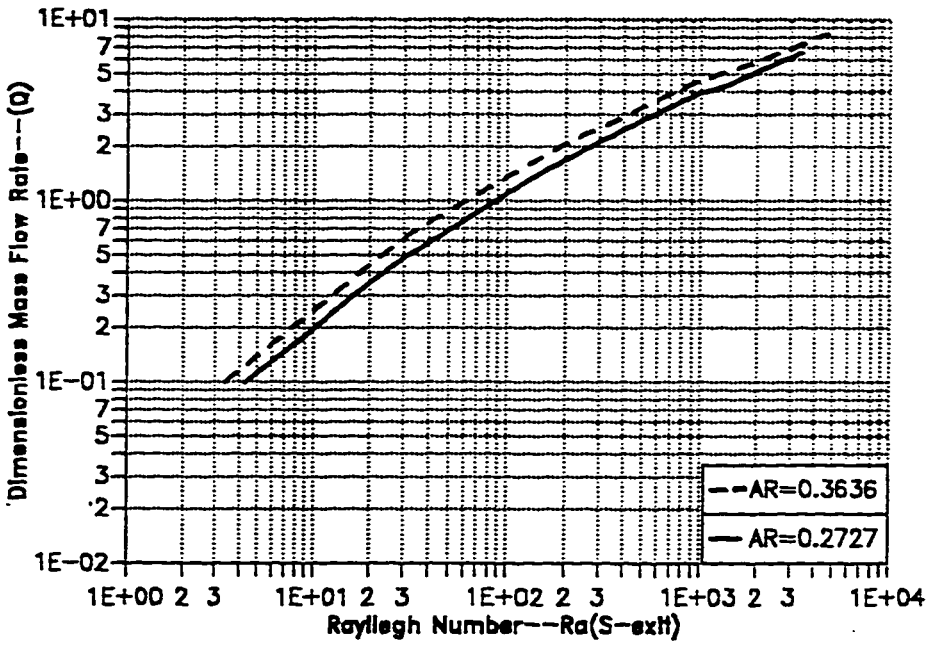

Figure 6.105 The Variation of Dimensionless Mass Flow Rate (Q) Versus the Rayliegh Number ($Ra_{S_{exit}}$) for the Convergent Obstructed Channel (γ = 10).

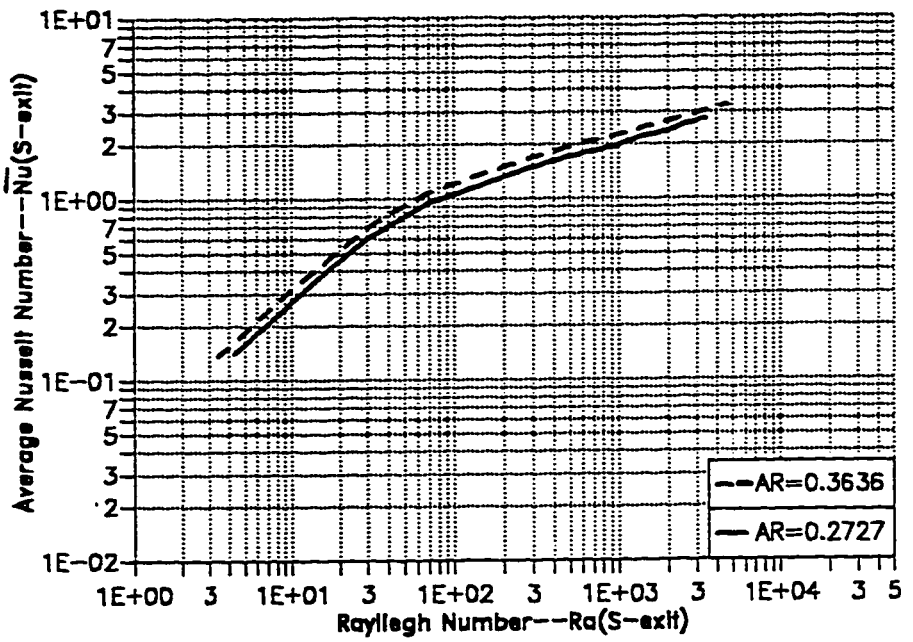

Figure 6.106 The Variation of Average Nusselt Number ($\overline{Nu}_{S_{exit}}$) Versus the Rayliegh Number ($Ra_{S_{exit}}$) for the Convergent Obtructed Channel (γ = 10).

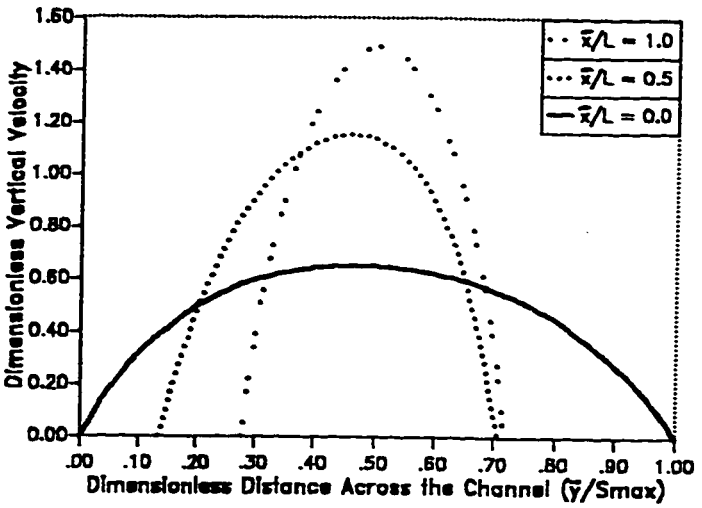

Figure 6.107 Transverse Velocity Distribution at Different Cross-Sections in the Channel for Ra = 29

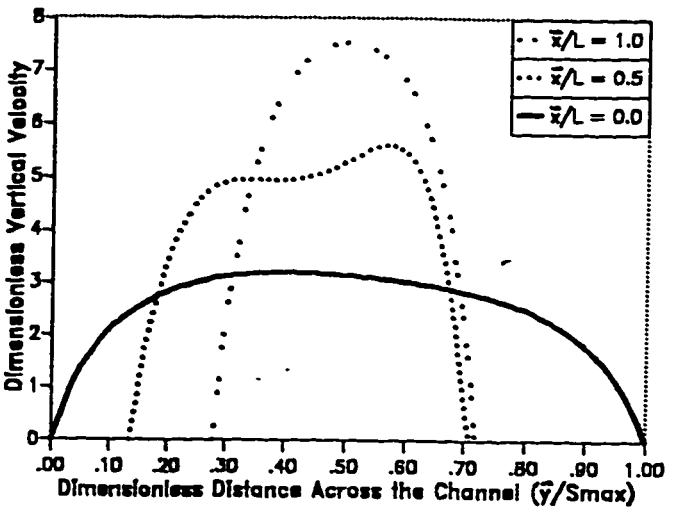

Figure 6.108 Transverse Velocity Distribution at Different Cross-Sections in the Channel for Ra = 491

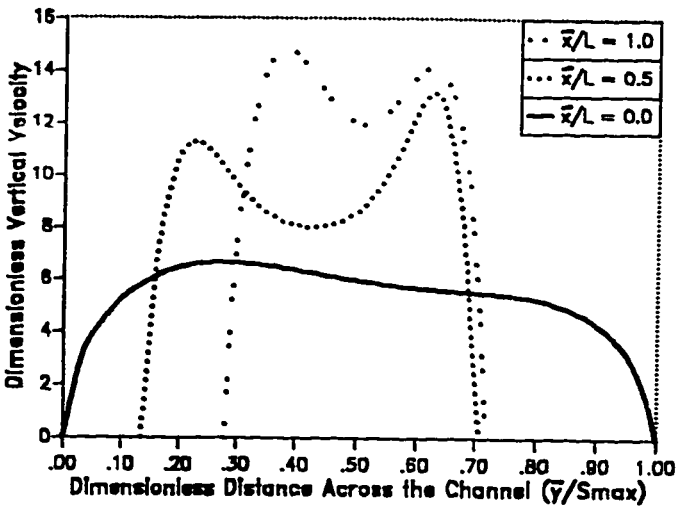

Figure 6.109 Transverse Velocity Distribution at Different Cross-Sections in the Channel for Ra = 3451

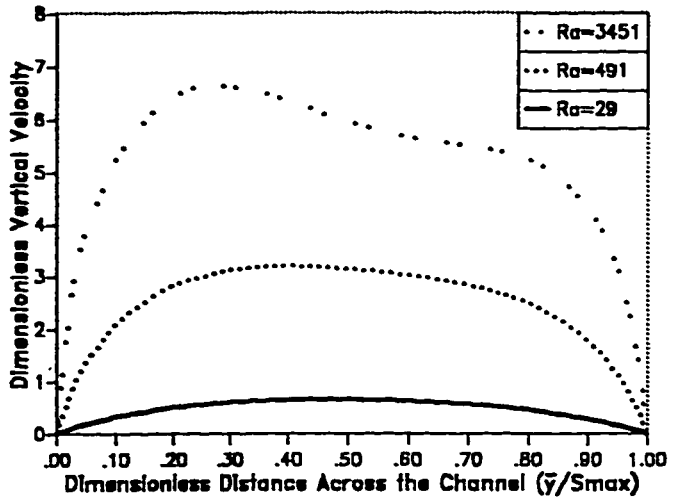

Figure 6.110 Transverse Velocity Distribution at the Entrance of the Channel for Different Values of Ra.

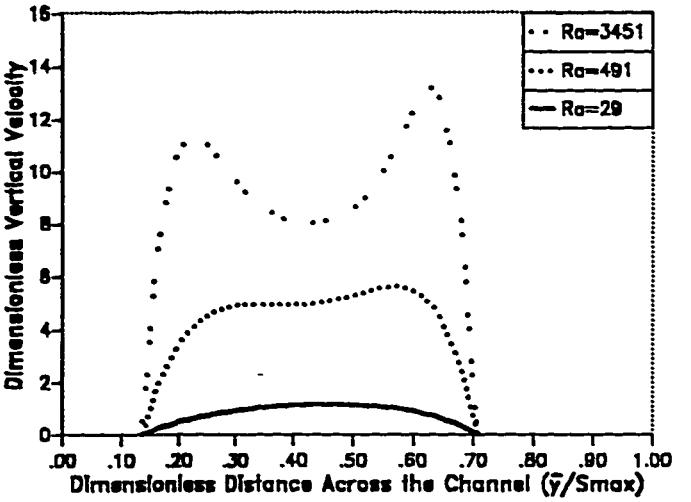

Figure 6.111 Transverse Velocity Distribution at the Obstruction Center-Line for Different Values of Ra.

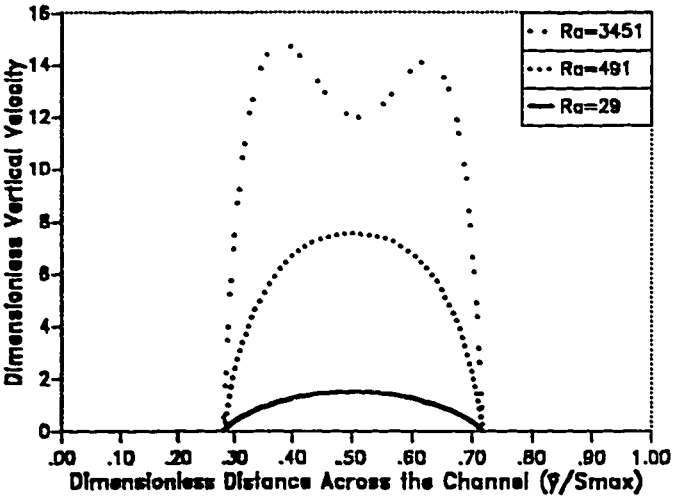

Figure 6.112 Transverse Velocity Distribution at the Exit of the Channel for Different Values of Ra.

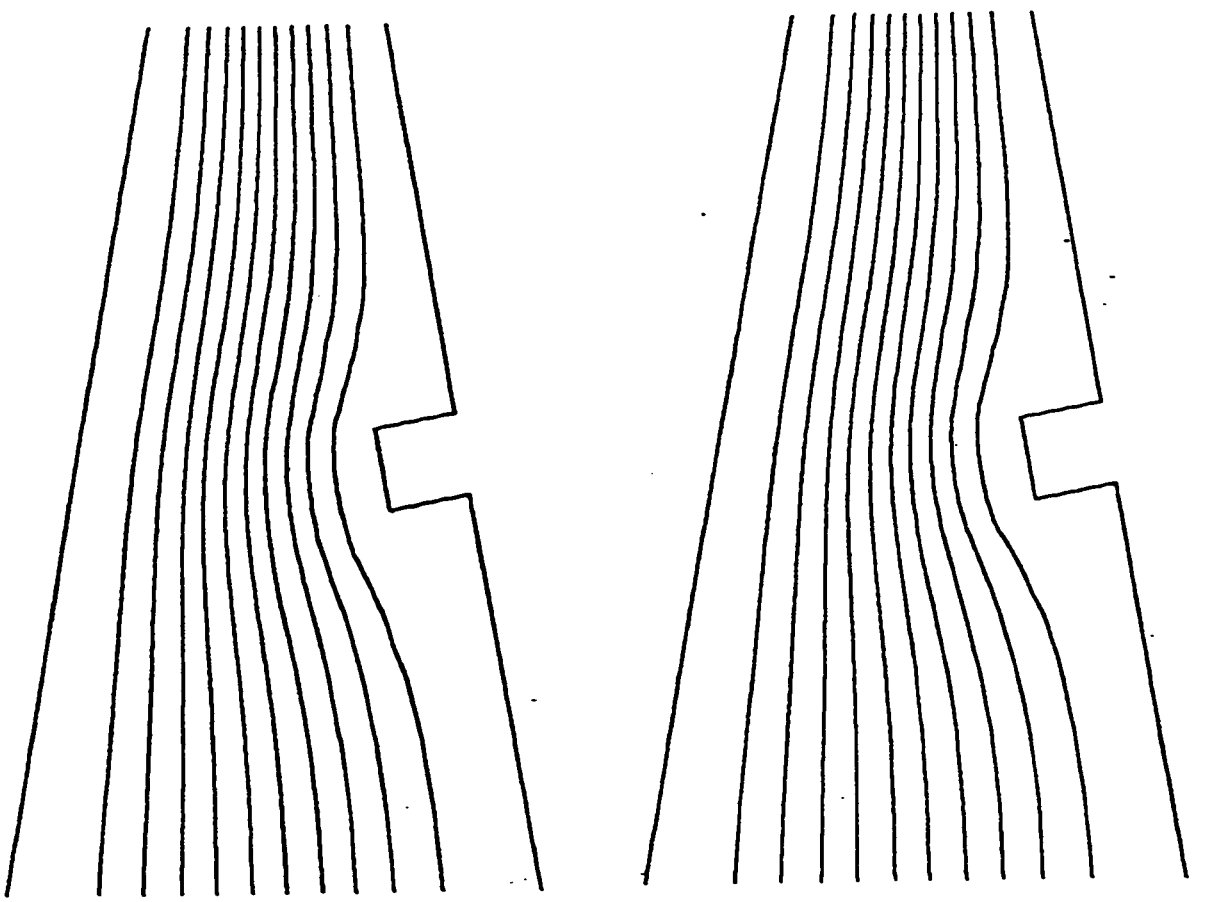

(a) Ra = 4.38 (b) Ra = 29

Figure 6.113 Computed Streamlines for AR = 0.2727, Pr = 0.72, Convergent (γ = 10), L_1 = 0.5 , L_2 = 0.0945 .

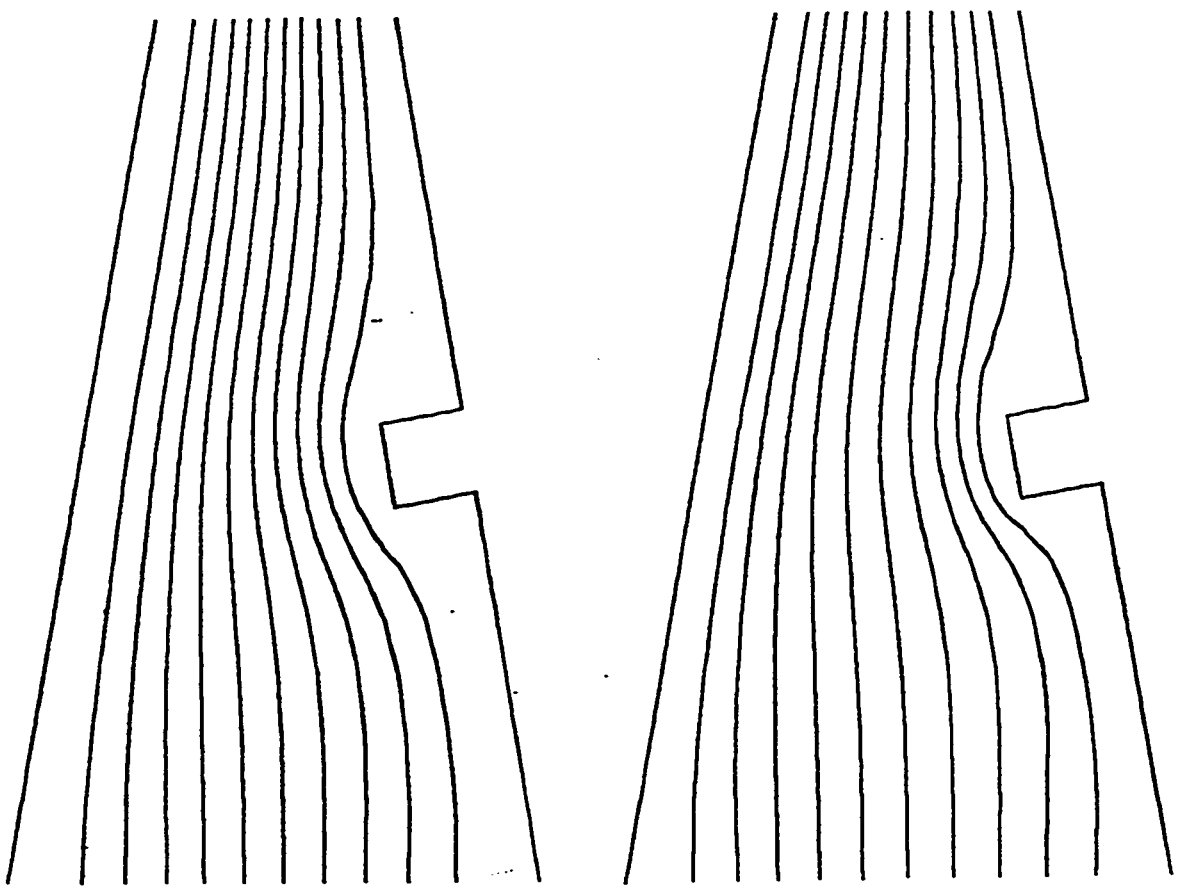

(c) Ra = 491

(d) Ra = 3451

Figure 6.113 Computed Streamlines for AR = 0.2727, Pr = 0.72, Convergent (γ = 10), L_1 = 0.5 , L_2 = 0.0945

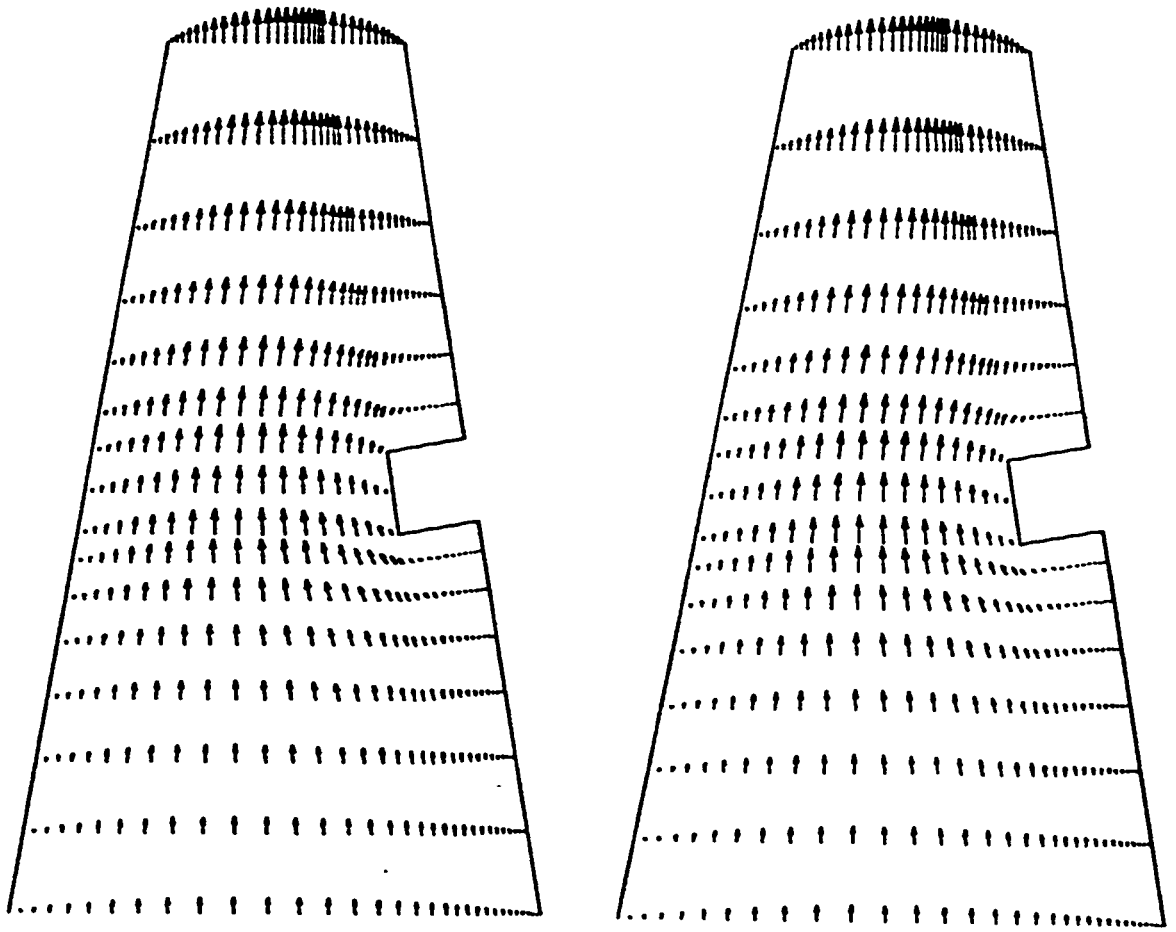

(a) Ra = 4.38 (b) Ra = 29

Figure 6.114 Computed Velocity Vectors for $\Lambda R = 0.2727, Pr = 0.72$ Convergent ($\gamma = 10$) , $L_1 = 0.5$, $L_2 = 0.0945$.

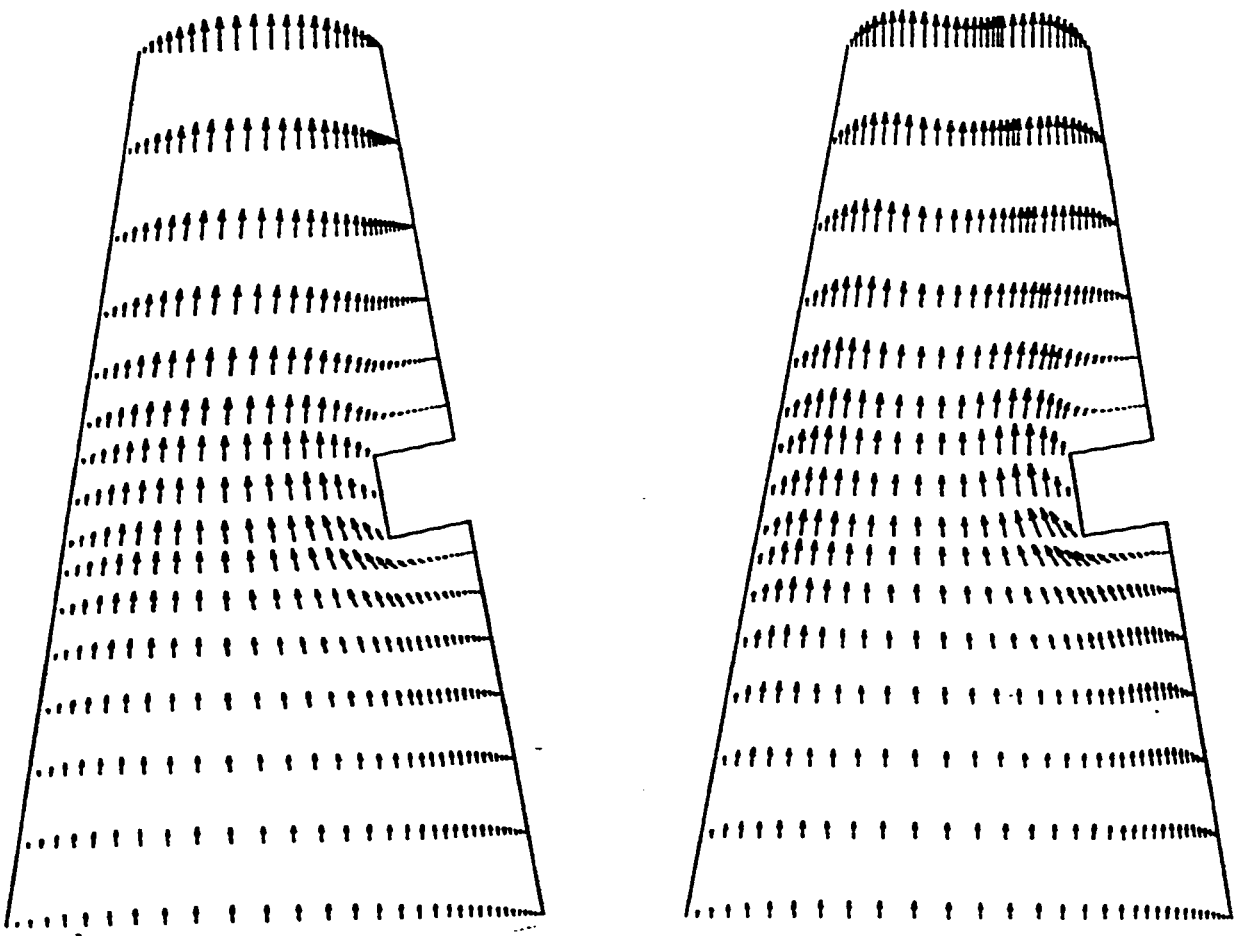

(c) Ra = 491

(d) Ra = 3451

Figure 6.114 Computed Velocity Vectors for AR = 0.2727, Pr = 0.72 Convergent (γ = 10), $L_1 = 0.5$, $L_2 = 0.0945$.

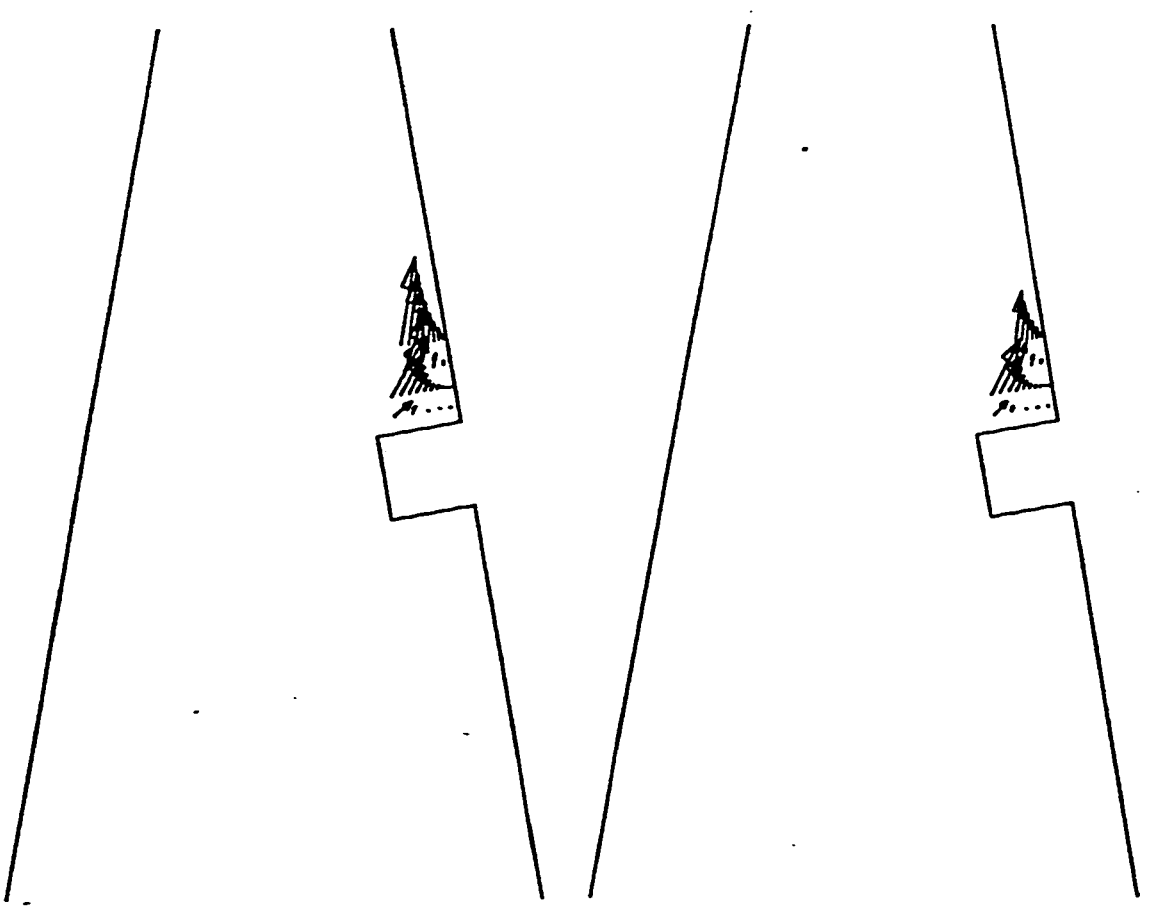

(a) Ra = 4.38 (b) Ra = 29

Figure 6.115 Computed Velocity Vectors (Enlarged) for AR = 0.2727, Pr = 0.72 Convergent (γ = 10), L_1 = 0.5 , L_2 = 0.0945 .

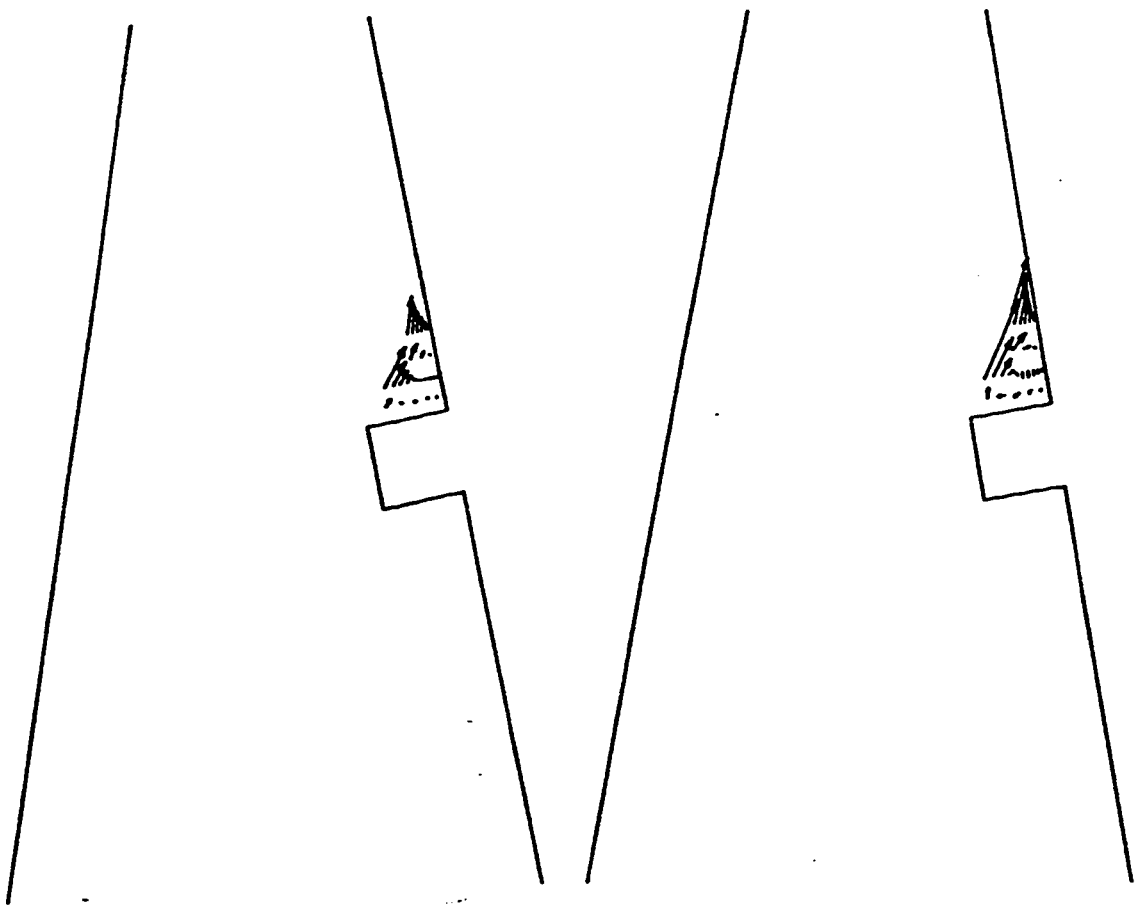

(c) Ra = 491 (d) Ra = 3451

Figure 6.115 Computed Velocity Vectors (Enlarged) for AR = 0.2727, Pr = 0.72 Convergent (γ = 10) .L_1 = 0.5 ,L_2 = 0.0945 .

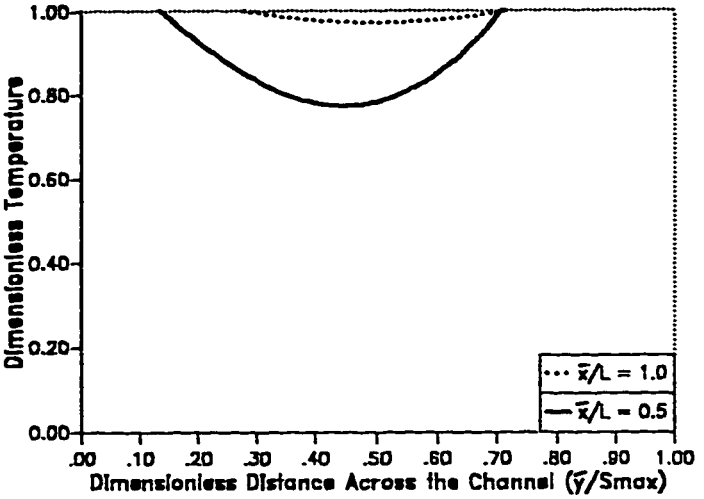

Figure 6.116 Transverse Temperature Distribution at Different Cross-Sections in the Channel for Ra = 29 .

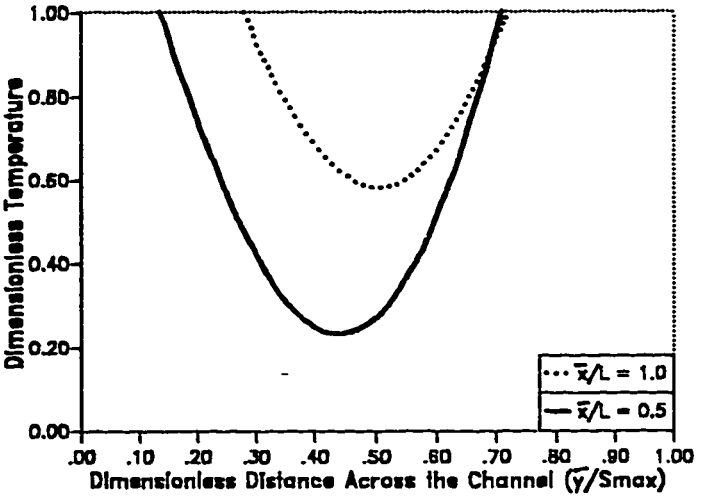

Figure 6.117 Transverse Temperature Distribution at Different Cross-Sections in the Channel for Ra = 491 .

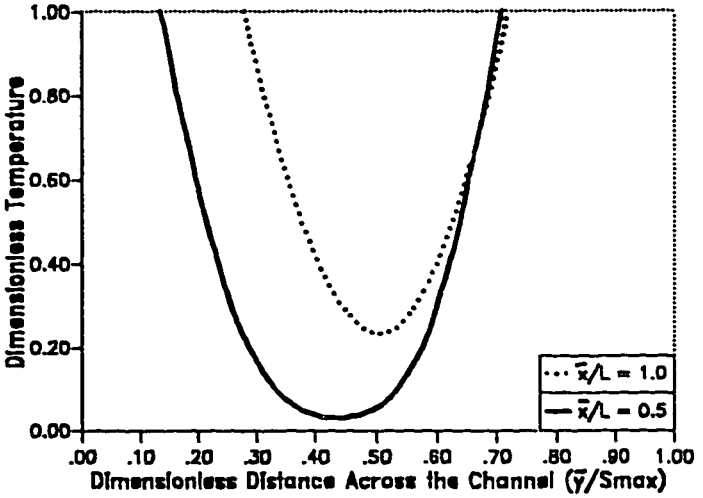

Figure 6.118 Transverse Temperature Distribution at Different Cross-Sections in the Channel for Ra = 3451 .

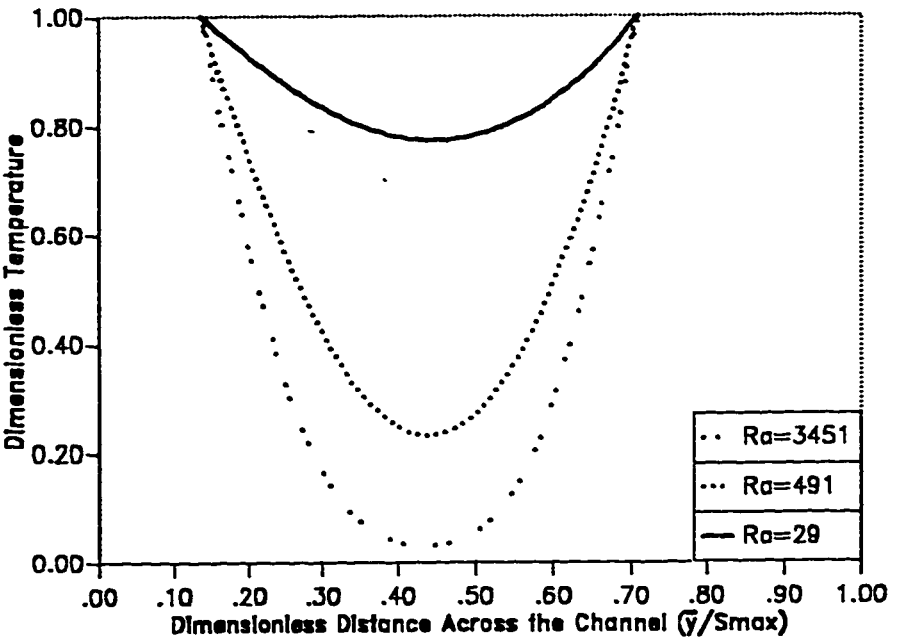

Figure 6.119 Transverse Temperature Distribution at the Middle Hight of the Channel for Different Values of Ra.

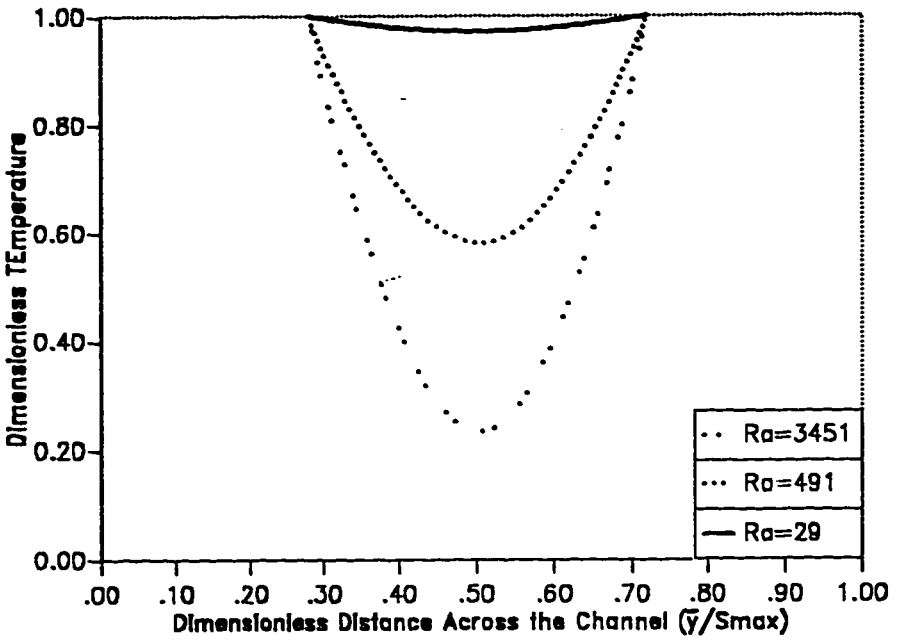

Figure 6.120 Transverse Temperature Distribution at the Exit of the Channel for Different Values of Ra.

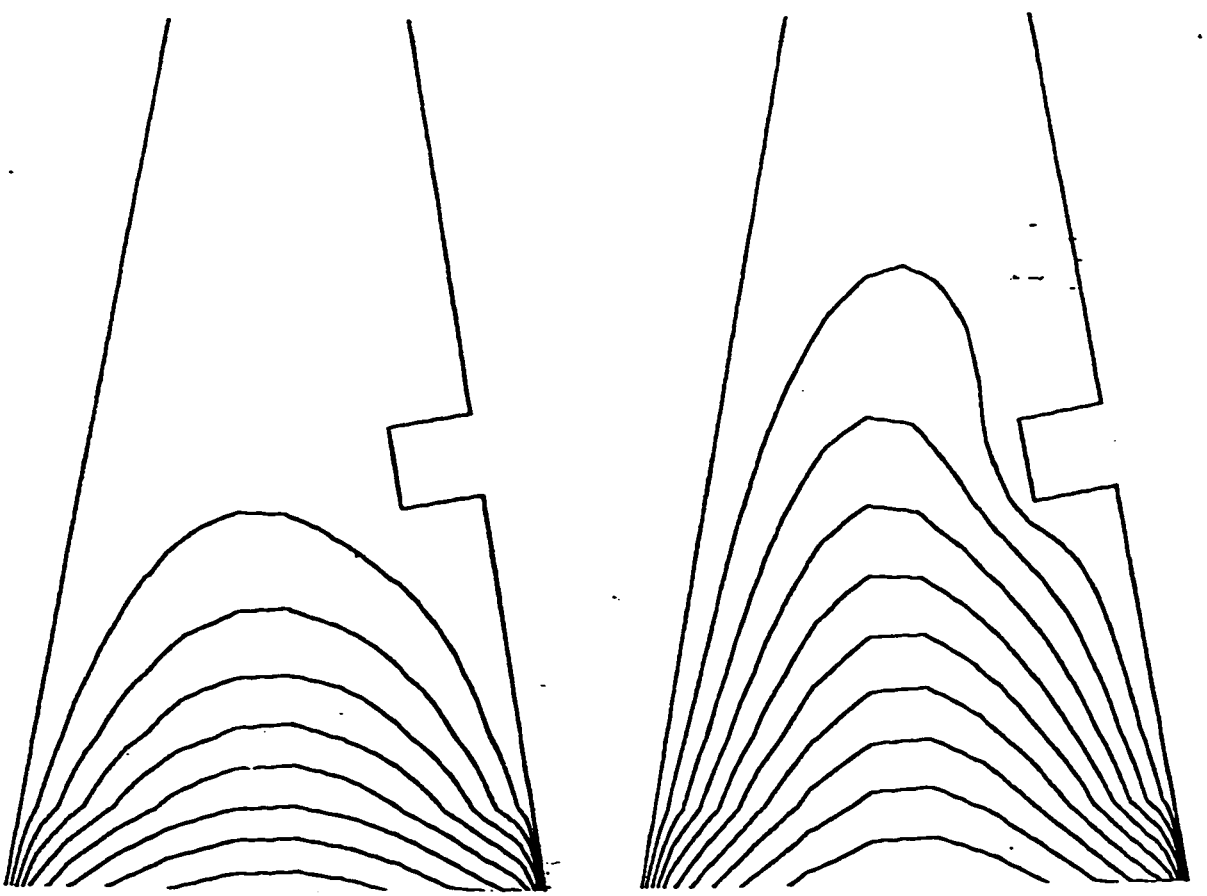

(a) Ra = 4.38 (b) Ra = 29

Figure 6.121 Computed Isotherms for AR = 0.2727, Pr = 0.72, Convergent (γ = 10), L_1 = 0.5 , L_2 = 0.0945 .

(c) Ra = 491 (d) Ra = 3451

Figure 6.121 Computed Isotherms for AR = 0.2727, Pr = 0.72, Convergent (γ = 10), L_1 = 0.5 , L_2 = 0.0945 .

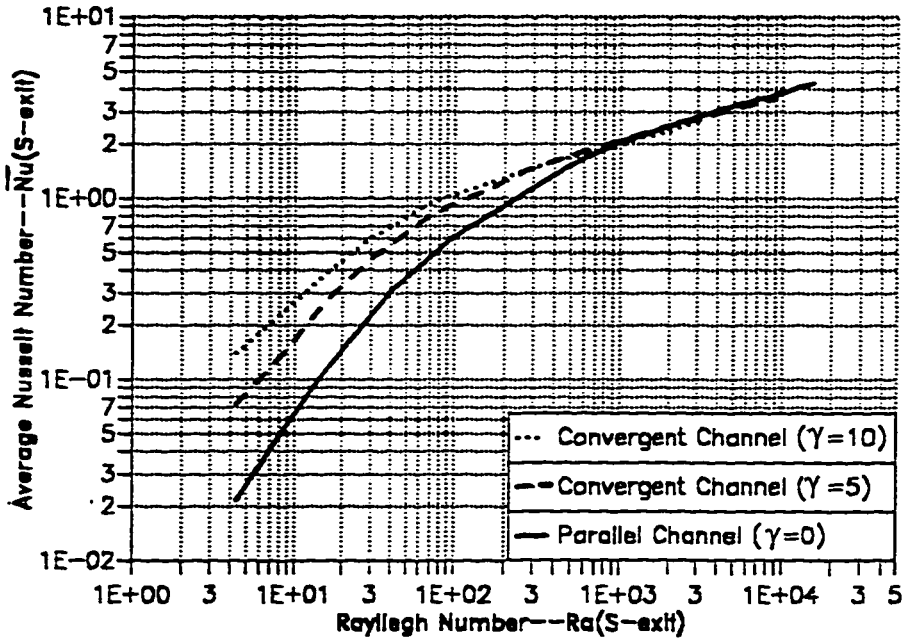

Figure 6.122 The Variation of Average Nusselt Number ($\overline{Nu}_{S_{exit}}$) Versus the Rayliegh Number ($Ra_{S_{exit}}$) for Parallel and Convergent Obstructed Channels with $AR_{S_{exit}}$ = 0.2727.

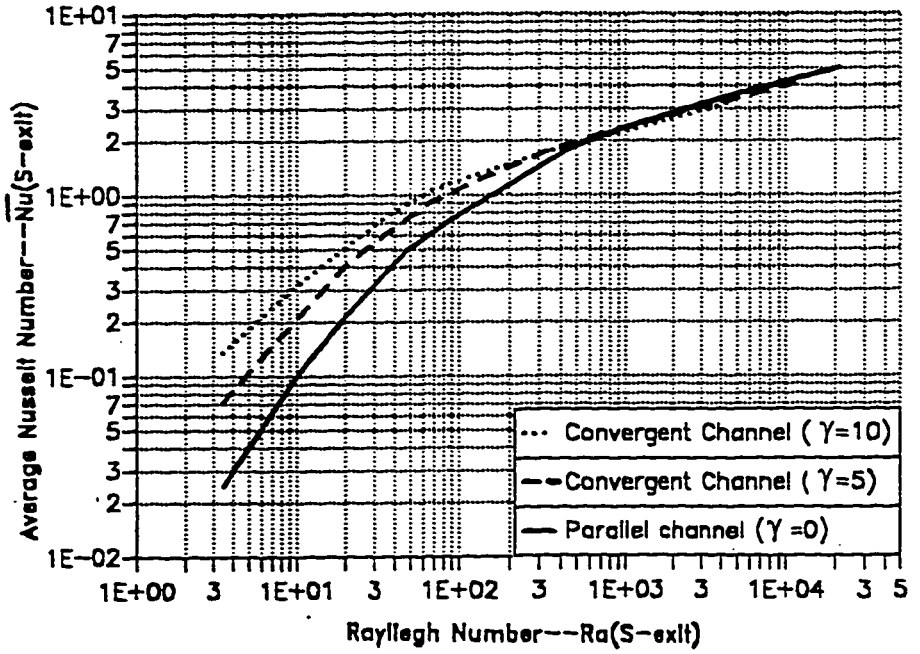

Figure 6.123 The Variation of Average Nusselt Number ($\overline{Nu}_{S_{exit}}$) Versus the Rayliegh Number ($Ra_{S_{exit}}$) for Parallel and Convergent Obstructed Channels with $AR_{S_{exit}}$ = 0.3636.

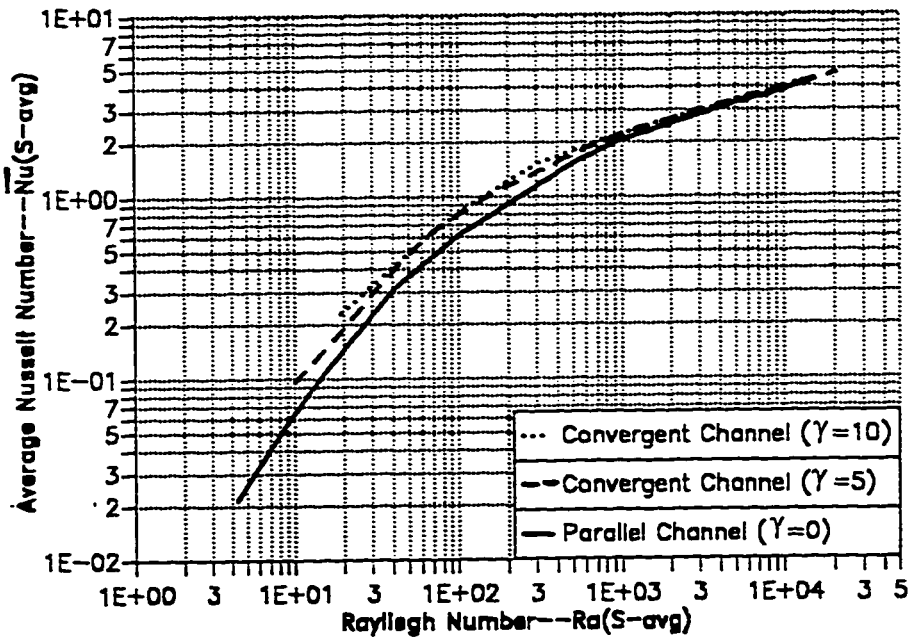

Figure 6.124 The Variation of Average Nusselt Number ($\overline{Nu}_{S_{avg}}$) Versus the Rayliegh Number ($Ra_{S_{avg}}$) for Parallel and Convergent Obstructed Channels with $AR_{S_{exit}} = 0.2727$.

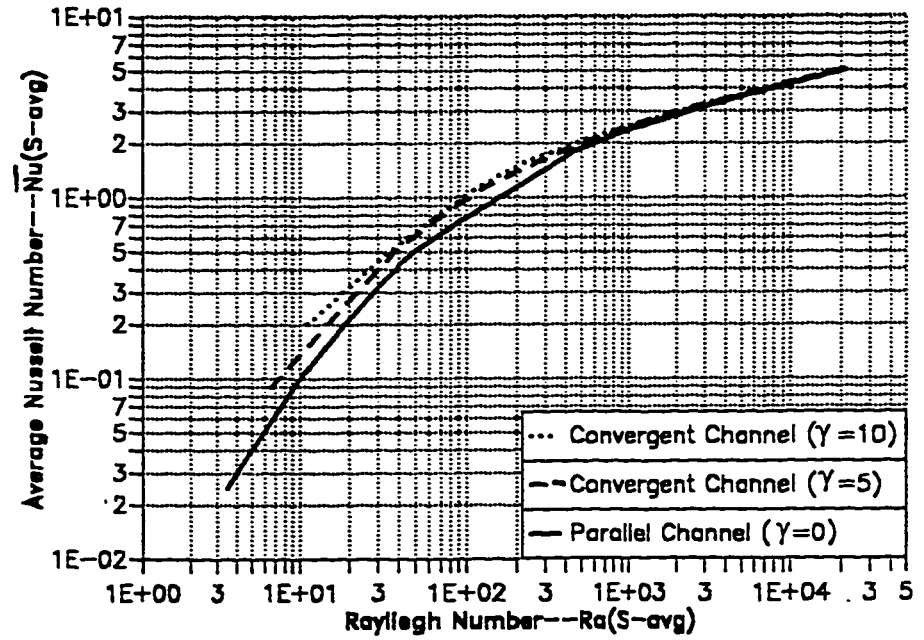

Figure 6.125 The Variation of Average Nusselt Number ($\overline{Nu}_{S_{avg}}$) Versus the Rayliegh Number ($Ra_{S_{avg}}$) for Parallel and Convergent Obstructed Channels with $AR_{S_{exit}} = 0.3636$.

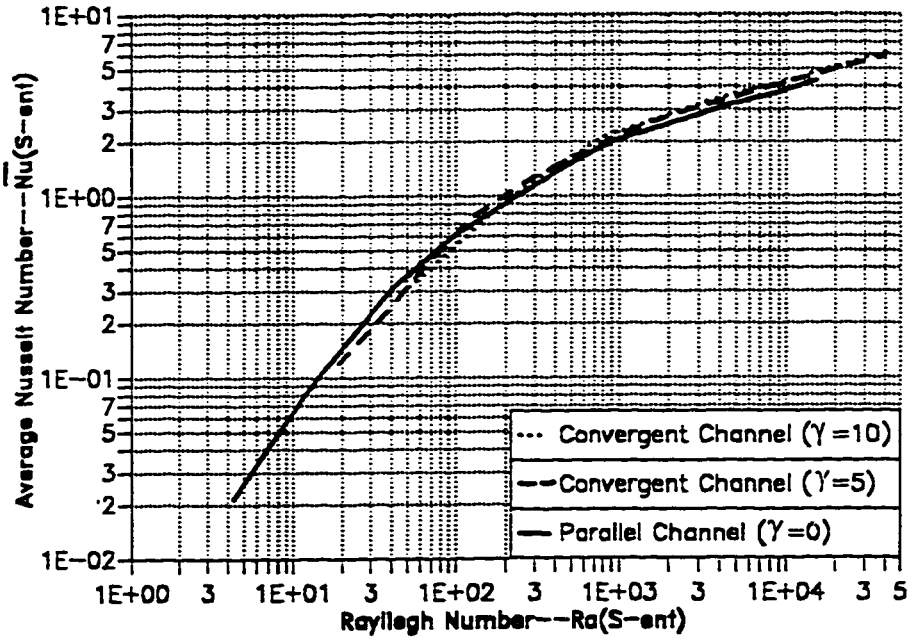

Figure 6.126 The Variation of Average Nusselt Number ($\overline{Nu}_{S_{ent}}$) Versus the Rayliegh Number ($Ra_{S_{ent}}$) for Parallel and Convergent Obstructed Channels with $AR_{S_{exit}} = 0.2727$.

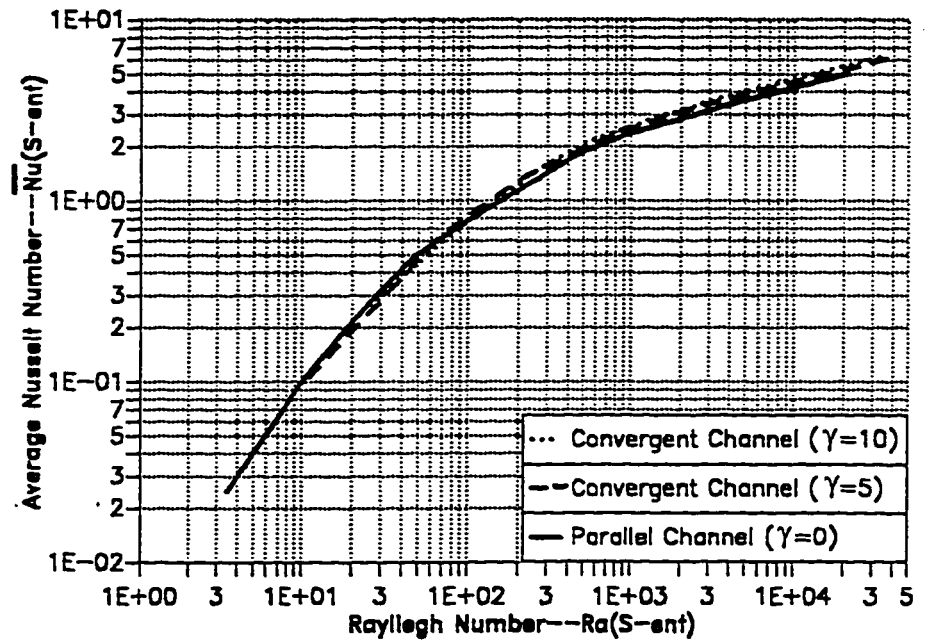

Figure 6.127 The Variation of Average Nusselt Number ($\overline{Nu}_{S_{ent}}$) Versus the Rayliegh Number ($Ra_{S_{ent}}$) for Parallel and Convergent Obstructed Channels with $AR_{S_{exit}} = 0.3636$.

6.6.2 Divergent Obstructed Vertical Channel

In this section, the effect of the angle of divergence on the flow field and the heat transfer characteristics will be presented. The hydrodynamic and thermal results of two divergence angles, namely, $\gamma = 5°$ and $10°$ will be presented seperately and then a comparison between the $\overline{Nu}$ for both angles along with the results of the parallel-walled obstructed channel $\gamma = 0°$ will be presented later. It should be pointed out that the dimensional parameter (b) is equal to the dimensional width at the channel entrance (S_{ent}) for the divergent channel. This was necessary so that the angle of divergence can be attained. Hence, the average Nusselt number, the Rayliegh number, and the aspect ratio for the divergent obstructed vertical channel will be based on S_{ent} .

6.6.2.1 Divergent Channel , $\gamma = 5°$

The effect of the divergence angle $\gamma = 5°$ on the average Nusselt number will be presented in this sub-section. The study was carried out for two values of $AR_{S_{ent}}$, namely, $AR_{S_{ent}} = 0.2727$ and 0.3636 and a range of $Ra_{S_{ent}}$ from 1.0 to 6.5×10^2 . Being constrained by the convergence criteria and the capability of the code, it was not possible to get solutions for higher Rayliegh numbers in the divergent case as for the convergent one. Due to the similar trend observed between the results of the two aspect ratios, only the results for the case of $AR_{S_{ent}} = 0.2727$ will be discussed. Curves of the

average Nusselt numbers and mass flow rates will be shown for both aspect ratios.

The mesh generated for the divergent obstructed vertical channel is shown in figure (6.128). The calculated values for the maximum dimensionless velocities, the dimensionless mass flow rates and the average Nusselt numbers ($\overline{Nu}_{S_{ent}}$) for seven different values of $Ra_{S_{ent}}$ are given in TABLE (6-7). Figures (6.129) and (6.130) show the plot of the dimensionless mass flow rates (Q) and the average Nusselt numbers ($\overline{Nu}_{S_{ent}}$) versus the $Ra_{S_{ent}}$. From these figures, it can be noted that as the $Ra_{S_{ent}}$ increases both Q and $\overline{Nu}_{S_{ent}}$ increase for each aspect ratio. It can also be noted that as the aspect ratio increases Q and $\overline{Nu}_{S_{ent}}$ increase.

Similar to the previous discussions, the hydrodynamic results will be presented in four different forms. The first form is the plot of dimensionless vertical velocity versus the dimensionless channel's width ($\bar{y}/S_{max}$) at three different hights ($\bar{x}$ /L) in the channel for a specific values of Rayliegh number $Ra_{S_{ent}}$. Figures (6.131) through (6.133) show the variation of the dimensionless vertical velocity at the channel entrance ($\bar{x}$ /L =0.0), channel mid-plane ($\bar{x}$/L=0.5)and channel exit ($\bar{x}$ /L=1.0) for $Ra_{S_{ent}}$ = 29 , 143 and 491 respectively. The maximum vertical velocity occurs at the entrance of the channel for each $Ra_{S_{ent}}$.

The second form of the hydrodynamic results is the plot of the dimensionless vertical velocity versus the dimensionless channel's width ($\bar{y}/S_{max}$) at a given cross-section in the channel for different values of Ryliegh numbers. Figure (6.134) shows the plot of the dimensionless vertical velocities at the entrance of the channel ($\bar{x}$ /L=0.0) for different Rayliegh numbers. Figure (6.135) shows the same plots at the mid-plane ($\bar{x}$ /L=0.5) of the channel while the plots of the dimensionless vertical velocities at the exit ($\bar{x}$ /L=1.0) of the channel are shown in figure (6.136). It can be noted that the dimensionless mass flow rates (the area under the dimensionless vertical velocity curve) increase as the Rayliegh number increases.

The third form of the hydrodynamic results is the streamlines plots. The plots of the computed streamlines at three different Rayliegh numbers are shown in figures (6.137-a) through (6.137-c). The fourth form of the hydrodynamic results is the velocity vector plots as shown in figures (6.138-a) through (6.138-c). The variation of the velocity vectors along the axial direction of the channel can be clearly noted.Examining the computed velocity data, it is observed that negative velocities occur at the top corner between the wall and the obstruction side. The magnitude of these velocities (in this region) is very small that they can not be observed from the streamlines and/or the velocity vector plots. These velocities have been magnified and plotted again in figures (6.139-a) through (6.139-c). From these figures it can be seen that regions of recirculating flow are formed at the top corner of the obstruction. The size of the recirculating zone increases as the Rayliegh number increases. Since across the the circulation zones heat is transfered by

conduction only, the existance of these zones will affect the heat transfer rate.

The thermal results are presented in four different forms. The first form is the plot of the dimensionless temperature versus the dimensionless distance across the channel ($\bar{y}/S_{max}$) for $Ra_{S_{ent}}$ = 29 , 143 and 491 as shown in figures (6.140) through (6.142) respectively. The plots were done at the mid-plane of the channel ($\bar{x}$ /L=0.5) and at the exit of the channel ($\bar{x}$ /L=1.0). As expected, the air temperature increases as $\bar{x}$ /L increases (i.e.as it moves along the axial direction of the channel). Figure (6.143) shows the variation of the dimensionless temperature at the mid-plane of the channel ($\bar{x}$ /L=0.5) for four different values of Rayliegh numbers,while figure (6.144) shows the same variation at the exit ($\bar{x}$ /L=1.0) of the divergent obstructed channel. From figures (6.143) and (6.144), it is noted that as the Rayliegh number increases the minimum temperature at these two planes ($\bar{x}$/L=0.5 and $\bar{x}$/L=1.0) decreases.

The third form of the thermal results is the isothermal lines. The plots for the computed isotherms are shown in figures (6.145-a) through (6.145-c). At $Ra_{S_{ent}}$ = 29 , the flow is fully developed which means that a thermal boudary layer has been developed at each wall and they emerge in the region just above the entrance cross-sectional area. For most portions of the channel entrance, the dimensionless temperature gradient in the axial direction approaches zero (i.e. $\frac{d\theta}{dx} \approx 0.0$) since the temperature of the air is almost equal to the wall's temperature. As the Rayliegh number increases, the boundary layer thickness (δ) decreases. This decrease will cause an increase

in the dimensionless temperature gradient in the y-direction (i.e. $\frac{d\theta}{dy} \propto \frac{1}{\delta}$). And since the heat transfer rate is directly proportional to the temperature gradient in the y-direction, hence the average Nusselt number will increase. From the isotherm plots, it can be seen that in the case of very large Rayliegh numbers, a boundary layers will be formed on each wall, and the single vertical plate limit will be approached. In the case of very low Rayliegh numbers, the fully developed limit will be approached.

The fourth form of the thermal results is the average Nusselt number ($\overline{Nu}_{S_{ent}}$). The computed average Nusselt number for both aspect ratios for the divergence angle $\gamma = 5$ is shown in figure (6.130). It can be noted that the difference in the $\overline{Nu}_{S_{ent}}$ increases as $Ra_{S_{ent}}$ decreases.

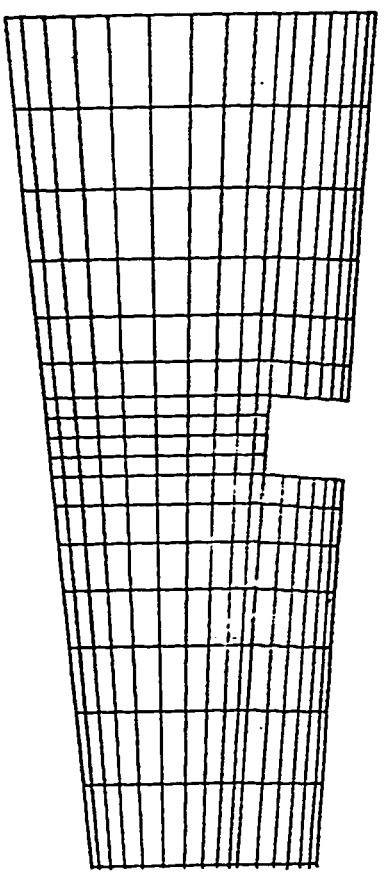

Figure 6.128 Generated Mesh for Divergent Obstructed Channel AR = 0.2727 , γ = 5 , L_1 = 0.5 , L_2 = 0.0945 .

TABLE(6-7) COMPUTED Umax,Q and $\overline{Nu}$ FOR DIVERGENT OBSTRUCTED VERTICAL CHANNEL WITH AR = 0.2727, $L_1 = 0.50$, $L_2 = 0.0945$ and $\gamma = 0$.

Ra	Umax	Q	$\overline{Nu}$
4.38	0.2126	0.0774	0.0290
8.76	0.6753	0.1298	0.0848
14.60	0.9467	0.3765	0.1776
29.00	1.2571	0.5026	0.3794
143.20	5.7823	1.9850	1.2234
274.80	9.3492	3.4651	1.7700
490.90	16.3529	6.8021	2.2300

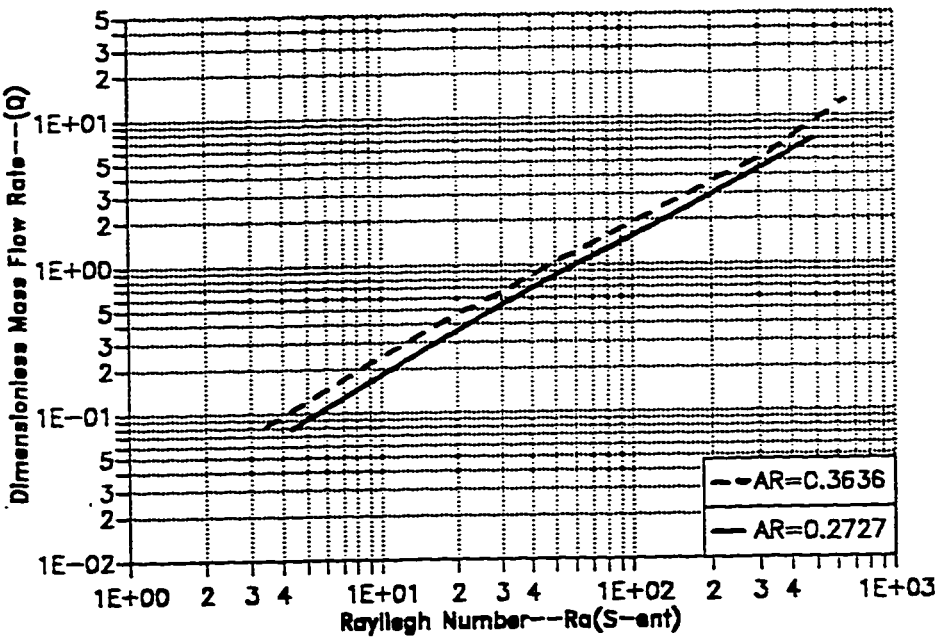

Figure 6.129 The Variation of Dimensionless Mass Flow Rate (Q) Versus the Rayliegh Number ($Ra_{S_{ent}}$) for the Divergent Obstructed Channel (γ = 5).

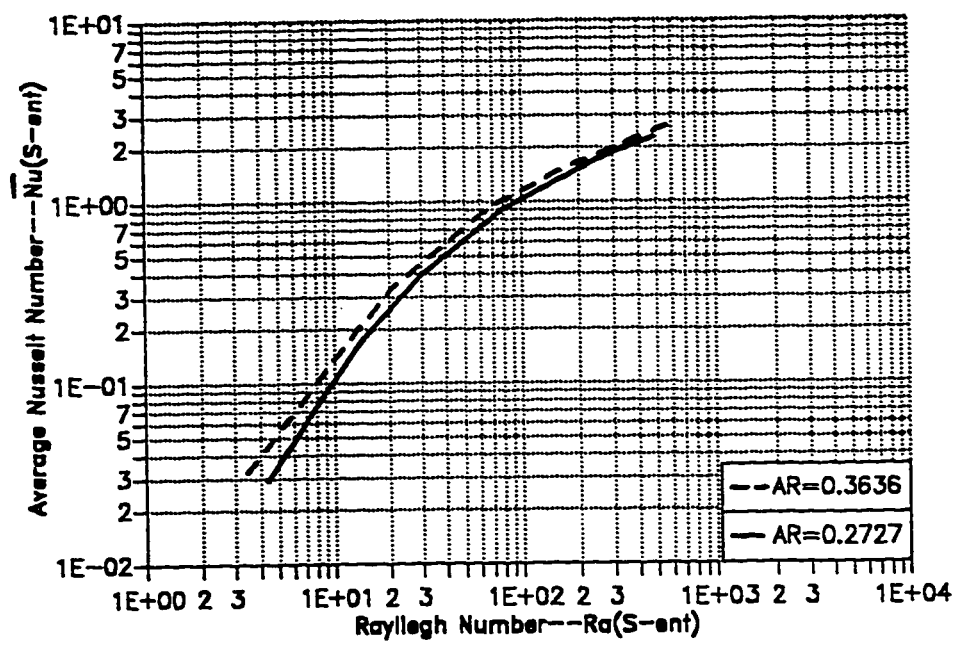

Figure 6.130 The Variation of Average Nusselt Number ($\overline{Nu}_{S_{ent}}$) Versus the Rayliegh Number ($Ra_{S_{ent}}$) for the Divergent Obtructed Channel (γ = 5).

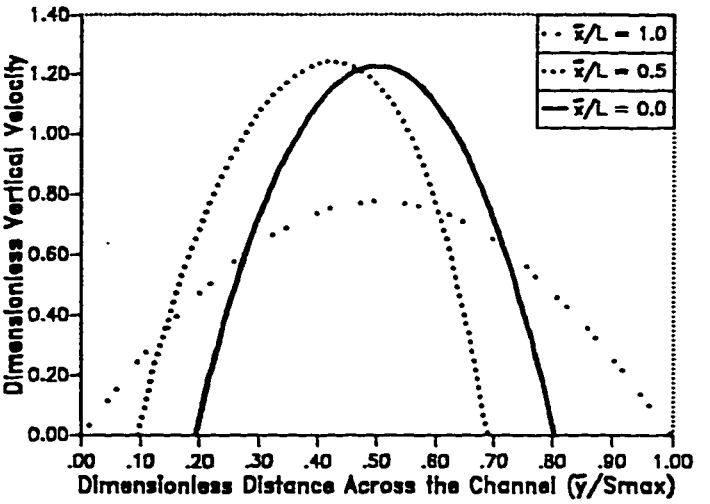

Figure 6.131 Transverse Velocity Distribution at Different Cross-Sections in the Channel for Ra = 29 .

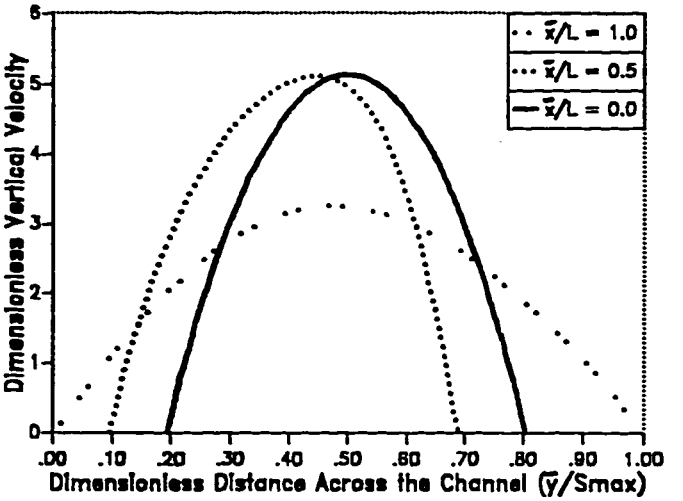

Figure 6.132 Transverse Velocity Distribution at Different Cross-Sections in the Channel for Ra = 143 .

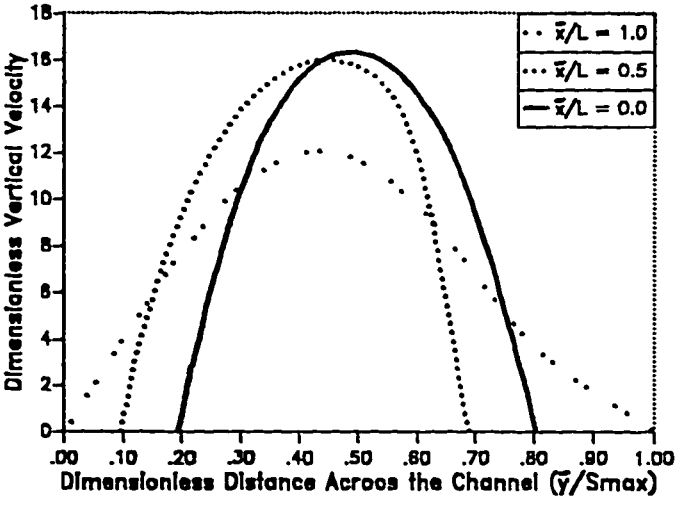

Figure 6.133 Transverse Velocity Distribution at Different Cross-Sections in the Channel for Ra = 491 .

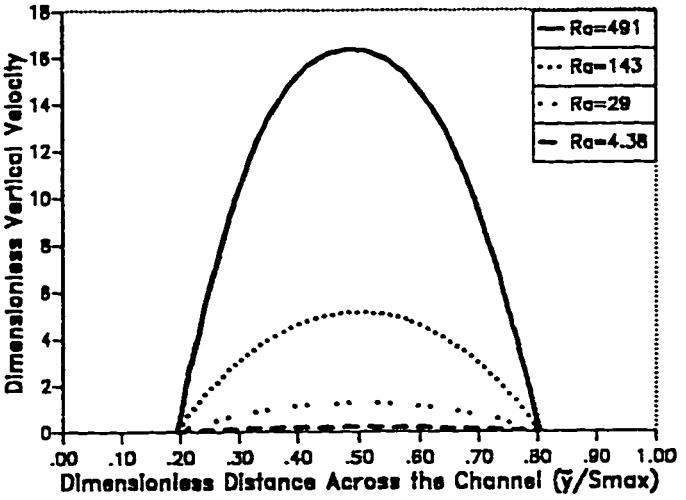

Figure 6.134 Transverse Velocity Distribution at the Entrance of the Channel for Different Values of Ra.

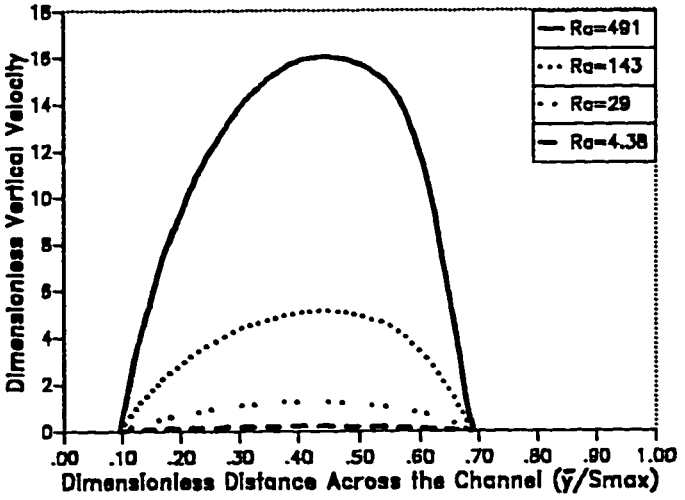

Figure 6.135 Transverse Velocity Distribution at the Middle Hight of the Channel for Different Values of Ra.

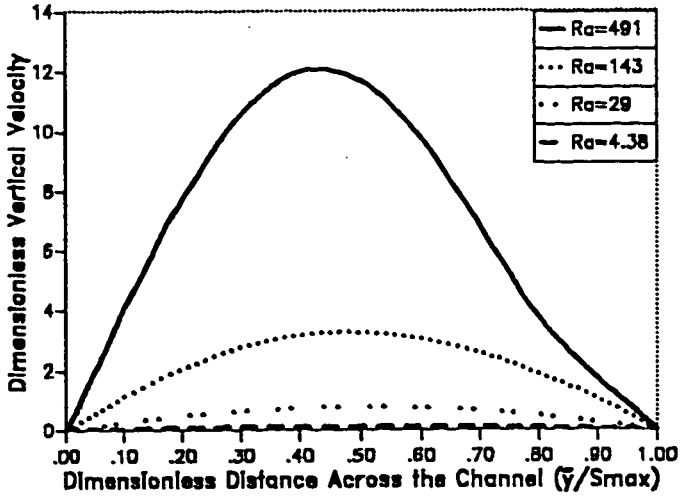

Figure 6.136 Transverse Velocity Distribution at the Exit of the Channel for Different Values of Ra.

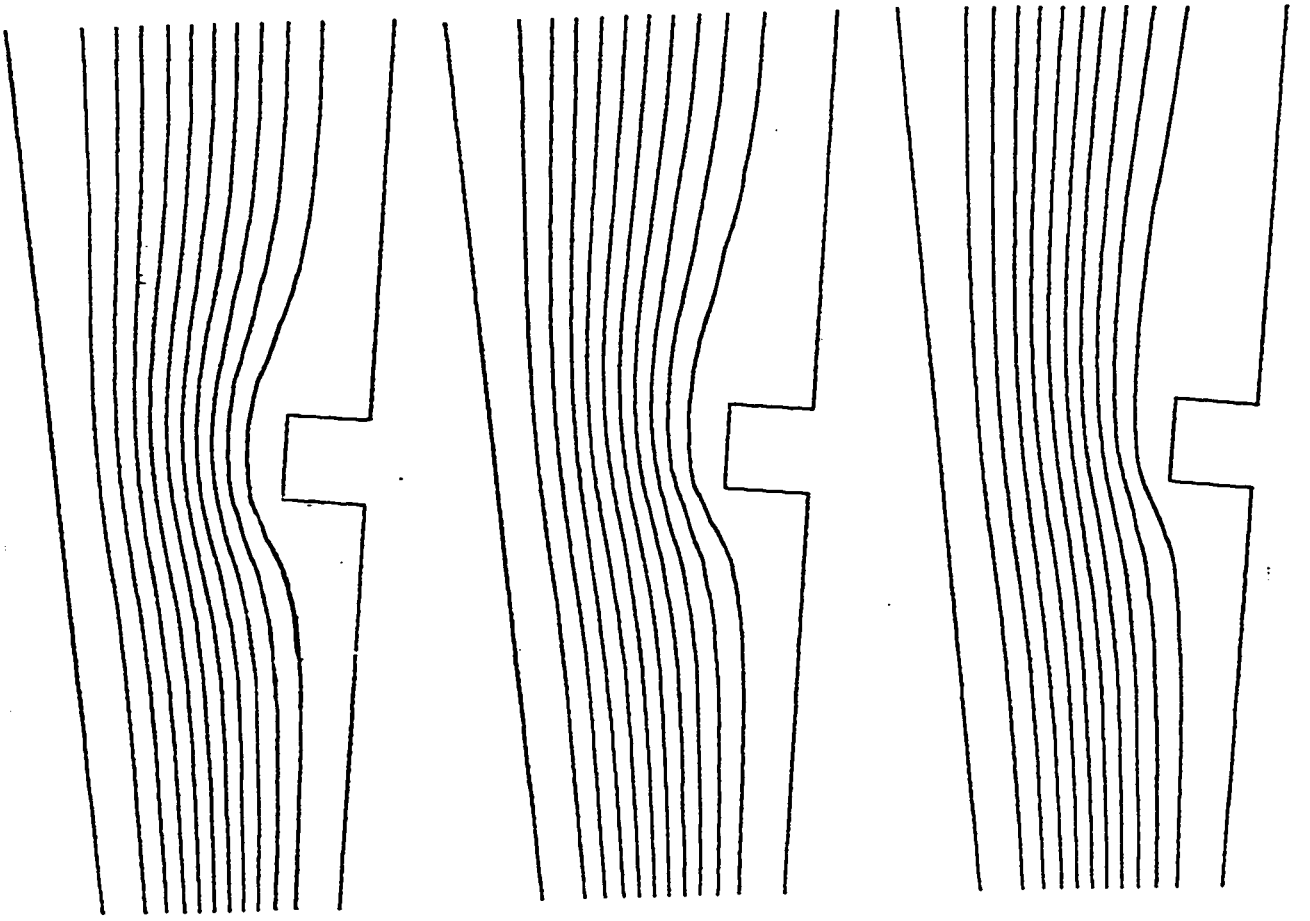

(a) Ra = 29 (b) Ra = 143 (c) Ra = 491

Figure 6.137 Computed Streamlines for AR = 0.2727, Pr = 0.72, Divergent (γ = 5), L_1 = 0.5 , L_2 = 0.0945 .

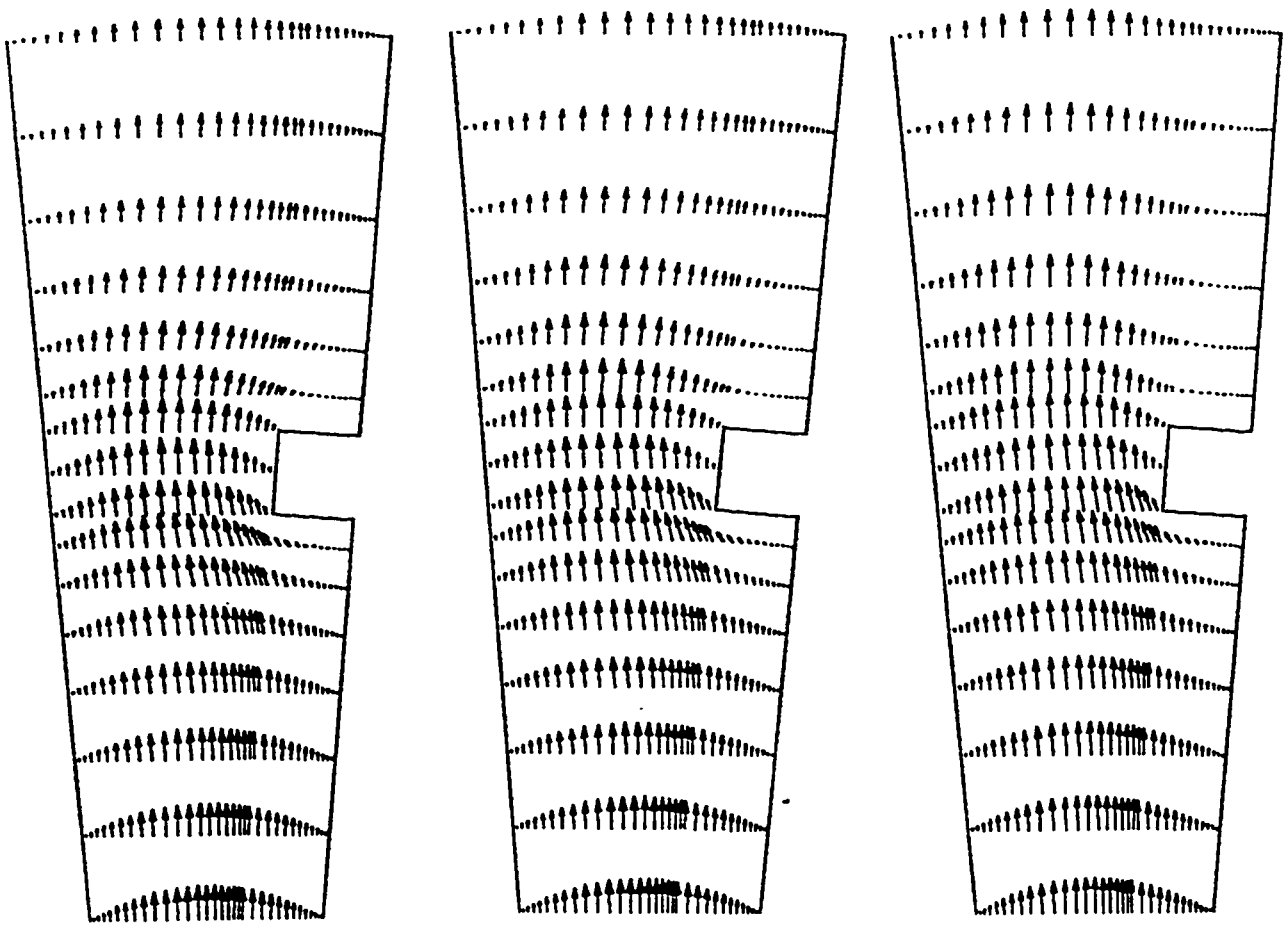

(a) Ra = 29 (b) Ra = 143 (c) Ra = 491

Figure 6.138 Computed Velocity Vectors for AR = 0.2727, Pr = 0.72, Divergent (γ = 5), L_2 = 0.0945 , L_1 = 0.5 .

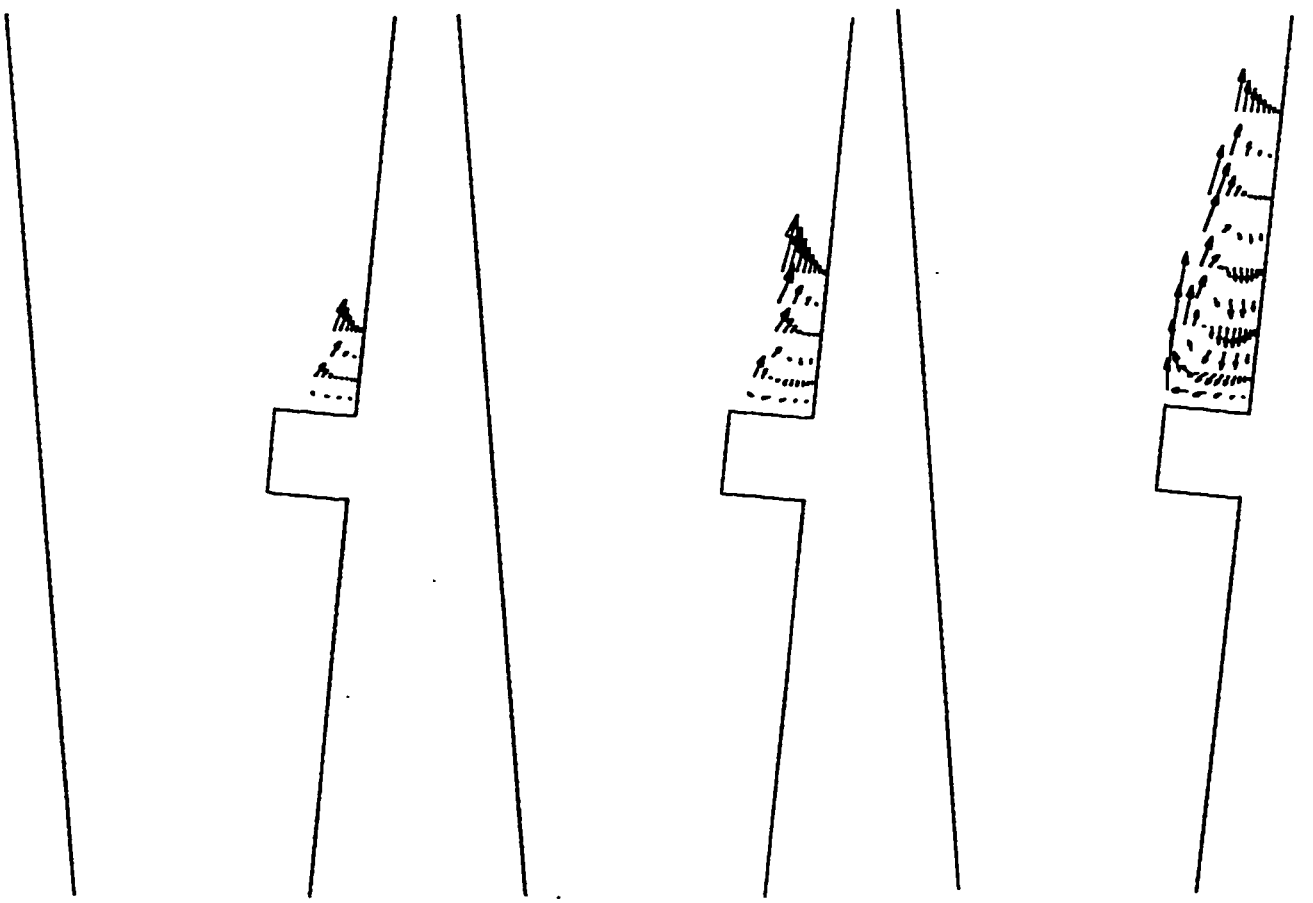

(a) Ra = 29 (b) Ra = 143 (c) Ra = 491

Figure 6.139 Computed Velocity Vectors (Enlarged) for AR = 0.2727, Pr = 0.72, Divergent (γ = 5), L_2 = 0.0945, L_1 = 0.5 .

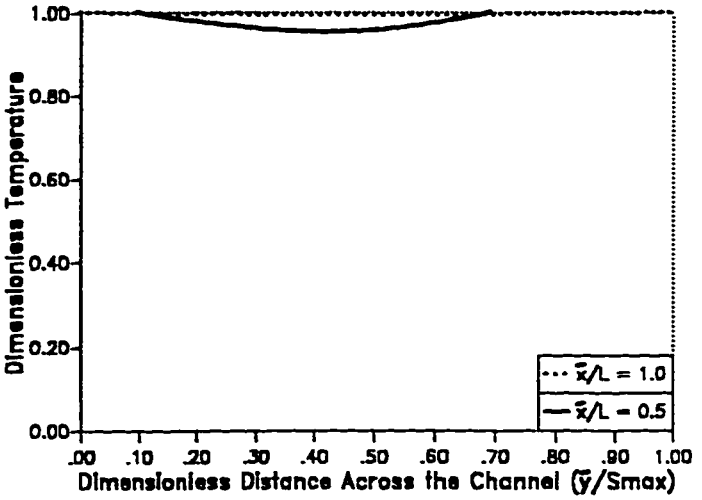

Figure 6.140 Transverse Temperature Distribution at Different Cross-Sections in the Channel for Ra = 29 .

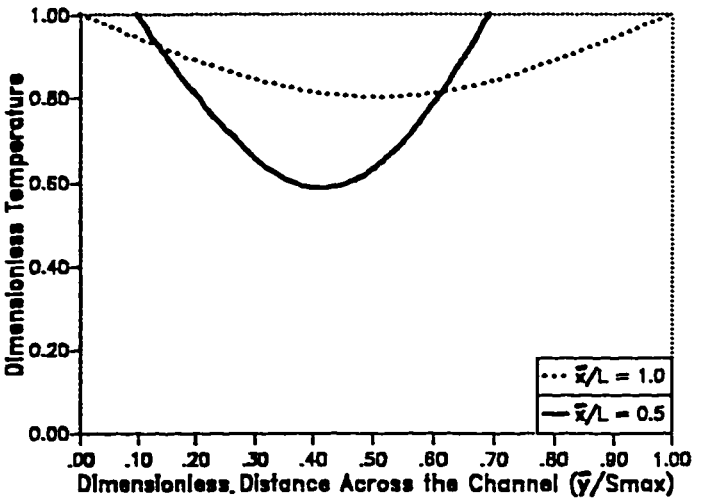

Figure 6.141 Transverse Temperature Distribution at Different Cross-Sections in the Channel for Ra = 143 .

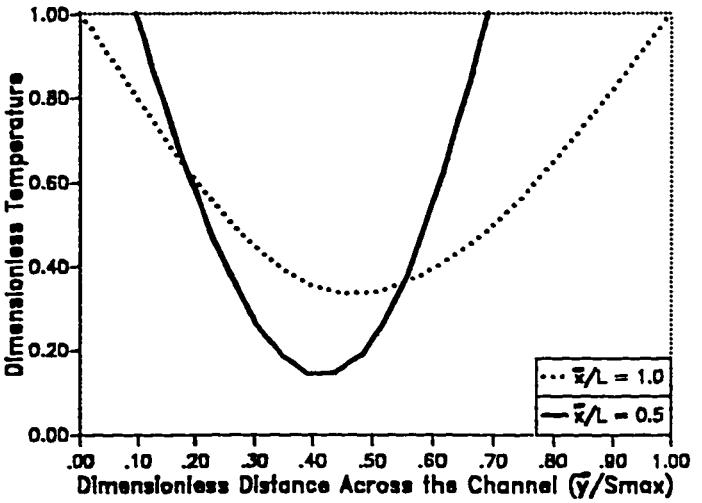

Figure 6.142 Transverse Temperature Distribution at Different Cross-Sections in the Channel for Ra = 491 .

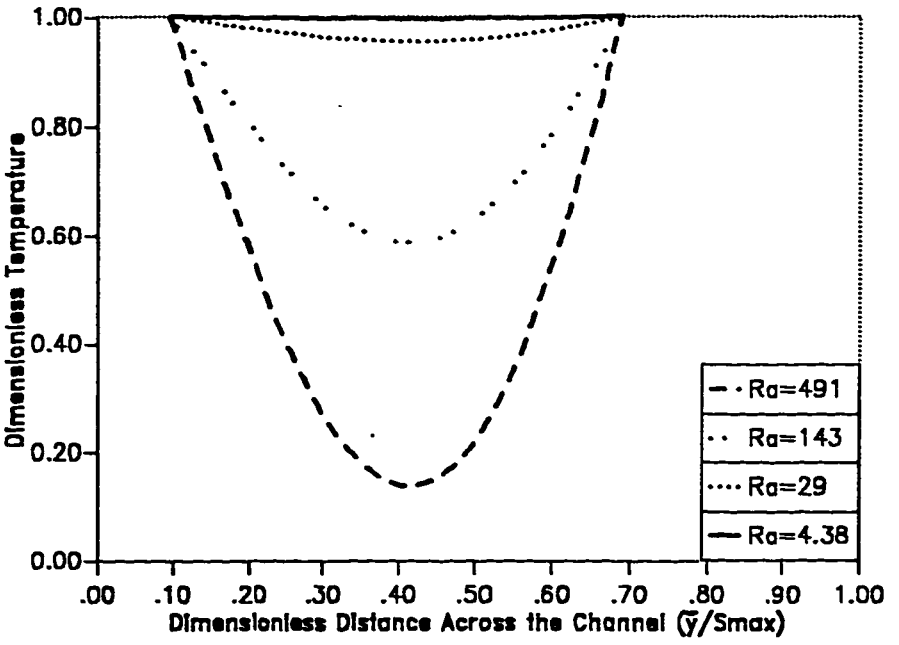

Figure 6.143 Transverse Temperature Distribution at the Middle Hight of the Channel ferent Values of Ra.

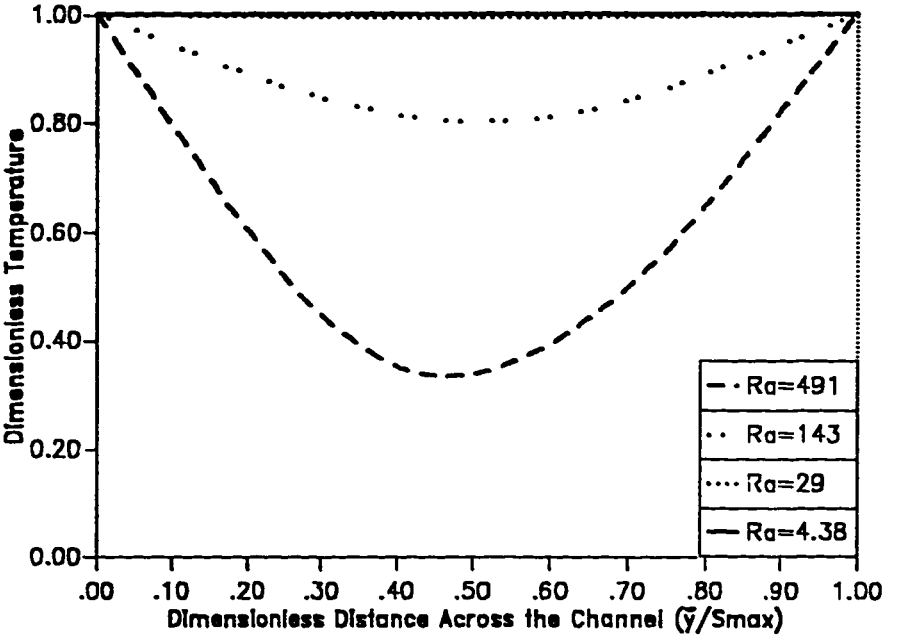

Figure 6.144 Transverse Temperature Distribution at the Exit of the Channel for Different Values of Ra.

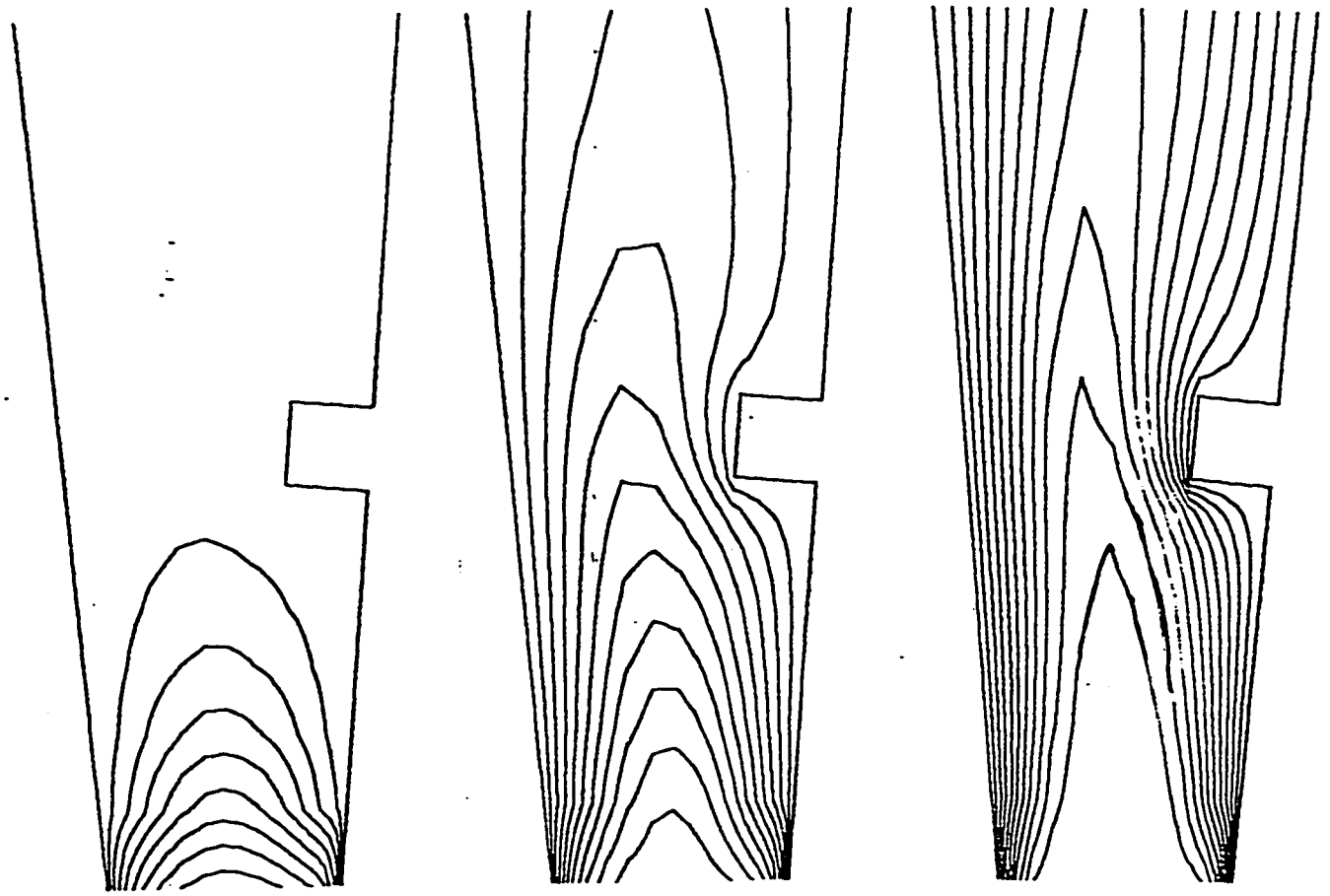

(a) Ra = 29 (b) Ra = 143 (c) Ra = 491

Figure 6.145 Computed Isotherms for AR = 0.2727, Pr = 0.72, Divergent (γ = 5), L_1 = 0.5 , L_2 = 0.0945 .

6.6.2.2 Divergent Channel , $\gamma = 10^{\circ}$

The effect of the divergence angle $\gamma = 10^{\circ}$ on the flow field and heat transfer and heat transfer characteristics on divergent obstructed vertical channel will be presented here. The study was carried out for two values of $AR_{S_{ent}}$, namely, $AR_{S_{ent}} = 0.2727$ and 0.3636 for the range of $Ra_{S_{ent}}$ from 1.0 to 70 . For the same reasons mentioned in the previous sections, it was not possible to obtain numerical solution for the divergent channel ($\gamma = 10$) at Rayliegh numbers higher than 70. The discussion of the results will be presented only for the case of $AR_{S_{ent}} = 0.2727$ due to the similar trend observed between the results of the two aspect ratios. The curves of the average Nusselt number and the dimensionless mass flow rate will be shown for both aspect ratios.

The computed maximum dimensionless velocities, the dimensionless mass flow rates and the average Nusselt numbers ($\overline{Nu}_{S_{ent}}$) for four different values of $Ra_{S_{ent}}$ are shown in TABLE (6-8). Figures (6.146 and 6.147) show the plot of the dimensionless mass flow rates (Q) and the average Nusselt numbers ($\overline{Nu}_{S_{ent}}$) versus the $Ra_{S_{ent}}$ for both aspect ratios. It can be noted that as the $Ra_{S_{ent}}$ increases both Q and $\overline{Nu}_{S_{ent}}$ increase for each aspect ratio. Also it can be noted that as the aspect ratio increases Q and $\overline{Nu}_{S_{ent}}$ increase. The effect of the aspect ratio decreases as the Rayliegh increases.

Similar to the previous discussions, the hydrodynamic results will be prsented in four different forms. The first form is the plot of dimensionless vertical velocity versus the channel's dimensionless width ($\bar{y}/S_{max}$) at different hights in the channel ($\bar{x}$ /L) for a specific value for some representative Rayliegh numbers as shown in figures (6.148 to 6.150). These figures show the dimensionless velocity profile at the entrance of the channel ($\bar{x}$ /L=0.0), at the channel mid-plane ($\bar{x}$ /L=0.5) and at the channel exit ($\bar{x}$ /L=1.0). The maximum dimensionless velocity decreases as $\bar{x}$ /L increases for the three cross-sections due to the increase in the cross-sectional area.

The second form of the hydrodynamic results is the plot of the dimensionless vertical velocity versus the dimensionless channel's width ($\bar{y}/S_{max}$) at a given cross-section in the channel for different values of Ryliegh numbers. Figure (6.151) shows the plot of the dimensionless vertical velocities at the entrance of the channel ($\bar{x}$ /L=0.0) for different Rayliegh numbers. Figure (6.152) shows the same plot at the mid-plane of the channel ($\bar{x}$ /L=0.5) while the plot of the dimensionless vertical velocities at the exit of the channel is shown in figure (6.153). It can be shown, that the dimensionless mass flow rates (the area under the dimensionless vertical velocity curve) increase as the Rayliegh number increases.

The third form of the hydrodynamic results is the streamlines plots. The plots of the computed streamlines for two different Rayliegh numbers are shown in figures (6.154-a) and (6.154-b). No circulation zones have been picked up by the streamline plots, although examining the computed values

indicate circulation zones at high Rayliegh number in the region right above and below the obstruction. Therefore, the velocity vector plots have been produced. Hence, the fourth form of the hydrodynamic results is the velocity vector plots as shown in figures (6.155-a) and (6.155-b). The variation of the velocity vectors along the axial direction of the channel can be noted clearly. The magnitude of velocities at the top and the bottom of the obstruction (where circualtion zones are expected) is very small. These velocities have been magnified and plotted again in figures (6.156-a) and (6.156-b). Very small Circulation zones are observed right at the top of the obstruction as shown in figure (6.156-b). Since heat is transfered by reduction only across the circulation zones,the existance of these zones will affect the heat transfer.

The thermal results are presented in four different forms. The first form is the plot of the dimensionless temperature versus the dimensionless distance across the channel ($\bar{y}/S_{max}$) for $Ra_{S_{ent}}$ = 4.38 , 29 and 58 as shown in figures (6.157) through (6.159) respectively. The plots were done at the mid-plane of the channel ($\bar{x}$ /L = 0.5) and at the exit of the channel ($\bar{x}$ /L = 1.0). As expected, the air temperature increases as $\bar{x}$ /L increases (i.e.as it moves along the axial direction of the channel).

The second form of the thermal results is the plot of the dimensionless temperature at a given hight of the channel ($\bar{x}$/L) for different values of $Ra_{S_{ent}}$. Figure (6.160) shows the variation of the dimensionless temperature at the mid-plane of the channel ($\bar{x}$ /L = 0.5) for four different values of Rayliegh number. Figure (6.161) shows the same variation at the exit ($\bar{x}$ /L = 1.0)

of the divergent obstructed channel. As can be seen from these figures, as the Rayliegh number increases, the minimum temperature at these two planes ($\bar{x}/L = 0.5$ and $\bar{x}/L = 1.0$) decreases.

The third form of the thermal results is the isothermal lines. The plots for the computed isotherms are shown in figures (6.162-a) and (6.162-b). At $Ra_{S_{ent}} = 29$ the flow is fully developed which means that a thermal boudary layer has been developed at each wall and they emerge in the region just above the channel entrance. At $Ra_{S_{ent}} = 58$, the flow is in the transition regime as shown by figure (6.162-b). As the Rayliegh number increases, the boundary layer thickness (δ) decreases. This decrease will cause an increase in the dimensionless temperature gradient in the y-direction (i.e. $\frac{d\theta}{dy} \propto \frac{1}{\delta}$). and since the heat transfer rate is directly proportional to the temperature gradient in the y-direction, therefore the average Nusselt number will increase.

The fourth form of the thermal results is the average Nusselt numbers. Similar to the analysis that has been carried out for the convergent obstructed vertical channel, the $\overline{Nu}_{S_{ent}}$ were plotted versus $Ra_{S_{ent}}$ for both parallel and divergent channels. These plots are shown in figures (6.163 and 6.164) for both aspect ratios. It can be noted that as the angle of divergence γ increases the $\overline{Nu}_{S_{ent}}$ increases. All the previous computations of the average Nusselt number and Rayliegh number for the divergent channel were based on S_{ent}. An attempt is made to change the base of the parameters and see if this will

collapse the average Nusselt number curves (for $\gamma = 0°$, $\gamma = 5°$ and $\gamma = 10°$) into one curve. Hence, the average Nusselt numbers and the Rayliegh numbers have also been computed based on S_{exit} and S_{avg}. S_{exit} is the distance between the walls at the exit of the channel while S_{avg} is the average value of S_{ent} and S_{exit} respectively. This has been done to find out which one of these parameters will give an average Nusselt number curve which is close to the parallel walled average Nusselt number curve. These plots are shown in figures (6.163 to 6.168). It can be noted from these figures that non of these figures will give an average Nusselt number curve for the divergent obstructed vertical channel which is close to the one of the parallel-walled channel. Another point that should be pointed out that basing the average Nusselt number on S_{exit} or S_{avg} will give average Nusselt number values lower than those ones for the parallel-walled channel for $Ra \approx 10^2$.

TABLE(6-8) COMPUTED Umax,Q and $\overline{Nu}$ FOR DIVERGENT OBSTRUCTED CHANNEL WITH AR = 0.2727, $L_1 = 0.50$, $L_2 = 0.0945$ and $\gamma = 10^{\circ}$.

Ra	Umax	Q	$\overline{Nu}$
4.38	0.2904	0.0848	0.0379
8.76	0.8246	0.1582	0.1092
14.60	1.7391	0.3812	0.2381
29.00	2.0579	0.5927	0.5396
43.50	3.2901	0.9183	0.8027
58.00	4.7639	1.2545	1.0445

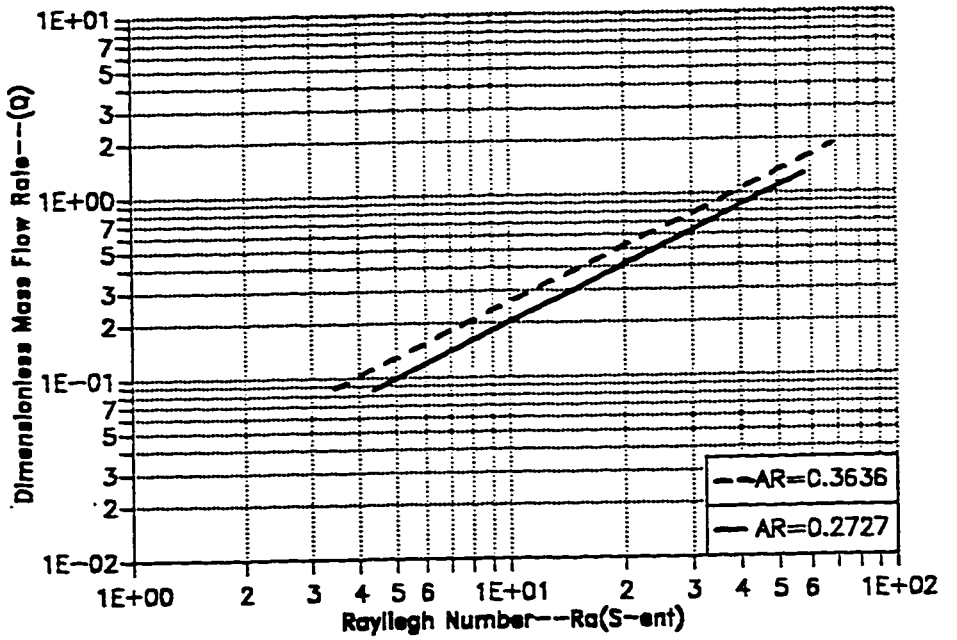

Figure 6.146The Variation of Dimensionless Mass Flow Rate (Q) Versus the Rayliegh Number ($Ra_{S_{ent}}$) for the Divergent Obstructed Channel (γ = 10).

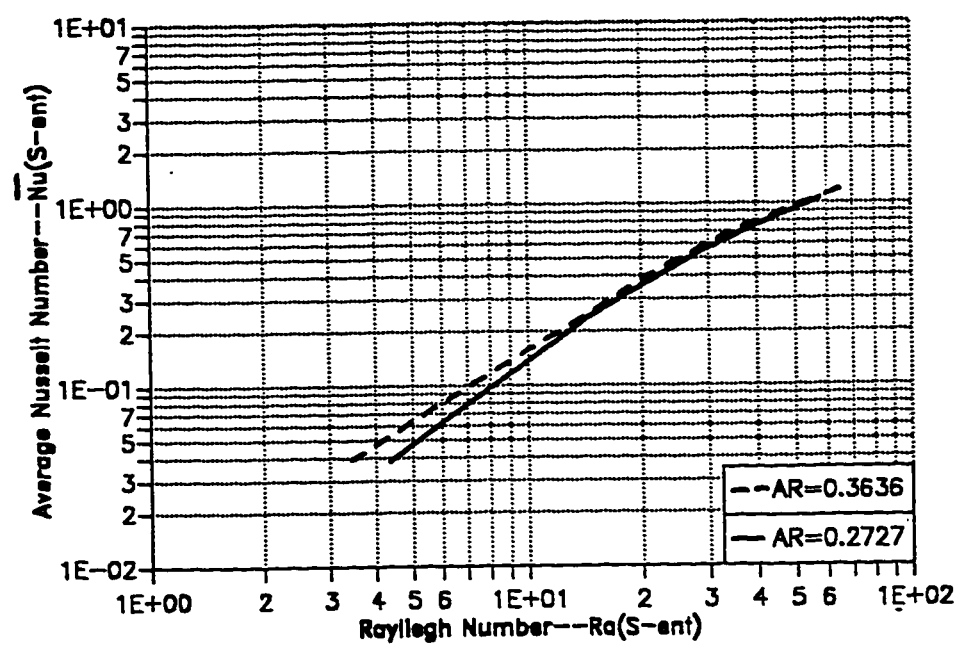

Figure 6.147The Variation of Average Nusselt Number ($\overline{Nu}_{S_{ent}}$) Versus the Rayliegh Number ($Ra_{S_{ent}}$) for the Divergent Obtructed Channel (γ = 10).

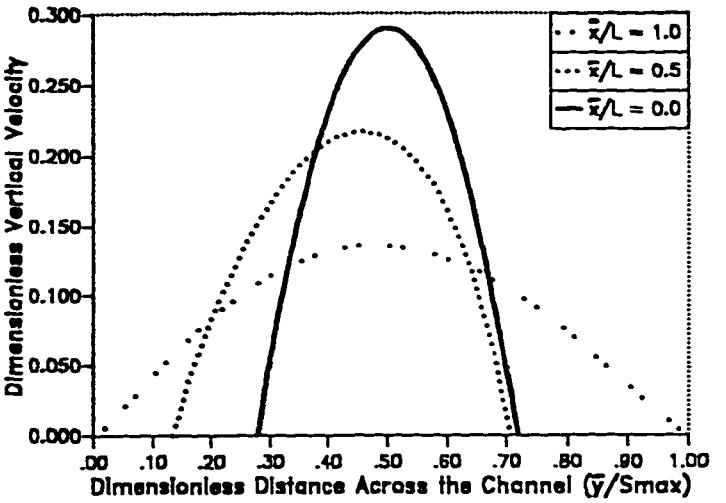

Figure 6.148 Transverse Velocity Distribution of the Divergent Channel (γ = 10) for Ra = 4.38 .

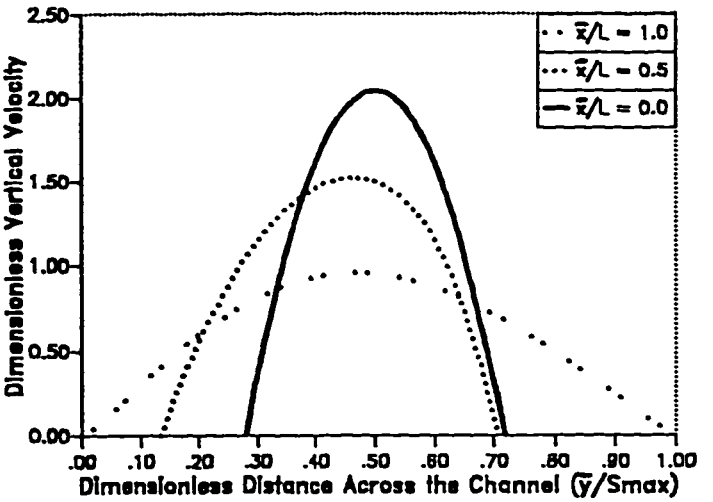

Figure 6.149 Transverse Velocity Distribution of theDivergent Channel (γ = 10) for Ra = 29 .

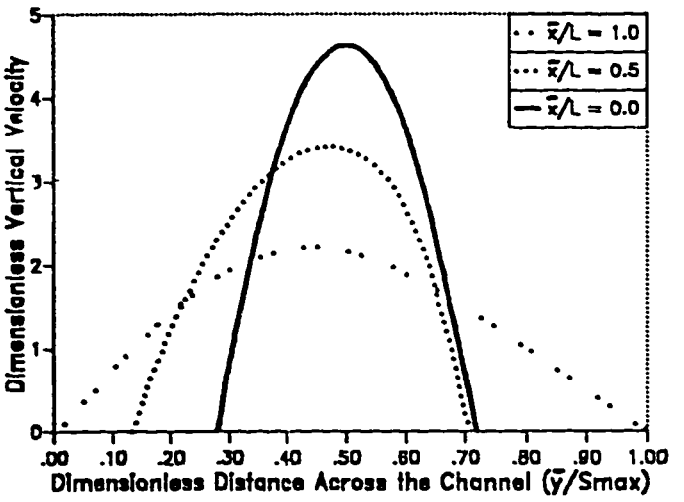

Figure 6.150 Transverse Velocity Distribution of the Divergent Channel (γ = 10) for Ra = 58 .

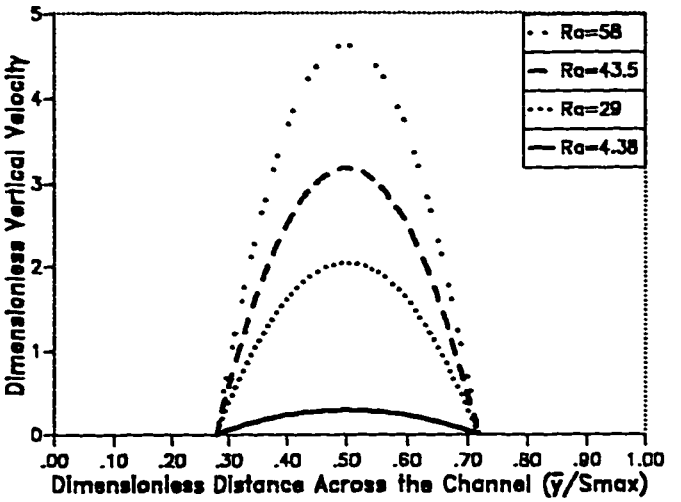

Figure 6.151 Transverse Velocity Distribution at the Entrance of the Divergent Channel (γ = 10) for Different Values of Ra .

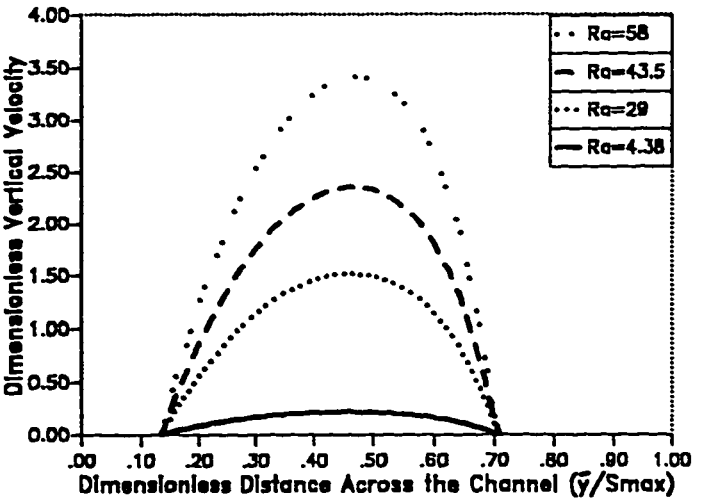

Figure 6.152 Transverse Velocity Distribution at the Middle High of The Divergent Channel (γ = 10) forDifferent Values of Ra .

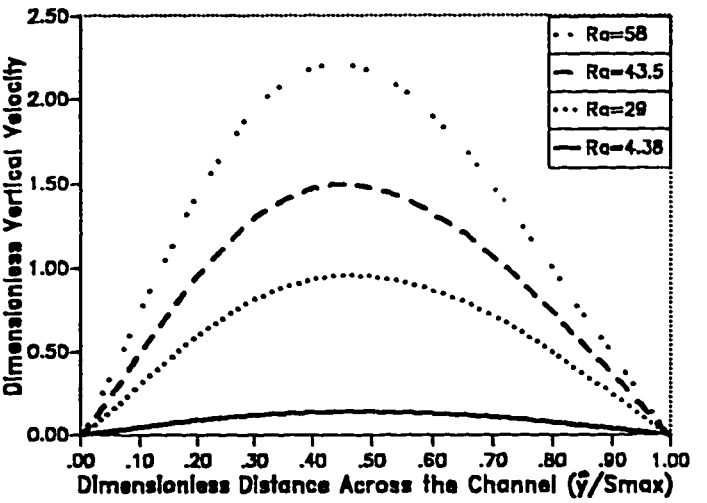

Figure 6.153 Transverse Velocity Distribution at the Exit of the Divergent Channel (γ = 10) for Different Values of Ra .

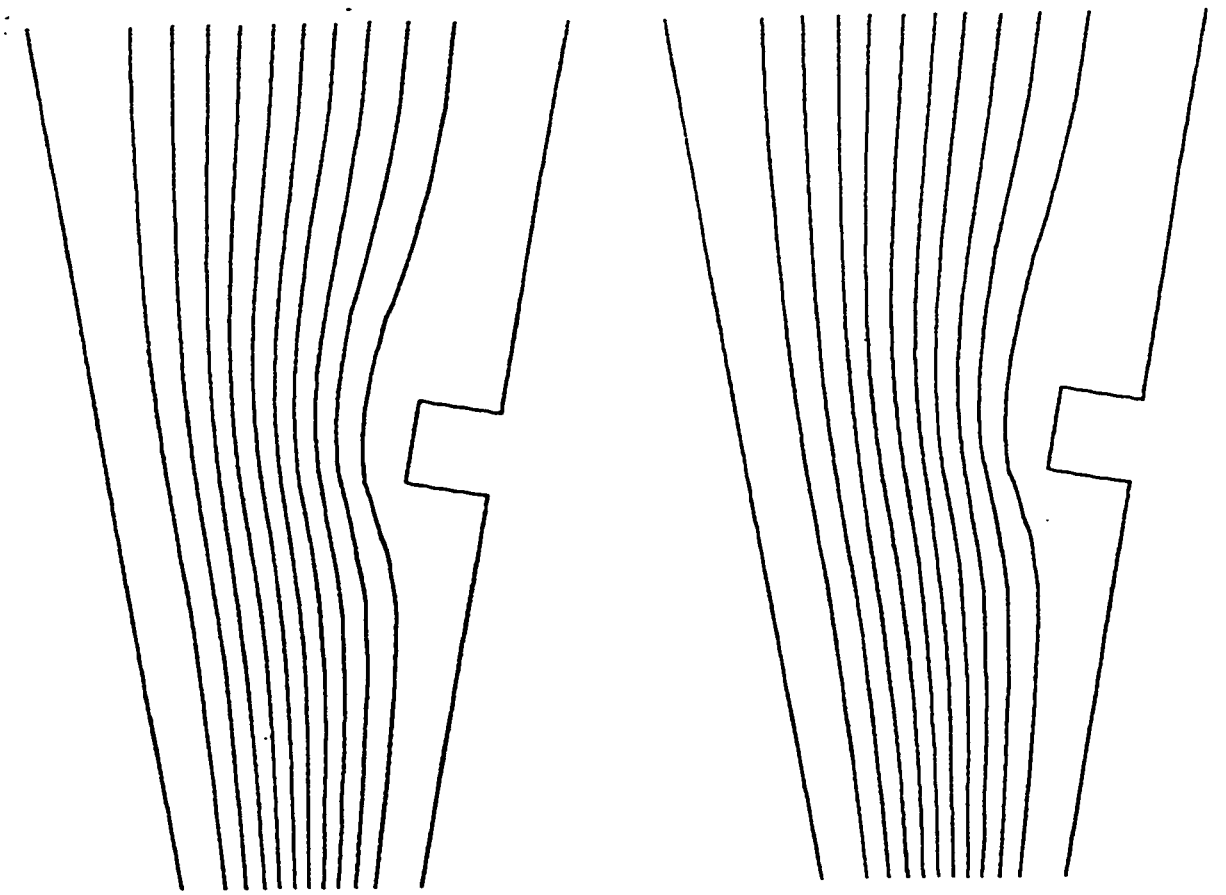

(a) Ra = 29 (b) Ra = 58

Figure 6.154 Computed Streamlines for AR = 0.2727, Pr = 0.72, Divergent (γ = 10), L_1 = 0.5 , L_2 = 0.0945 .

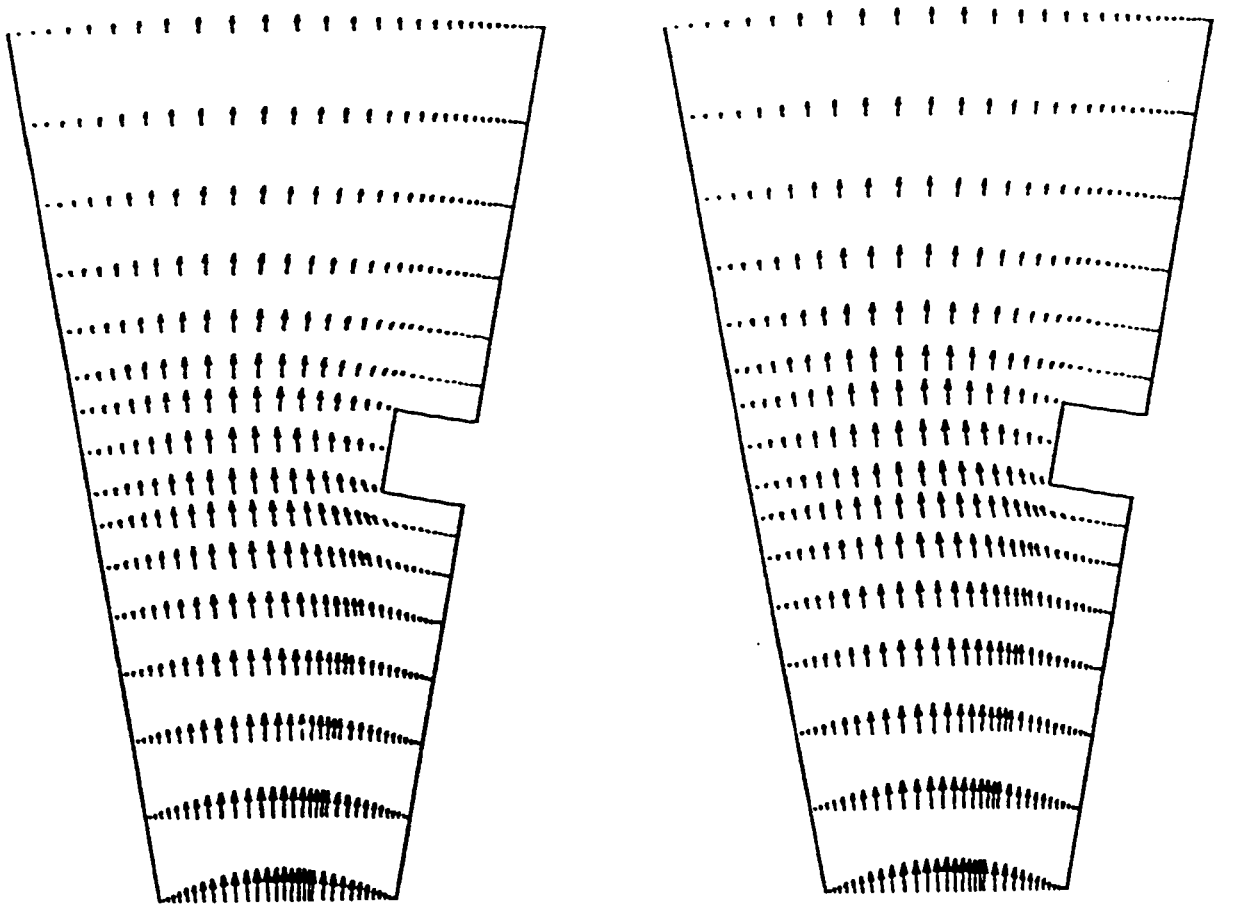

(a) Ra = 29 (b) Ra = 58

Figure 6.155 Computed Velocity Vectors for AR = 0.2727, Pr = 0.72, Divergent (γ = 10), L_1 = 0.5 , L_2 = 0.0945 .

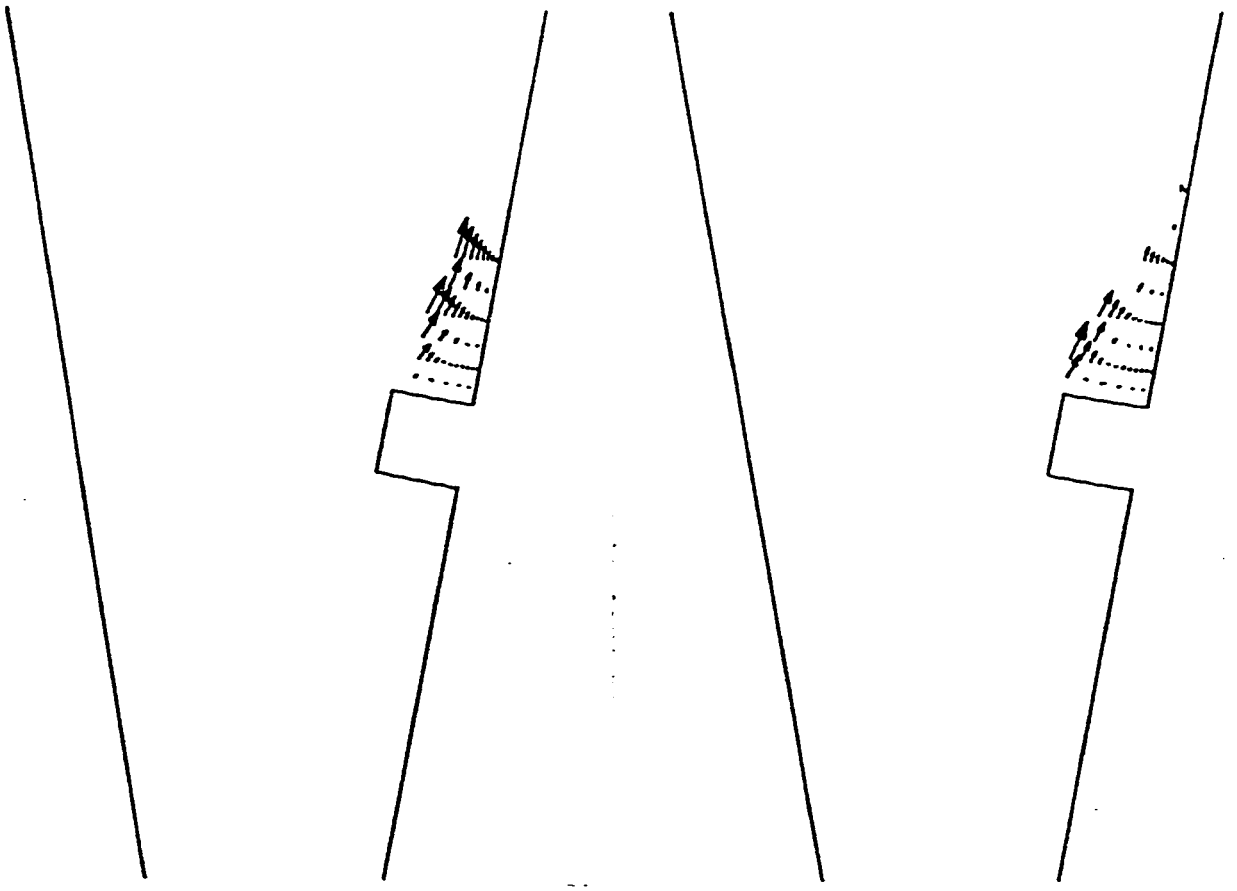

(a) Ra = 29 (b) Ra = 58

Figure 6.156 Computed Velocity Vectors (Enlarged) for AR = 0.2727, Pr = 0.72, Divergent (γ = 10), L_1 = 0.5 , L_2 = 0.0945 .

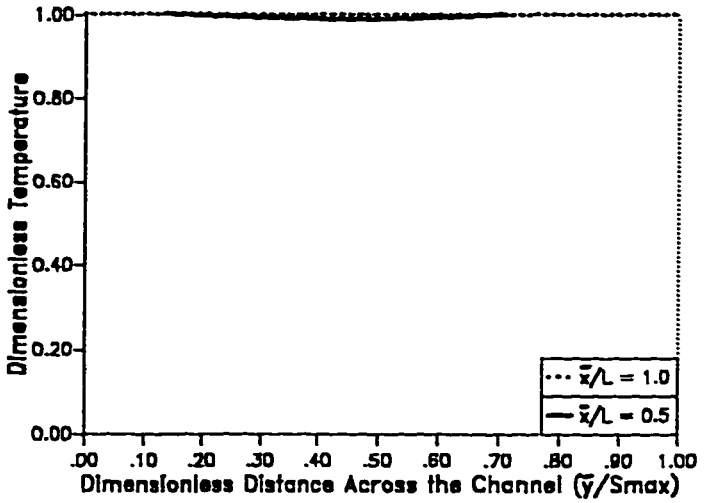

Figure 6.157 Transverse Temperature Distribution of the Divergent Channel (γ = 10) for Ra = 4.38 .

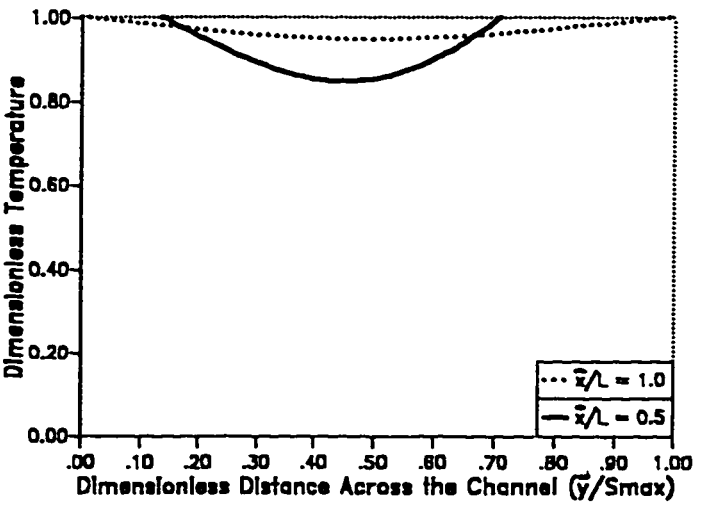

Figure 6.158 Transverse Temperature Distribution of theDivergent Channel (γ = 10) forRa = 29 .

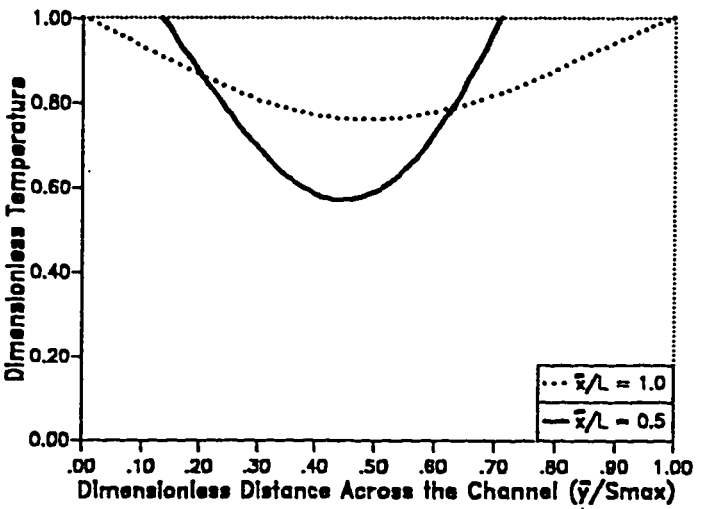

Figure 6.159 Transverse Temperature Distribution of the Divergent Channel (γ = 10) for Ra = 58 .

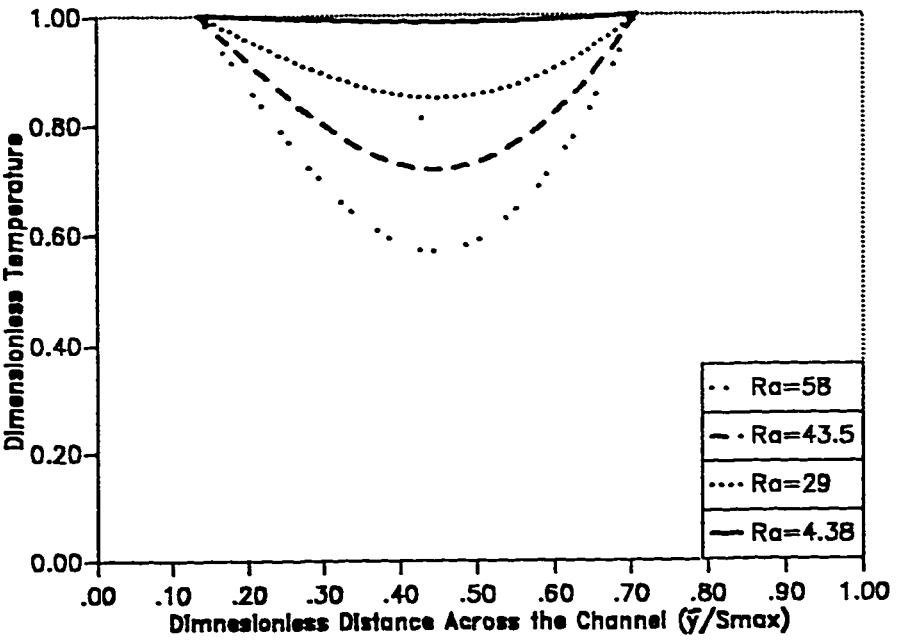

Figure 6.160 Transverse Temperature Distribution at the Middle High of The Channel for Different Values of Ra.

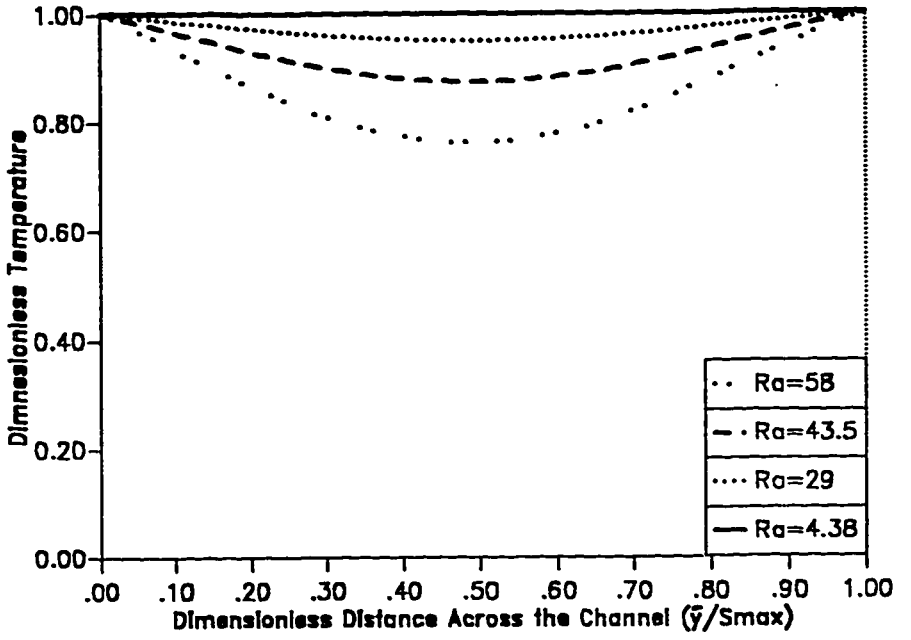

Figure 6.161 Transverse Temperature Distribution at the Exit of the Divergent Channel for Different Values of Ra.

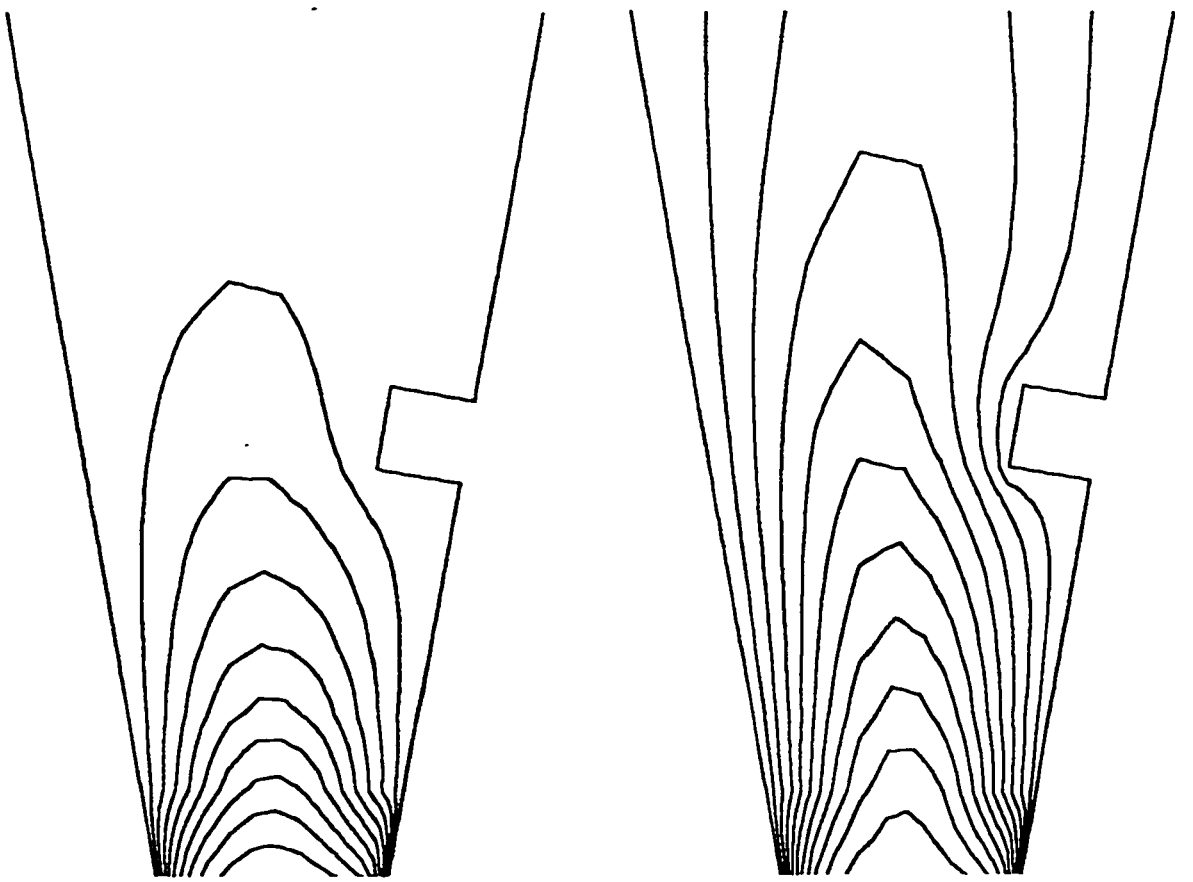

(a) Ra = 29 (b) Ra = 58

Figure 6.162 Computed Isotherms for AR = 0.2727, Pr = 0.72, Divergent (γ = 10). L_2 = 0.0945 , L_1 = 0.5 .

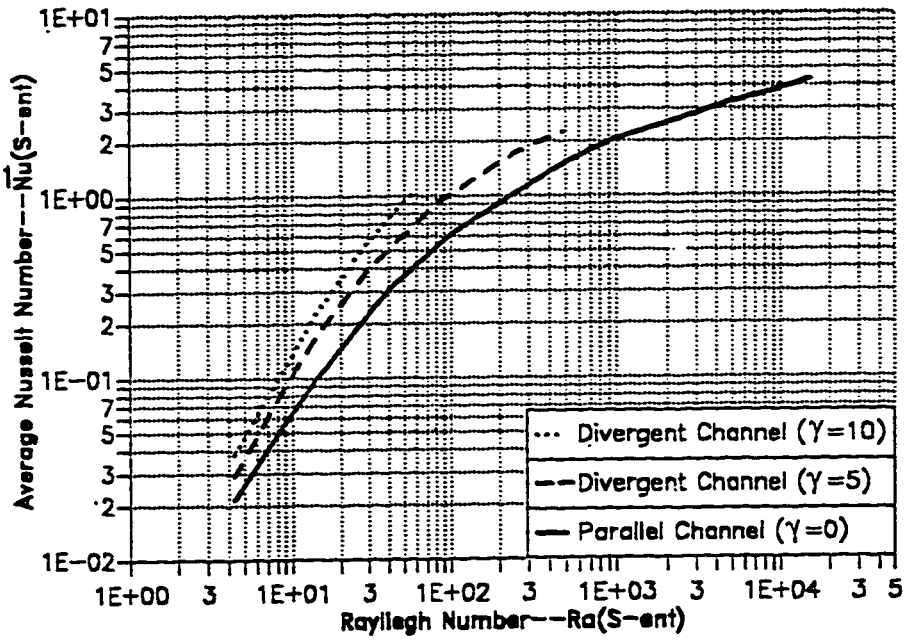

Figure 6.163 The Variation of Average Nusselt Number ($\overline{Nu}_{S_{ent}}$) Versus the Rayliegh Number ($Ra_{S_{ent}}$) for Parallel and Divergent Obstructed Channels with $AR_{S_{ent}} = 0.2727$.

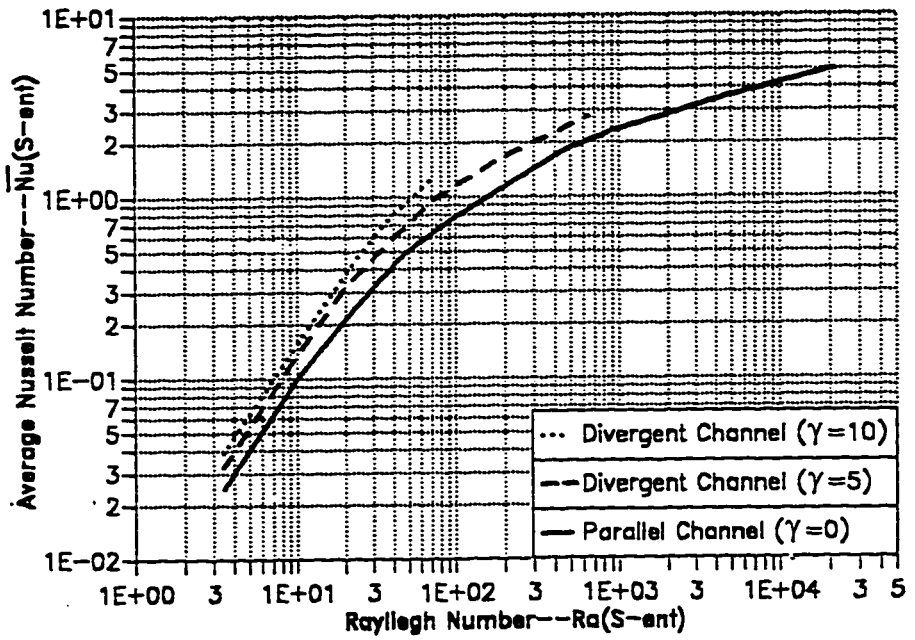

Figure 6.164 The Variation of Average Nusselt Number ($\overline{Nu}_{S_{ent}}$) Versus the Rayliegh Number ($Ra_{S_{ent}}$) for Parallel and Divergent Obstructed Channels with $AR_{S_{ent}} = 0.3636$.

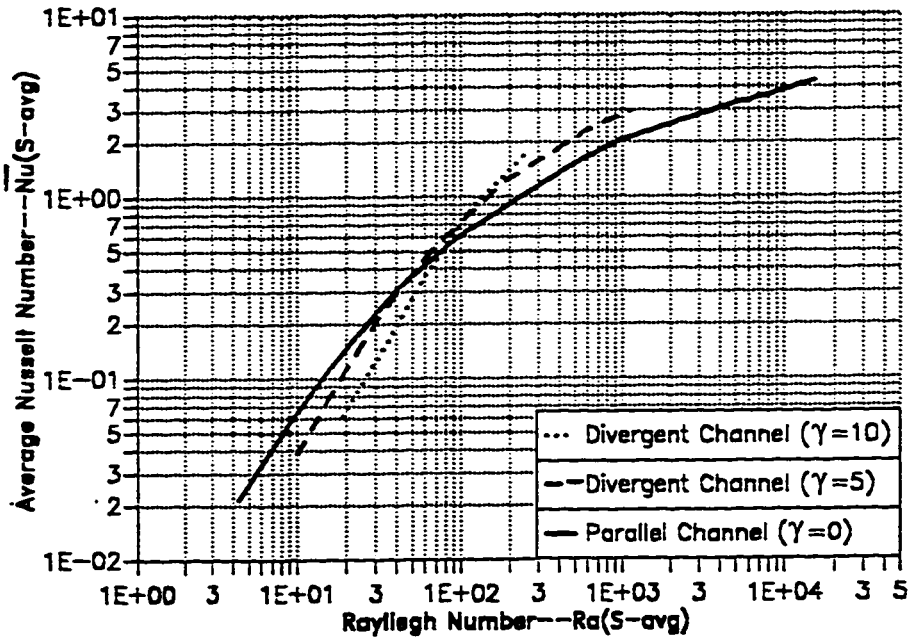

Figure 6.165 The Variation of Average Nusselt Number ($\overline{Nu}_{S_{avg}}$) Versus the Rayliegh Number ($Ra_{S_{avg}}$) for Parallel and Divergent Obstructed Channels with $AR_{S_{ent}} = 0.2727$.

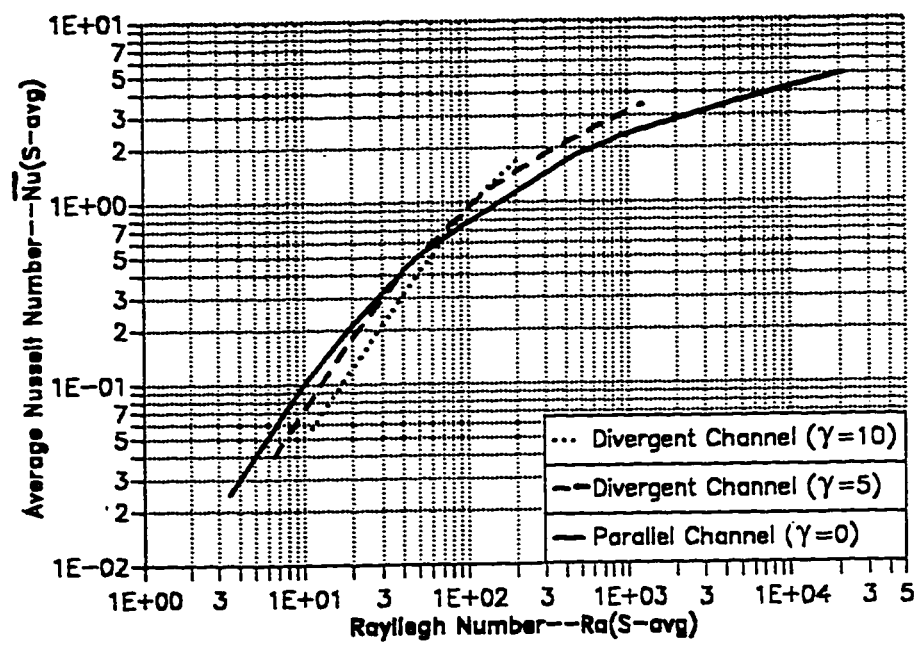

Figure 6.166 The Variation of Average Nusselt Number ($\overline{Nu}_{S_{avg}}$) Versus the Rayliegh Number ($Ra_{S_{avg}}$) for Parallel and Divergent Obstructed Channels with $AR_{S_{ent}} = 0.3636$.

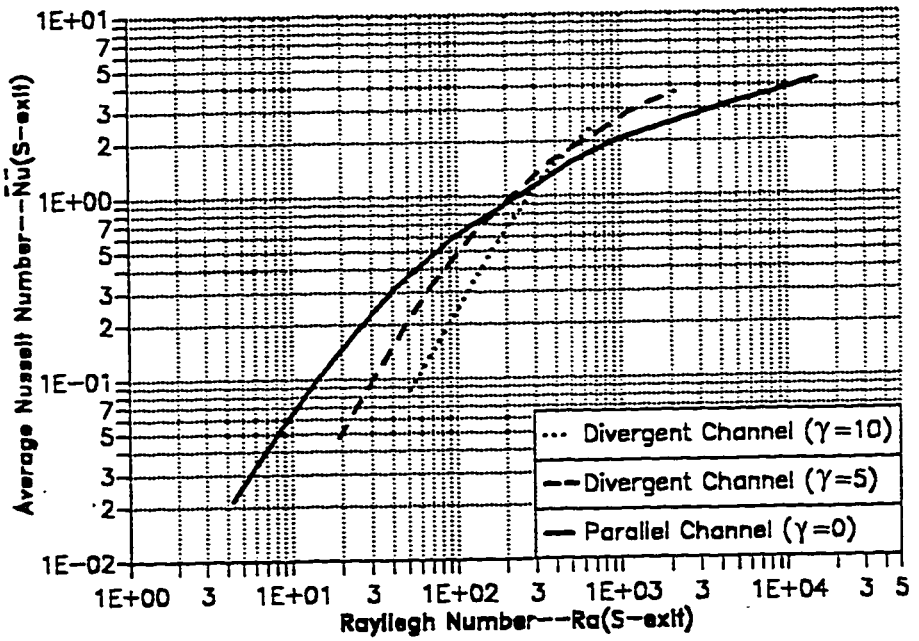

Figure 6.167 The Variation of Average Nusselt Number ($\overline{Nu}_{S_{exit}}$) Versus the Rayliegh Number ($Ra_{S_{exit}}$) for Parallel and Divergent Obstructed Channels with $AR_{S_{ent}} = 0.2727$.

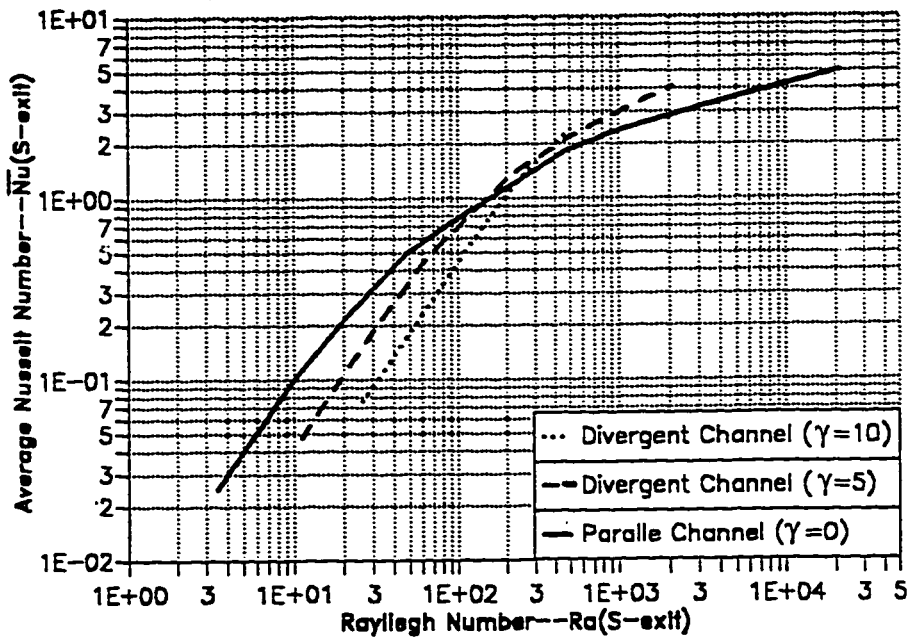

Figure 6.168 The Variation of Average Nusselt Number ($\overline{Nu}_{S_{exit}}$) Versus the Rayliegh Number ($Ra_{S_{exit}}$) for Parallel and Divergent Obstructed Channels with $AR_{S_{ent}} = 0.3636$.

6.7 Comparison Between Convergent, Divergent and Parallel-Walled Obstructed Vertical Channels

The effect of the convergence and divergence angles on the average Nusselt number have been studied for obstructed vertical channels. A comparison for the average Nusselt numbers and the dimensionless mass flow rates between parallel-walled, convergent and divergent channels has been performed. The aspect ratio, the average Nusselt number and the Rayliegh number were based on S_{min} where S_{min} is the smallest cross-sectional area at either the exit or at the entrance of the vertical channel. Therefore, $S_{min} = S_{exit}$ for the convergent obstructed vertical channels, $S_{min} = S_{ent}$ for the divergent obstructed vertical channels and finally $S_{min} = S_{exit} = S_{ent}$ for the parallel-walled obstructed vertical channel. Hence, figure (6.169) shows the variation of the $\overline{Nu}_{S_{min}}$ versus $Ra_{S_{min}}$ for $AR_{S_{min}} = 0.2727$, where figure (6.170) shows the variation of the dimensionless mass flow rate versus the $Ra_{S_{min}}$ for the same aspect ratio. Similarly, figure (6.171) shows the variation of the $\overline{Nu}_{S_{min}}$ versus $Ra_{S_{min}}$ for $AR_{S_{min}} = 0.3636$, where figure (6.172) shows the variation of the dimensionless mass flow rate versus the $Ra_{S_{min}}$ for the same aspect ratio. Each of these figures encountered the five tested cases of the angle (γ).

From figure (6.169), the $\overline{Nu}_{S_{min}}$ of the convergent obstructed vertical channels are larger than those of divergent and parallel-walled obstructed vertical channels for very low Rayliegh numbers ($Ra_{S_{min}} < 15$). The average Nusselt numbers for the parallel-walled obstructed vertical channel case were

the lowest of all the cases for $Ra_{S_{min}} < 700$. It can be noticed from figure (6.169) that for $\gamma = 5°$ the convergent obstructed vertical channel has higher $\overline{Nu}_{S_{min}}$ than that for the divergent obstructed channel for the Rayliegh number range $Ra_{S_{min}} < 550$. Similarly, it can be noticed that for $\gamma = 10°$ the convergent obstructed vertical channel has higher $\overline{Nu}_{S_{min}}$ than that for the divergent obstructed channel for the Rayliegh number range $Ra_{S_{min}} < 30$ only. At $Ra_{S_{min}} = 29$, the angle of convergence $\gamma = 10°$ gives the largest $\overline{Nu}_{S_{min}}$. The second largest value of $\overline{Nu}_{S_{min}}$ is that for the divergence angle $\gamma = 10°$ where the third highest value of $\overline{Nu}_{S_{min}}$ at $Ra_{S_{min}} = 29$ is that for the divergence angle $\gamma = 5°$. As shown in figure (6.169), the fourth highest value of $\overline{Nu}_{S_{min}}$ at $Ra_{S_{min}} = 29$ is that for the convergence angle $\gamma = 5°$ and the lowest value of the $\overline{Nu}_{S_{min}}$ is that for $\gamma = 0°$. At $Ra_{S_{min}} = 491$, the largest $\overline{Nu}_{S_{min}}$ is found to be that of the divergence angle $\gamma = 5°$. In this study, the computation of $\overline{Nu}_{S_{min}}$ for the angle of divergence $\gamma = 10°$ could not be obtained with the constraint of the convergence criteria. For $Ra_{S_{ent}} > 850$, the parallel-walled obstructed vertical channel gives the maximum values of $\overline{Nu}_{S_{min}}$. Figure (6.169) shows that the curves of the $\overline{Nu}_{S_{min}}$ of the parallel-walled and the convergent obstructed vertical channels overlap at $Ra_{S_{ent}} \approx 850$. This means that as the angle of convergence increases the $\overline{Nu}_{S_{min}}$ decreases. This means that, eventhough the convergence angles cause a dramatic increase in the $\overline{Nu}_{S_{min}}$ at

low Rayliegh numbers, the effect of the convergence angle on the increase of $\overline{Nu}_{S_{min}}$ decreases as Rayliegh number increases. On the other hand, the effect of the divergence angles on the increase of the $\overline{Nu}_{S_{min}}$ increases as $Ra_{S_{min}}$ increases. For more clarification, a comparison between the isotherms and the velocity vector plots at $Ra_{S_{min}}$ = 29 , 491 and 3451 for $AR_{S_{min}}$ = 2727 for different angles will be carried out.

The isotherms plots for $Ra_{S_{min}}$ = 29 are shown in figure (6.173-a) through (6.173-e). It can be noted that as the divergence angle increases the boundary layer thickness decreases which should increase the $\overline{Nu}_{S_{min}}$ (i.e. the heat transfer rate increases) as shown in figures (6.173-a,c,e). Also, it can be noticed from figure (6.170) that the dimensionless mass flow rate increases as the divergence angle increases which leads to an increase in the heat transfer rate. It should be pointed out that the heat transfer area has not been changed (i.e. walls dimensions) by changimg the divergence angle. The previous disscusion agrees with the average Nusselt number curves shown in figure (6.169). The same disscusion can be said about the convergent obstructed vertical channel and the same results can be obtained. The variation of the velocity vectors plots for $Ra_{S_{min}}$ = 29 for the five different cases are shown in figures (6.174-a) through (6.174-e). Figures (6.175-a) through (6.175-e) show the plots of the isotherms for $Ra_{S_{min}}$ = 491 for $\gamma = 0°$, divergence angle $\gamma = 5°$ and convegence angles $\gamma = 5°$ and 10° respectively. It is shown that the divergent obstructed vertical channel reaches the isolated vertical walls limit faster than the other channels and the boundary layer thickness is the

smallest one which lead to higher rate of heat transfer and average Nusselt number. This agrees also with the curves plotted in figure (6.169). The variation of the velocity vector plots for $Ra_{S_{ent}} = 491$ are shown in figures (6.176-a) through (6.176-d) for the same values of angles. The velocities right at the top of the obstruction have been magnified and shown in figures (6.177-a) through (6.177-d). It is shown that as the angle of convergence decreases the size of the circulation zone increases where the case of divergence angle $\gamma = 10°$ has the largest circulation zone for the different cases. Finally, figures (6.178-a) throught (6.178-c) show the computed isotherms for the parallel walled channel $\gamma = 0°$ and the convergent channels with an angle of convergence of $\gamma = 5°$ and $10°$ respectively. It is shown that the boundary layer thickness (δ) increases as the convergence angle increases. This causes the temperature gradient to decrease which will directly decrease the average Nusselt number. Also, It can be seen from figure (6.170) that the dimensionless mass flow rate decreases as the convergece angle increases at $Ra_{S_{min}} = 3451$. This also decreases the average Nusselt number. This results agrees with the curves shown in figure (6.169). The velocity vector plots for $\gamma = 0°, 5°$ (c) and $10°$ (c) are shown in figures (6.179-a) through (6.179-c) respectively. IT can be noticed that two velocity peaks are observed for $\gamma = 10°$ (c) which means that a boundary layer is in processing to be formed at each wall. The velocities right at the top of the obstruction have been magnified as shown in figures (6.180-a) through (6.180-c). It is shown that as the convergence angle decreases the size of the size os the circulation zone increases.

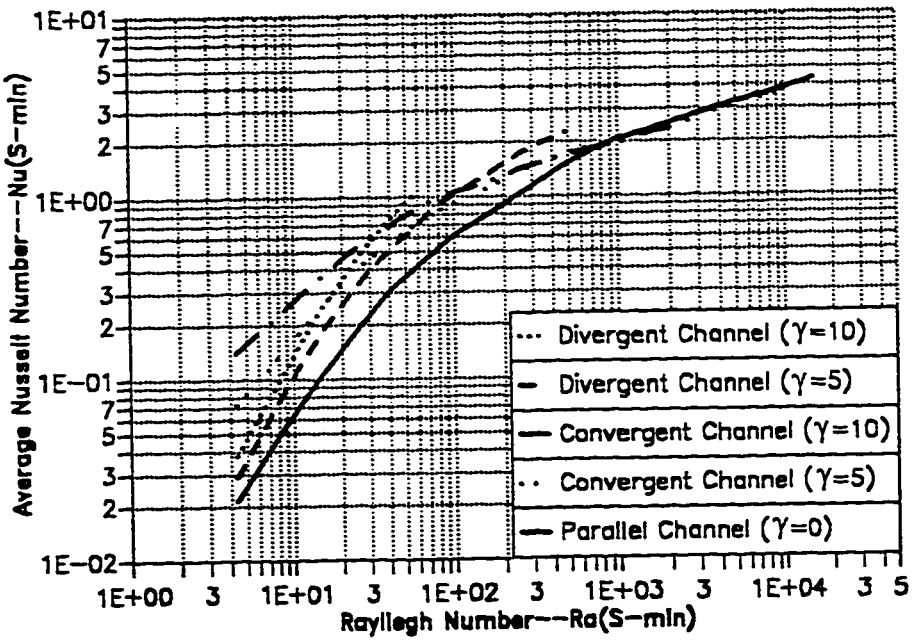

Figure 6.169 The Variation of Average Nusselt Number ($\overline{Nu}_{S_{min}}$) Versus the Rayliegh Number ($Ra_{S_{min}}$) for Obstructed Channels (AR = o.2727).

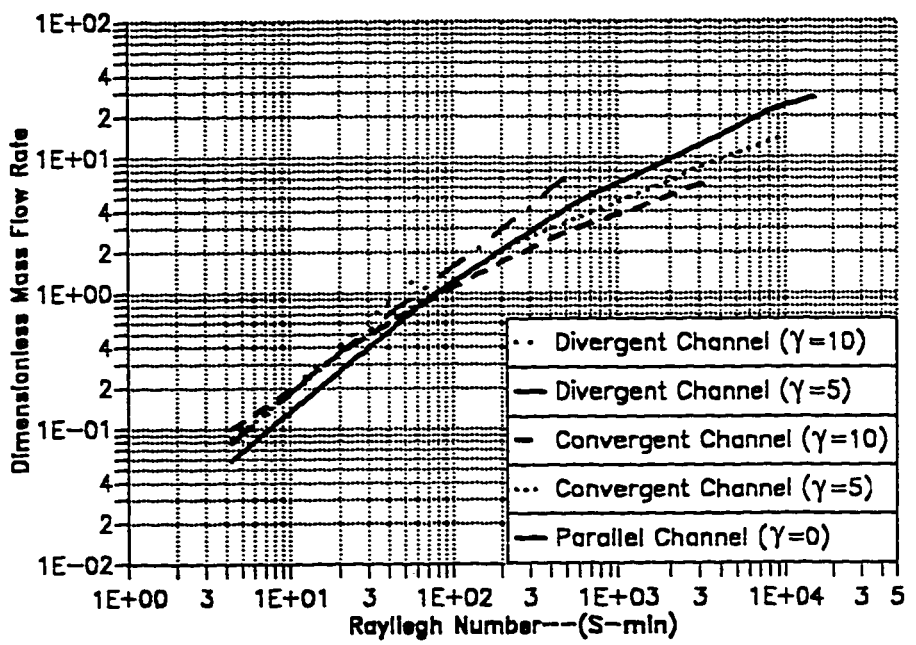

Figure 6.170 The Variation of Dimensionless Mass Flow Rate (Q) Versus the Rayliegh Number ($Ra_{S_{min}}$) for Obstructed Channels (AR = 0.2727).

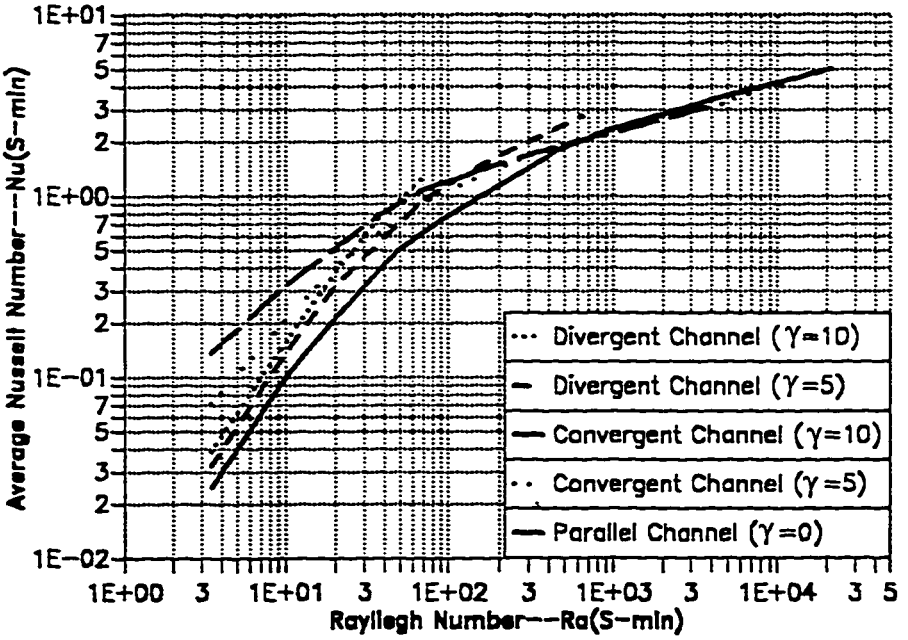

Figure 6.171 The Variation of Average Nusselt Number ($\overline{Nu}_{S_{min}}$) Versus the Rayliegh Number ($Ra_{S_{min}}$) for Obstructed Channels (AR = o.3636).

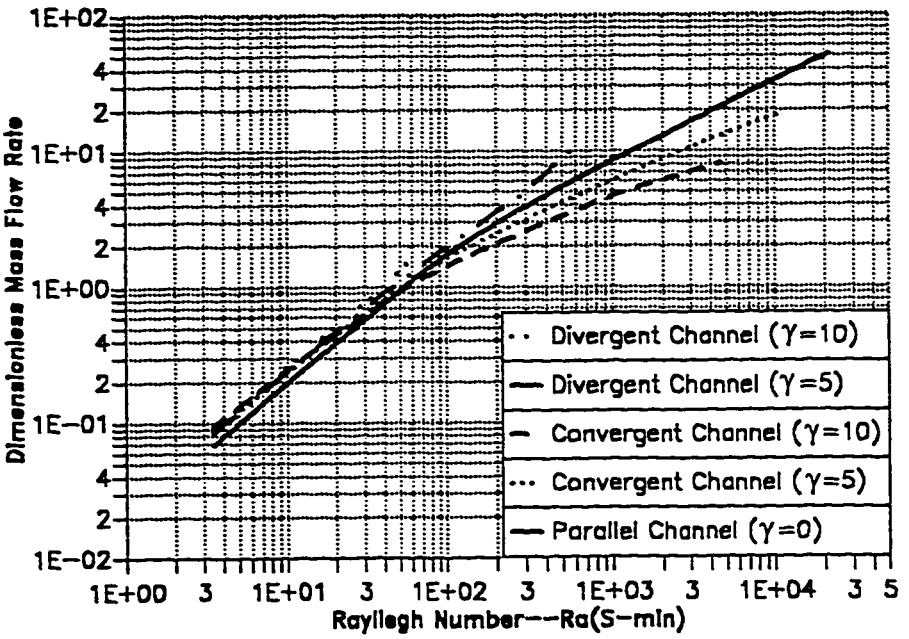

Figure 6.172 The Variation of Dimensionless Mass Flow Rate (Q) Versus the Rayliegh Number ($Ra_{S_{min}}$) for Obstructed Channels (AR = 0.3636).

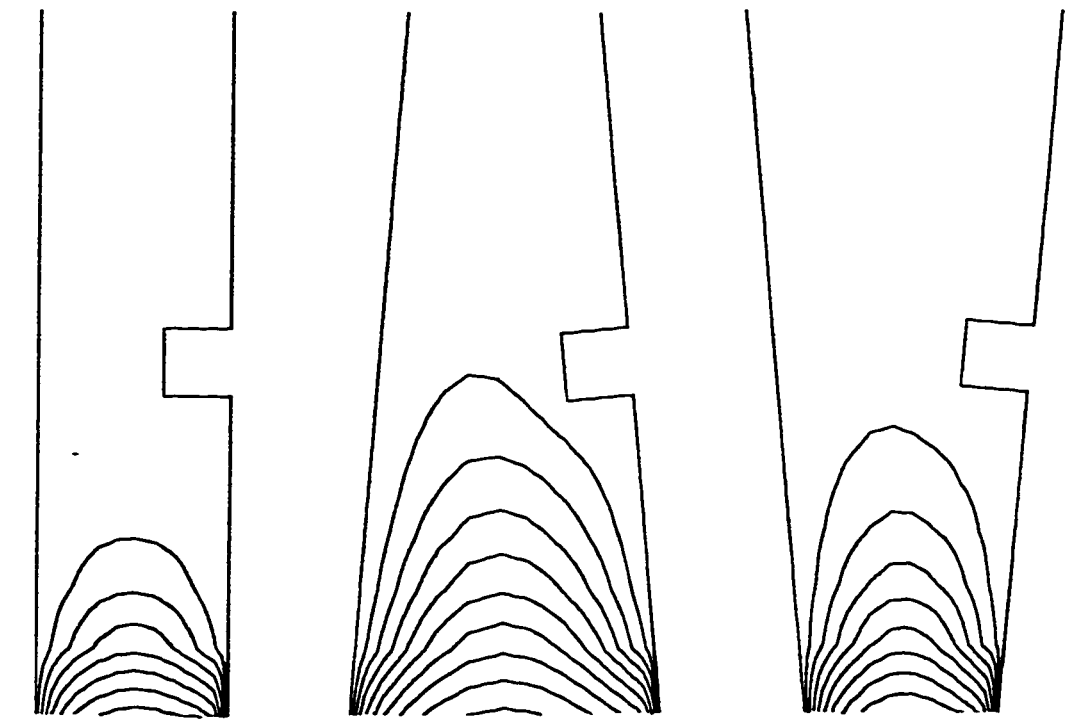

(a) Parallel ($\gamma = 0$) (b) Convergent ($\gamma = 5$) (c) Divergent ($\gamma = 5$)

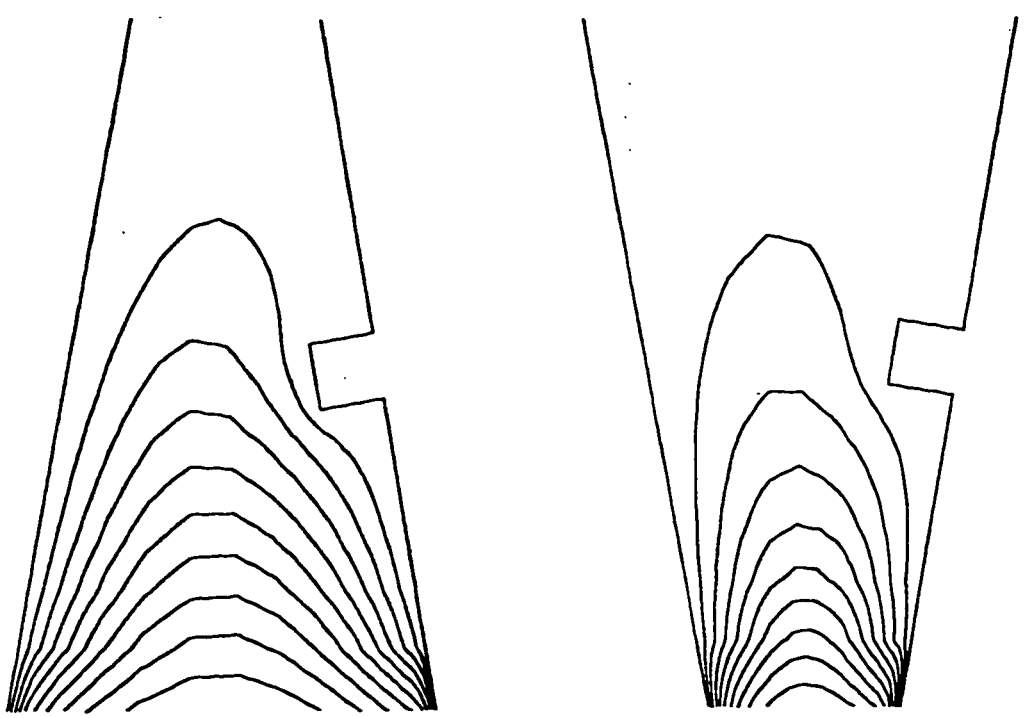

(d) Convergent ($\gamma = 10$) (e) Divergent ($\gamma = 10$)

Figure 6.173 Computed Isotherms for AR = 0.2727, Pr = 0.72, Ra = 29, $L_1 = 0.5$, $L_2 = 0.0945$ for Parallel, Convergent and Divergent Channels.

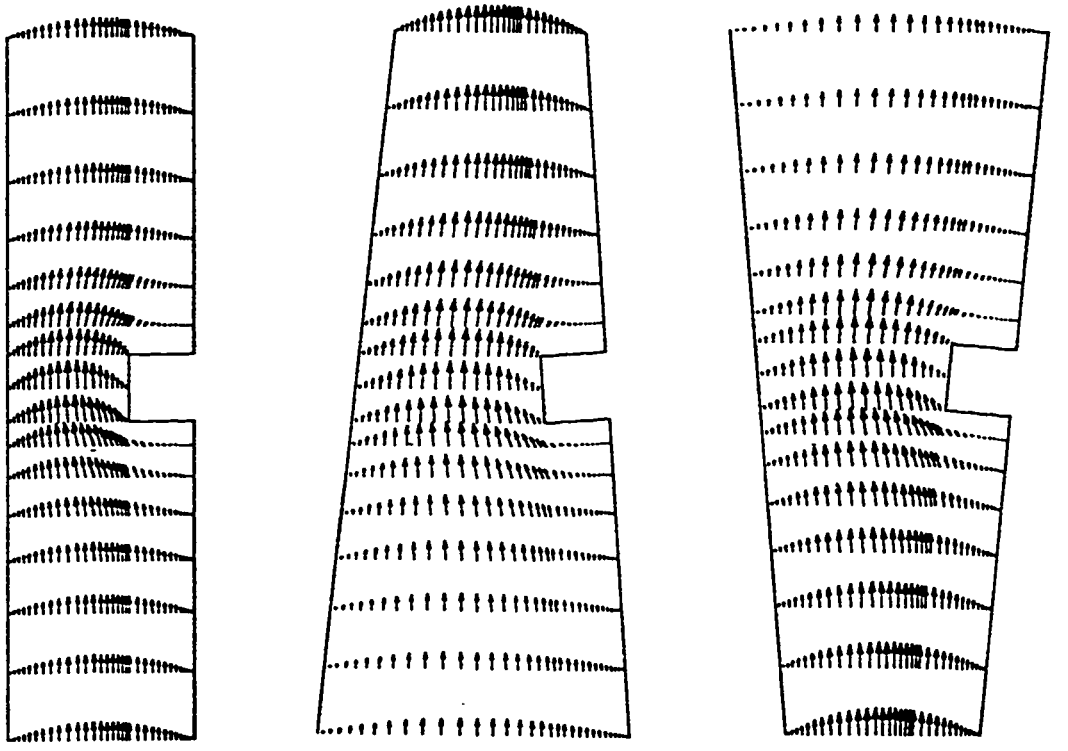

(a) Parallel ($\gamma = 0$) (b) Convergent ($\gamma = 5$) (c) Divergent ($\gamma = 5$)

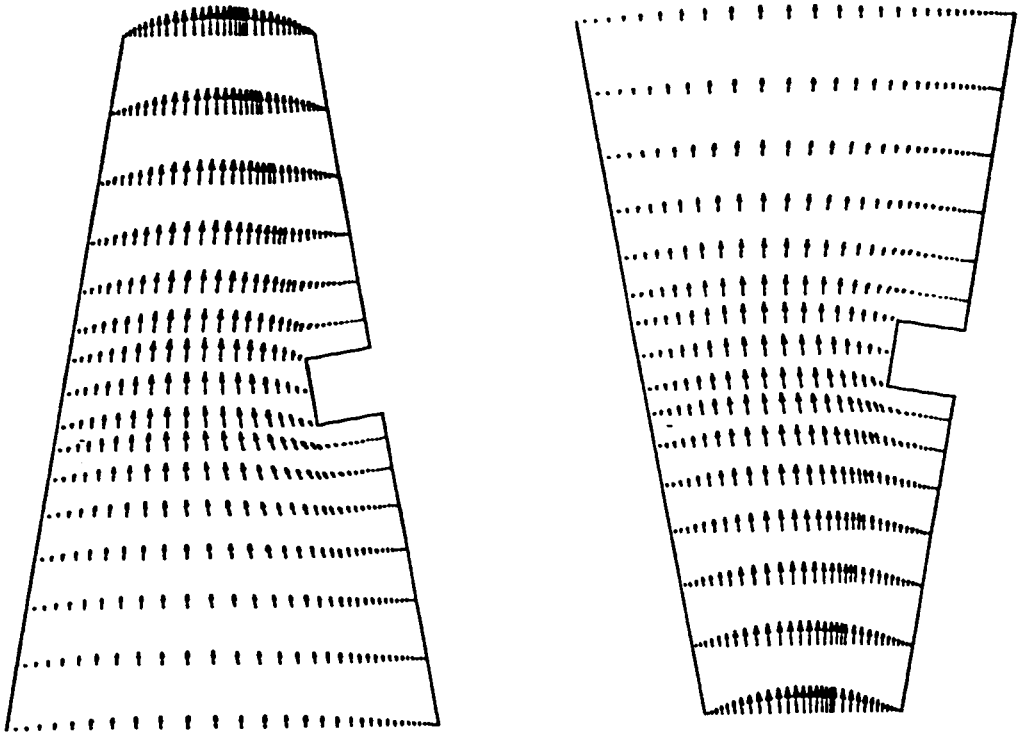

(d) Convergent ($\gamma = 10$) (e) Divergent ($\gamma = 10$)

Figure 6.174 Computed Velocity Vectors for AR = 0.2727, Pr = 0.72 , Ra = 29 , L_1 = 0.5 , L_2 = 0.0945 , for Parallel , Convergent and Divergent Channels.

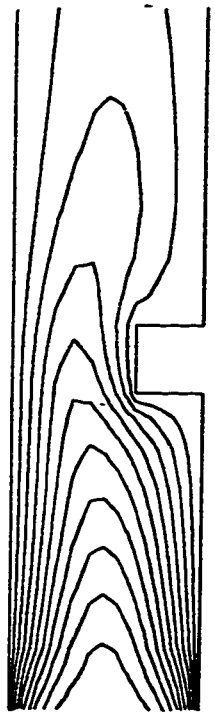

(a) Parallel ($\gamma = 0$)

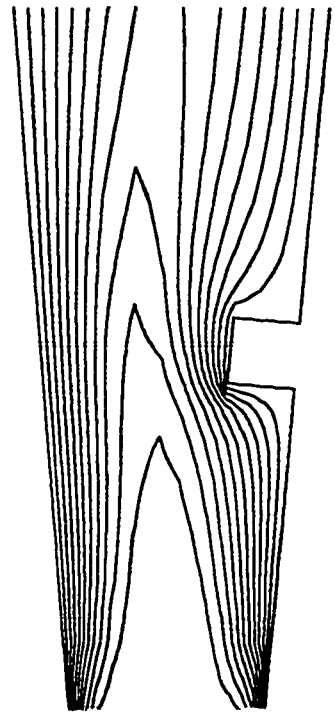

(b) Divergent ($\gamma = 5$)

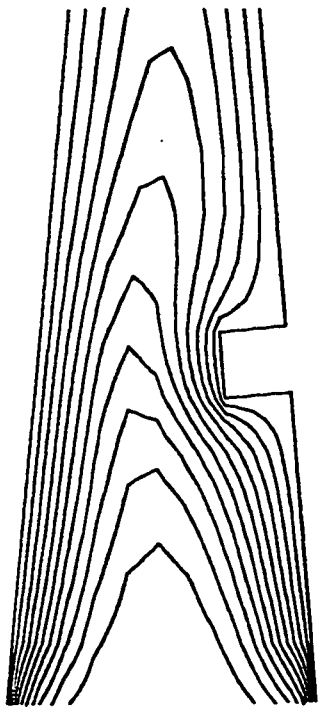

(c) Convergent ($\gamma = 5$)

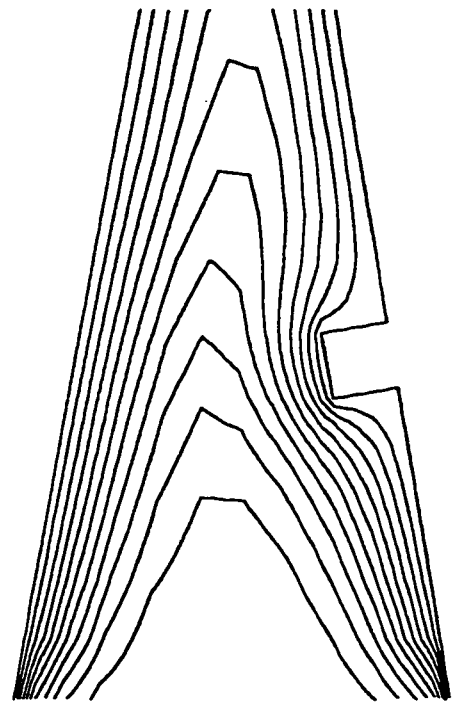

(d) Convergent ($\gamma = 10$)

Figure 6.175 Computed Isotherms for AR = 0.2727, Pr = 0.72, Ra = 491, $I_1 = 0.5$, $I_2 = 0.0945$ for Parallel, Convergent and Divergent Channels.

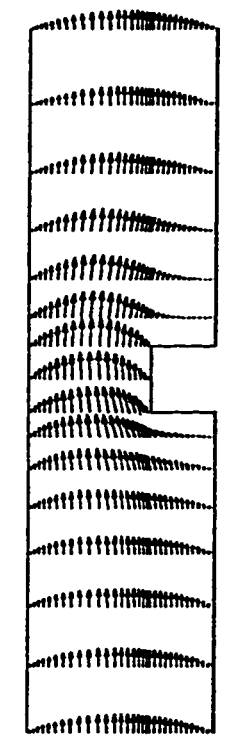

(a) Parallel ($\gamma = 0$)

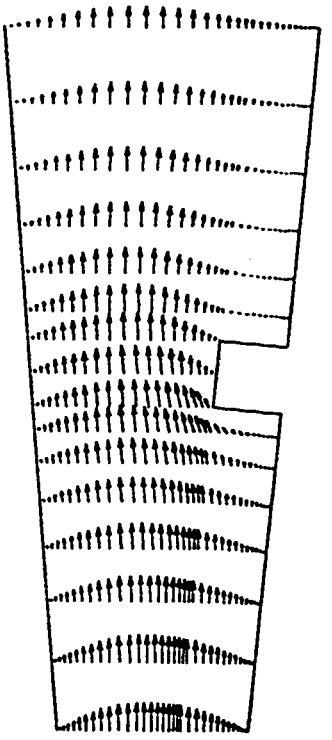

(b) Divergent ($\gamma = 5$)

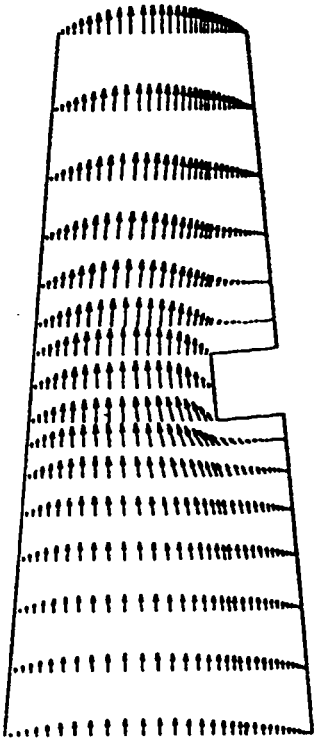

(c) Convergent ($\gamma = 5$)

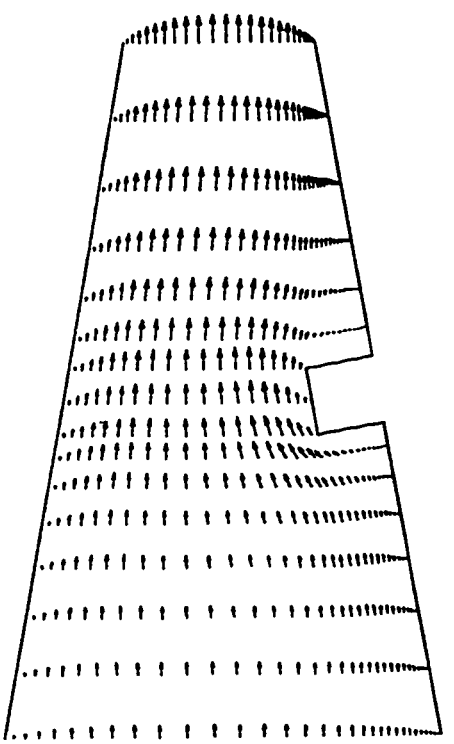

(d) Convergent ($\gamma = 10$)

Figure 6.176 Computed Velocity Vectors for AR = 0.2727, Pr = 0.72, Ra = 491, $I_1 = 0.5$, $I_2 = 0.0945$, for Parallel, Convergent and Divergent Channels.

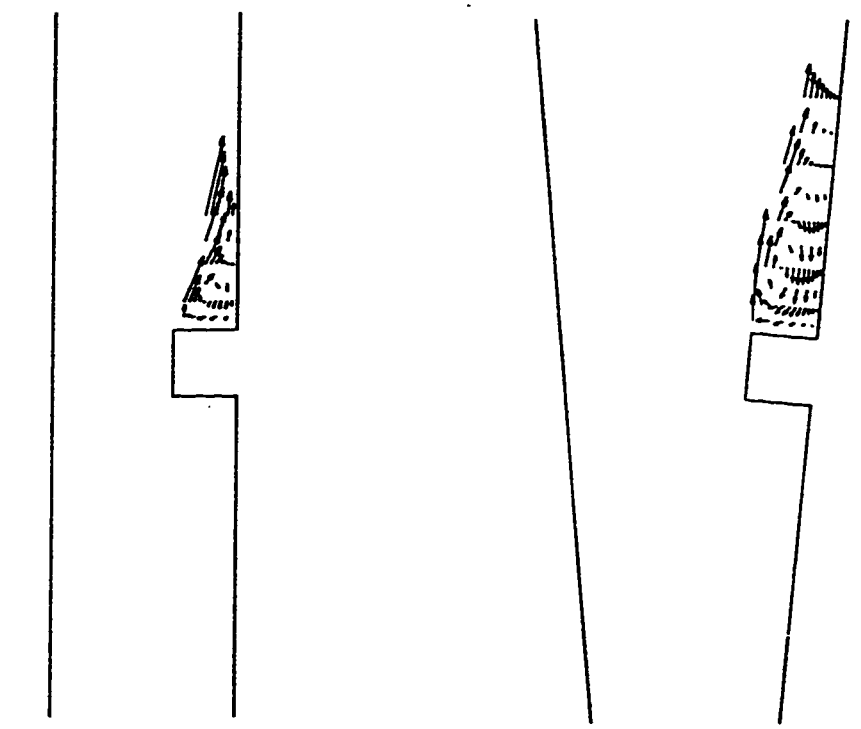

(a) Parallel ($\gamma = 0$)

(b) Divergent ($\gamma = 5$)

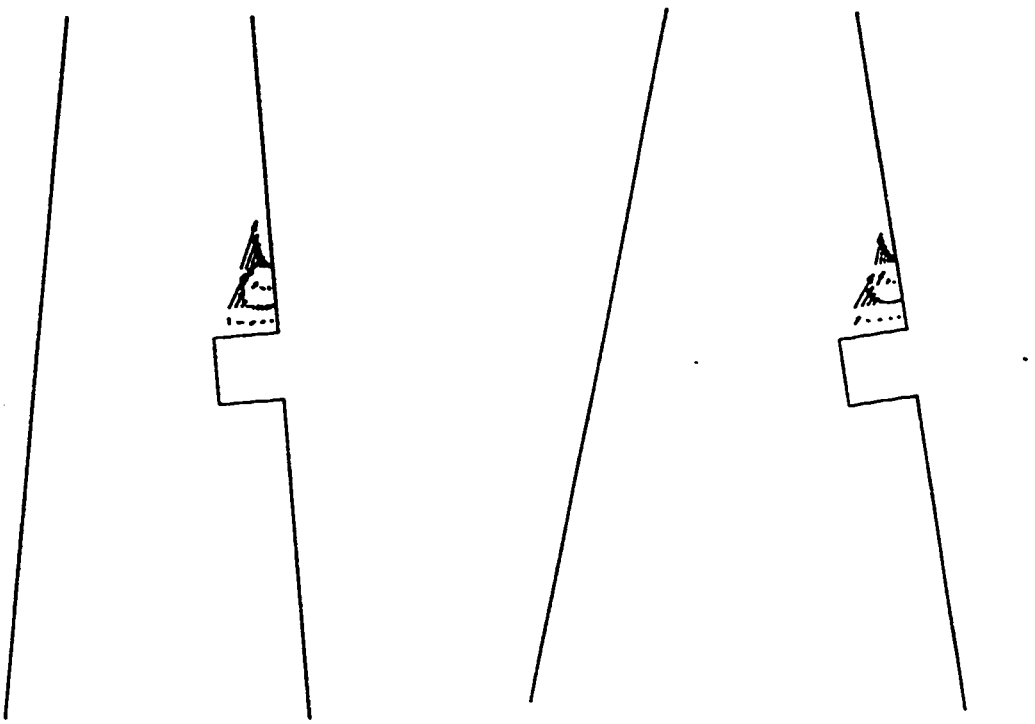

(c) Convergent ($\gamma = 5$)

(d) Convergent ($\gamma = 10$)

Figure 6.177 Computed Velocity Vectors (Enlarged) for AR = 0.2727 , Pr = 0.72 , Ra = 491 , $L_1 = 0.5$, $L_2 = 0.0945$, for Parallel , Convergent and Divergent Channels.

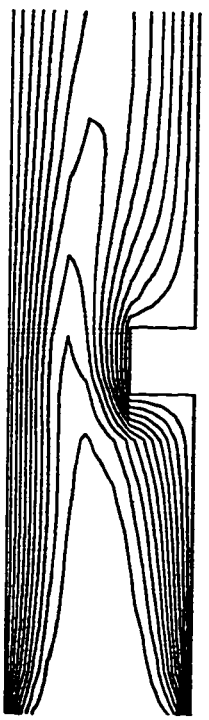

(a) Parallel ($\gamma = 0$)

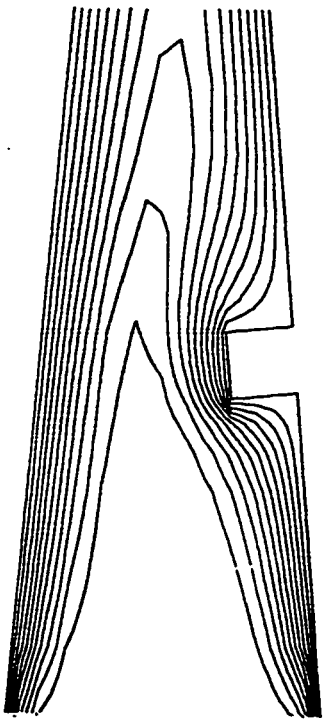

(b) Convergent ($\gamma = 5$)

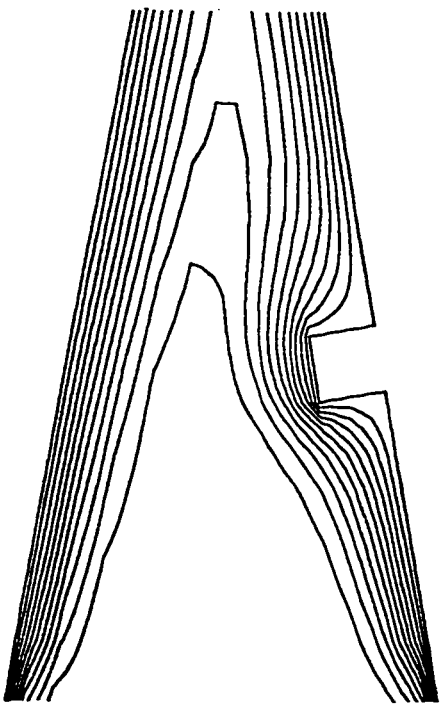

(c) Convergent ($\gamma = 10$)

Figure 6.178 Computed Isotherms for AR = 0.2727, Pr = 0.72, Ra = 3451, $I_1 = 0.5$, $I_2 = 0.0945$ for Parallel and Convergent Channels.

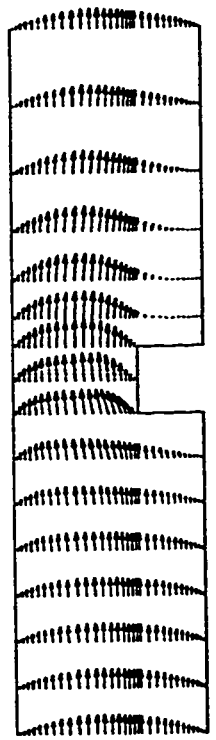

(a) Parallel ($\gamma = 0$)

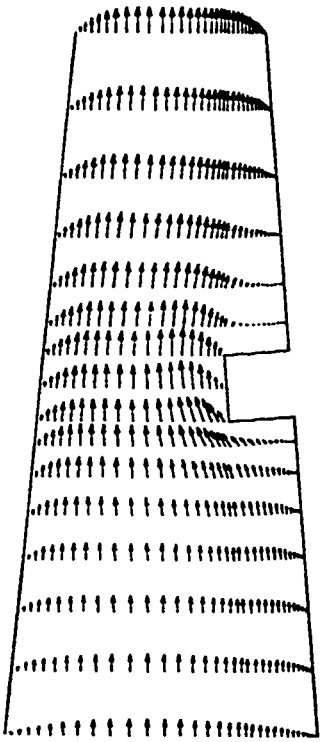

(b) Convergent ($\gamma = 5$)

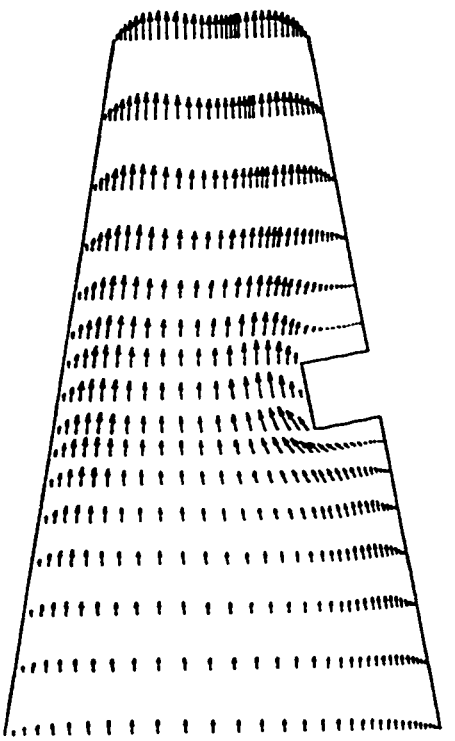

(c) Convergent ($\gamma = 10$)

Figure 6.179 Computed Velocity Vectors for AR = 0.2727 , Pr = 0.72 , Ra = 3451 , $L_1 = 0.5$, $L_2 = 0.0945$, for Parallel and Convergent Channels.

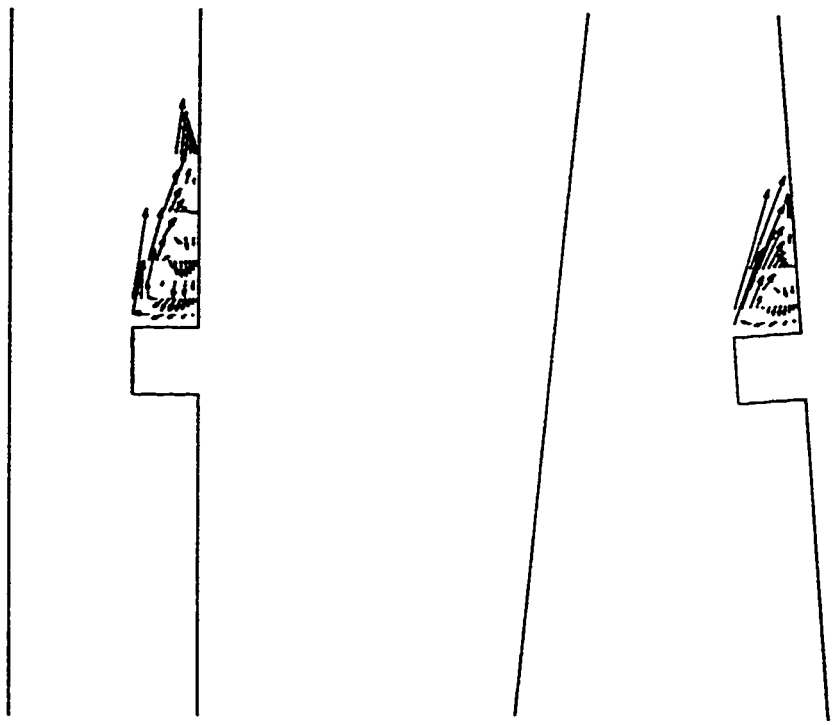

(a) Parallel ($\gamma = 0$)

(b) Convergent ($\gamma = 5$)

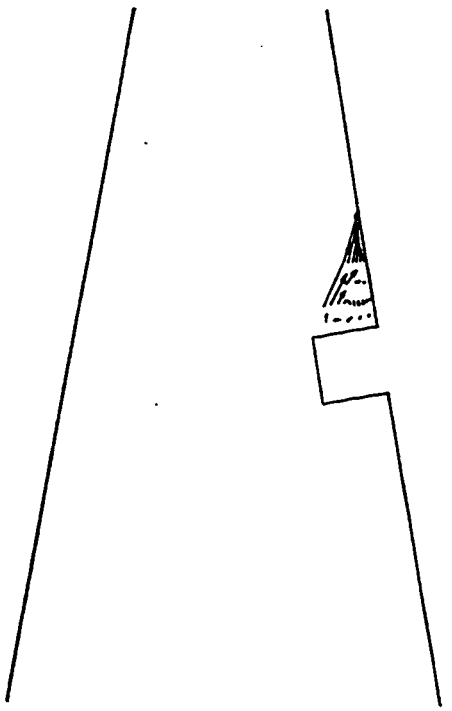

(c) Convergent ($\gamma = 10$)

Figure 6.180 Computed Velocity Vectors (Enlarged) for AR = 0.2727 , Pr = 0.72 , Ra = 3451 , $L_1 = 0.5$, $L_2 = 0.0945$, for Parallel and Convergent Channels.

CHAPTER 7

CONCLUSIONS & RECOMENDATIONS

7.1 Conclusions

Steady-state natural convection inside an isothermally heated vertical channel with a single square obstruction has been numerically investigated. The working fluid was air. The dimensionless parameters of interest are the Rayliegh number, the aspect ratio, the size of the obstruction, the obstruction hight and the angle of convergence and divergence. The effect of these parameters on the heat transfer characteristics was studied and the following were found :

1) The obstructed parallel-walled vertical channel average Nusselt number curve represents three flow regimes similar to the average Nusselt number curve for the unobstructed parallel-walled vertical channel.
2) Although the heat transfer area increases due to the presence of the obstruction, the average Nusselt number decreases due to the decrease in the mass flow rate and the increase in the boundary layer thickness, caused by the presence of the obstruction.
3) The average Nusselt number for the obstructed parallel-walled vertical channel increases as the Rayliegh number increases.
4) The average Nusselt number for the obstructed parallel-walled vertical channel increases as the aspect ratio increases.
5) The average Nusselt number for the obstructed parallel-walled vertical channel decreases as the obstruction moves away from the channel

entrance towards the exit. This is due to the decrease of the mass flow rate and the increase in the boundary layer thickness, due to the location of the obstruction away from the channel entrance.

6) The average Nusselt number decreases as the obstruction width increases. Although the heat transfer area increased by increasing the obstruction width, the average Nussel number decreased due to the decrease in the mass flow rate and the increase in the boundary layer thickness.

7) The comparison between the average Nusselt number $\overline{Nu}_{S_{exit}}$ curves for convergent and parallel-walled channels shows that convergence increases the average Nusselt number for $Ra_{S_{exit}} < 700$ and decreases the average Nusselt number for $Ra_{S_{exit}} > 700$.

8) Increasing the angle of convergence, increases the average Nusselt number $\overline{Nu}_{S_{exit}}$ for $Ra_{S_{exit}} < 700$ and decreases it for $Ra_{S_{exit}} > 700$.

9) Basing the Rayliegh number and the average Nusselt number on the entrance width of the convergent channel S_{ent}, the curves of the average Nusselt number for the parallel-walled and convergent channels show a better agreement with each other with a maximum difference of about 20%.

10) The comparison between the average Nusselt number curves $\overline{Nu}_{S_{ent}}$ for divergent and parallel-walled channels shows that divergence increases the average Nusselt number for $\overline{Nu}_{S_{ent}} < 500$. The effect of divergence on high $Ra_{S_{ent}}$ was not studied due to the limited capability of the numerical code.

11) Increasing the angle of divergence, increases the average Nusselt number $\overline{Nu}_{S_{ent}}$ at low Rayliegh numbers $Ra_{S_{ent}}$.

12) A comparison between convergent and divergent channels having the same angle of convergence and divergence, show that the average Nusselt number $\overline{Nu}_{S_{min}}$ for a convergent channel is higher than for the divergent one at low Rayliegh numbers $Ra_{S_{min}}$.

7.2 RECOMMENDATIONS FOR FURTHER STUDIES

The effect of the following aspects on the heat transfer characteristics can be studied :

1) The presence of more than one obstruction.

2) Other obstruction geometries.

3) Other boundary conditions.

4) Other angles of convergence and divergence.

REFERENCES

1) Aung, W. and Chaimah B., "Laminar Heat Exchange in Vertical Channels-Applications to Cooling of Electronic Systems". In *Low Reynolds Number Flow Heat Exchange* (Edited by S. Kakac, R. K. Shah and A. E. Bergles), p.395. Hemisphere, Washington,DC (1983).

2) Jaluria, Y. "Natural Convection Cooling of Electronic Equipment". In *Natural Convection, Fundamentals and Applications*, p.961. Hemisphere, Washington,DC (1985).

3) Kraus, A. D. and Bar-Cohen, A. *Thermal Analysis and Control of Electronic Equipment*, McGraw-Hill, New york (1983).

4) Steinberg, D. S. *Cooling Techniques for Electronic Equipment.* John Wiley & Sons, Inc. New York (1980)

5) Bergles, A. E. "The Evolution of Cooling Technology for Electrical, Electronic and Microelectronic Equipment". In *Heat Transfer in Electronic Equipment.* ASME/AIAA proceedings, (Edited by A. Bar-Cohen) Boston, June (1986).

6) Incorpera, F. P. "Convection Heat Transfer in Electronic Equipment Cooling". In *Journal of Heat Transfer.* ,Vol 110,1097-1111, November(1988).

7) Ortiga, A. and Moffat, R. j. "Heat Transfer From an Array of Simulated Electronic Components: Experimental Results for Free Convection With and Without a Shrounding Wall",In *Heat Transfer in Electronic Equipment*, (Edited by S. Oktay and R. J. Moffat) ASME publication NO. HTD-Vol 48, pp.5-15,Colorado,August(1985).

8) Meara, T. O. and Poulikakos, D. "Experiments on The Cooling by Natural Convection of an Array of Vertical Heated Plates With Constant Heat Flux,". *The International Journal of Heat and Fluid Flow*, Vol.8,No.4,313-319, December(1987).

9) Karki, K. C. and Patankar, S. V. "Cooling of a Vertical Shrouded Fin Array by Natural Convection: A Numerical Study". In *Fundamentals of Natural Convection /Eloctronic Equipment Cooling* (Edited by L. C. Witte and L. S. Saxena), ASME Publication NO. HTD-Vol 32, 33-40 (1984).

10) Ostrach, S. "An Analysis of Laminar Free Convection Flow and Heat Transfer about A Flat Plate Parallel to the Direction of the Generating Body Force", *NACA*, TN 2635 (1952).

11) Sparrow, E.M. and Gregg, J.L. "Laminar Free Convection From A Vertical Plate with Uniform Surface Heat Flux", *Trans. ASME* 78, 435-440 (1956).

12) Kierkus, W.T. "An Analysis of Laminar Free Convection Flow and Heat Transfer about An Inclined Isothermal Plate", *Int. J. Heat Mass Transfer* 11, 241-253 (1968).

13) Pera, L. and Gebhart, B. "Natural Convection Boundary Layer Flow over Horizontal and Slightly Inclined Surfaces", *Int. J. Heat Mass Transfer* 16, 1131-1146 (1973).

14) Hasan, M.M. and Eichhorn, R. "Local Nonsimilarity Solution of Free Convection Flow and Heat Transfer from An Inclined Isothermal Plate", *J. Heat Transfer* 101,642-647 (1979).

15) Gebhart, B. "Buoyancy Induced Fluid Motions Characteristics of Applications in Technology" The 1978 Freeman Scholar Lecture, *J. Fluid Engng* 101, 5-28 (1979).

16) Chen, T.S. and Tzuoo, K.L. "Vortex Instability of Free Convectin Flow over Horizontal and Inclined surfaces", *J. Heat Transfer* 104, 637-643 (1982).

17) Shaukatullah, H. and Gebhart, B. "An Experimental Investigation of Natural Convection Flow on An Inclined Surface", *Int. J. Heat Mass Transfer* 21, 1481-1490 (1978).

18) Yousef, W.W. , Tarasuk, J.D. and McKeen, W.J. "Free Convection Heat Transfer from Upward-Facing Isothermal Horizontal Surfaces", *J. Heat Transfer* 104, 493-500 (1982).

19) Vliet, G.C. "Natural Convection Local Heat Transfer on Constant Heat-Flux Inclined Surfaces", *J. Heat Transfer* 91, 511-516 (1969).

20) Fujii, T. and Imura, H. "Natural-Convection Heat Transfer From A plate With Arbitrary Inclination,". *Int.J.Heat and Mass Transfer*, ,Vol.15 ,755-767(1972).

21) Vliet, G.C. and Ross, D.C. "Turblent Natural-Convection On Upward and Downward Ficing Inclined Constant Heat Flux Surfaces",. *J.Heat and Mass Transfer*, ,Vol.97 ,549-555 (1975).

22) Siebers, D.L. , Moffat, R.J. and Schwind, R.G. "Experimental, Variable Properties Natural Convection From a Large- Vertical, Flat Surface, *Proc. ASME-JSME Thermal Engng Joint Conf.* , Vol.37, 269-275 (1983).

23) Chen, T. S. , Tien, H. C. and Armaly, B. F. "Natural Convection on Horizontal,Inclined and Vertical Plates with Veriable Surface Temperature or Heat Flux,". *Int.j.Heat Mass Transfer*, Vol.29, No.10, 1465-1478 (1986).

24) AL-Arabi, M. and Sakr, B. "Natural Convection Heat Transfer From Inclined Isothermal Plates,". *Int.j.Heat Mass Transfer*, Vol.31, No.3, 559-566 (1988).

25) Elenbass, W. "Heat Dissipation of Parallel Plates by Free Convection.", *Physica* 9,1-28 (1942).

26) Bodoia, J. R. and Osterle, J.F. "The Development of Free Convection Between Heated Vertical Plates.", *ASME J. Heat Transfer* 84, 40-44 (1962).

27) Engel, R. K. and Mueller, W. K. "An Analytical Investigation of Natural Convection in Vertical Channels", *ASME Paper* No. 67-HT-16. Presented at the ASM-AICHE Heat Transfer Conf. ,Seattle, Washington, 6-8 August(1967).

28) Aung, W. "Fully Developed Laminar Free Convection Between Vertical Plates Heated Asymmetrically,". *Int.J.Heat Mass Transfer*, Vol.15, 1577-1580,Pergaman Press(1972).

29) Aung, W. ,Fletcher, L. S. and Sernas, V. "Development of Laminar Free Convection Between Vertical Flat Plates with Asymmetric Heating", *Int.J .Heat Mass Transfer* 15, 2293-2328 (1972).

30) Currie, I. G. and Newman,W. A. "Natural Convection between Isothermal Vertical Surfaces", Preprints 4th *Int.Heat Transfer Conf.*, Versailles, Vol.4, NC 2.7 (1970).

31) Levy, E. K. "Optimum Plate Spacings for Laminar Natural Convection Heat Transfer From Parallel Vertical Isothermal Flat Plates." *Journal of Heat Transfer*, November (1971).

32) Bar-Cohen, A. and Rohsenow, W. M. "Thermally Optimum Spacing of Vertical ,Natural Convection Cooled, Parallel Plates" *ASME HTD*, Vol.20, 11-23 (1981).

33) Akbari, H. T. and Borges, R. "Finite Convective Laminary Flow Within Trombe Wall Channel" *Solar Energy*, 22, 165-174 (1979).

34) Sparrow, E. M. and Bahrami, P. A. "Experiments in Natural Convection From Vertical Parallel Plates With Either Open or Closed Edges" *ASME J. Heat Transfer*, 102, 221-227 (1980).

35) Joshi, Y. and Gebhart, B. "Effect of Pressure Stress Work and Viscous Dissipation in Some Natural Convection Flows" *Int. J. Heat and Mass Transfer*, Vol.24, No.10, 1577-1588 (1981).

36) Yao, L. S. "Free and Forced Convection in The Entry Reagion of A Heated Vertical Channel" *Int. J. Heat Mass Transfer*, Vol.26, No.1, 65-72 (1983).

37) Sparrow, E. M., Chrysler, G. M. and Azevedo, L. F. "Observed Flow Reversals and Measured-Predectived Nusselt Numbers for Natural Convection in a One Sided Heated Vertical Channel" *Journal of Heat Transfer*, Vol.106, 325-332, May(1984).

38) Azevedo, L. F. A. and Sparrow, E. M. "Natural Convection in Open-Ended Inclined Channels." *Journal of Heat Transfer*, Vol.107, 893-901, November(1985).

39) Burch, T. Rhodes, T. and Acharya, S. "Laminar Natural Convection Between Finitely Conducting Vertical Plates" *Int. J. Heat Mass Transfer*, 28, 1173-1186 (1985).

40) Azevedo, L. F. A. and Sparrow, E. M. "Natural Convection in a Vertical Channel Vented to the Ambiant Through an Aperture in the Channel Wall" *Int.J. Heat Mass Transfer*, Vol.29, No.6 , 819-830 (1986).

41) Sparrow, E. M. and Azevedo, L. F. A. "Vertical-Channel Natural Convection Spanning Between the Fully- Developed Limit and the Single-Plate Boundary-Layer Limit" *Int.J. Heat Mass Transfer*, Vol.28, No.10, 1847-1857 (1985).

42) Sparrow, E. M. ,Ruiz, R. and Azevedo, L. F. A. "Experimental and Numerical Investigation of Natural Convection in Convergent Vertical Channels" *Int.J. Heat Mass Transfer*, Vol.31, No.5, 907-915 (1988).

43) Sparrow, E. M. and Ruiz, R. "Experiments on Natural Convection in Divergent Vertical Channels and Corellation of Divergent,Convergent and Parallel- Channel Nusselt Numbers" *Int.J. Heat Mass Transfer*, Vol.31, No.11, 2197-2205(1988).

44) Habchi, S. and Acharya, S. "Laminar Mixed Convection in a Partially Blocked Vertical Channel" *ASME/AIAA Preceedings*, Boston,June(1986).

45) Patankar, S. V. *Numerical Heat Transfer and Fluid Flow* ,1st Edition,Hemisphere,New York(1980).

46) Sparrow, E. M. and Chrysler, G. M. "Natural Convection Heat Transfer Coefficients for a Short Horizontal Cylinder Attached to A Vertical Plate" *ASME Journal of Heat Transfer* ,103, 630-637(1981).

47) Said, S. A. and Krane, R. J. "An Analytical and Experimental Investigation of Natural Convection Heat Transfer in Vertical Channels With a Single Obstruction", *Int.J. Heat Mass Transfer*, Vol.33, No.6, 1121-1134 (1990).

48) Richtmyer, R. D. and Morton, K. W. *Difference Methods for Initial-Value Problems*. Jone Wiley & Sons, New York (1967).

49) Mitchell,A. R. and Griffiths, D. F. *Finite Difference Method in Partial Differential Equation*, Jone Wiley & Sons, New York,(1980).

50) Peyret, R. and Taylor, T. D. *Computational Methods for Fluid Flow*, Springer-Verlag, New York (1983)

51) Baker, A. J. , *Finite Element Computational Fluid Mechanics*, Mc Grow-Hill, New York (1983).

52) Zienkicoicz, O. C. *The Finite Element Method*, Mc Grow- Hill, New York (1977).

53) Huebner, K. H. *The Finite Element Method for Engineers*, Jone Wiley & Sons, New York (1975).

54) Gartling, D. K. *NACHOS-a Finite Element Computer program for Incompressible Flow Problems,Part I- Theortical Background*, SAND 77-1333, Sandia Laboratories, Albuquerque,NM(1978a).

55) Gartling, D.K. *NACHOS-a Finite Element Computer program for Incompressible Flow Problems,Part II- Users Manual*, SAND 77-1334, Sandia Laboratories, Albuquerque,NM(1978b).

56) Finlayson, B.A. *The Method of Weighted Residuals and Variational Principles*, Academic Press, New York (1972).

57) Gartling, D. K. , Nickell, R. E. and Tanner, R. I. "A Finite Element Convergence Study for Accelerating Flow Problems" ,*Int. J. Num. Meth. Engr.*, 11, p.1155 (1977).

58) Irons, B. M. A Frontal Solution Program for Finite Element Analysis, *Int. J. Num. Meth. Engr.*, 3, p.519 (1971).

59) Davis, G. and Games, I.P. "Natural Convection In A Square Cavity," *Int. J. Num. Meth. in Fluids*, vol.3, 227-248 (1983).

60) Churchill, S. W. "A Comprehensive Correlating Eqaution for Bouyancy-Induced Flow in Channels", *Letters in Heat and Mass Transfer* 4, 193-199 (1977).